CHARACTERIZATION AND MECHANICAL MODELING OF UV-AGED SEMICRYSTALLINE POLYMERS

A Dissertation

by

ANA KARINA RODRIGUEZ ATENCIO

Submitted to the Office of Graduate and Professional Studies of
Texas A&M University
in partial fulfillment of the requirements for the degree of

DOCTOR OF PHILOSOPHY

Co-Chairs of Committee,	Amine Benzerga
	Bilal Mansoor
Committee Members,	Jaime Grunlan
	Matt Pharr
Head of Department,	Ibrahim Karaman

December 2020

Major Subject: Materials Science and Engineering

ABSTRACT

Polymers inevitably undergo various types of aging in service, which depend on environmental factors such as UV radiation, heat, and humidity. Previous work on polymer aging has focused on either its chemical or mechanical features; however, little attention has been paid to the chemo-mechanical aspects of oxidative embrittlement. In order to determine to what extent the UV-induced changes at the molecular level are coupled to the mechanical behavior, it is necessary to consider the processes at the mesoscale, which are often overlooked in the literature.

In this work, the effects of UV aging on a semicrystalline polymer are investigated at various scales through a combination of physico-chemical, damage, and mechanical characterization. For this, low-density polyethylene (LDPE) films and plates were submitted to three types of photo-initiated aging processes: UV, hydrothermal-UV (HUV), and natural aging. Various phenomena on the mesoscale were uncovered. Characterization of the chemo-mechanical aspect of aging showed that photo-oxidation leads to microcracking in the absence of mechanical loads. Through damage characterization, we showed that aged LDPE cavitates, in contrast with pristine LDPE that is known not to cavitate. Mechanical experiments evidenced that a UV-induced transient strengthening occurs at intermediate radiation doses. Moreover, this transient strengthening was common to all aging types and specimen geometries (film and bulk). All these phenomena are discussed here in terms of competition between multi-scale processes: chain scission and cross-linking at a fine scale, chemi-crystallization, oxidation-induced cracking, and mechanical damage at the meso and coarse scales. In addition, whether accelerated aging can be correlated to natural aging is not totally settled. A comparison of mechanical results shows a correlation between accelerated aging (HUV) and natural aging. Whether this translates into a correlation in mechanical damage is evaluated through fractography. Lastly, the oxidation of bulk polymer specimens is known to be heterogeneous due to diffusion-limited oxidation. A strategy was implemented

to estimate the extent of diffusion-limited oxidation via inverse modeling with a macromolecular model. The results provide insight into how oxidation affects changes in the internal state, which ultimately affects damage and the progression of oxidative embrittlement of semicrystalline polymers.

DEDICATION

To my family spread around the world: my parents Ali and Thais, my siblings Hilda y Ali, and my husband Nicola.

ACKNOWLEDGMENTS

Firstly I would like to thank my advisor Dr. Amine Benzerga for his guidance, patience, and encouragement throughout my Ph.D. degree. His scientific vision and curiosity are an inspiration. Special thanks to Dr. Bilal Mansoor for his advice and support during the last years. I would also like to thank the committee members: Dr. Jamie Grunlan, Dr. Matt Pharr, and Dr. Quentin Michaudel for their time and support. Special thanks to Dr. Georges Ayoub (University of Michigan) and Dr. Yazid Madi (MINES Paristech) for their invaluable advice and feedback. I would also like to thank to Dr. Xavier Colin (Arts et Métiers ParisTech) for his help with the physico-chemical characterization and fruitful discussions on polymer oxidation. I gratefully acknowledge Dr. Jacques Besson from MINES ParisTech for his time, guidance, and for implementing the macromolecular model in the Z-set software.

Nothing would get done without the invaluable help of Erin Banzda and Jules Henry from the MSEN department, Olga Sauseda from the AERO department, Cherine Hamad and Hania Ayyash from TAMUQ, to whom I will always be indebted.

I would like to thank all my friends and peers, in particular Marwa Abdelgawad, Jan Rojek, Hari Krishnan, Tim Brown and Kyungjun Lee. Special thanks to Kenneth Cundiff for all the fruitful discussions, advice, technical and moral support throughout the years.

I would like to thank my family: mami, papi, Hilda and Ali, for their unconditional love and support, which they let me feel even thousands of miles away. Their courage and constancy are my inspiration and motivation. Finally, to my husband, Nicola: we met, fell in love, and got married during this Ph.D., thanks for your love, support and patience during the last stage of this dissertation.

CONTRIBUTORS AND FUNDING SOURCES

Contributors

This work was supported by a dissertation committee consisting of Professor Amine Benzerga [advisor], Professors Bilal Mansoor [co-advisor], Jamie Grunlan of the Department of Materials Science and Engineering and Professor Matt Pharr of the Department of Mechanical Engineering. The following people also made a contribution to this work: Dr. Xavier Colin contributed to the physico-chemical characterization of the aged LDPE films presented in Chapter 2. Dr. Jacques Besson implemented the macromolecular model in the Z-set FEM software used in Chapter 5. All other work conducted for the dissertation was completed by the student independently.

Funding Sources

Graduate study was supported by the NPRP grant No. 7-1562-2-571 from the Qatar National Research Fund (a member of Qatar Foundation), graduate and teaching assistantships and scholarships from Texas A&M University, and by the Chateaubriand Fellowship of the Office for Science & Technology of the Embassy of France in the United States.

TABLE OF CONTENTS

Page

LIST OF FIGURES

FIGURE Page

LIST OF TABLES

TABLE Page

1. INTRODUCTION

1.1 Motivation

Semicrystalline polymers represent the largest portion of polymers produced worldwide; they are ubiquitous as commodity materials, high strength reinforcement, and structural polymers. semicrystalline polymers are materials composed of macro-molecules in which disordered, amorphous regions coexist with highly ordered crystalline domains. During their service life, polymers inevitably undergo some type of aging. There are multiple aging processes that a polymer typically goes through, and they can be classified as physical or chemical aging. Physical aging refers to changes in the molecular morphology of the polymer due to annealing and in the absence of other external factors, such as load or chemical reactions [12, 13], and it can occur during storage and thermal aging [14].

On the other hand, chemical aging involves chemical reactions of the macro-molecules and can be further divided into hydrolysis and oxidation reactions, such as thermal-oxidation and photo-oxidation. Depending on its application, a polymer can also experience various types of aging at the same time. Polymers in outdoor applications, for example, can experience thermal-oxidation, photo-oxidation and hydrolysis. Understanding the degradation, i.e., the loss of properties due to aging, of semicrystalline polymers is fundamental for several important applications, such as predicting the service life of materials, enhancing the durability of polymers during processing, extending the useful lifespan of a final product, improving material design and selection, increasing biodegradability, etc. Moreover, due to the recent COVID-19 pandemic, UV radiation is now widespread used for sterilization beyond the usual medical context, for instance on buses, subway carts and in offices. This exposes to UV radiation some plastic components that may not have been designed with such exposure in mind.

Additionally, environmental policies, such as the Environmental Protection Agency (EPA)

Trash-Free Waters program [15] is focused on

> "...reducing the land-based types of products and packaging (primarily single-use disposables) that end up as marine debris. Through source reduction, we can greatly reduce the amount of trash getting into waterways, and marine debris."

while the European Union's "Circular Economy Package" [16], launched in 2015, calls for:

> "A strategy on plastics in the circular economy, addressing issues of recyclability, biodegradability... and the Sustainable Development Goals target for significantly reducing marine litter."

Similar policies can be expected to increase in the future, which emphasizes the importance of having a fundamental and clear knowledge of how the diverse aging processes will translate into key properties of recycled material. For polymers used in outdoor applications, this is of much concern considering the depletion of the stratospheric ozone and its potential consequences on aging, due to enhanced ultra-violet (UV) reactions [17]. Such is the case of polyethylene (PE), used in structural applications, such as pipelines, greenhouses, composites in automotive and aerospace industries, as well as functional applications in electrical insulation, and as composites in thermal energy storage applications.

In many of the applications where UV aging is an issue, it is the change in the mechanical behavior of the polymer that leads to the premature end of service life of the product. Even in their pristine condition, the mechanical behavior of amorphous polymers is complex due to its rate, temperature and pressure dependence. In addition, even at fixed temperature or rate, the nominal stress-strain response has an "up-and-down" behavior that evidences various hardening and softening mechanisms. A post-yield softening is related to a molecular rearrangement after plastic flow that makes the polymer more compliant [18]. At large strains, an entropic hardening is observed, which arises from the molecular re-orientation that occurs during deformation and that changes the configurational entropy of the material

[19]. The panorama is even more intricate in semicrystalline polymers due to the presence of crystalline domains embedded in amorphous regions. The response of semicrystalline polymers is dictated by the interaction between these two regions and involves the rotation, separation and stretching of crystallites, alternated with the uncoiling and stretching of amorphous regions [5, 20, 21].

Additionally, it is widely accepted that polymers are pressure sensitive [22]. Polymers shown higher flow stress in compression relative to tension [23]. In fact, a linear pressure dependence of the flow strength was demonstrated by Rabinowitz et al. [24] and Sauer et al. [25], confirmed experimentally by G'sell [26], and accounted for in the macromolecular model developed by Boyce and Arruda [22]. If plastic flow of polymers is associative, then this pressure sensitivity implies that the deformation of polymers is not volume preserving. Indeed, that large plastic deformation may lead to volume change in polymers has become increasingly accepted in the literature. However, the mechanisms involved in volume change are not fully understood. Whether volume change is due to crazing or mere cavitation (microvoids), the outcome is dilation and pressure-sensitivity of the mechanical behavior [27]. Crazing and cavitation are related since crazing is unavoidably preceded by some degree of voiding [28]. But they differ in that crazes propagate perpendicular to the loading axis and are able to transfer stress, while cavities are unable to transfer stress and can also propagate parallel to the loading axis. They also exhibit different patterns in small angle X-ray scattering (SAXS) [28, 29].

Works by Pawlak, Galeski, Laiarinandrasana and Morgeneyer [30–33] have shown the role of voiding and cavitation on the deformation of semicrystalline polymers such as polypropylene, polyamide 6 and high density polyethylene (HDPE). It is believed, however, that polymers with small crystals such as low density polyethylene (LDPE) do not develop cavities during tensile deformation [30] since the small crystals deform plastically before the critical stress necessary for voiding in the amorphous phase can be reached. The extent to which this hypothesis holds true has not been fully explored. Additionally, the literature remains

elusive on how physico-chemical aspects of UV affect cavitation damage in aged polymers. This can be significant since it has been established that chemical degradation alone may not be sufficient to predict the changes in mechanical properties of aged polymers [34].

Previous studies in polymer oxidation have investigated the changes in the chemistry of polymers with UV aging, paying special attention to the kinetics of the oxidation reactions and the formation of specific chemical groups [2,35,36]. On the other hand, the effects of UV aging on mechanical behavior have also been reported in the literature [1]. Special emphasis is generally given to the characterization of oxidative embrittlement, which manifests in the decrease of the (nominal) strain to fracture with increasing oxidation.

In general, previous work has focused on either chemical or mechanical aspects of aging, but little attention has been paid to the chemo-mechanical aspects of oxidative embrittlement. Fayolle et al. [37] correlated the oxidation chemical kinetics responsible for chain scissions with the decrease in strain to fracture by means of a critical molecular weight concept. This is illustrated in Fig. 1.1. According to such model, there is a critical molecular weight below which a drastic ductile to brittle transition occurs as measured by elongation to fracture. However, Fig. 1.1 shows that low molecular weights can lead to a wide range of elongation to fractures. Thus, molecular weight alone cannot determine the embrittlement of aged polymers, and other aging phenomena concurrent with chain-scission must play a role in the embrittlement of the material.

In order to identify these phenomena, it is necessary to look in the mesoscale, specifically, the processes of chemical and mechanical damage. In fact, damage characterization in the aged state and even unaged states of polymers has been widely overlooked, with the notable exception of the work by Qayyum and White in the late 80's [38, 39]. However, their work focussed only on naturally aged material, and the damage characterization was done after fracture. So the effects of accelerated aging on damage, as well as the progression of damage post-aging and during deformation remain unknown.

Determining to what extent the chemical aspects of UV aging are coupled to the mechan-

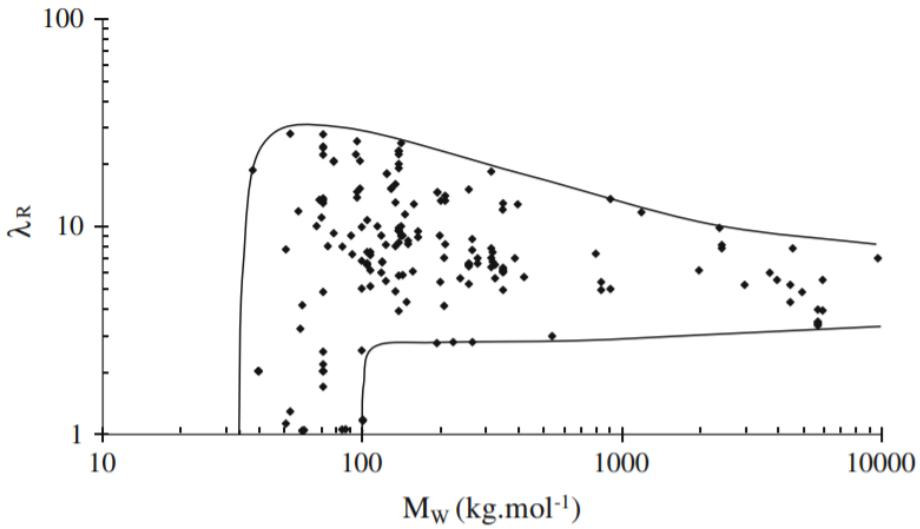

Figure 1.1: The ultimate tensile draw ratio γ_r versus weight average molecular weight M_w. Reprinted by permission from Springer Nature [1], Copyright 2008.

ical response of semicrystalline polymers is fundamental for the development of models that predict the service life of polymers. Decoupling chemical from mechanical effects involves experimentally assessing how UV aging affects the stress strain response of the material, damage and fracture process, as well as its temperature, pressure and strain rate sensitivity.

Such decoupling implies *per se* an exhaustive experimental campaign. The degradation of polymers under natural conditions is a complex process that combines UV radiation, temperature and humidity [14]. However, natural aging experiments present some practical drawbacks: (i) they require long term exposures due to low oxidation rates; (ii) the concurrency of several factors impedes proper discrimination of their individual contributions to the material's performance, and; (iii) the varying exposure conditions hinder any correlation between the aging factors and the resulting properties. Thus, a more appropriate way to study the individual contributions and mechanisms of the aging factors is to use a laboratory accelerated weathering tester, where the exposure of the material to UV, temperature and/or humidity is controlled and decoupling their effects on the behavior of the material becomes feasible. Understanding the chemo-mechanical aspect of oxidative embrittlement is even

more complex on bulk specimens due to oxygen diffusion limited oxidation (DLO). This results in a heterogeneous material composed of an oxidation layer and a pristine core. Lastly, whether accelerated and natural aging of polymers can be correlated is not settled [40], and damage studies of both can further our understanding of their connection.

The aforementioned aspects highlight the necessity to investigate oxidative embrittlement at intermediate scales, in particular chemical and mechanical damage processes. Thus, the overarching goal of this research is to characterize the photo-oxidation of semicrystalline polymers and investigate the role of aging-induced damage in oxidative embrittlement.

1.2 Research Objectives

With this goal in mind, the main objectives of this study are:

1. Investigate the chemo-mechanical aspects of UV aging prior to loading.
2. Examine the effects of UV aging on the mechanical behavior and damage progression.
3. Establish a connection between accelerated aging and natural aging.
4. Estimate the extent of diffusion-limited oxidation by means of inverse modeling.

With the first two objectives, we aim at a better understanding of the damage mechanisms operative in the degradation of semicrystalline polymers and its relationship with changes in the micro (chemical) and macro (mechanical) scales. This is achieved by a characterizing the damage in: (i) aged and unaged states, (ii) accelerated and natural aging, (iii) undeformed, deformed, and fractured states, (iv) film and plates, and; (iv) transverse and parallel planes. As stated above, kinetic models have been developed with increasing levels of sophistication which describe the effect of thermal and photo-oxidation on the chemical reactions via mechanistic schemes thereby predicting the evolution of key physical parameters, such as molecular weight and crystallinity. However, the prediction of UV-induced embrittlement *per se* remains elusive as it is based on phenomenological correlations between the said physical parameters and a measure of strain to failure (exclusively restricted to uniaxial

loading conditions). While useful under circumstances of homogeneous oxidation and simple mechanical measures of embrittlement, the resulting models cannot be used in predicting the structural response of polymeric components subjected to UV aging. This would enable photo-oxidation degradation models to be established, which would provide valuable input to material development and selection, but most importantly, that can inform physically based mechanical models.

In order to decompose these complex problems into smaller problems that can be separately tackled, we focused on one type of semicrystalline polyolefins, namely polyethylene. In addition to its technological importance, polyethylene belongs to a class of semicrystalline polymers that do not undergo severe hydrolysis, at least under ambient conditions. This choice of the material of the study therefore allowed us to focus on the processes of thermal and mostly photo-oxidation. With this in mind, although pristine PE is not reported to be sensitive to humidity, the issue of whether the UV induced chemical degradation is itself sensitive to water intake is far from settled. For this reason, the effect of humidity on the basic processes underlying UV aging, namely photolysis and possibly concurrent thermolysis, is investigated here. To put in context the results obtained from the aging under controlled laboratory conditions, the material was also subjected to natural aging. Moreover, photo-oxidation is a diffusion controlled process, in which the extent of the degradation is controlled by the diffusion of oxygen from the atmosphere at the surface to the core of the specimen. For this reason, both films and plates of polyethylene were used in this study to investigate the role of diffusion. Additionally, using films and plates allowed the study of any extrinsic (structural) effects on the resulting mechanical behavior of polyethylene.

The application of a physically based macro-molecular model allowed us to explore structural effects in the as-received material, replicate the response of the UV-aged material by inverse identification, and, to predict the extent of the oxidation layer in the diffusion controlled aging of bulk polymeric material. This is particularly relevant in the case of polymers due to their complex mechanical behavior which is rate and temperature dependent

and greatly influenced by molecular weight, crystallinity and anisotropy. Moreover, polymer oxidation is *per se* a complex phenomenon, especially in bulk specimens, since it is a diffusion controlled process that acts selectively on the amorphous regions, resulting in a heterogeneous material. Ultimately, the developed methodology can be a valuable tool in the study of degradation processes under various conditions.

1.3 Background and Literature Review

1.3.1 Mechanisms of Photo-oxidation of Polymers

Photo-oxidation of polymers share some similarities with thermal-oxidation, both are chain reaction processes initiated by free radicals [14]. However, the initiation process in photo-oxidation is more complex, and the species sensitive to the action of light are not necessarily the same species that would react under thermal energy. In fact, most polymers would not be expected to undergo photo-degradation based on their structure, since they are formed uniquely by C−C, C−O, C−Cl or C−H bonds, which cannot absorb radiations beyond 290 nm [41]. However, the inevitable presence of impurities that result from the synthesis and processing of polymers provide them with the necessary groups for absorption of UV radiation. These groups, known as chromophores (i.e. photon absorbing groups), can be classified as internal, external, and, chromophores that form part of the polymer structure [41]. Internal chromophores are located in the main backbone of the polymer, and result from the polymerization process, or thermal oxidation during processing. External chromophores are low molecular weight compounds that can be residues from the catalysts used in the polymerization, or additives (stabilizer, plasticizers, pigments, lubricants). Lastly, there are cases in which the chromophore is part of the monomer itself. Such is the case of polystyrene; whose benzene pendant group is light-absorbing [41].

In the presence of oxygen and light, polymers can undergo photo-oxidation degradation. Several specific mechanisms can be involved in the photo-oxidation of polymers depending on their chemical structure. These mechanisms include hydrogen abstraction, photoreaction of

carbonyl groups (R(C=O)R) or hydroperoxide groups (ROOH), energy transfer from phenyl (C_6H_5) to hydroperoxide (ROOH) groups, among others (R represents the macromolecule). These mechanisms are further detailed in the literature [41].

In the initiation step, chromophores species present in the polymer absorb a quantum of UV light, forming free radicals, as shown in the first three reactions of Fig.1.2, where the photo-oxidation reactions of polyethylene are presented. Attention is focused on the role of hydroperoxide groups (ROOH) in the photo-oxidation of PE. The reaction of oxygen with free radicals result in the formation of hydroperoxides (ROOH). These undergo photolytic decomposition to form hydroxyl ($ROH^{\bullet}$) and alkoxy ($RO^{\bullet}$) radicals. The alkoxy ($RO^{\bullet}$) radicals can react by several routes. When they react with the hydroxyl radicals ($ROH^{\bullet}$), ketones (ROR) are formed. An important distinction between thermal and photo-oxidation resides precisely in the role of ketones. In thermal-oxidation, ketones, together with other carbonyl species produced in the initial steps of oxidation, build up in the polymer since they are not thermolabile, thus they are not able to react further. However, during photo-oxidation, the ketones produced in the initial steps are able to react further since they are photosensitive, absorbing light at UV irradiance above 290 nm.

Ketones then undergo photolysis reactions, in special Norrish I and II reactions, which are described in more detail in in Fig. 1.3. These reactions are exclusive of photo-initiated oxidation, thus cannot occur during thermal-oxidation of polymers [2]. Norrish type I reaction results in the formation of carbonyl groups and lead to random chain scission of the polymer chain. On the other hand, Norrish type II reactions results from a ring decomposition mechanism and yield unsaturations (R=R). Eventually, these reactions lead to random chain scission and crosslinking. Finally, termination of the oxidation reactions occurs when bimolecular recombination occurs, or low molecular weight radicals react with each other [41].

The photo-oxidation of polyolefins depends on their physical properties, such as crystallinity, molecular weight and orientation. As crystalline regions are densely packed rigid zones, they reduce the chemical reactivity of the polymer chains by restricting their mobility.

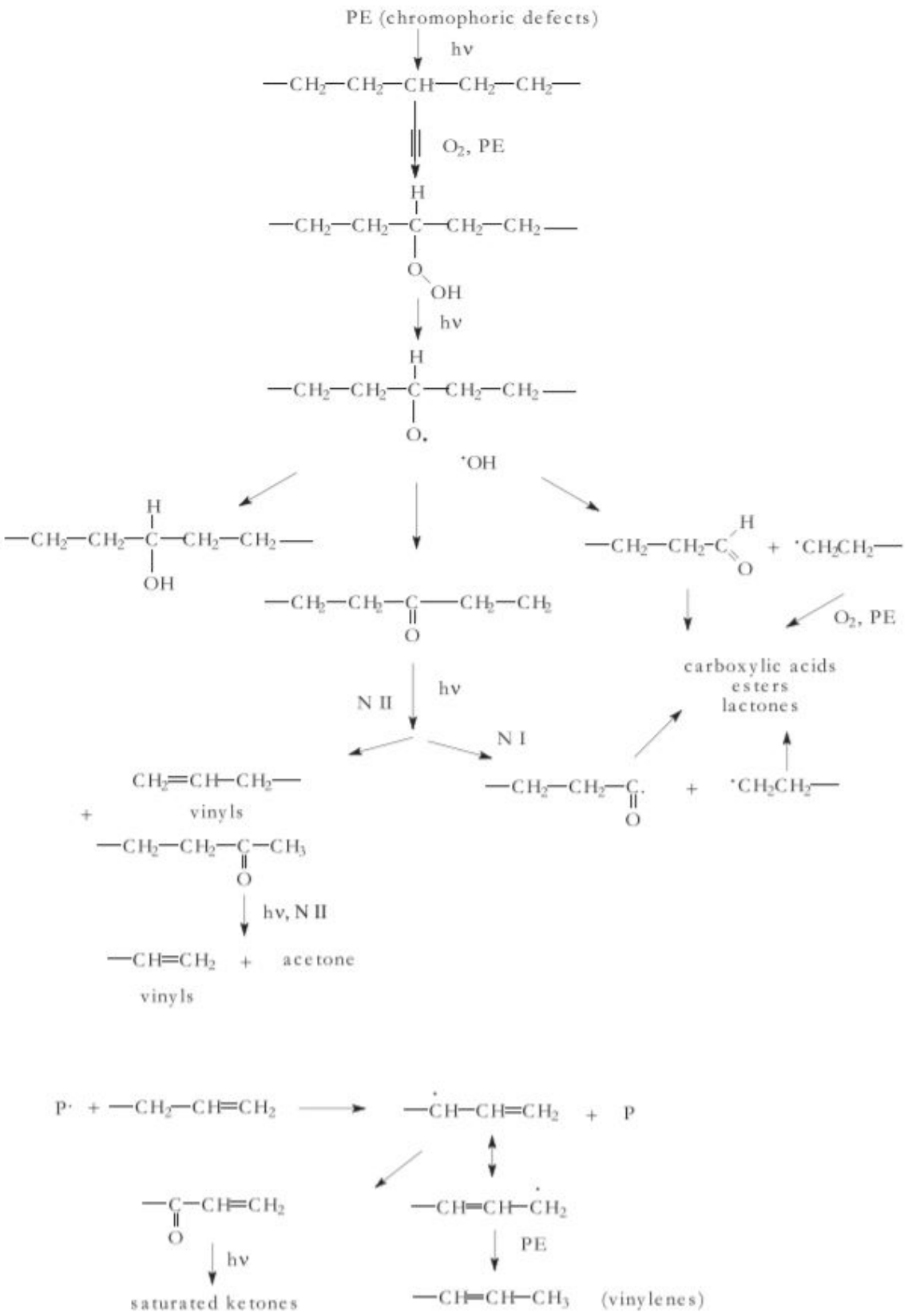

Figure 1.2: Scheme of photo-oxidation reactions taking place during the photo-oxidation of polyethylene (PE). Reprinted by permission from Elsevier [2], Copyright 2008.

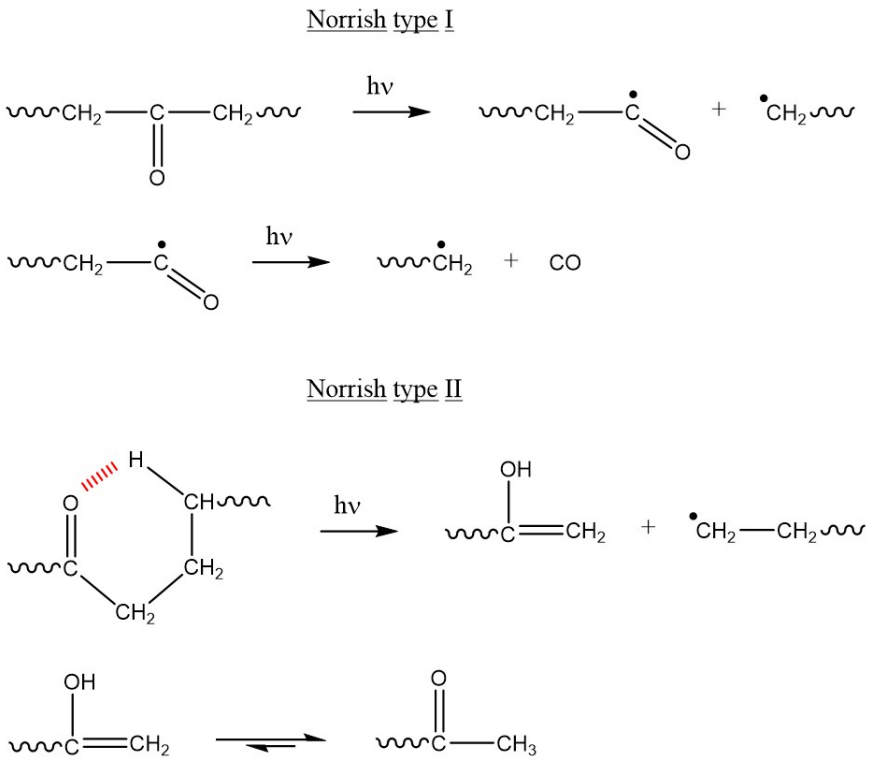

Figure 1.3: Initiation mechanisms of photo-oxidation in polyethylene: chain scission via a free radical chain mechanism (Norrish type I); and ring decomposition mechanism (Norrish type II). Reprinted by permission from Elsevier [3], Copyright 2011.

Additionally, the close packing prevents the diffusion of oxygen, affecting the propagation step of the photo-oxidation reaction (note the initial step of photo-absorption is not inhibited by the crystalline region) [42]. For this reason, it is generally assumed that the photo-oxidation reaction in semicrystalline polymers takes place in the amorphous region. The latter, which is 'trapped' between crystalline domains, is where chain scission and crosslinking would occur. Since photo-oxidation is a diffusion controlled process, larger molecular weights can become deterrents of degradation. However, longer chains can be more sensitive to chain scission, since fewer cuts would be required to significantly decrease its molecular weight, compared to polymers of lower molecular weight [42]. Thickness also plays a crucial role in the photo-oxidation of the polyolefins. Because oxidation depends on the diffusion of oxygen into the material, it is the outer layers that undergo the highest levels of oxidation. An oxidation layer is developed on thick samples, which would correspond to the profile of oxygen diffusion [42]. External factors such as temperature and humidity, can also affect the progress of the photo-oxidation reaction. In the case of PE, it has been shown that the rate of degradation is influenced by temperature, with some studies suggesting that every increase of 10^{o}C doubles the degradation rate [42].

1.3.2 Kinetic Modeling of Polymer Oxidation

A kinetic model is a non-empirical mathematical tool developed from a mechanistic scheme (such as the one in Fig. 1.4). The main goal of kinetic modeling is to predict the lifetime of polymers by evaluation of the reactions and underlying mechanisms of their oxidation. This is achieved in general by deriving the rate constant of the reaction mechanisms.

The best mechanistic scheme to describe the oxidation kinetics of polyolefins is initiated by bimolecular peroxide (ROOH) decomposition [4], as shown in Fig. 1.4. Most analytical kinetic models for polyolefins oxidation have been developed from this scheme and have traditionally included the following hypothesis or assumptions: (i) a steady state of radical concentrations; (ii) excess concentration of oxygen; (iii) steady state at low conversions; (iv) unicity of the reactive site; and (v) homogeneity of the reactive medium at the pertinent scale.

$$2\,\mathrm{ROOH} \longrightarrow \mathrm{R}^{\bullet} + \mathrm{RO}_2^{\bullet} \qquad (k_1)$$
$$\mathrm{R}^{\bullet} + \mathrm{O}_2 \longrightarrow \mathrm{RO}_2 \qquad (k_2)$$
$$\mathrm{RO}_2 + \mathrm{RH} \longrightarrow \mathrm{ROOH} + \mathrm{R}^{\bullet} \qquad (k_3)$$
$$\mathrm{RO}_2 + \mathrm{RO}_2 \longrightarrow \text{ inactive product } + \mathrm{O}_2 \qquad (k_6)$$

Figure 1.4: Bimolecular closed loop scheme. Reprinted by permission from Jon Wiley and Sons [4], Copyright 2006.

A summary of these common assumptions can be found in [43]. Certain assumptions, such as (ii) can be appropriate under certain circumstances, for example, when the specimen is thin enough, or when oxygen concentration is high enough to consume all alkyl radicals (R^{o}). But other assumptions, in particular the steady state of radical's concentrations (i) are more problematic. Further developments in kinetic modeling included consideration of systems of lower oxygen concentration, additional termination reactions such as alkyl–alkyl ($\mathrm{R}^{o} + \mathrm{R}^{o}$) and alkyl–peroxy radicals ($\mathrm{R}^{o} + \mathrm{RO}_2$) bimolecular combinations, and additional assumptions such as long kinetic chain interrelationship between termination rate constants [44, 45]

The assumption of steady state of radical concentration is particularly troublesome, and while models that make this assumption can predict well the production of $\mathrm{RO}_2^{\bullet}$ and ROOH species, they fail to reproduce the concentration of alkyl radicals R^{o}. By omitting this hypothesis, and assuming instead that $[\mathrm{RO}_2^{\bullet}]=(\mathrm{k}_1/\mathrm{k}_6)^{\frac{1}{2}}\,[\mathrm{ROOH}]$, Colin et al. [4] were able to obtain accurate predictions of the concentration of alkyl radicals R^{o} while maintaining good estimation of $\mathrm{RO}_2^{\bullet}$ and ROOH groups.

Despite this progress, main challenges remain for more accurate kinetic models, namely, the capability to consider the heterogeneous and overly-complex nature of oxidation of polymers. The former refers to the spatial heterogeneity that results from diffusion limited oxidation, while the latter arises from the fact that once oxidation begins, there are more secondary reactions that can take place beyond the main reactions usually taken into account in mechanistic schemes [40, 43]. Moreover, when prediction of UV-induced embrittlement is made based on kinetic models, it relays on phenomenological correlations between the pre-

dicted chemical species, molecular weight or crystallinity and a measure of strain to failure (exclusively restricted to uniaxial loading conditions).

1.3.3 Effect of Photo-Oxidation on Polymer Properties

As highlighted in the previous discussion, the photo-oxidation of polyolefins alters the chemical structure of the polymer. The effect of photo-oxidation on the chemistry of polyethylene has been studied by several authors [35, 46–58]. During the photo-oxidation of polyethylenes, mostly carbonyl and vinyl groups are created. The presence of carbonyl and vinyl groups have been monitored in these previous studies by Fourier Transform Infrared Spectroscopy (FTIR). The most commonly studied parameter in photo-oxidation degradation of polyolefins is the carbonyl index (CI). The carbonyl index measures the absorbance of carbonyl species with respect to chemical groups that are not expected to be altered during degradation. An increase in the carbonyl index indicates an increase in the carbonyl group concentration, which not only signals the advance of the photo-oxidation, but specifically points to the occurrence of Norrish type I reactions. Similarly, other relevant indexes include the vinyl index (VI). An increase in the vinyl index indicates a Norrish type II reaction. Several studies have reported an increase in carbonyl groups with degradation time for LDPE, LLDPE, HDPE and XLPE (crosslinked polyethylene), under natural or accelerated weathering [35, 46–58]. While carbonyl and vinyl groups concentrations are good indicators of the photo-oxidation process and mechanisms, other changes in the chemistry of PE can evidence the ongoing reactions. Carrasco et al. [48] studied the artificial aging of HDPE. Through FTIR analysis, the changes in chemical groups were determined and the progression of the degradation was established as follows: i) chain scission as evidenced by the appearance of end methyl groups (at 1380 cm^{-1}) and the disappearance of methylene groups (1310 and 1142 cm^{-1}), ii) branching and crosslinking supported by the appearance of double bonds (at 909 and 965 cm^{-1}), and iii) formation of carbonyl groups (between 1410 and 1715 cm^{-1}).

Once the photo-oxidation reactions are in motion, other changes start to occur in the polymer. As discussed earlier, photo-oxidation leads to random chain scission and/or crosslinking,

so the molecular weight of the polymer is expected to be affected. Due to the challenge of dissolving polyethylene, the amount of data on the effect of photo-oxidation on molecular weight is rather minimal in comparison to that of carbonyl index, crystallinity, or elongation to fracture. Miyagawa et al. [56] reported on the changes of the molecular weight distribution (MWD) of an LDPE film after photo-degradation. Chain scission caused a shift of the peak position to lower molecular weights. As the degradation continued, higher molecular weight components appeared, which were attributed to crosslinking reactions. The gradual decrease of this high molecular weight components at longer degradation times was believed to be caused by the growth of the crosslinked structure, rendering it insoluble, and thus, could not be seen in the MWD curves. Fayolle et al. [1, 37], paid particular attention to the relationship between the decrease of the molecular weight and the embrittlement of semicrystalline polymers, establishing that a critical molecular weight exists, below which the polymer becomes brittle. Overall, the dominant trend reported is a decrease in the average molecular weight, an increase in polydispersity, and an increase in crosslinked structures due to photo-degradation of polyethylene [57, 59].

As previously discussed, it is assumed that photo-oxidation reactions take place in the amorphous phase of the polymer, since oxygen diffusion is favored in this area, compared to the crystalline regions. An increase in crystallinity due to photo-oxidation results from the random chain scission in the amorphous region. Chain scissions may lead to chemicrystallization, a type of (low temperature) secondary crystallization [60,61] where the newly liberated chain segments are able to enter the crystalline phase (given they have enough mobility). A challenge in the study of photo-oxidation induced crystallization is annealing. Since photo-oxidation studies can be accompanied of thermal aging, it must be considered that chemicrystallization can coexist with annealing [1]. Besides the changes in crystallinity percent, photo-oxidation can also affect lamellar thickness, and while experimental data in this regard is rather limited [1, 57], it is assumed that photo-aging will result in lamellar thickening due to chemicrystallization.

So far, we have seen how the photo-oxidation reactions can alter the molecular weight and crystallinity of a polymer, which are properties that play a key role in defining the behavior of the material. Indeed, molecular weight and crystallinity are fundamental in defining the mechanical response of a semicrystalline polymer. To understand the importance of these properties on the mechanical behavior of polymers, it is necessary to consider the deformation mechanisms of a semicrystalline polymer. First, we consider a semicrystalline polymer as an arrangement consisting of amorphous phases trapped between crystalline regions (lamellae). In the case of polyethylene, the crystalline region has an orthorhombic structure, with its zigzagging chains along the c axis (Fig.1.5). Both phases are tied together by tie chains, as seen in Fig.1.6. The deformation of a semicrystalline polymer involves the deformation of the amorphous phase and that of the crystalline region. Various deformation mechanisms have been proposed for the amorphous region: interlamellar slip, interlamellar separation, and lamellar stack rotation, which are illustrated in Fig.1.6 [5, 20, 21]. Deformation in the crystalline region is attributed to two types of crystallographic slip: chain slip that occurs along the chains, and transversal slip. Moreover, the deformation depends on the orientation of lamellae relative to the deformation direction. In this sense, one needs to take into account the supramolecular morphology and orientation of the polymer. For example, films manufactured by blown extrusion develop a row nucleated a row-nucleated lamellar structure consisting of stacks of lamellae aligning along the machine direction (MD) and amorphous zones between the crystalline stacks, similar to the sketched in Fig. 1.6. On the other hand, bulk specimens manufactured by injection or compression molding develop a spherulitic morphology. Deformation is heterogeneous within a spherulite, depending on the position of lamellae relative to the loading direction, as sketched in Fig. 1.7. These mechanisms illustrate that the deformation of semicrystalline polymers depends on the degree of crystallinity, the thickness of the lamellar regions, the length of chains, i.e., its molecular weight. Therefore, photo-oxidation can have a significant impact on the mechanical properties of semicrystalline polymers [5, 20, 21].

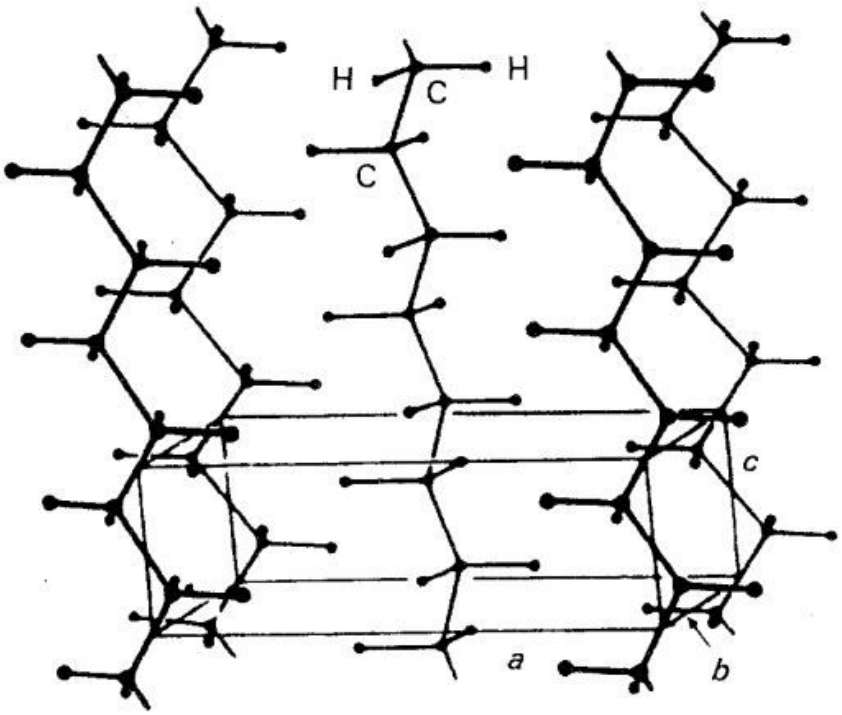

Figure 1.5: Orthorhombic crystalline structure of polyethylene. Reprinted by permission from Springer Nature [5], Copyright 1994.

Among the mechanical properties studied in photo-oxidation and weathering of polyolefins, strain at break (ε_b) is the most widely (and sometimes the only) mechanical property reported [52]. Strain at break tends to decrease as the degradation proceeds [1, 37, 52, 57]. The rate at which strain at break decreases depends on the degradation conditions and the specific material (crystallinity, molecular weight, orientation, thickness). It has been suggested that the formation of carbonyl groups during photo-oxidation correlates well with the strain at break, ε_b. However, there is currently no agreement on the order of correlation (linear or more complex) [52]. Briassoulis et al. [62,63] have argued that the strain at break, especially in the case of films, is a quantity easily affected by defect localization. Thus, premature failure and high standard deviations can result, suggesting to monitor instead the tensile strength. The widespread use of strain to break has led to arbitrary definitions of embrittlement in the context of photo-oxidation, with definitions spreading between 50-95%

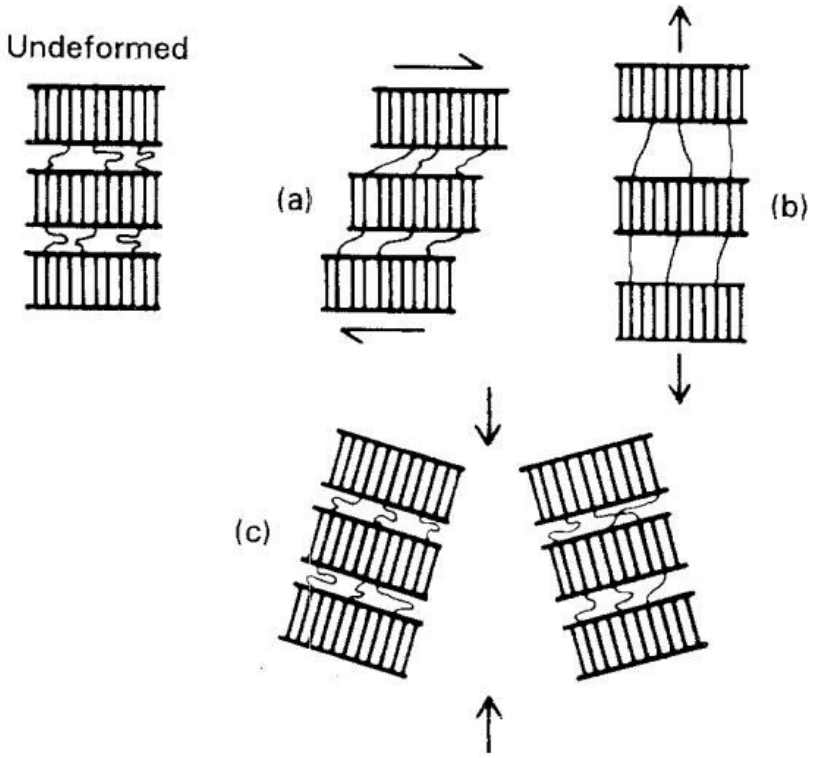

Figure 1.6: Scheme of the morphology of a semicrystalline structure and the deformation mechanisms of the interlamellar region: a) interlamellar slip, b) interlamellar separation and c) lamellar stack rotation. Reprinted by permission from Springer Nature [5], Copyright 1994.

loss of strain [57]. A more appropriate definition, as recognized by Fayolle et al. [37], is to define embrittlement as whenever an abrupt, sudden change in strain to fracture occurs, characteristic of a ductile to brittle transition.

The exact process by which photo-oxidation induces embrittlement in PE is not completely clear [37]. While most studies link the embrittlement of PE during photo-oxidation to the random chain scission reaction, there is no agreement on how the mechanism moves forward from that initial event. Random chain scission leads to a decrease in the molar mass of the polymer. However, from this point, two different paths can lead to embrittlement: i) a decrease in molar mass leads to a decrease of tie chains concentration, the polymer loses its load transfer capacity, and thus becomes brittle; ii) the decrease in molar mass

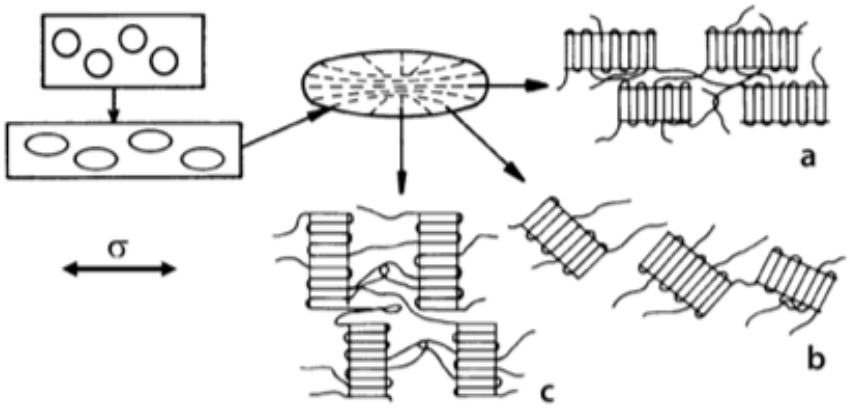

Figure 1.7: Possible lamellar orientations within a spherulite relative to the loading direction and resulting deformation mechanisms. Reprinted by permission from Springer [6], Copyright 2008.

leads to a recrystallization, which reduces the interlamellar spacing, leading to embrittlement. Discerning between the two paths above is not trivial, especially since measuring the concentration of tie molecules can be challenging [57]. Since tie molecules can be associated with the yielding process of the polymer, some studies [56, 57] have tried to account for the degradation induced change in tie-molecules by analyzing the changes in yielding with degradation. Hsu et al. [57] reported a disappearance of the second yield for LLDPE films after photo-oxidation, implying that the chain scission of tie molecules in the amorphous region prevented the load transfer necessary to promote chain slip. A similar conclusion was reached by Migiyawa et al. [56], for photo-oxidation of LDPE films.

The effect of photo-oxidation on the stiffness and hardness of polyethylene has been studied by few authors [48–50, 53]. The general trend found is an increase in hardness and elastic modulus as the degradation proceeds. Gulmine et al. [49] attributed the increase in hardness to chemicrystallization, crosslinking reactions, and the introduction of polar groups which can also lead to further crystallization. Tavares et al. [50] included nanoindentation measurements in their analysis of LDPE sheets photo-oxidation, finding that hardness and elastic modulus decrease from surface to bulk with exposure time, in correspondence with

the carbonyl index profile of the sheet.

1.3.4 Modeling of The Mechanical Behavior of polymers

The mechanical response of semicrystalline polymers is characterized by temperature and strain rate sensitivity, post-yield softening, and strain hardening. To capture such complicated phenomena, viscoelastic and viscoplastic models have proven to be most effective. Physically based models, that represent the evolution of the structure during yielding, are grouped under the molecular theory of yielding family. Continuous refinement of such theories includes the incorporation of pressure effects [64], and thermal activation of yielding [65–67]. A simple expression for the rate and temperature sensitivity of yielding was derived by Argon [68]. Pressure sensitivity would be later incorporated by Boyce et al. [22]. The model was refined by Arruda et al. [69] to account for the adiabatic heating induced strain hardening. Enhanced orientation hardening was introduced by Wu et al. [70]. Chowdhury et al. [71] modified the model to better account for the small strain behavior, and to independently model pre-peak hardening and post-peak softening, characteristic of glassy polymers. Kweon and Benzerga [72] implemented this model as a user material subroutine (UMAT) for the commercial finite element software ABAQUS-Standard, by recasting the constitutive equations using a co-rotational formulation. Poulain [18, 73] built up on the macro-molecular model in order to capture the thermomechanical response of an amorphous polymer. Additionally, Poulain established a solid protocol for the identification of the model parameters based on a minimum amount of experimental data [73]. Ayoub et al. [74, 75] modified Boyce et al. [76] and Ahzi et al. [77] models, directly incorporating the non-linear viscosity effects on the elastic part by modifying the inter-molecular resistance. Their model assumes that the amorphous and crystalline molecular resistances act in parallel. The model allowed them to study the effect of crystallinity on the mechanical behavior of polyethylene and to capture the behavior at large strains for HDPE.

Some studies have tried to incorporate the degradation process into models for the prediction of mechanical properties of polymers. Most of these studies are focused on polymers for

biomedical applications such as polylactic acid (PLA) and polycaprolactone (PCL). Thus, such research has aimed to hydrolytic degradation. Belbachir et al. [75] extended Boyce et al. [76] model to account for the effect of photo-oxidation on PLA. For this, they defined a photodegradation parameter based on the change in molecular weight of PLA. Based on Ward and Hadley's entropy spring model [78], which links Young's modulus with the number of polymer chains per unit volume; Wang et al. [79] proposed a model that relates the molecular weight of an amorphous, biodegradable polymer with the elastic modulus. For this, they coupled the elastic spring theory model with the biodegradation model created by Wang et al. [80] and Han and Pan [81], which is a phenomenologically based diffusion reaction model that describes the relationship between monomer diffusion and the hydrolysis process. Shirazi et al. [82] coupled Wang's [79] phenomenological degradation model for MWD evolution during hydrolytic degradation, with an entropy spring model that describes the variation of elastic modulus with the MWD.

Some of these studies focused solely on the evolution of Young's modulus. Ding et al. [83] used molecular dynamics (MD) and Monte Carlo steps to model an amorphous region trapped between two lamellae. By simulating hydrolytic degradation through random cuts of the polymer chains, they evaluated the effect of hydrolytic random chain scission on PGA's Young's modulus.

More recently, Zhao et al. [84, 85] used an elasto-plastic formulation to predict the mechanical response of semicrystalline poly(3-hexylthiophene-2,5-diyl)(P3Ht) thin film. To consider the effect of oxidation on the mechanical model, they used a stress coupling term based on a modification of Fick's second law for stress assisted diffusion reaction. Soares et al. [86, 87] used an hyperelastic, neo-Hookean model to describe the mechanical response of a biodegradable polymer stent. They linked this model to the deformation induced degradation by defining a scalar field that captures the local state of degradation of the material.

Both Vieira et al. [88, 89] and Breche et al. [90, 91] have taken physically based models and incorporated a hydrolytic degradation damage parameter. Viera et al. [89] adapted

the Bergstrom and Boyce model [92] inspired by the hydrolytic degradation kinetics to predict the behavior of PLA-PCL blends. They considered a constant degradation rate, despite hydrolytic degradation being heterogeneous, especially due to autocatalysis effects [82]. Through a parametric study, they identified the model parameters that were most sensible to the hydrolytic degradation process and incorporated them as a hydrolytic damage scalar field, without altering the formulation of the constitutive relations. Breche et al. [90,91] considered an adaptive quasi-linear viscoelastic model calibrated on the as-received material. The degradation scalar parameter was obtained by using the evolution of the normalized relaxation function during the degradation time.

1.4 Approach

In order to characterize the effect of photo-oxidation and accelerated weathering on a semicrystalline polymer, low density polyethylene (LDPE) FB3003, provided by QAPCO (Doha, State of Qatar) in the form of films of 50 μm thickness and 2 mm plates has been used. The films and plates were submitted to three types of UV aging conditions: i) fixed UV irradiance at 1.55 W/m^2 and 60°C at ambient humidity and various aging times; ii) fixed humidity and UV irradiance at 1.55 W/m^2, 60° with controlled humidity and various aging times; iii) natural irradiance and temperature (natural weathering) at various aging times. The accelerated weathering chamber available was capable of using UVA (315-400 nm) and UVB (280 to 315 nm) lamps. UVA lamps were chosen in order to better simulate the spectral irradiance during daylight. UVA lamps degrade material at a slower rate than UVB lamps, but correlate better to outdoor sunlight, since most of the UV light that reached the surface of the Earth is UVA. The ASTM G-154 [93] standard suggests various cycles of UV irradiance, temperature and humidity for the exposure of non-metallic materials to UV and water to reproduce weather effects. However, in order to independently analyze the contribution of UV irradiance and humidity on the photo-oxidation of polyethylene, modified versions of the UV cycles suggested in the standard were used. To study the effect of UV, an irradiance of 1.55 W/m^2 was selected, with no water condensation cycles and at a

temperature of 60°C. The selected irradiance and times of 48, 96, 192 and 240 hours of UV exposure correspond to an energy of 267-1340 kJ/m^2. Films and plates were submitted to natural ambient conditions for a period between 1 and 8 months. Specifically, the natural aging was done in the State of Qatar, who sponsored this research project through a National Priorities Research Program (NPRP) grant and where LDPE is the most widely produced polymer. The average UVA radiance for Qatar is approximately 5000 kJ/m^2/year, with 1, 2 and 4 months being equivalent to 417, 833 and 1668 kJ/m^2 [94, 95].

The progress of the degradation process has been assessed by the changes in the chemical structure, crystallinity, molecular weight and mechanical response of the polymer. The advance of the oxidation reactions was evaluated by Fourier transform infrared spectroscopy (FTIR). The evolution of the crystallinity has been determined by differential scanning calorimetry (DSC). The mechanical response of flat film and plate specimens was evaluated in tension under quasistatic conditions. Digital image correlation (DIC) measurements were used to obtain the intrinsic behavior of the polymer. To better capture the effect of degradation on the stiffness of the material, nanoindentation measurements were done on selected conditions. Scanning electron microscopy (SEM) was used to study the interplay between oxidation, damage and the mechanical response of the aged polymer.

A version of the macro-molecular model by Kweon and Benzerga [72] was implemented in the FEM software Z-set. The model allowed us to study possible structural effects on the as-received films and plates. Then, the effect of photo-oxidation on the mechanical behavior of the polymer films and was captured by inverse identification of the aged materials parameter. Lastly, the model is used to identify the extent of the oxidation layer on the diffusion controlled oxidation of bulk specimens.

1.5 Outline of the Dissertation

This dissertation is organized in the following manner: Chapter 2 presents the material of study, the procedures and conditions selected for artificial and natural aging, as well as the physico-chemical characterization of pristine and aged materials. The later, in particular,

allows us to address objective 1 of section 1.2. In Chapter 3, all the results of mechanical characterization are reported. This includes tensile testing and nanoindentation of smooth films and plates of graded geometry, in pristine, artificially aged, and naturally aged conditions. Thus, Chapter 3 partially addresses objectives 2 and 3. Damage characterization of the mechanical tests are presented in Chapter 4, allowing us to complete objective 2. In Chapter 5, the constitutive modeling is introduced. The model is then calibrated based on UV-aged thin film data, which is assumed to age homogeneously. Then, a modeling strategy is proposed that enables to estimate the depth of the oxidation in plates, thus addressing objective 4. Finally, chapter 6 presents the conclusions and suggestions for future work.

2. MATERIAL AND AGING*

An unstabilized low density polyethylene (LDPE) grade FB3003, provided by Qatar Petrochemical Company (QAPCO, Doha, State of Qatar) was used. Besides its economic importance to the State of Qatar, where LDPE is the most produced polymer, the basic chemical structure of LDPE (Fig. 2.1) combined with its semicrystallinity makes it optimal for this study. Additionally, this is an unstabilized grade that allowed us to avoid complications due to the presence of additives, which are not in the scope of this study. The LDPE FB3003 is produced via free radical polymerization in an autoclave high pressure process. This grade is recommended for heavy duty film applications such as heavy duty bags, industrial shrink film, construction and agricultural films, as well as drip irrigation pipes and small blow molded bottles.

In order to characterize the effect of homogeneous and diffusion controlled photo-oxidation, as well as any possible structural effects, two different forms of LDPE were used: a 50 μm thick film and a 2 mm thick plate. The films were prepared by QAPCO from LDPE FB3003 pellets in an OCS cast film extruder. The extruder temperature profile was in the range 180-210 °C while maintaining a melt temperature of about 195°C. Upon exiting the die, the film was cooled in a water bath and collected on a winder. The 2 mm thick plates were prepared from LDPE FB3003 pellets in a compression molding press. The molding cycle consisted of 5 min at a temperature of 180°C and zero pressure, followed by 5 min at T = 180 °C and pressure $P = 1400\,\text{psi}$, and finally cooling to room temperature at a rate of about 15 °C/min.

The degradation of polymers under natural conditions is a complex process that combines UV radiation, temperature and humidity [14]. Experiments involving natural aging of

*Part of the data reported in this chapter is reprinted with permission from "Effect of UV-aging on the mechanical and fracture behavior of low density polyethylene" by A.K. Rodriguez, B. Mansoor, G. Ayoub, X. Colin, and A.A. Benzerga. *Polymer Degradation and Stability*, vol. 180, pp. 109185, 2020. Copyright [2020] by Elsevier [96]

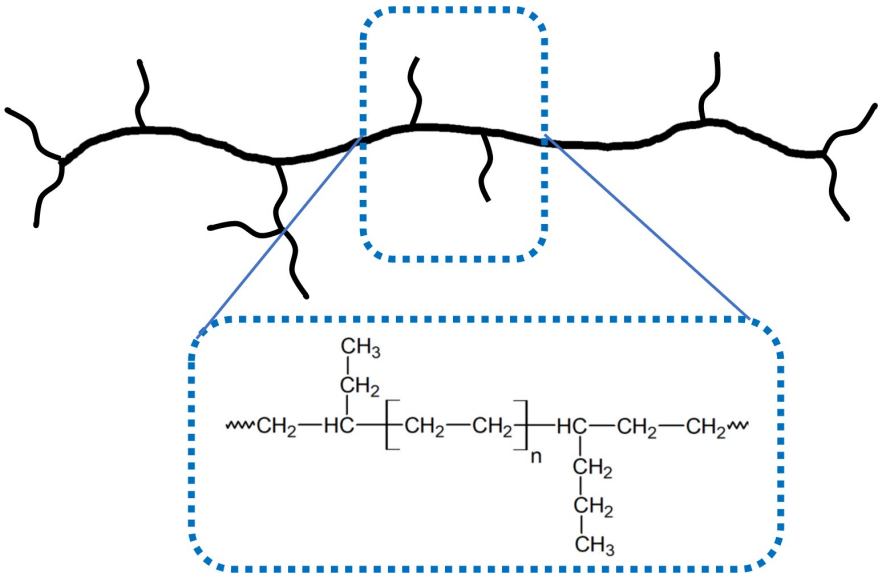

Figure 2.1: Structure of low-density polyethylene (LDPE): morphology of branched backbone chain, chemical structure and 3D molecular structure.

polymers allow the estimation of the exposure time required for the decay of the properties of interest. However, in terms of better understanding and predicting the response of polymers to environmental factors, natural aging experiments present certain drawbacks. The obvious disadvantage in practical terms is the low oxidation rate in natural conditions, requiring long term exposures. But even when exposure time is not an issue, the fact that several factors act concurrently impedes proper discrimination of their individual contribution to the material's performance. Lastly, natural aging unavoidably involves varying exposure conditions, so establishing any correlation between the aging conditions and the resulting properties becomes troublesome.

In this context, a more appropriate way to study the individual contributions and mechanisms of different aging factors is to use a laboratory accelerated weathering tester. These devices allow the exposure of the material to controlled UV, temperature and/or humidity. By selecting and controlling the weathering factors of interest it is thus possible to decouple their effects on the behavior of the material. Of special interest is the effect of UV light. While it accounts for only $\approx 5\%$ of the total solar radiation, UV light is the strongest portion

of the solar radiation, being therefore responsible for most of the damage to materials [97]. The UV wavelength range (100-400 nm) is divided into: UVA (315-400 nm), UVB (280-315 nm) and UVC (100-280 nm). The radiation below 290 nm (UVC), as well as most of the UVB radiation is filtered by the atmosphere before reaching the Earth [14].

Therefore, in order to replicate the effect of solar UV in polymeric materials it suffices to reproduce the UVA portion of the spectrum. Different light sources are available to use in accelerated aging testers. Xenon arc lamps can simulate visible light (400-700 nm) and long wavelength (365–400 nm) UV light [98]. On the other hand, fluorescent UVA-340 lamps are excellent in replicating the spectrum responsible for the damage to polymers, i.e., 280 to 360 nm [93, 98]. This can be appreciated in Fig.2.2, which compares the irradiance of a typical UVA-340 fluorescent lamp with the sunlight irradiance: UVA-340 lamps offer a good match to the sunlight radiation in the region of interest (280-360 nm) [98].

In this chapter, the as-received and aged materials are characterized in terms of their chemical composition, molecular weight, morphology, crystallinity, and its surface finish. The results of the aged specimens are compared with those of the pristine material and within the different types of aging, in an attempt to discriminate the effects of the various weathering factors studied.

2.1 Experimental Methods

2.1.1 Aging Experiments

The ASTM G-154 standard [93] suggests various cycles of UV irradiance, temperature and/or humidity to replicate the weathering effects that occur when non-metallic materials are directly or indirectly exposed to sunlight. Modified versions of the weathering cycles suggested in the standard were used in order to decouple the effects of UV radiation and humidity on the photo-oxidation of polyethylene. They are described in Table 2.1. The cycles involving UVB radiation were discarded for the reasons discussed in the previous section.

The accelerated weathering experiments were carried out in a QUV Weathering Tester

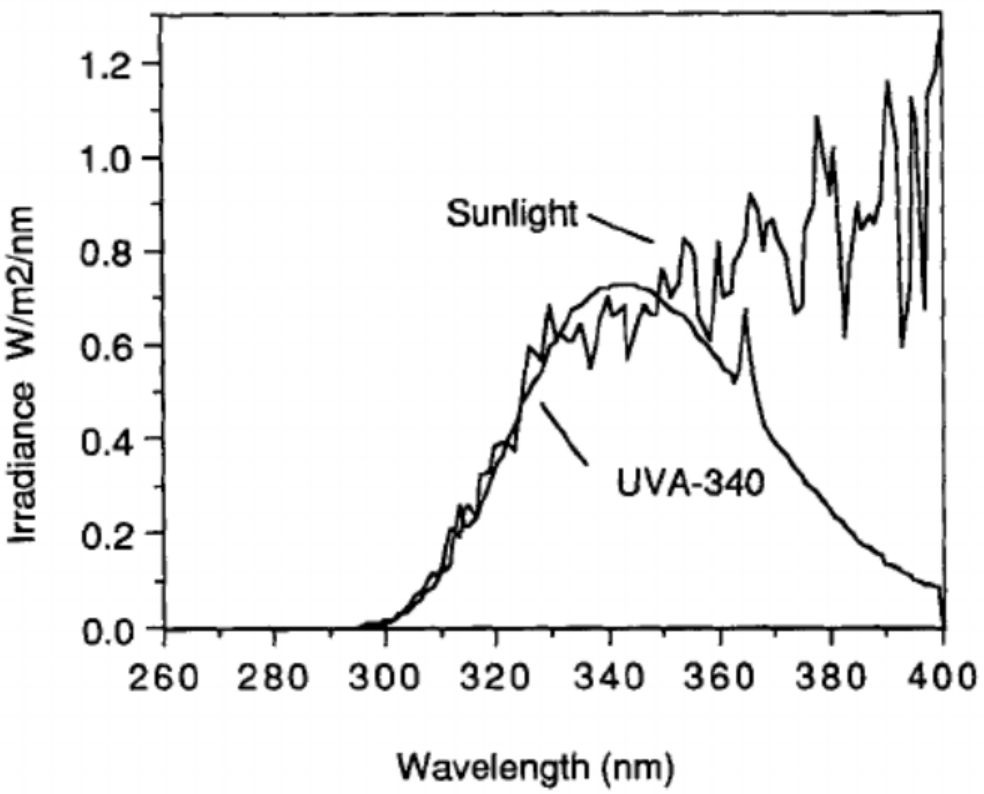

Figure 2.2: Irradiance of a UVA-340 lamp compared to the sunlight radiation. Reprinted by permission from Jon Wiley and Sons [7], Copyright 2004.

(QPanel Lab Products) equipped with fluorescent UVA bulbs. To determine the effect of UV on LDPE, a modified version of an ASTM G-154 standard cycle was used with irradiance of 1.55 w/m^2, no water condensation cycles and a temperature of 60^{o}C. The UV exposure times for the LDPE films and plates were: 48, 96, 192 and 240 hours. Additional exposure times of 24 and 72 hours were performed for the films. This was done because the faster embrittlement of the films impeded appropriate mechanical testing at high UV dosage. The additional UV exposures allowed us to obtain a more complete set of mechanical data. This aging program is from now on referred to as "UV".

The effect of humidity on the oxidation of LDPE was evaluated by submitting the material to cycles with irradiance of 1.55 w/m^2 at 60 ^{o}C for 20 hours, followed by 4 hours of water condensation (100 % humidity). The exposure time was such that the total UV

Type of Aging	Conditions
UV Aging "UV"	UVA fluorescent lamps 1.55 W/m^2 60°C Ambient humidity
Hygrothermal Aging "HUV"	UVA fluorescent lamps 1.55 W/m^2 60°C Controlled humidity cycles of: 4h Water Condensation (100 % humidity) and 20 h of UV
Natural Aging	Natural weathering conditions of Qatar Location: Rooftop of TAMUQ building See Table 2.2

Table 2.1: Details of the various aging conditions used.

	Temperature (°C)						Humidity (%)					
	April	May	June	July	August	September	April	May	June	July	August	September
Max	41	45	47	47	47	44	83	84	89	89	89	89
Min	22	26	30	31	30	29	9	7	7	9	9	11
Average	28	33	37	38	38	35	47	38	33	42	46	61

Table 2.2: Environmental conditions in Doha, Qatar, during natural aging experiments.

irradiance time amounted to 48, 96, 192 and 240 hours, to allow comparison with the UV aging experiments. This aging program is from on now referred to as "HUV".

Finally, natural aging experiments were carried out in order to establish a practical benchmark and attempt to correlate the observed effects of controlled UV and HUV aging to real, natural aging conditions. The experiments were performed by placing LDPE films and plates on the rooftop of the Texas A&M at Qatar Engineering building between 1 and 8 months. Film specimens were exposed for up to 4 months, while plates were exposed for up to 8 months. The weather conditions during the exposure time are detailed in Table 2.2. The total UVA radiance for Qatar is approximately 5000 kJ/m^2/year [94, 95]. To give an

idea, the maximum aging time of 240 hours used in the lab-controlled experiments corresponds approximately to the UVA radiation received in Qatar for 3 to 4 months. Selected experiments were carried out in the naturally aged material, focusing on their mechanical response. However, the last section of this chapter is dedicated to the characterization of the chemical damage post-aging for a naturally aged plate.

Since oxidation is a diffusion controlled process, the rate and extent of the consequent degradation depends on exposure time, oxygen diffusivity and sample thickness [99]. Diffusion limited oxidation (DLO) occurs in sufficiently thick specimen of polymers with medium to low oxygen diffusivity, and can result in heterogeneous material profiles with oxidized surfaces and pristine interiors. With this in mind, both films and plates of LDPE were submitted to the various oxidation programs in order to study the response of LDPE in nominally homogeneous and heterogeneous oxidation.

2.1.2 Fourier Transform Infrared Spectroscopy

The IR spectra of virgin PE films were determined with a Perkin-Elmer Frontier device within the 4000-400 cm^{-1} range by averaging the 32 scans obtained with a minimal resolution of 4 cm^{-1}. For this, a Brucker IFS 28 IR spectrophotometer was used to follow the absorption bands of the carbonyl groups at a wavelength of 1720 cm^{-1} and vinyl groups at 908 cm^{-1} [41]. The concentrations of carbonyl and vinyl groups were calculated using the classical Beer−Lambert′s law [100, 101]:

$$[\text{Concentration}] = \frac{A}{b\epsilon} \tag{2.1}$$

where A is the absorbance of the carbonyl or vinyl group, b is the thickness of the sample and ϵ is the molar absorptivity coefficient. The molar absorptivity was taken as 405 $lmol^{-1}cm^{-1}$ for carbonyl groups and 122 $lmol^{-1}cm^{-1}$ was used for the vinyl groups [100, 101].

2.1.3 Differential Scanning Calorimetry

To determine the crystallinity ratio and the lamellar thickness of the LDPE film, differential scanning calorimetry (DSC) was used. The crystallinity ratio (in percent) was calculated according to Equation 2.2 [102]:

$$\%X_C = \frac{\Delta H_m}{\Delta H_m^0}\text{x}100 \tag{2.2}$$

where ΔH_m is the heat of melting of the specimen and ΔH_m^0 is the heat of melting of the crystal. For polyethylene, $\Delta H_m^0 = 290$ J/g [102].

The lamellar thickness of the main crystals, l_c, are estimated using the Gibbs-Thompson equation:

$$l_c = \frac{2\ T_{m0}\ W}{\Delta H_m^0}\frac{1}{T_{m0} - T_m} \tag{2.3}$$

where T_m is the equilibrium melting point, T_{m0} the experimental melting point and W the surface energy. The following values reported in the literature for PE have been used: $T_m = 415$K, $W = 70.0$ mJm^{-2} [102].

2.1.4 Gel Permeation Chromatography

The molecular weight of the LDPE was measured at 140°C with high temperature gel permeation chromatography (HT-GPC). Experiments were carried out at ENSAM Paris with a PL-GPC 220 Agilent Technologies device equipped with a guard column, two columns branded PlGel Olexis connected in series, and three different (refractive index, viscometer and light scattering) detectors acting in concert and providing distinct but complementary information. This advanced technology allows a direct measurement of the molecular masses (without extrapolation, correction or column calibration) and degree of branching in a single experiment. The eluent was 1,2,4-trichlorobenzene (TCB) stabilized by 0.025 wt% of 2,6-di-

tert-butyl-4-methylphenol (BHT). It was filtered with a 1 μm pore size membrane (in glass fiber) before use. The injection volume was 100 μ L and the flow rate was 1 mL.min^{-1}. PE samples were dissolved in BHT/TCB (at a concentration of 2 g.L^{-1}) at 140°C under stirring for 1 hour. The weight average (M_w) and number average (M_n) molecular weights were calculated. Additionally, the polydispersity index (PDI), was calculated as:

$$PDI = \frac{M_w}{M_n} \tag{2.4}$$

2.1.5 Microscopy

The initial surface of the LDPE films and plates were observed via scanning electron microscopy (SEM). For this, the film surfaces were gold coated and observed under a SEM FEI model Quanta 400 with 15 kV voltage and a spot size of 3.5.

2.2 As-Received Material

2.2.1 Physico-chemical Characterization

2.2.1.1 FTIR Spectra

The FTIR spectra of the as-received LDPE was recorded to characterize the initial material and to quantify later the formation of oxidation products in the aged material. The photo-oxidation of polyethylene is expected to result in the production of one or several carbonyl groups C=O such as ketones, carboxyl acids, aldehydes and esters, which are formed and decomposed according to the Norrish type I reaction, as shown in Fig. 1.3 [2,3,41]. The photo-oxidation reaction can also take another initiation path, resulting in the formation of vinyl groups via Norrish type II reaction (Fig. 1.3) [2, 3, 41]. Accordingly, the analysis of the FTIR spectra of the as-received material was focused on the regions where bands corresponding to the aforementioned groups could appear.

The recorded FTIR spectra of the as-received LDPE is shown in Fig. 2.3. The strong bands recorded at wavelengths of 2900 and 3000 cm^{-1} correspond to the CH_2 symmetric

and asymmetric stretching, respectively [103], and are of no special interest in the context of this study. The analysis is instead centered on the wavelength regions corresponding to: i) unsaturations (RC=CR) between 850 and 965 cm^{-1}; ii) terminal methyl groups ($-CH_3$) at 1300-1400 cm^{-1}, and; iii) carbonyl groups (R(C=O)R) between 1600 to 1800 cm^{-1}) [103].

In the 850-965 cm^{-1} region we obtain details about the type and ratio of unsaturations in the as-received material. The characterization of these groups is important since changes in the type and amount of unsaturations provides information about the specific photo-oxidation reactions occurring [104]. Details of this region and relevant peaks are highlighted in Fig. 2.4a, namely, vinyl groups CH_2=CH_2 at 908 cm^{-1} and vinylidene groups $-$RCH=CHR$-$ at 890 cm^{-1}. Vinyl and vinylydene are common unsaturations groups found in commercial polyethylenes. The vinyl groups can be a product of radical disproportionation reaction during polymerization (Fig. 2.5a) [8]; while the vinylidene groups are presumed to result from chain transfer of tertiary radical during polymerization (Fig. 2.5b) [8]. The dominance of vinylidene groups terminal vinyl group is characteristic of LDPE.

Another sign of the LDPE 'imperfections' appears in the 1400-1300 cm^{-1} region (Fig. 2.4b) where a peak is obtained at 1376 cm^{-1}. This peak, absent in highly ordered HDPE, corresponds to the CH_3- terminal groups of short and long branches of LDPE. Branches in LDPE are the result of the free radical polymerization process, representing an important portion of the polymer and giving it its low density character.

The region corresponding to carbonyl groups, i.e. 1600-1800 cm^{-1} does not show any strong or mild peaks. The initial carbonyl and vinyl group concentrations (which is later used in the assessment of the oxidation progress) were measured at 1720 and 908 cm^{-1} respectively. The initial carbonyl concentration was 0.0062 mol/L, while the initial vinyl concentration was 0.0297 mol/L. The initial concentration of vinyl groups is higher than the initial concentration of carbonyl groups, in accordance with the previous observation regarding the radical polymerization chemistry [103, 104].

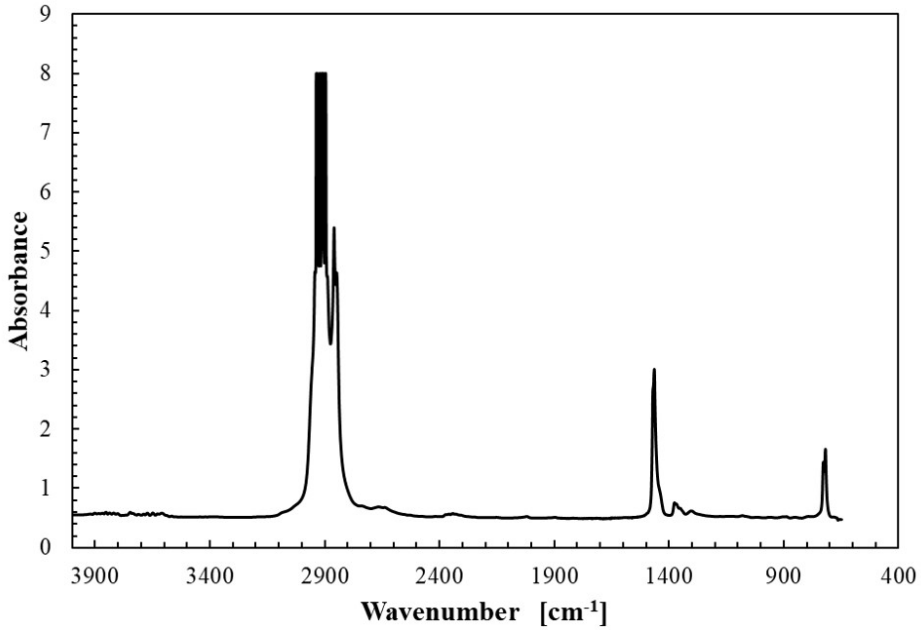

Figure 2.3: FTIR spectrum of the as-received LDPE.

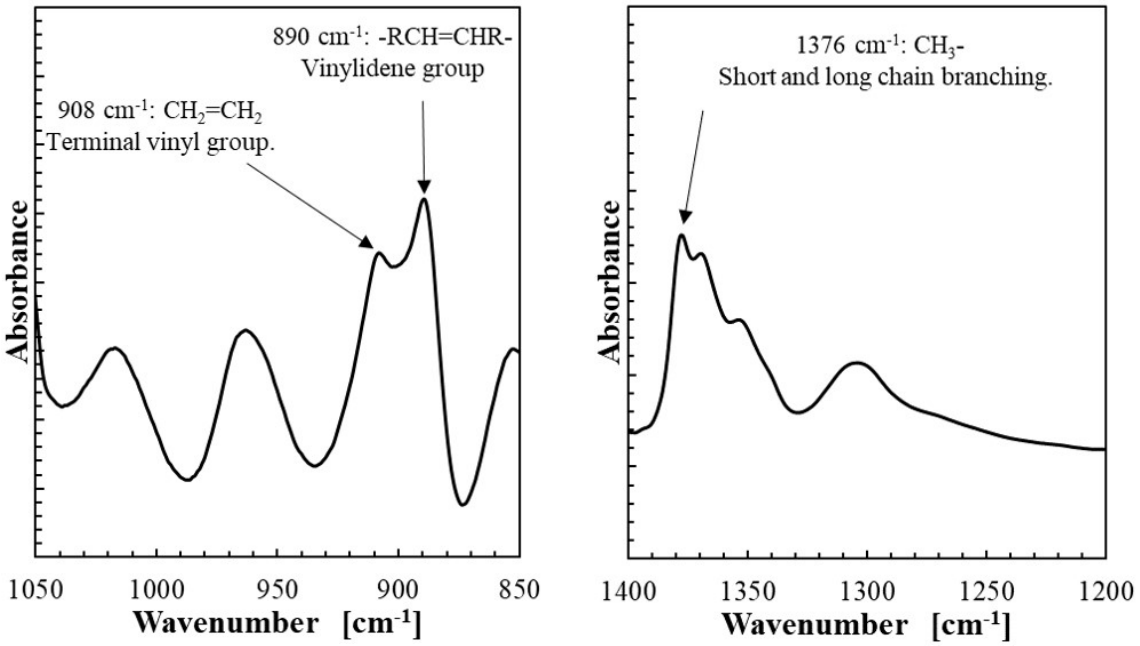

(a) Unsaturation region

(b) Methyl region

Figure 2.4: Detail of the FTIR spectra of the as-received LDPE in: a)Unsaturation region, and; b) Methyl end group region.

(a) Formation of vinyl groups

(b) Formation of vinylidene groups

Figure 2.5: Formation of the unsaturation groups in LDPE: a)vinyl groups, and; b)vinylidene groups [8]

2.2.1.2 Molecular Weight

Besides having an important role in the determination of polymer properties and response, the molecular weight of the polymer allow us to follow the progress of the degradation and to determine the presence of mechanisms such as chain scission, branching, and crosslinking. The initial weight and number average molecular weights for the LDPE used in this study were $M_n = 18,200\, g/mol$ and $M_w = 164,500\, g/mol$, respectively. The effect of the initial molecular weight on photo-oxidation is complex and it relates to the free volume of the material and the probability of molecular chains to suffer chain scission. A higher free volume promotes photo-oxidation by facilitating oxygen diffusion, as well as the formation of cyclohexane during Norrish II [42]. The free volume (V_f) of a polymer is inversely proportional to the number average molecular weight M_n, sinceM_n accounts for the chain ends which are the main contributors to the free volume of the material. Thus, at a higher initial M_n, higher V_f, and easier O_2 diffusion [42]. At the same time, longer chains are more prone to oxidation and chain scission than shorter chains. M_w will also be more drastically affected during chain scission, since only one chain rupture is required to reduce the length of the chain by half [42].

Besides the molecular weight averages, GPC can also give us information regarding the

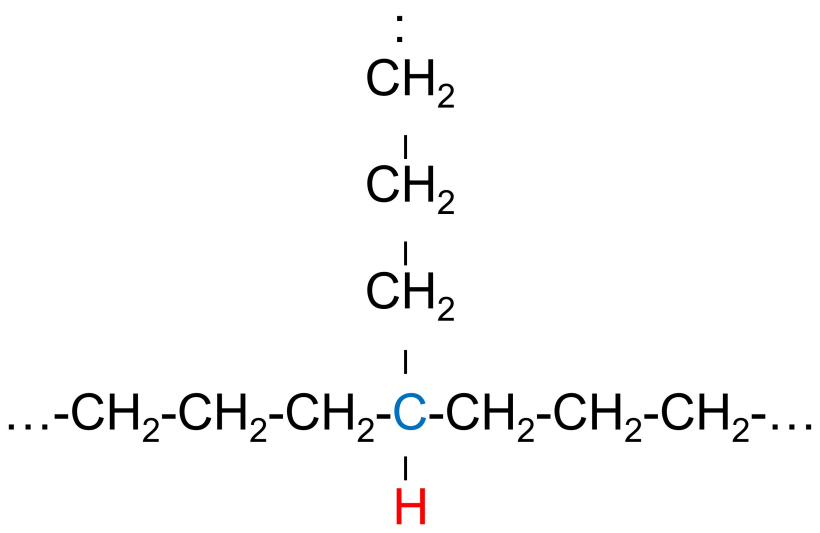

Figure 2.6: Tertiary carbon in branched polyethylene, with labile H.

structure of the polymer chain itself, since it can give hints of branching and crosslinking, which results in a behavior different to that of a more linear polymer [103]. The polydispersity index of the as-received material is $PDI = M_n/M_w = 9$. The polydispersity index provides an indication of how broad is the molecular weight distribution: a low PDI indicates a narrow molecular weight distribution (with PDI=1 encountered almost exclusively in natural polymers). The high PDI of the as-received material is typical of free radical polymerization processes and indicates the presence of long chain branches (LCB). These branches hinder the movement necessary for the backbone chain to crystallize, resulting in the low crystallinity that characterizes LDPE.

Branching also makes LDPE more susceptible to oxidation than other polyethylenes. This is because at the points where branching occurs, a labile hydrogen is formed because it is bonded to a tertiary carbon (i.e. a carbon attached to other 3 carbon atoms) as shown in Fig. 2.6. The hydrogen atom linked to a tertiary atom is easier to detach than an hydrogen linked to a secondary C atom in the backbone chain, making them likely points for oxidation initiation [14].

2.2.1.3 Crystallinity and Morphology

The ratio of crystallinity, as well as the conformation of the amorphous and crystalline regions have an impact on the progress of photo-oxidation. This is because oxidation acts on the amorphous region where oxygen diffusion is easier than in the dense, compact crystalline regions. Additionally, crystallinity and crystalline morphology are determinant factors on the mechanical response of the polymer. The crystallinity ratio and the lamellar thickness of the LDPE film were measured by differential scanning calorimetry (DSC). The heating thermogram is shown in Fig. 2.7, where we can see the melting peak at 108.78 °C, in accordance with the properties provided by the manufacturer and summarized in table 2.3. Given that the T_g of LDPE is approximately at -156 °C [105], it was not possible to record it due to limitations in the DSC minimum available temperature. The percent crystallinity calculated from the obtained heat of fusion is $\%X_C = 55.54\%$, which is in the upper range of crystallinity for commercial LDPE.

The lamellar thickness of the main crystals can be estimated from the melting temperature reported above. This is achieved via the Gibbs-Thompson equation (Eq. 2.3). The lamellar thickness of the as-received LDPE films is $l_c = 6.40nm$, which is in the range reported in other studies for LDPE blown films [106, 107].

Further information regarding the crystalline morphology is deduced from the forming process of the material. The macro-conformation of a semicrystalline polymer ultimately depends on on the crystallization conditions [61]. The films were manufactured by a blown cast process and then cooled in a water bath. Blown films of semicrystalline polymers develop a preferred orientation during processing [108–110]. For LDPE, this means a row-nucleated lamellar structure consisting of stacks of lamellae aligning along the machine direction (MD) and amorphous zones between the crystalline stacks, as sketched in Fig. 2.8.

On the other hand, the LDPE plates used in this study were made via compression molding followed by air cooling. The compression molding results in a material that is transversely isotropic. Another difference with films is in terms of the cooling method and rate. The

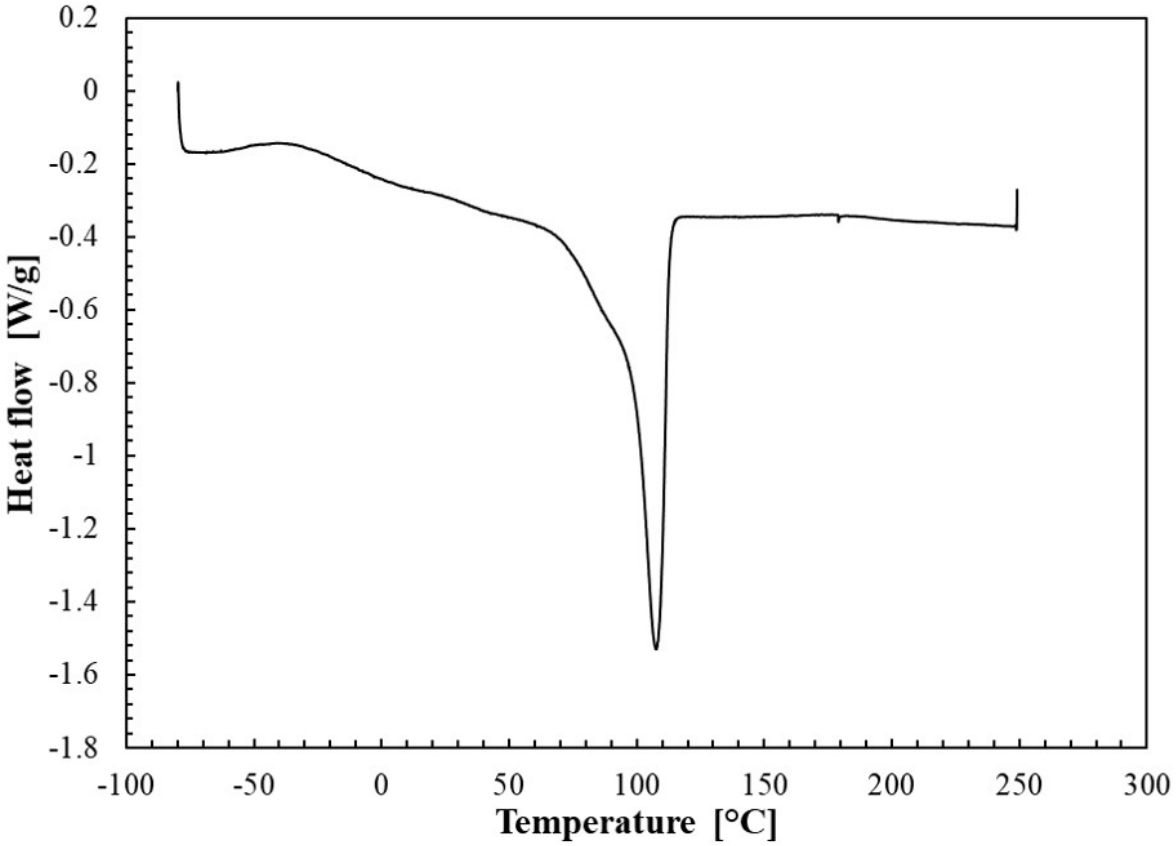

Figure 2.7: DSC heating thermogram of as-received LDPE film.

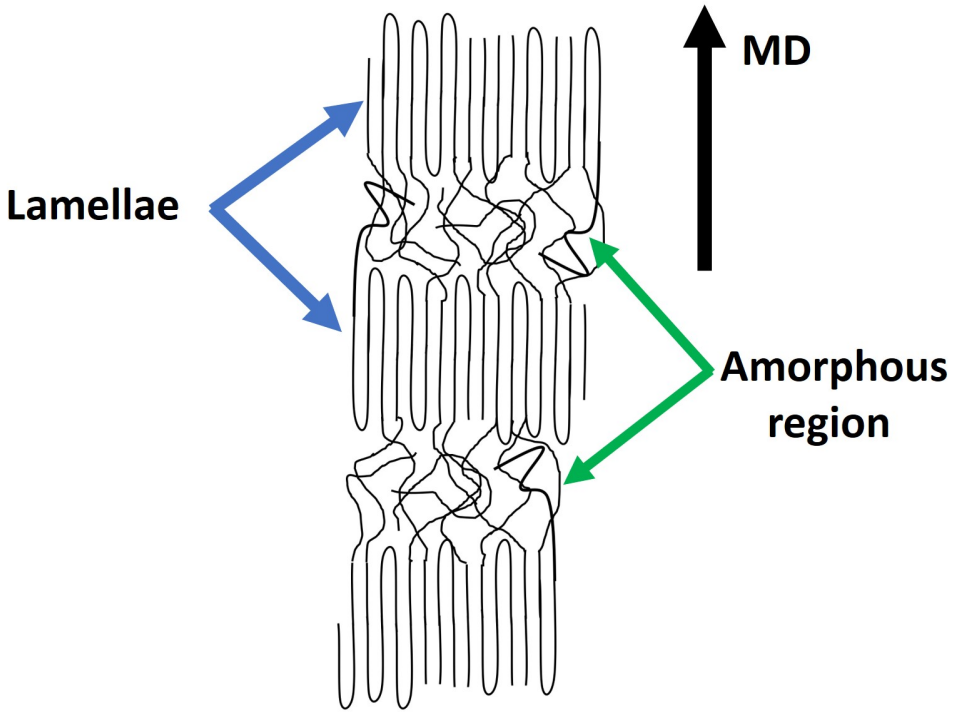

Figure 2.8: Sketch of the row-nucleated lamellar structure of LDPE films consisting of stacks of lamellae aligning along the machine direction (MD), with amorphous zones between them.

lamellar thickness of semicrystalline polymers is mostly determined by the degree of supercooling, that is, the difference between the melting temperature T_m and the crystallization temperature T_c. The supercooling is thus lower in the plates than in the films. In fact, this difference is amplified by the difference in heat dissipation due to geometrical reasons: the films are 50 μm thick while the plates have a thickness of 2 mm. This smaller supercooling leads to a higher lamellar thickness in the plates, as seen in Fig. 2.9. Thus we can assume the crystal thickness of the plates to be greater than the $l_c = 6.40$ nm estimated for the films. Also as a consequence of the slow cooling, the plate is expected to develop a skin/core structure since the most internal part of the sample will take longer to cool down compared to the surface.

Property	Value	Unit
Melt Flow Index	0.30	g/10min
Density @ 23 °C	0.920	g/cm^3
Crystalline Melting Point	109	°C
Vicat Softening Point	96	°C

Table 2.3: Properties provided by the manufacturer for LDPE FB3003.

Property	Value	Unit
X_C	55.54	%
T_m	108.78	°C
l_c	6.40	nm

Table 2.4: Crystalline and thermal properties of LDPE film obtained by DSC.

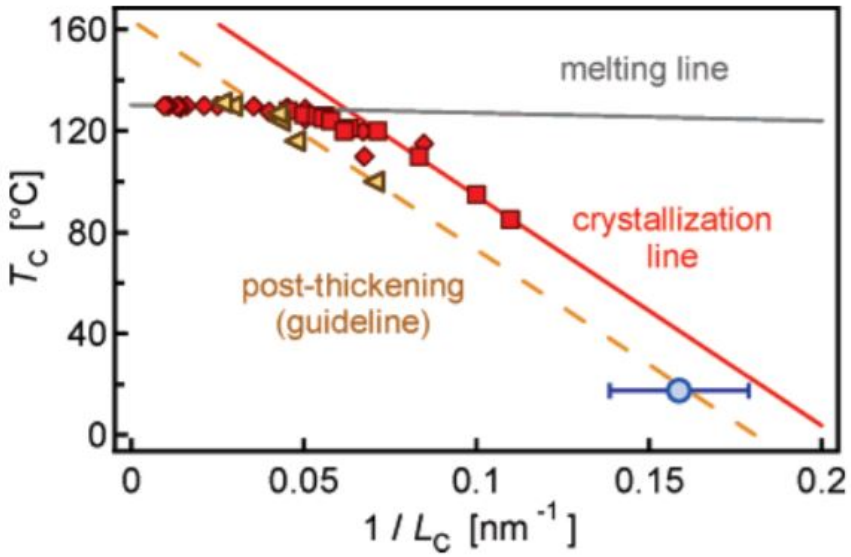

Figure 2.9: Crystallization temperature (T_C) as function of the inverse lamellar thickness (l_c) for isothermally crystallized PE. Reprinted by permission from American Chemical Society [9], Copyright 2007.

2.2.2 Microscopy

The surface of the as-received film was observed under the SEM and it is shown in Fig. 2.10. The film looks overall smooth at a big scale (Fig. 2.10a) and no major defects were distinguished at this magnification, and only a slight surface roughness is observed at a higher resolution ((Fig. 2.10b)) in accordance with what is typically observed for LDPE [107, 111]. The surface of the as-received LDPE plates is shown in Fig. 2.11. The surface is overall smooth (Fig. 2.11a) with some scratches and artifacts from manufacturing. Closer examination in Fig. 2.11b shows a close up of said scratches and artifacts.

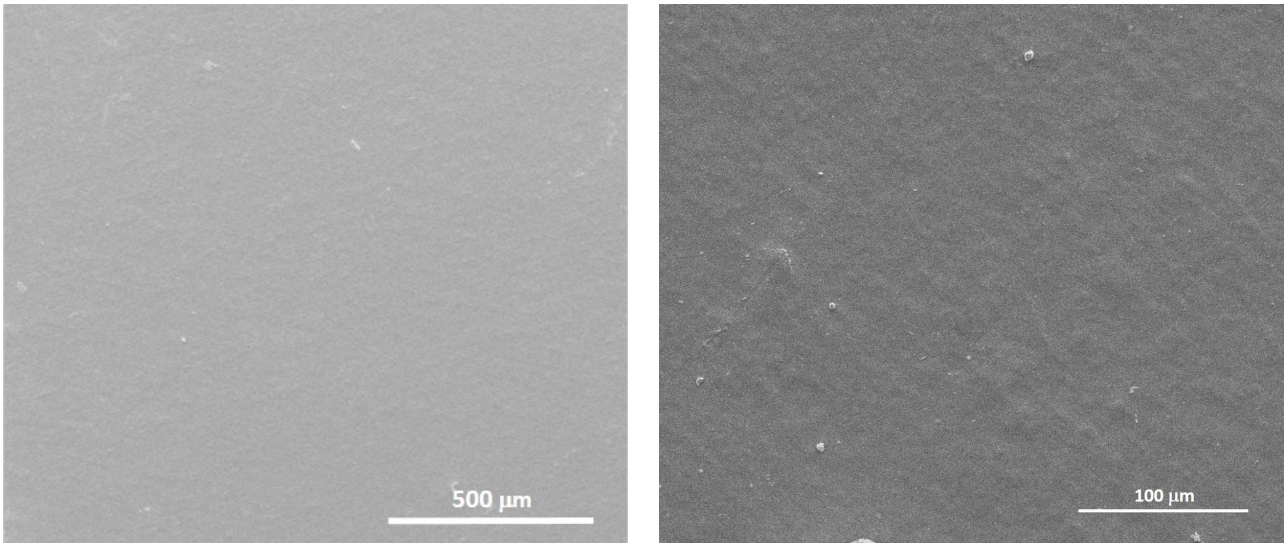

(a) (b)

Figure 2.10: SEM micrographs of the surface of the as-received LDPE films.

2.3 UV Aging

2.3.1 Physico-chemical Characterization

2.3.1.1 FTIR Spectra

During the photo-oxidation of polyethylene, several carbonyl groups (C=O) such as ketones, carboxylic acids, aldehydes and esters can be formed. Ketones can be decomposed

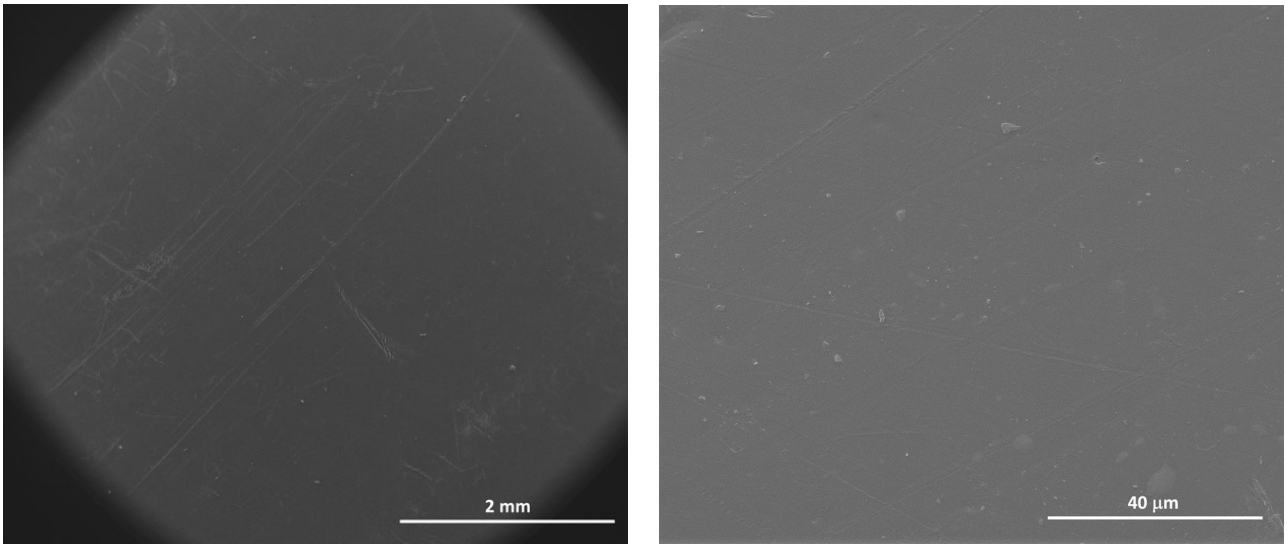

(a) (b)

Figure 2.11: SEM micrographs of the surface of the as-received LDPE plates.

according to the Norrish type I reaction, as shown in Fig. 1.3, thus leading to a chain scission. Alternatively, the photo-oxidation reaction can take another path resulting in a formation of vinyl groups via a Norrish type II reaction [3].

To determine the changes in the chemical composition of the polymer due to these possible oxidation paths, FTIR spectra was recorded for the as-received and the aged LDPE films. The regions of interest of the spectra are compared in Fig. 2.12. The carbonyl functional groups that result from the Norrish type I reaction were evaluated in the 1700 cm^{-1} region, which is shown in Fig. 2.12 a. For clarity, the spectra after 24 h of aging is not shown. There is a gradual increase in the absorbance at 1720 cm^{-1} between 48 hours and 192 hours, followed by a drastic increase after 240 hours of aging, revealing the increasing formation of carbonyl groups. This was accompanied by the formation of vinyl products, which were evidenced by the 900 cm^{-1} region, as shown in Fig. 2.12 b. The spectra shows a peak of low intensity at 908 cm^{-1} for the pristine material, which corresponds to the terminal groups of the polymer [103]. The intensity of the peak increased considerably after 48 hours of aging, signaling the chain scission of the polymer chains. The peak at 890 cm^{-1} corresponds to

the vinylidene groups, and seems to disappear with aging time. This decrease in vinylidene groups could indicate that they have been consumed in reactions with alkyl radicals R−H to form crosslinks [53]. However, it is also possible that disappearance of the vinylidene peak is a visual effect caused by the overlapping of the increasing 908 cm^{-1} peak. Nevertheless, the occurrence of crosslinking was investigated by GPC, and it is discussed in the following section.

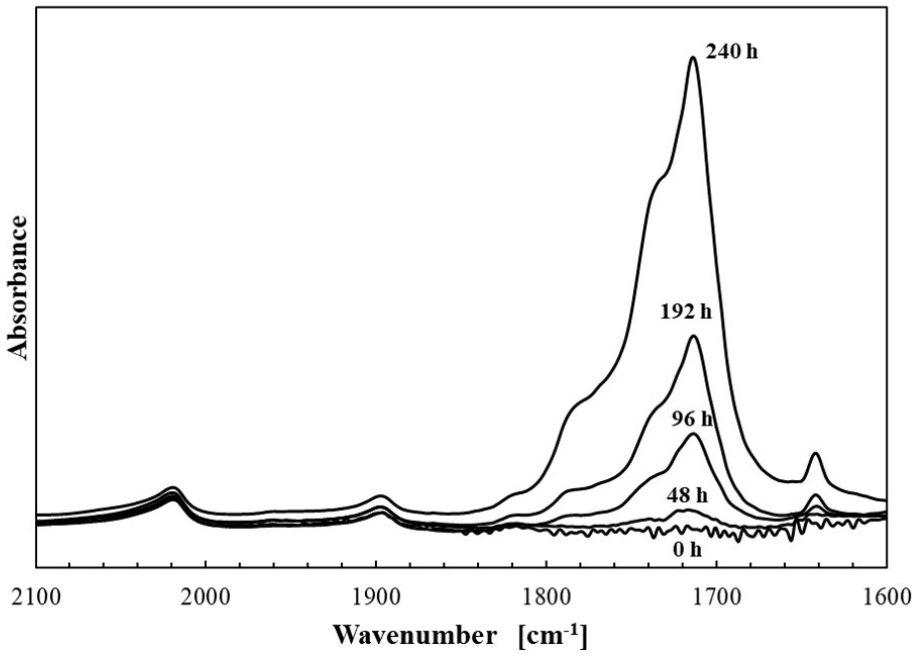

(a)

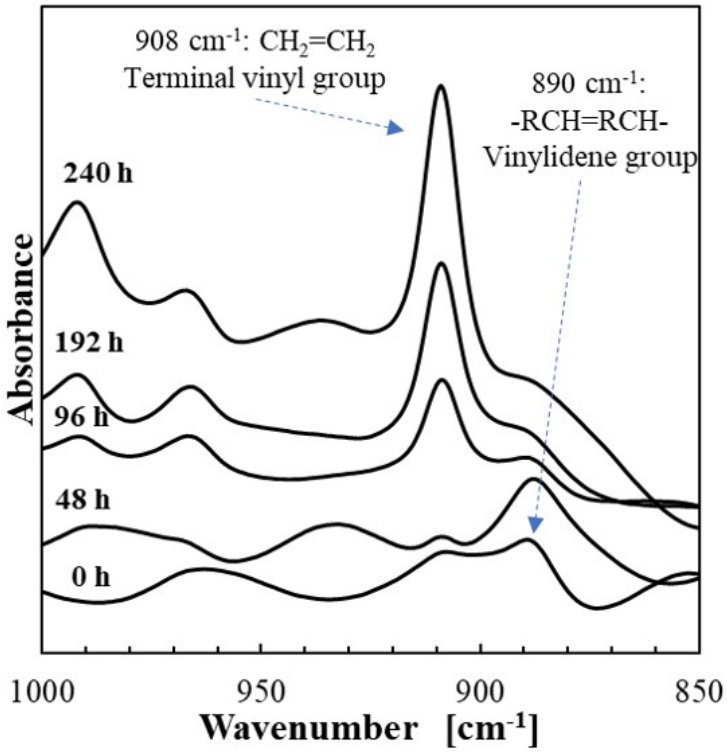

(b)

Figure 2.12: The FTIR spectra of the as-received and UV-aged LDPE films: a) The spectra in the carbonyl region (1700 cm^{-1}), and; b) the unsaturation region (900 cm^{-1}).

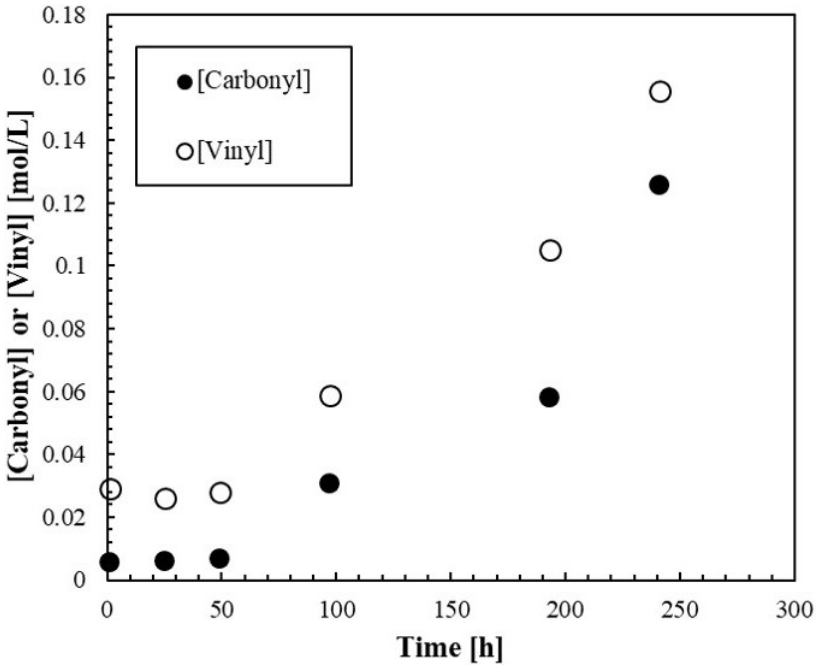

Figure 2.13: Concentrations of carbonyl and vinyl groups measured by FTIR spectroscopy versus UV aging time.

The oxidation kinetics is informed by the formation of carbonyl and vinyl groups. A quantitative analysis of the formation of these groups is possible by calculating their concentration using the Beer−Lambert′s law. The results are plotted in Fig. 2.13, and it suggests that there is an induction time of at least 48 hours for the reactions to take place under the conditions of the experiments. In Fig. 2.13, it is clear that the initial concentration of vinyl groups is higher than that of carbonyl groups; this is expected since vinyl groups correspond to end-groups in nearly unoxidized LDPE [103]. The increasing vinyl index indicates an increase in the concentration of double bonds, which are associated with Norrish type II reactions [112], Fig. 1.3.

Meanwhile, the carbonyl index also increases but remains lower than the vinyl index. This indicates that during UV aging, carbonyl groups decompose via Norrish type I and type II reactions, thus generating profuse chain scissions [59].

2.3.1.2 Molecular Weight

The evolution of the weight average (M_w) and number average (M_n) molecular weights with UV aging time is shown in Fig. 2.14. The molecular weight averages were initially $M_n = 18,200$ g/mol and $M_w = 164,500$ g/mol then rapidly decrease with increasing aging time up to 96 hours. Between 96 and 192 hours, the molecular weight remained largely unchanged. At 192 hours of UV exposure, both M_n and M_w reach a minimum, but M_w increases thereafter.

The initial decrease in the molecular weight suggests a predominant chain scission process (presumably resulting from Norrish type I reactions) in this stage. The noticeable change of molecular weight after just 24 hours is in contrast with the observations from FTIR, where the concentration of carbonyl and vinyl species remained unchanged after 48 hours of UV exposure. This observation may be explained by considering the higher sensitivity of gel permeation chromatography compared to FTIR [101].

It is worth noting that the PDI, which indicates the width of the molecular weight distribution, follows a trend similar to M_w, Fig. 2.14. The evolution of the PDI suggests a homogeneous random chain scission before 192 hours, then a prevalence of crosslinking reactions between 192 and 240 hours of UV irradiation [37, 113, 114]. Indeed, if there were no crosslinking, PDI would tend towards the final value of 2 [37].

2.3.1.3 Crystallinity and Morphology

Fig. 2.15 a shows the heating thermograms for the as-received and UV-aged materials, as obtained from DSC. The melting peak remains at the same temperature. However, as the aging time increases, the appearance of endothermic shoulders (circled) below the melting temperature indicates the formation of new crystallites of smaller lamellar thickness. After 24 h of aging, the thermogram shows that the peak melting temperature of these crystallites is below the exposure temperature (60°C).

To confirm the origin of the new crystallites, an additional test was performed in which a

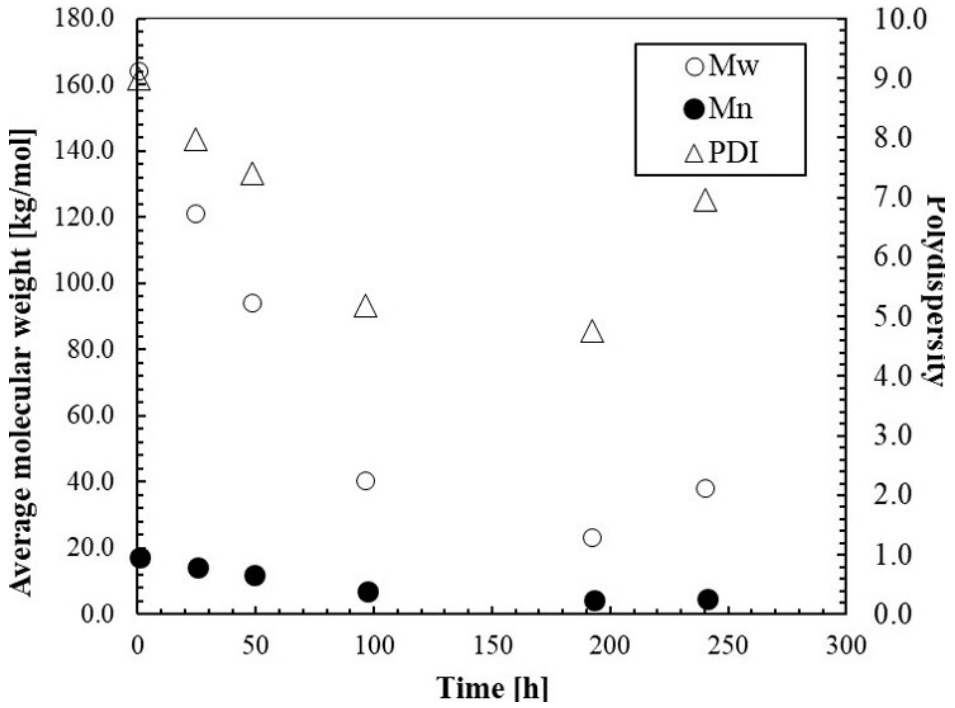

Figure 2.14: Number-average molecular weight, M_n, weight-average molecular weight, M_w, and polydispersity index (PDI), measured by GPC, versus UV aging time.

sample was held for 24 h in 60°C in the absence of oxygen. This thermal aging under vacuum resulted in the creation of some crystallites with a melting peak of 60°C. Thus, these results indicate that the crystallites formed during photo-thermal aging at 60°C in air are slightly less perfect (thinner) than those formed in the absence of oxygen (thermal aging at 60°C under vacuum). This could be attributed to oxidation-induced defects such as hydroxyls and carbonyls, which are incorporated to the polymer chains during photo-thermal aging, thus preventing crystallization. But this could also be attributed to crosslinking induced by oxidation.

The concurrency in chain scission and crosslinking processes (evidenced in the molecular weight results discussed previously) makes the analysis of crystallinity more complicated. Oxidation-induced chain scissions can promote chemi-crystallization, a process in which the resulting shorter polymer chains can more easily reorganize and crystallize [1], presumably around pre-existing crystallite seeds in the amorphous phase, that are too small to be initially

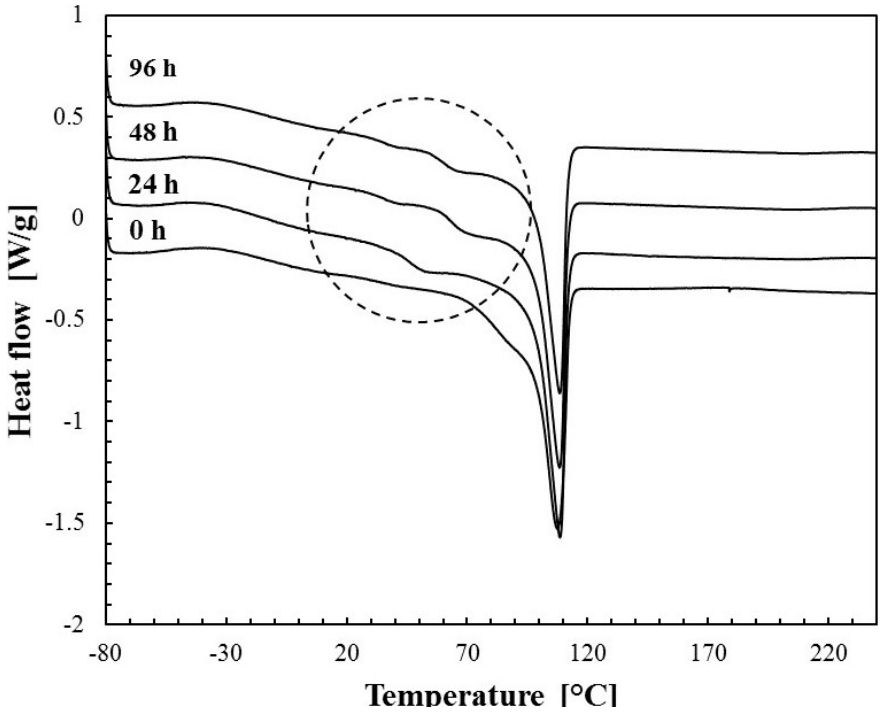

(a)

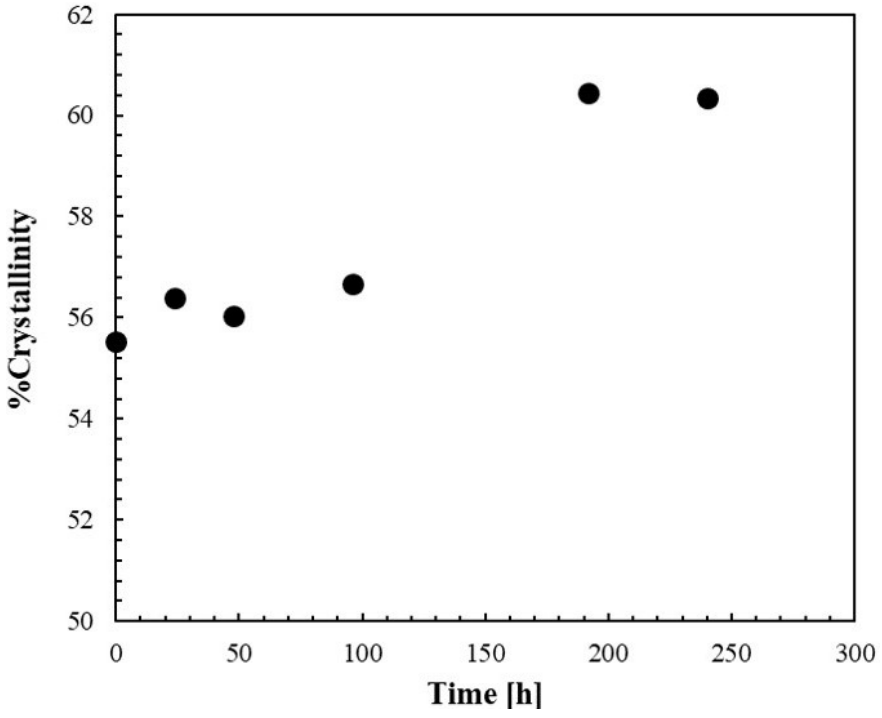

(b)

Figure 2.15: (a) Heating thermograms of LDPE for various UV aging times, showing the appearance of small crystallites (circled). (b) The overall percent crystallinity versus aging time.

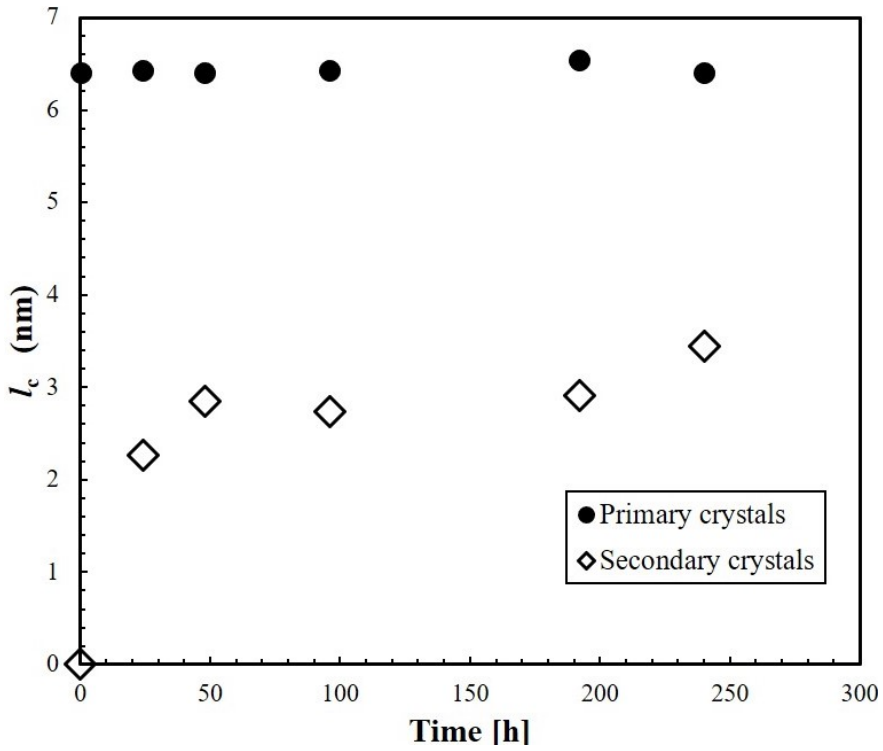

Figure 2.16: Lamellar thickness of primary and secondary crystals versus aging time.

detected by DSC. At the same time, the concurrent crosslinking prevents crystallization. As the UV exposure time increases, the melting peak of these secondary crystals increases, moving towards the main melting peak, and additional endothermic shoulders appear as well. These might indicate the increasing contribution of oxidation-induced chain scissions to secondary crystallization upon aging.

In spite of the changes described above, the variation in the overall percent crystallinity with UV aging were rather small ($\sim 6\%$), as can be seen in Fig. 2.15 b, indicating that the formation of the thin crystallites has a low impact on the bulk percent crystallinity of the material. However, if these thin crystallites are homogeneously distributed into the LDPE matrix, they could play the same role as crosslinks, thus affecting the mechanical behavior of LDPE. The thickness of these secondary crystallites was estimated using the Gibbs-Thomson equation (Eq. 2.3) and the results are shown in Fig. 2.16. It is found indeed that the thickness of secondary crystallites rapidly increases at intermediate UV aging doses. This finding is

key to explaining the transient UV-induced strengthening reported and discussed in the upcoming chapters.

2.3.2 Chemical Damage Characterization

The nominally smooth surface of a film becomes increasingly wrinkled with increasing UV radiation dose. Wrinkling is barely detectable in the 48 h and 96 h films, but becomes visible in SEM after 192 h (Fig. 2.17a). Eventually, superficial cracking occurs after sufficient radiation, as becomes visible in the 240 h film (Fig. 2.17b). A network of parallel microcracks is seen to have formed in these films. It was later seen that the 240 h films were not mechanically "testable" as they broke while being mounted in the grips. This network of microcracks explains their extreme brittleness .

The largest microcracks are 100–200 μm long and oriented along the transverse direction TD. The crack pattern is believed to stem from the film's in-plane anisotropy, which is processing induced, Fig. 2.17c. The MD oriented specimens exhibit higher flow stress and strain hardening rate, as well as lower strain to fracture in comparison with TD oriented specimens (this point is further discussed in a following section.)

Further details at increasingly higher resolution are provided in Fig. 2.18 for the film after 240 h of UV aging. Parallel microcracks, about 200 μm long, can be seen in Fig. 2.18a. The cracks do not traverse the full thickness and appear to wedge into the film. Also, note that the film's surface is rather smooth near cracks. This is likely due to stress relief after cracking.

Away from regions with high density of such cracks, surface wrinkling is observed, Fig. 2.18b. It is believed that some extent of wrinkling is seen in all aged films at various degrees. Eventually, nascent microcracks nucleate at an apex of a wrinkle, as illustrated in Fig. 2.18c. The nascent crack has more roughness along TD than the fully developed crack (compare Fig. 2.18c with Fig. 2.18a).

The damage observed in Figs. 2.17 and 2.18 was generated by mere UV irradiation, that is prior to any mechanical loading. A rationale for this "chemical damage" is provided next.

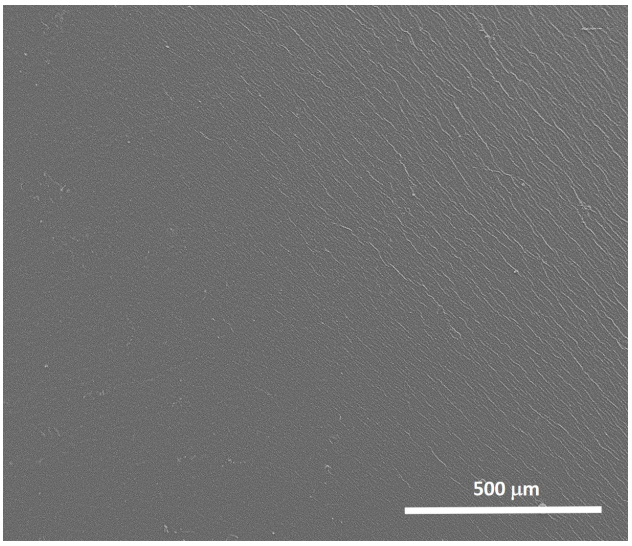

(a) 192 hours

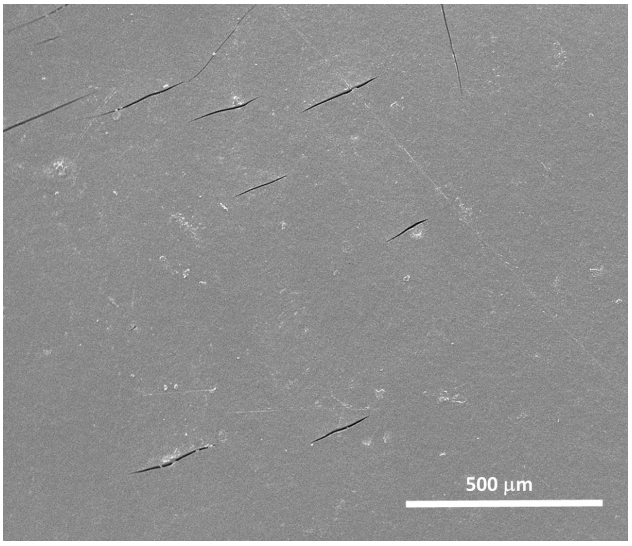

(b) 240 hours

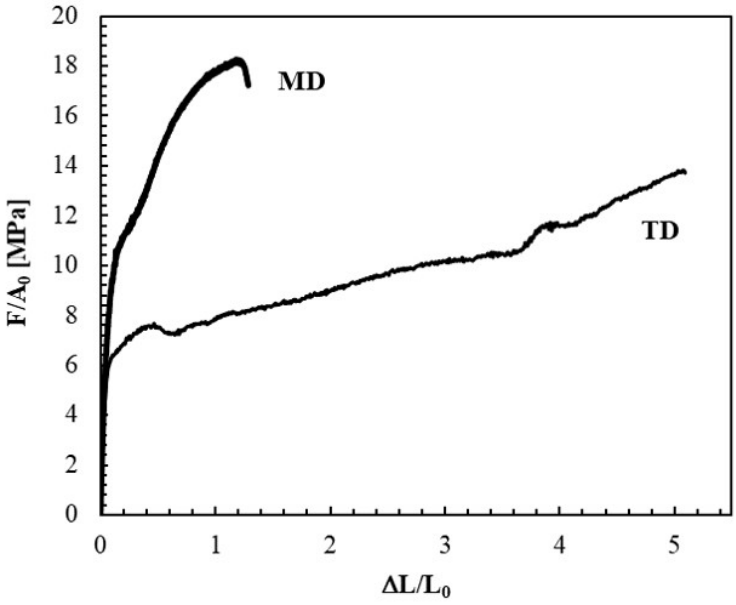

(c) Film anisotropy

Figure 2.17: SEM observations of "chemical damage" (a) 192 h film; (b) 240 h film (cracks oriented along TD). (c) Nominal stress–strain curves for MD and TD rectangular specimens.

The appearance of "chemical cracks" in the absence of mechanical loading can be attributed to a "chemical stress" [115], which is a residual stress related to the chemical reactions of oxidation. This residual stress may have its origin in the volume change concurrent with the thickening of the oxidized layer, or in density gradients due to chemi-crystallization.

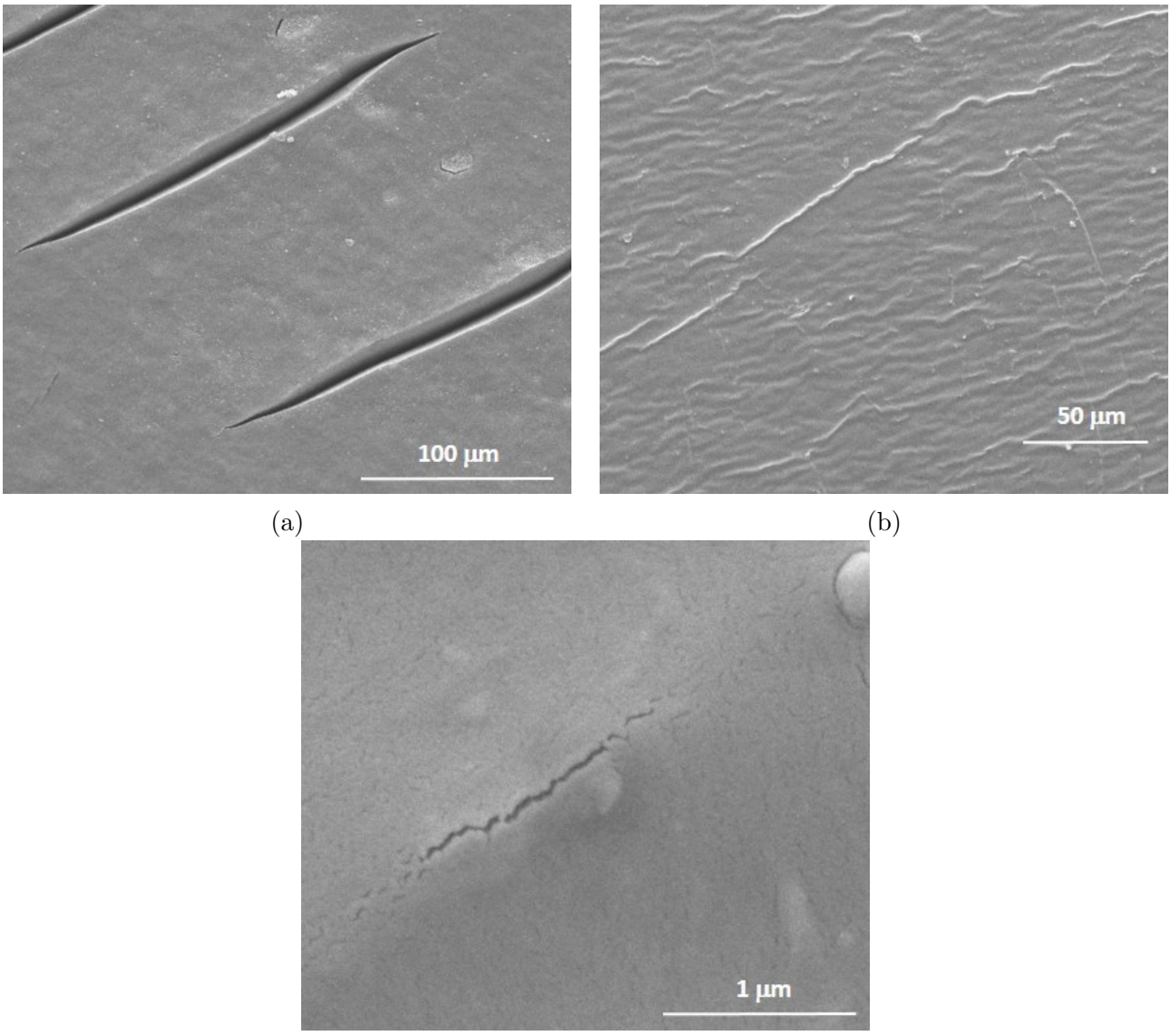

(a) (b)

(c)

Figure 2.18: Observations of chemical damage at higher resolutions after 240 hours of UV aging: (a) Well-developed parallel cracks; (b) Surface wrinkling; and (c) Nascent microcrack. All features are perpendicular to the machine direction MD.

In fact, the system can be seen as a brittle layer adhered to a more complaint substrate. Such mixed-mode problems have been described with detail by Hutchinson and Suo [116]. Using a dimensionless parameter, Z to characterize various cracking patterns, an estimation of the critical stress required for cracking can be obtained using Eq.2.5 [115]:

$$\sigma_{\text{chem}} = \sqrt{\frac{\Gamma E_s}{Z h_c}} \tag{2.5}$$

where Γ is the fracture resistance of the oxidized layer, E_s its elastic modulus, and h_c is the thickness of the oxidized layer. Taking $E_s = 236$ MPa from the experiments (Chapter 3, $\Gamma = 5$ KJ/m^2 for LDPE [117], and h_c as a fraction of the film thickness, say 25 μm, one obtains a critical chemical stress of $\sim$110 MPa for surface cracking and 150 MPa for channeling. Compared with the flow stress of LDPE (Chapter 3), the estimated value for surface cracking is large enough to produce local cracking.

The pattern of these chemical cracks can be explained in terms of the film's orientation and the changes in its morphology. Blown films of semicrystalline polymers develop a preferred orientation during processing [108–110]. For LDPE, the preferred orientation means a row-nucleated lamellar structure consisting of stacks of lamellae aligning along the machine direction (MD) and amorphous zones between the crystalline stacks [108–110], as sketched in Fig. 2.19a.

The orientation dependence is manifested in the tensile anisotropy of the as-received film (Fig. 2.17c), where the orientation of the lamellae along MD results in higher flow stress and strain hardening, and lower strain to fracture in comparison with TD. Fig. 2.19b depicts how the thickness of the interlamellar space l_{a0} is reduced at least by a factor of 2 as a result of the introduction of new and thin crystallites via chemi-crystallization. The reduction of the interlamellar space leads to embrittlement of PE [1, 37] therefore promoting the formation of cracks. The results obtained from DSC for lamellar thickness of primary and secondary crystalline regions (Fig. 2.16) together with the observed cracking lead us to presume that the new interlamellar thickness l_{a1} (Fig. 2.19b), falls below the critical interlamellar thickness

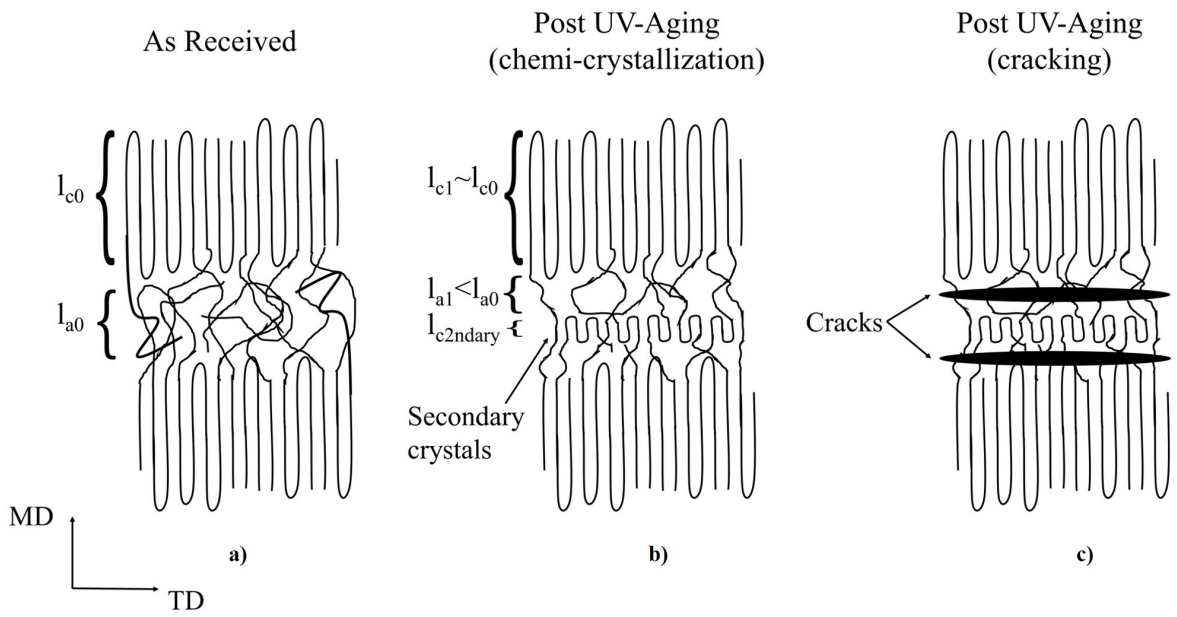

Figure 2.19: Schematic scenario of UV-induced cracking in the absence of mechanical loading along the transverse direction (TD) in oriented LDPE films.

established by Fayolle et al. for polyethylene $l_{ac} = 6$ μm [1, 37], below which a sharp ductile to brittle transition occurs.

Additionally, since oxidation occurs on the amorphous region, it is expected to act specifically in the interlamellar spaces along TD, making them more vulnerable to the formation of cracks, Fig. 2.19c. Studies of the tear resistance of PE have shown that the low tear resistance along TD of LDPE relative to its linear counterparts (such as HDPE and LLDPE) stems from the low number of tie molecules between lamellar stacks in LDPE. In the case of oxidized LDPE, the advance of the chain scission reactions leads to the decrease of these tie chains, which could make the transverse direction more prone to cracking. These oxidation-induced cracks contribute to the weakening observed at larger UV doses and the lower ductility reported and discussed on Chapter 3.

The as-received plate exhibited a nominally smooth surface (Fig. 2.20) a. Upon radiation, superficial cracking occurs, as shown in Fig. 2.20 b for the 240 h aged plate. The cracks formed networks that showed certain size and shape regularity, arranging themselves into a

polygonal, isotropic pattern. One can distinguish a primary polygonal array formed by the longer, wider cracks which do not always join. A secondary array is formed by smaller cracks that define a denser network of polygons. The larger cracks can be up to ≈ 1.4 mm long.

A salient feature is the difference in the crack patterns produced by UV aging in films and plates. This difference can be related to the manufacturing process of each. In the UV-aged films the orientation of the cracks along TD resulted from the anisotropy induced during the manufacturing process. The plates were produced by compression molding instead, resulting in a material that is isotropic in-plane, unlike the films. Thus, it seems reasonable that the crack pattern in the UV-aged plate does not have a preferred orientation like the one observed in aged films. A similar contrast in crack patterns due to processing has been previously reported for aged polypropylene (PP) [34]. Oxidized injection molded specimens showed chemical cracks that were concentric with the injection gate (i.e. the place of entrance of the molten polymer into the mold), indicating that the pattern was linked to the polymer flow during molding. On the other hand, the compression molded specimens exhibited a random pattern [34].

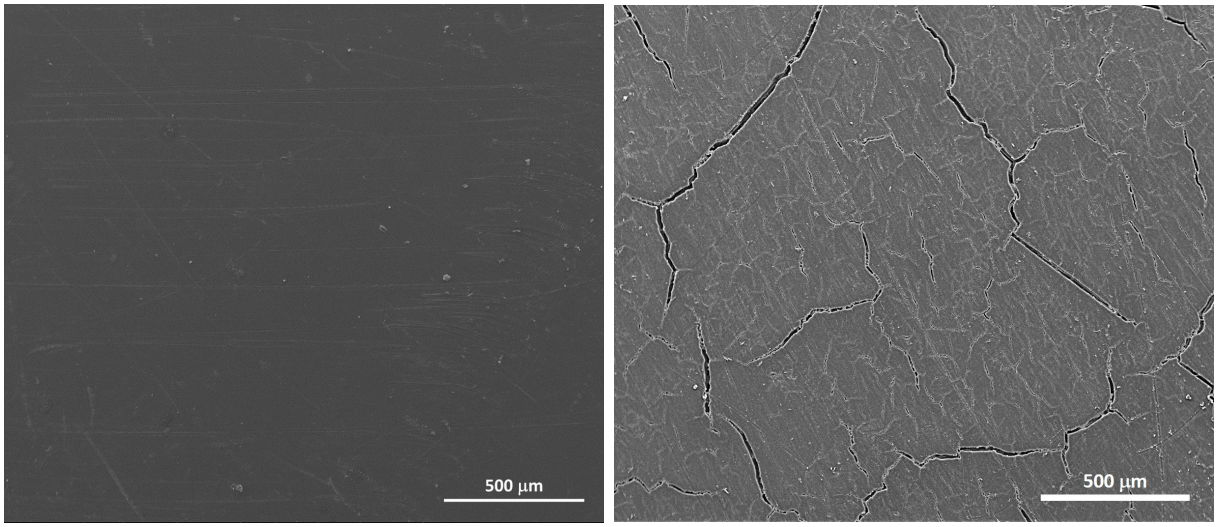

(a) 0 hours (b) 240 hours

Figure 2.20: The surface of LDPE plates after UV exposure. The surface of the as-received LDPE plate is smooth and free of any cracks (a). The effect of UV aging can be observed as cracks in the 240 hours plate (b).

These cracks, like those observed in the films, are "chemical cracks", i.e. they are a product of the oxidation reactions and their resulting residual stresses in the material. Because of the plate's thickness ($\approx$ 2 mm) and the fact that oxidation is a diffusion controlled process, the aged plates developed a superficial oxidized layer (this is demonstrated by SEM and nanoindentation results in Chapters 3 and 4). This layer, usually $\approx$ 100 μm [42], results in an heterogeneous material that can be considered as a brittle layer adhered to a more compliant substrate. If the superficial layer was unconstrained, its modification due oxidation would induce volume change or swelling. However, since the oxidized layer is fixed to the compliant core, a biaxial stress state develop on the thin layer, which could lead to cracking [115]. Using Eq.2.5 with $E_s = 350$ MPa from the experiments (Chapter 3), and $h_c = 100$ μm, the estimated critical chemical stress for surface cracking is $\sim$65 MPa. When compared with the flow stress of the plates (see Chapter 3), these critical values are large enough to produce local cracking.

Fig. 2.21 provides further details at increasingly higher resolution for the plate after 240

h of UV aging. The range of cracks sizes can be better appreciated in Fig. 2.21a, b and c. Fig. 2.21c shows"Y" junctions formed by 3 micro-cracks converging at ≈120°. These junctions seem to be the origin of the larger hexagonal crack pattern observed in the plate. Such "Y" joints crack patterns have been observed in nature over many orders of magnitude in length.

To make sense of the crack patterns of the UV-aged plates it is helpful to consider the supramolecular morphology of the plate and the depth of the oxidized layer. For the former, one recalls that oxidation acts mainly on amorphous regions, where oxygen absorption is facilitated. Compression molded LDPE plates are known to have a spherulitic structure [118]. The spherulites form polygonal pattern defined by the amorphous inter-spherulitic material [119]. It is thus possible that the polygonal, isotropic character of the crack pattern results from cracks nucleated preferably at the amorphous interspherulitic material. Next, the influence of the oxidation depth is considered. Studies of various layered material systems with similar crack patterns have concluded that the thickness of the superficial layer influence both the size of the cracks arrays as well as its rectilinear character (i.e. proportion of "Y" junctions to"T" junctions) [120–122]. In general, thicker layers lead to bigger polygon areas and more rectilinear pattern. This will be further discussed in light of the observations made in HUV and naturally aged material.

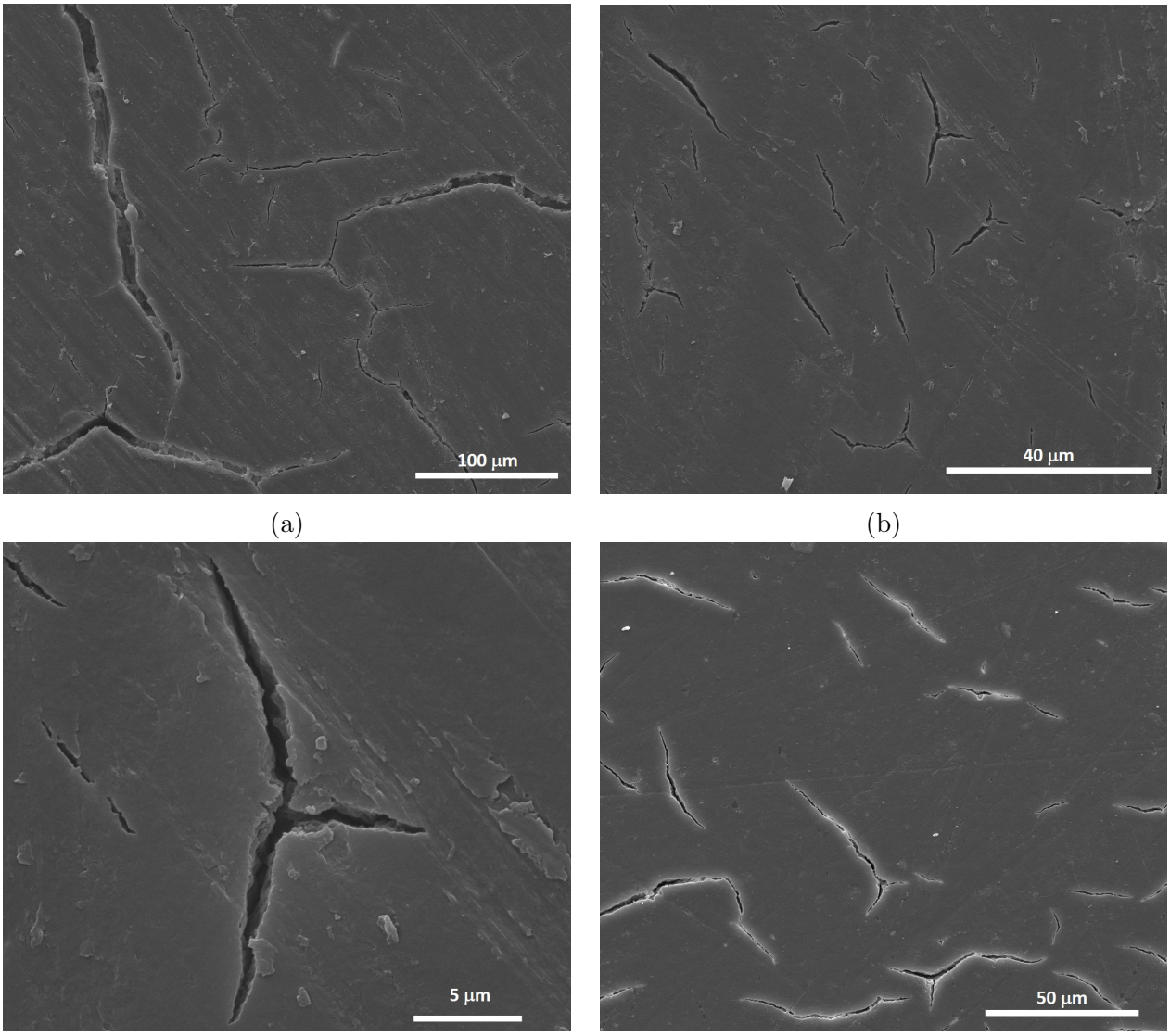

Figure 2.21: Observations of chemical damage in LDPE plates after UV aging: (a) Well-developed cracks concurrent with thinner cracks in the 240 h specimen; (b) and (c) Nascent microcracks in in the 240 h specimen, forming "Y" joints. (d) Similar "Y" joints microcracks observed in certain regions of the 192 h specimen.

2.4 HUV Aging

Given its chemical structure, PE is hydrophobic. It has, therefore, weak interactions with polar substances like water, making it resistant to hydrolytic decomposition. Most of the studies of the effect of water or humidity in aging have been in the context of thermal aging.

Moreover, focus has been laid on anti-oxidant containing polyolefins, thus, any accelerating effect of water is usually contributed to the removal of antioxidants. However, whether the UV induced chemical degradation is itself sensitive to water intake is not settled. In fact, if one takes into account the high gas permeability of PE, then it is expected that the dissolution of oxygen in PE increases with humidity absorption by the polymer [123], which could affect the oxidation kinetics of the material. Moreover, photo-oxidation introduces carbonyl groups and other functional groups, which are polar, making the polymer surface more hydrophillic than the pristine material [124]. This, in turn, would make the oxidized material more susceptible to water and to further UV oxidation compared to the pristine material.

2.4.1 Physico-chemical Characterization

2.4.1.1 FTIR Spectra

Fig. 2.22 shows the spectra for the HUV-aged material in the carbonyl region. The spectrum of the pristine material is shown for reference. The carbonyl band increases with aging time, indicating that Norrish type I reactions also take place during the HUV aging of LDPE, similarly to what was observed for UV aging. To visualize the effect of humidity on the concentration of carbonyl groups produced during photo-oxidation, Fig. 2.23 compares the spectra of UV and HUV-aged specimens after 96 hours of exposure. HUV aging resulted in a higher absorbance, suggesting a higher concentration of carbonyl groups in the HUV aging compared with UV aging.

The unsaturated groups are depicted by the spectra in Fig. 2.24. For the terminal vinyl groups the trend is also analogous to that of UV aging, with the intensity of the 908 cm^{-1} band increasing with aging time. However, the 890 cm^{-1} peak disappeared almost completely after 48 h of HUV aging, in contrast with the observed for UV aging, where after 96 h the vinylidene group was still visible (Fig. 2.12). This indicates that in HUV aging the vinylidene groups are consumed faster than during UV aging. Recall that a decrease in vinylidene groups

could indicate their reaction with alkyl radicals R−H to form crosslinks [53]. Accordingly, humidity seems to promote a higher activity of the crosslinking reactions during oxidation.

Fig. 2.25 shows the concentration of carbonyl and vinyl groups during HUV aging as calculated by Beer−Lambert′s law. The trend is similar to that of UV, with the exception that in HUV aging the concentration of carbonyl groups surpass that of vinyl groups after large doses (240 h). This indicates that at this stage of HUV aging, Norrish type II mechanism dominates (Fig. 1.3), where vinyl groups are first formed and then consumed in the production of carbonyl species [125].

Additionally, the concentration of carbonyl groups seems to increase as early as in 48 hours, indicating that the induction time in HUV (at least the one captured by FTIR) is shorter than in UV aging. A clearer idea of the effect of humidity on UV aging is obtained by comparing the concentration of these functional groups after UV and HUV aging, as shown in Fig. 2.26. Fig. 2.26a shows a drastic acceleration of HUV relative to UV aging in the production of carbonyl groups after 48 hours of HUV aging. A similar trend is observed for vinyl groups in Fig. 2.26b, even if the production of vinyl groups seems to stagnate after 240 hours of HUV aging, likely a result of dominant Norrish type II reactions, as mentioned earlier. Overall, these results demonstrate the accelerating effect of humidity in the photo-oxidation of LDPE.

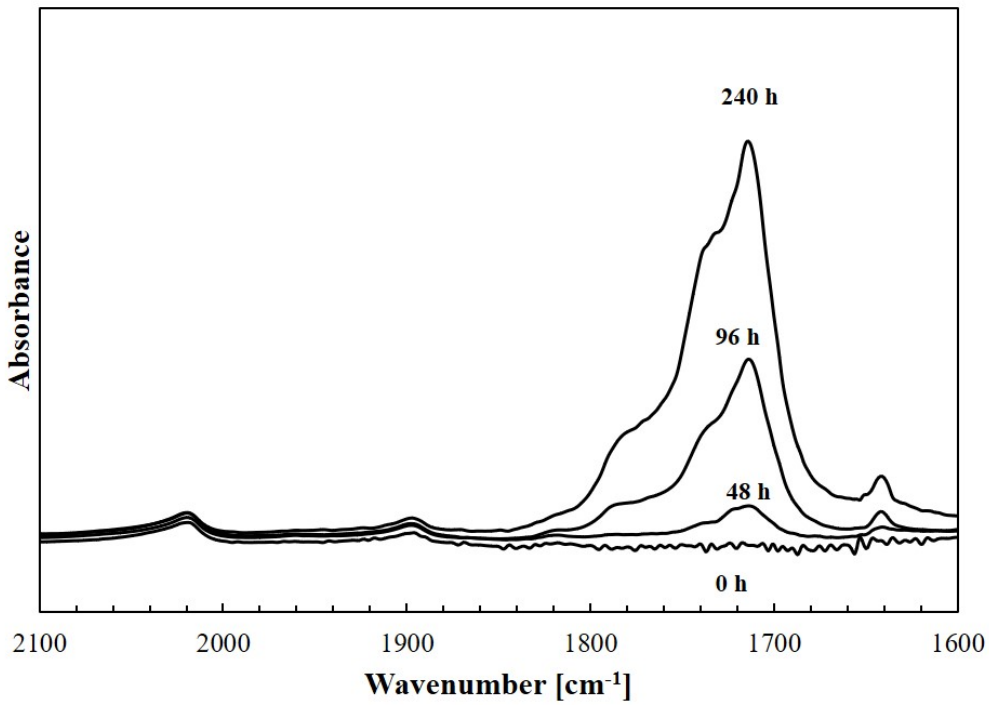

Figure 2.22: The FTIR spectra of the as-received and HUV-aged LDPE films in the 1700 cm^{-1} region.

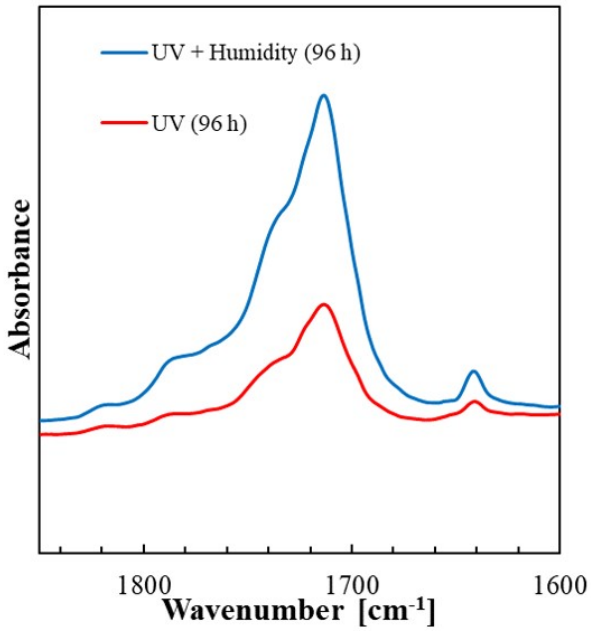

Figure 2.23: Comparison of the FTIR spectra of UV and HUV-aged specimens in the carbonyl region, after 96 hours of exposure.

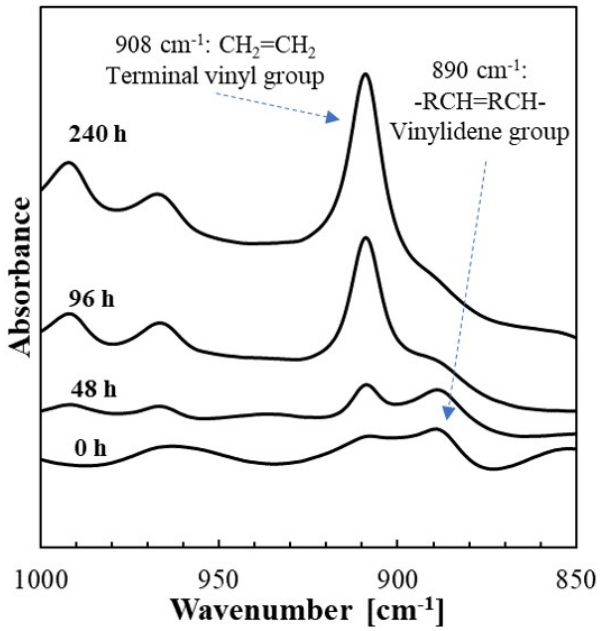

Figure 2.24: FTIR spectra of the as-received and HUV-aged LDPE films in the unsaturation region.

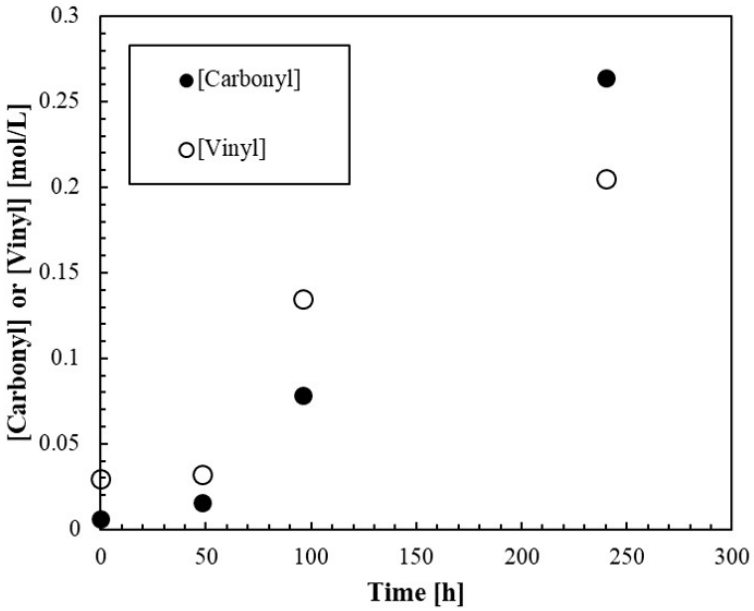

Figure 2.25: Concentrations of carbonyl and vinyl groups measured by FTIR spectroscopy versus HUV aging time.

2.4.1.2 Molecular Weight

The evolution of the weight average (M_w) and number average (M_n) molecular weights with HUV aging time is shown in Fig. 2.27. The molecular weight averages decreased rapidly with increasing aging time up to 48 hours. A slight increase in recorded for 96, and lastly, all the properties reach a minimum value after 240 hours of HUV aging.

As in the UV case, the initial decrease in the molecular weight suggests a predominant chain scission process, likely a result of Norrish type I reactions in this stage. Unlike the UV case, no increase in average molecular weight is attained at high doses, suggesting that chain scission is even more prominent in HUV aging at this stage.

Curiously, the accelerated kinetics of the HUV aging, as demonstrated by the concentration of carbonyl and vinyl groups (see Fig. 2.26), do not seem to be accompanied by an accelerated decrease in average molecular weight M_w (Fig. 2.28), (nor of the M_n or PDI, for that matter). These seemingly contradictory facts can be reconciled by invoking the

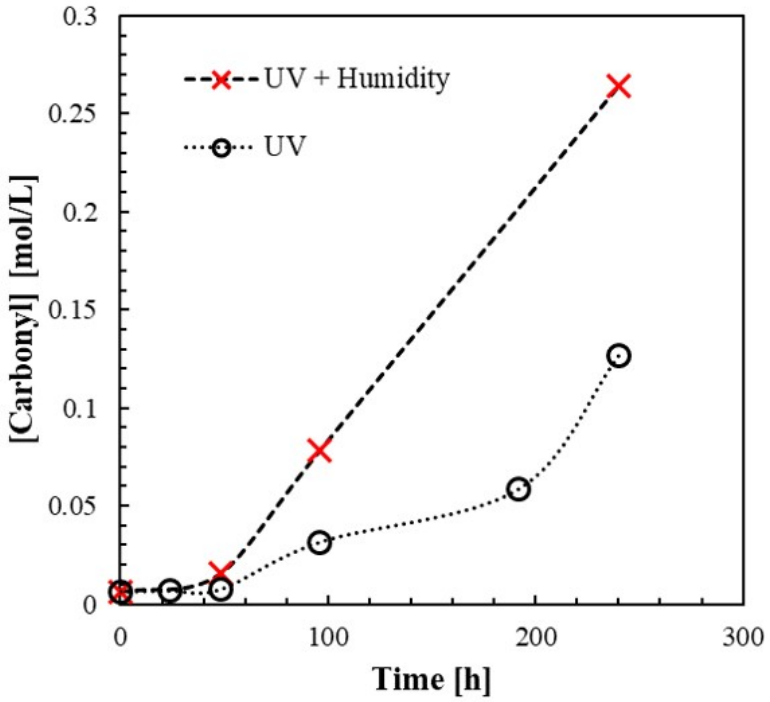

(a)

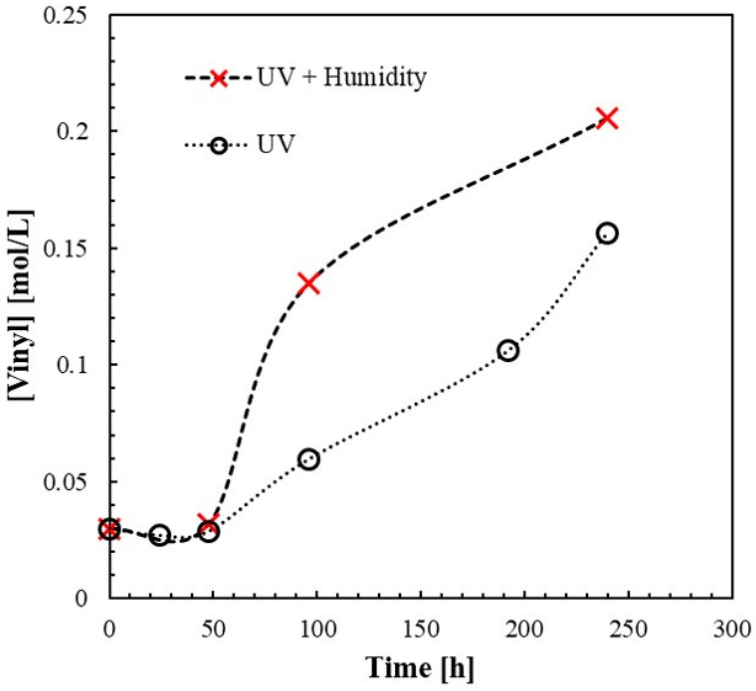

(b)

Figure 2.26: Comparison of the concentrations of: a) carbonyl, and; b)vinyl groups measured by FTIR spectroscopy for UV and HUV. Dashed lines are included to guide the eye.

action of crosslinking. In fact, the M_n at 96 h does not share the slight increase in value that M_w exhibits, resulting in an increased PDI after 96 h of HUV aging. This increase in PDI is characteristic of crosslinking reactions. In this light, one can indeed associate the stagnation in molecular weight reduction after 96 h with the disappearance of the 890 cm^{-1} band in the FTIR spectra of the 96 h aged material (Fig. 2.24). Recall that this band is associated with the RH=RH groups, which are usually present in the pristine material, and whose disappearance suggests its consumption in crosslinking reactions [53].

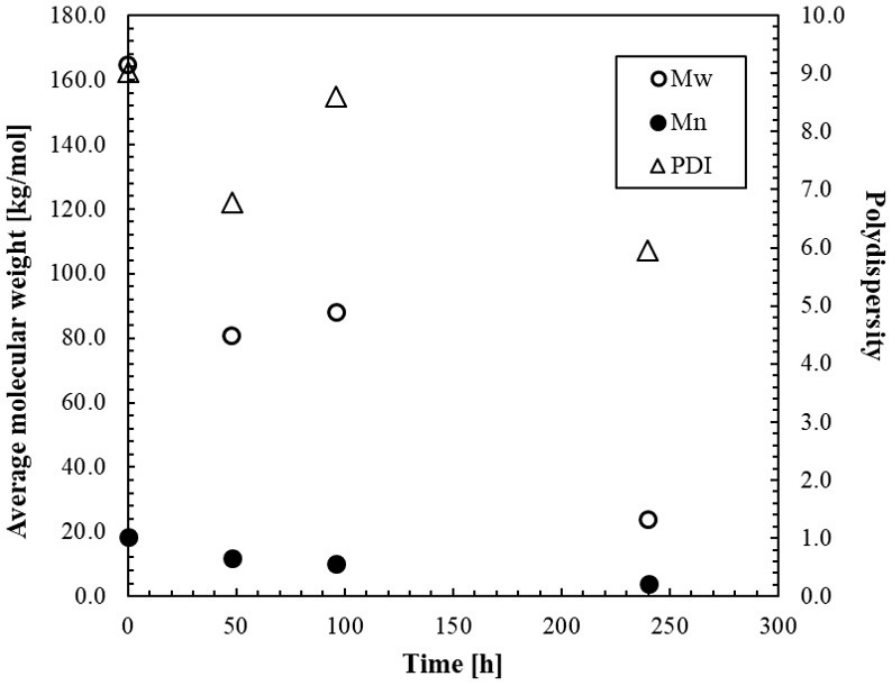

Figure 2.27: Number-average molecular weight, M_n, weight-average molecular weight, M_w, and polydispersity index (PDI), measured by GPC, versus HUV aging time.

2.4.1.3 Crystallinity and Morphology

The heating thermograms for the HUV-aged materials are shown in Fig. 2.29a. As in the UV case, a formation of smaller crystals is revealed by the appearance of small

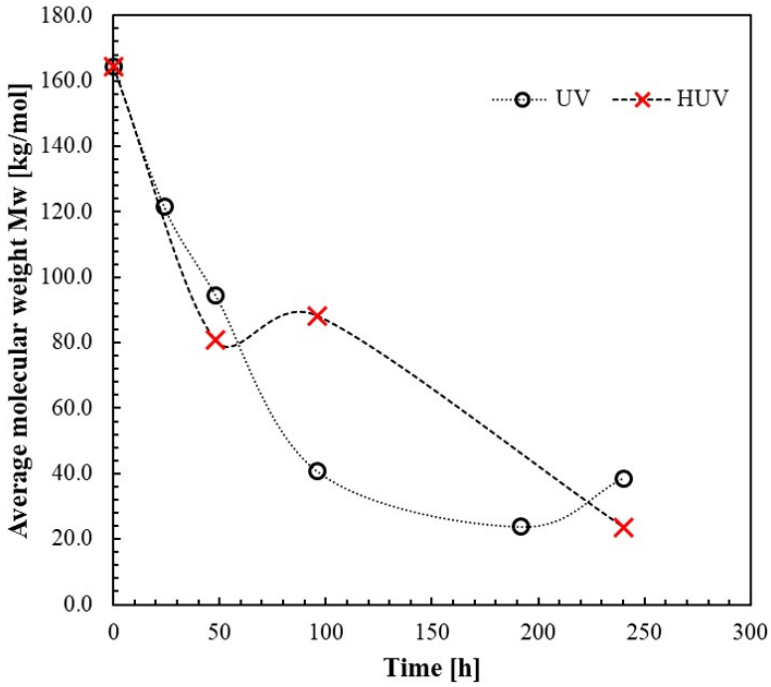

Figure 2.28: Comparison of the weight-average molecular weight, M_w versus aging time for UV and HUV-aged LDPE. Dashed lines are included to guide the eye.

endothermic shoulders with aging (highlighted by the dotted circle). Fig. 2.29b shows the percent crystallinity during HUV aging, compared to that of UV. The trends are similar, while at 48 h there is a greater decrease in crystallinity in the HUV case. In the previous sections it was demonstrated that there is active crosslinking (at least) in the first 96 hours of HUV aging. A stagnation of the bulk crystallinity could thus be a result of the competition between chain scission and crosslinking. On the one hand, chain scission promotes chemi-crystallization by improving chain mobility. On the other hand, the concurrent crosslinking has a deterrent effect on chain movement, thus slowing or impeding chemi-crystallization. However, this competition does not seem to justify the decrease in crystallinity (if only of 3.9 %) observed after 48 hours. In general, the incorporation of humidity cycles resulted in a greater increase of the overall crystallinity at high exposure times (96 and 240 hours), in accordance with the greater chain scission rate evidenced for HUV in the previous sections

and that is known to promote chemi-crystallization in the material [60, 126].

The lamellar thickness of the new crystallites revealed by the endothermic shoulders on the thermograms (Fig. 2.29b) was estimated and the results plotted in Fig. 2.30. For comparison, the thickness of the primary crystals, as well as the results obtained for UV aging are also plotted. The overall trend of secondary l_c during HUV is similar to that of UV. Humidity seems to promote a greater thickening of the secondary lamellae at intermediate exposure times (48 and 96 h). However, at large doses (240 h), HUV results in basically the same secondary l_c as UV aging. This may suggests that: i) at doses large enough, the effect of humidity on the thickening secondary crystals is negligible compared to UV; or ii) there is a saturation for secondary lamellar thickening in the conditions studied. Lastly, the humidity cycles seem to have no effect on the thickness of the primary crystals, in accordance with the observed in UV aging. Likewise, the higher percent crystallinity in HUV after 240 h, despite having similar secondary l_c as the UV-aged material is in accordance with the observed for UV aging, where the contribution of secondary crystallites to bulk crystallinity was negligible.

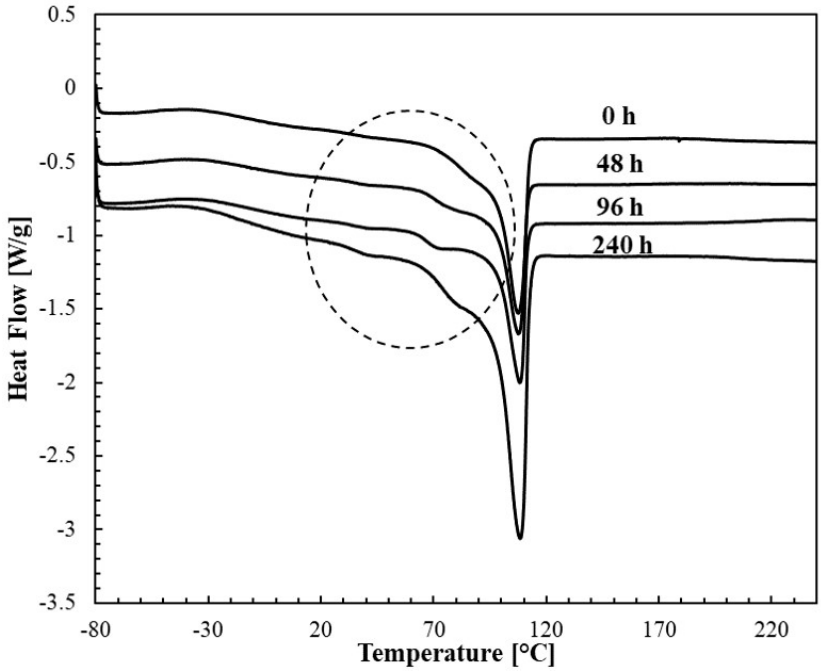

(a)

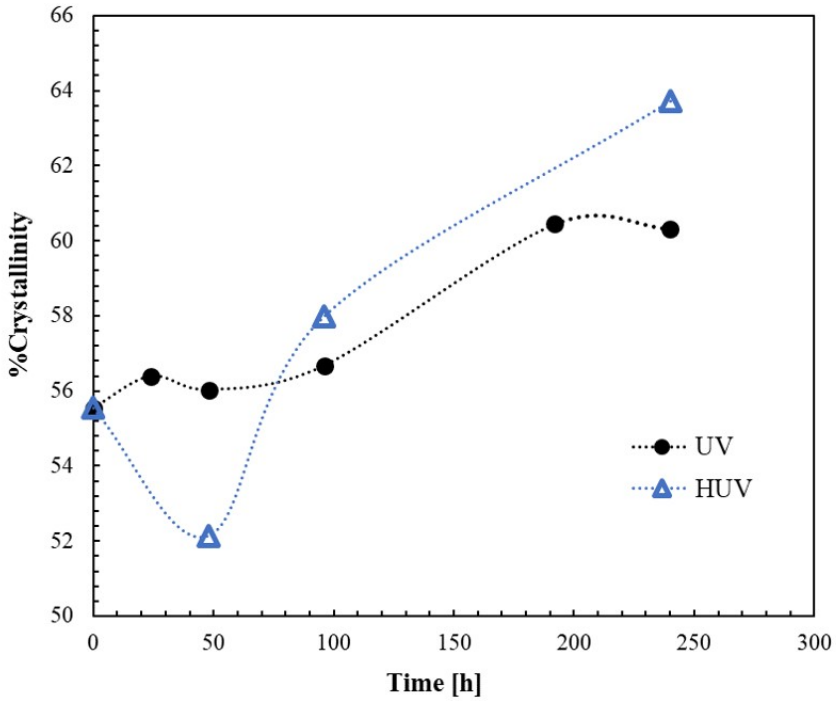

(b)

Figure 2.29: (a) Heating thermograms of LDPE for various HUV aging times, showing the appearance of small crystallites (circled). (b) The overall percent crystallinity versus aging time. Dashed lines are included to guide the eye.

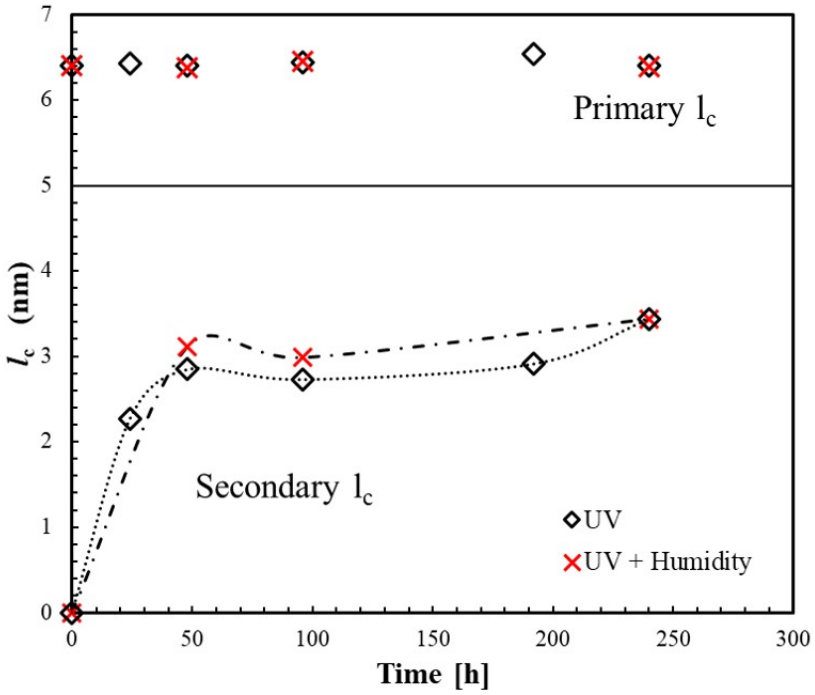

Figure 2.30: Lamellar thickness of primary and secondary crystals versus aging time for UV and HUV aging; see equation (2.3). Dashed lines are included to guide the eye.

2.4.2 Chemical Damage Characterization

Fig. 2.31 compares the surface of an LDPE film after 96 hours of UV and HUV aging. In the 96 h UV-aged film, defects are barely detectable (Fig. 2.31a). The inclusion of humidity cycles seems to promote the appearance of surface irregularities in the 96 h HUV-aged films, as observed in Fig. 2.31b. This is in accordance with the accelerating effect of humidity on oxidation described in the previous section. Superficial cracking also occurs in plates after 240h of HUV aging, as shown in Fig. 2.32, where the surface of pristine and UV-aged material are also shown for comparison. Similar to UV aging, HUV aging resulted in the creation of a polygonal array of thicker, big cracks, concurrent with a denser network of thinner, secondary cracks. The crack in the HUV specimen appeared to be wider and deeper than those of the UV-aged specimen. The cracks pattern in the HUV-aged material appears more rectilinear, and seems to have more"T" junctions (Fig. 2.33)than its UV counterpart,

which showed mostly "Y" junctions. The greater rectilinear character of the crack pattern might indicate that the oxidized superficial layer in HUV is thicker than that of UV, as thicker layers lead to more rectilinear crack patterns [120]. Incidentally, an estimation of the oxidation layer depth was attempted using the micrographs in Fig. 2.34. The images focus on the plate surface and then on the bottom of the crack. By determining the difference the working distance (WD) of each micrographs, one estimate the depth of the crack (and thus oxidation layer) to ≈ 0.2 mm (200 μm).

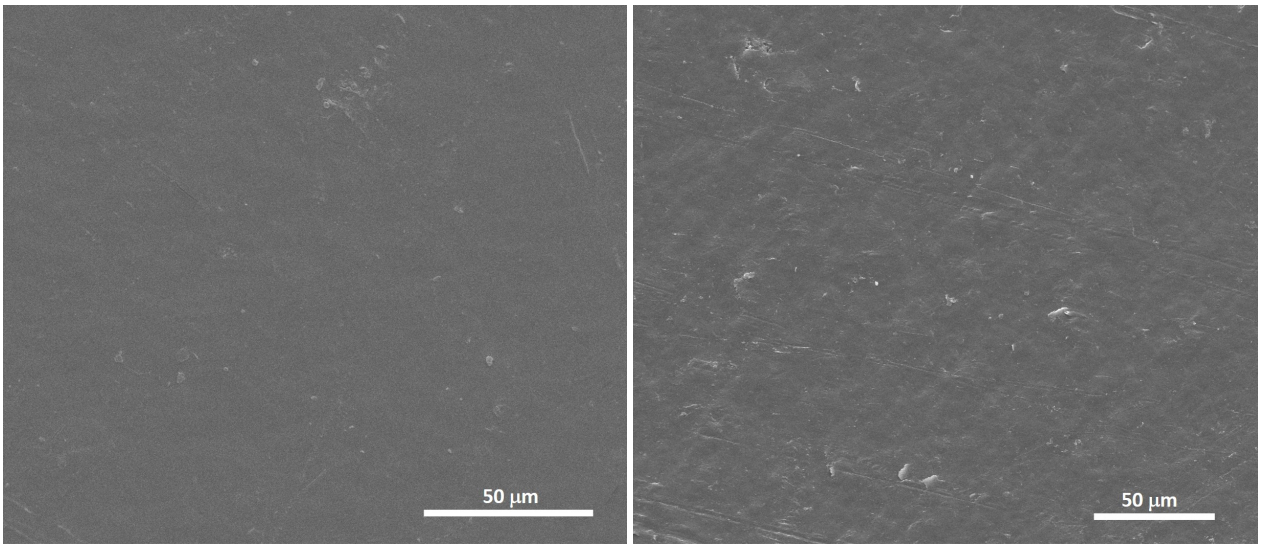

(a) UV (b) HUV

Figure 2.31: The surface of LDPE films after 96 hours of (a) UV and (b) HUV exposure. The effect of humidity can be observed as more defects and irregularities in (b).

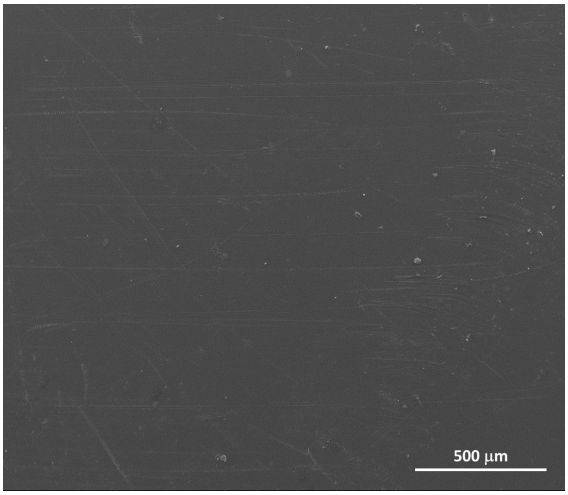

(a) as-received

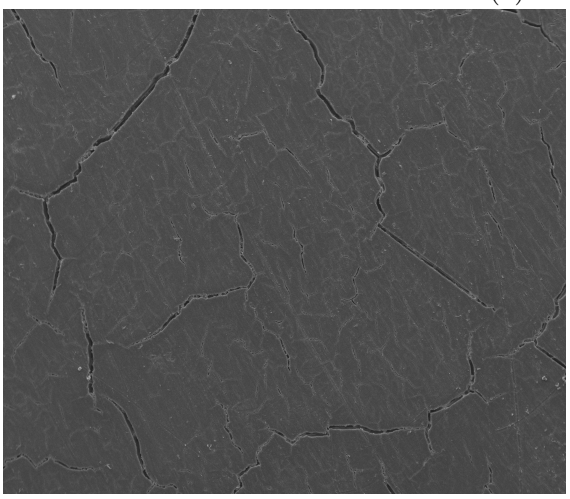

(b) UV: 240 hours

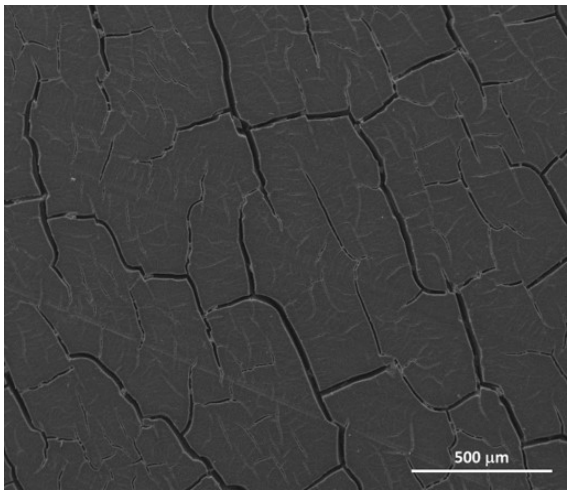

(c) HUV: 240 hours

Figure 2.32: Comparison of the surface of as-received LDPE plate (a) with (b) plate UV-aged for 240 h, and (c) plate HUV-aged for 240 h.

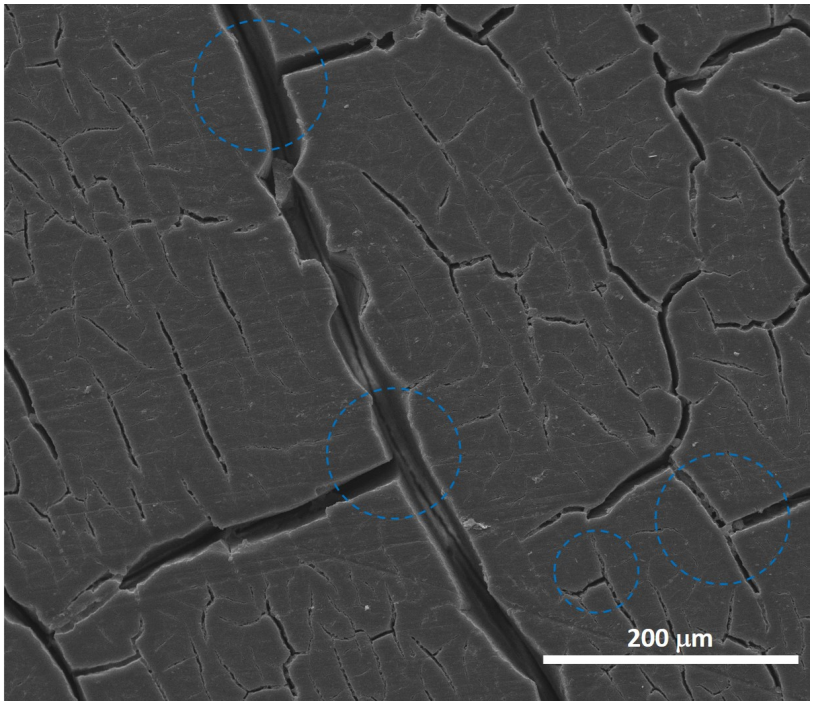

Figure 2.33: Observations of chemical damage in LDPE plate after HUV aging showing "T" junctions of cracks.

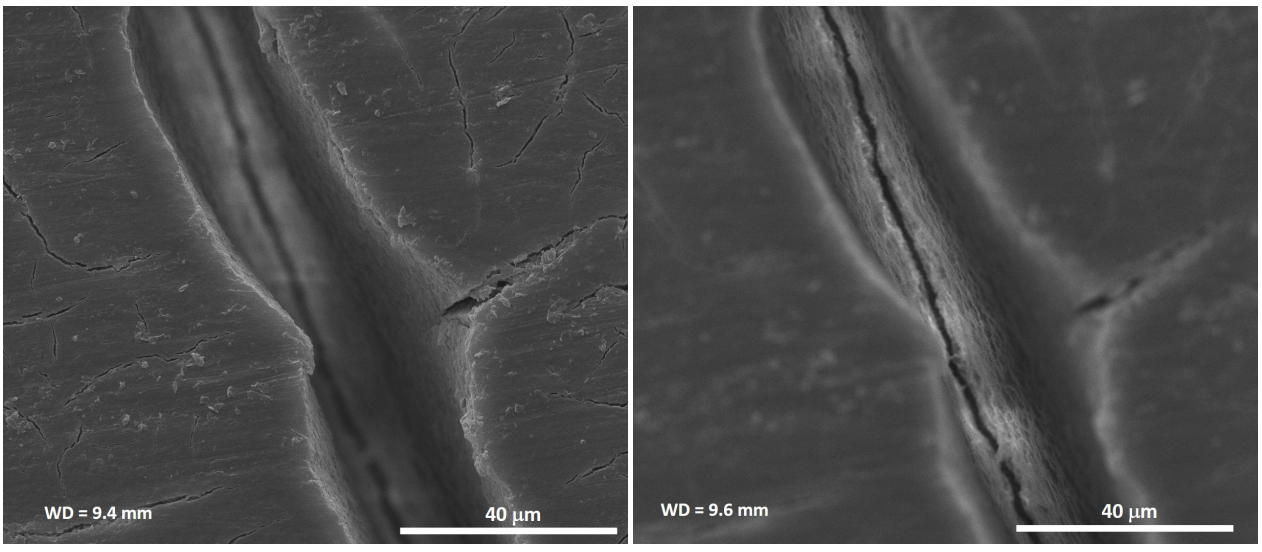

(a) (b)

Figure 2.34: Detail of chemical crack after 240 h of HUV aging. The crack depth is estimated as $\approx$ 0.2 mm (200 μm) from the difference in the working distances (WD) of the SEM micrographs.

2.5 Natural Aging

2.5.1 Chemical Damage Characterization

After 8 months of natural aging, the LDPE plates showed a cracked surface as observed in Fig. 2.35. Salient features include the erosion of the plate and the presence of numerous artifacts on its surface. The erosion is caused by the exposure of the sample to wind, sand and dust [127]. The artifacts are dust particles mainly composed by calcite, dolomite, and quartz [128]. Some of these particles have also agglomerated inside the cracks of the specimen, as shown in Fig. 2.35 b, c, and d.

It is worth noting that the crack pattern in the naturally aged plate differed from that of the UV and HUV-aged plates in at least two main ways. Firstly, the crack pattern of the naturally aged plate appears more rectilinear than that of the laboratory-aged plates. Fig. 2.35a shows several occurrences of 90° junctions ("T" junctions), while a detail of such junction is provided in Fig. 2.35b. Unlike its UV and HUV counterparts, few "Y" junctions were observed. Secondly, the area of the polygons formed by cracks (Fig. 2.36) is higher in the naturally aged plates in comparison, at least, with the HUV-aged plates (since the crack patterns in the UV-aged plates did not close, a comparison of pattern area is difficult). Lastly, there seems to be less secondary cracks in the naturally aged plate, however they could actually be concealed by the agglomeration of dust particles.

The observed difference in crack patterns could be an indication of the advance of oxidation into the material in each oxidation type. As mentioned earlier, it has been established for other materials systems which exhibit similar crack patterns, that the area of the polygons formed by the cracks is proportional to the thickness of the thin layer [121, 122]. Thus, one might infer that the larger crack polygons observed in the naturally aged plate indicate a thicker oxidation layer. Similarly, some of these studies have shown that a thicker layer results in a more rectilinear pattern [120], reinforcing the idea that the oxidized layer in the naturally aged plates is thicker than in the other conditions analyzed.

Indeed, a thicker oxidation layer is expected considering on average an exposure of 8 months is equivalent to $\approx$ 3,333 J/m^2, more than twice the radiation received by the plates aged in UV and HUV after 240 h ($\approx$ 1240 J/m^2). Additionally, the erosion from wind and dust particles could, at least in the primary stages of degradation, create additional exposure surface [129] which facilitate oxidation in comparison with the lab-controlled aging environment. The advanced aging after 8 months of natural aging is confirmed by the mechanical response discussed in Chapter 3.

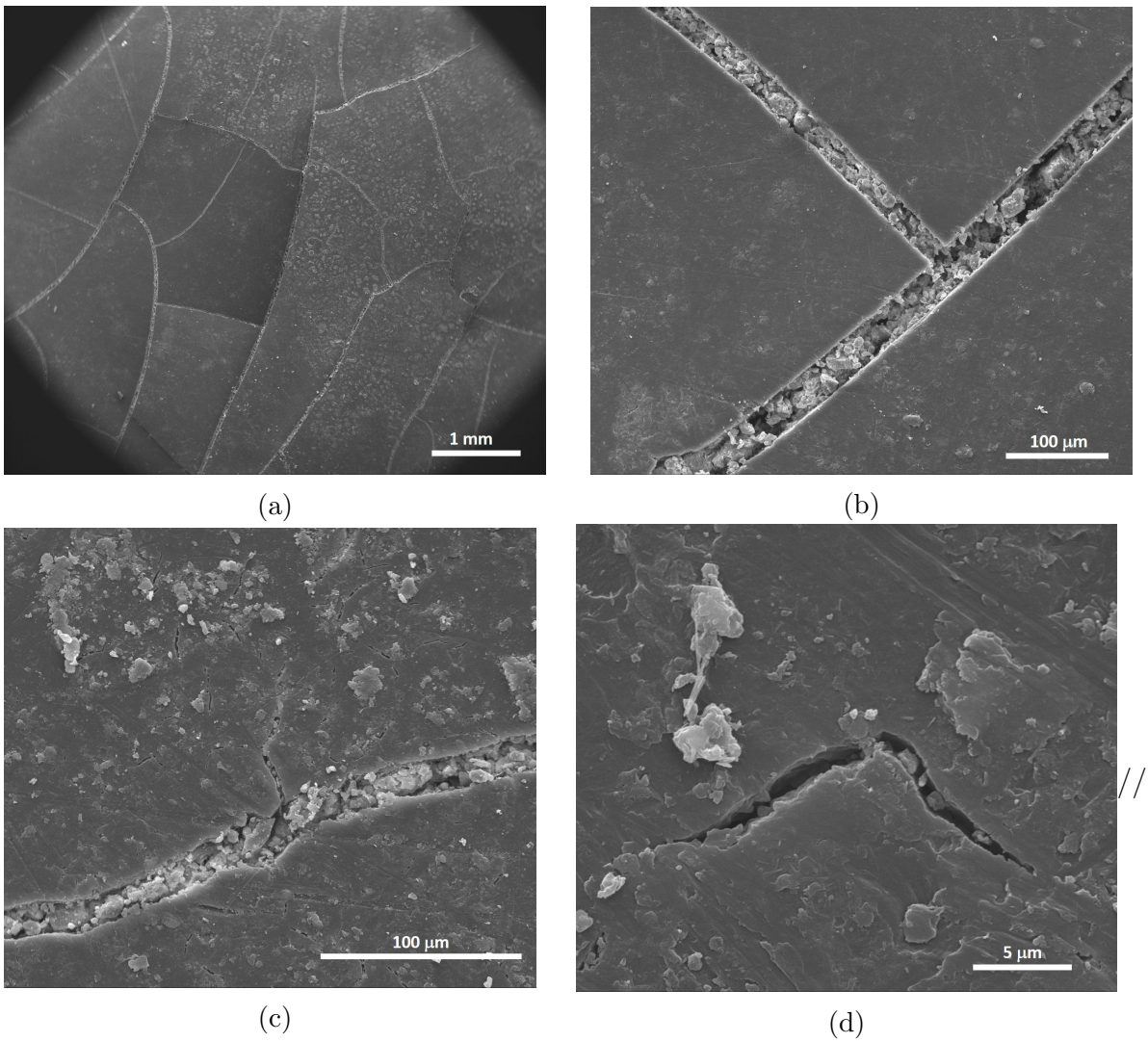

(a) (b)

(c) (d)

Figure 2.35: Observations of damage in LDPE plates after 8 months of natural aging: (a) Polygonal array of cracks; (b) Detail of a "T" junction. (c) Crack filled with dust particles. (d) Microcrack with dust particles.

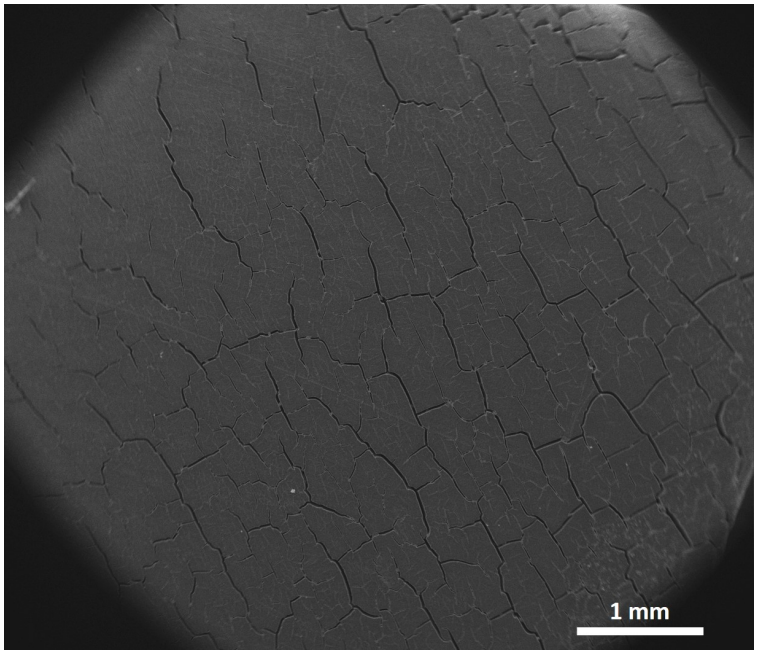

(a)

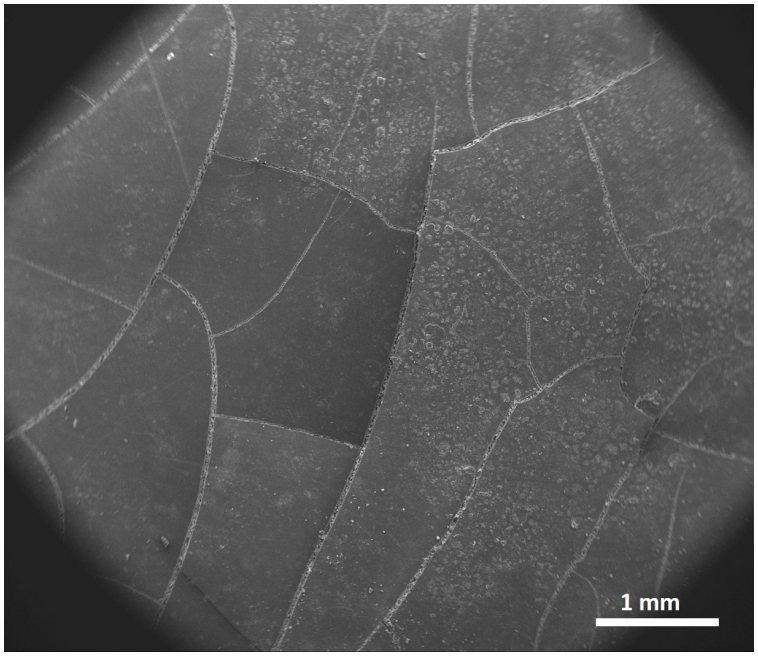

(b)

Figure 2.36: Comparison of the crack patterns: (a) after 240 h of HUV aging, and; (b)after 8 months of natural aging.

3. MECHANICAL CHARACTERIZATION*

The study of the mechanical response of aged LDPE films and plates involved both macro and nano characterization. The macro response was studied via tensile testing. Tensile testing has traditionally been used in the study of UV-aged polymers; however, it has focused almost exclusively on the decrease of the nominal strain to fracture as a measure of embrittlement. Little attention has been paid to the effect of oxidation on the strength of semicrystalline polymers, or to the chemo-mechanical aspects of oxidative embrittlement. Additionally, after high radiation doses, the embrittlement of polymer films is such that accessing the mechanical response through tensile testing is no longer possible. In this context, nanoindentation provided an effective way to gain access to the mechanical behavior at high radiation doses, while offering a better understanding of the effect of diffusion limited oxidation (DLO) in bulk specimens.

The results described in this chapter lay the basis for discussing the competition between multi-scale phenomena during oxidation in Chapter 4. Lastly, the results are employed in Chapter 5 in the development of the modeling strategy aimed at inverse identification of the extent of diffusion-controlled UV aging in bulk polymers.

3.1 Experimental Methods

3.1.1 Tensile Testing

Tensile specimens of as-received and aged films and plates were cut out using custom-made metallic punches. Film specimens were cut along the machine direction (MD). The specific geometries shown in Fig. 3.1 are intended to localize the deformation in the central part of the specimen [74]. Tensile tests were conducted at room temperature using an MTS Insight machine equipped with a 1 kN load cell. A *true* axial strain rate of $5 \cdot 10^{-3}\mathrm{s}^{-1}$ was

*Part of the data reported in this chapter is reprinted with permission from "Effect of UV-aging on the mechanical and fracture behavior of low density polyethylene" by A.K. Rodriguez, B. Mansoor, G. Ayoub, X. Colin, and A.A. Benzerga. *Polymer Degradation and Stability*, vol. 180, pp. 109185, 2020. Copyright [2020] by Elsevier [96]

imposed. To this end, the crosshead speed was adjusted with the feedback of a LX MTS laser extensometer. This implies a constant true strain rate prior to necking. The laser extensometer was also used to measure elongation, and the two dots in Fig. 3.1 represent the locations of the reflective tape marks. The repeatability of the mechanical response was checked by carrying out at least three, and up to six realizations of the same test condition.

Full field strain measurements were obtained for as-received and UV-aged LDPE using a Digital Image Correlation (DIC) setup by Dantec. Tensile specimens were painted with a black and white speckle, and the displacement of the speckle pattern was tracked during deformation using a Stingray high performance 2 Megapixel FireWire camera. Data processing was performed using the Istra4D software by Dantec.

The true (axial) stress was calculated using the formula [130]:

$$\sigma = \frac{F}{S_0} \exp(-2\bar{\varepsilon}_{11}) \tag{3.1}$$

where F is the force, S_0 is the initial cross-sectional area of the specimen, and $\bar{\varepsilon}_{11}$ constitutes direct output from the DIC software of the true strain in the transverse direction (TD) extracted at the center of the specimen; see Fig. 3.1. The cross-sectional area is $S = wt$ with w the width and t the thickness. Let $\epsilon_{\mathrm{T}} = \ln(w/w_0)$ and $\epsilon_{\mathrm{N}} = \ln(t/t_0)$ be the transverse and normal true strains, respectively. Assuming transverse isotropy, $\epsilon_{\mathrm{T}} = \epsilon_{\mathrm{N}}$. Hence, $2\epsilon_{\mathrm{T}} = \ln(w/w_0) + \ln(t/t_0) = \ln(S/S_0)$. Finally, equation (3.1) is obtained by identifying ϵ_{11} from DIC with ϵ_{T}. Note that equation (3.1) assumes transverse isotropy and a negligible strain gradient in the transverse direction, which are generally good assumptions, but does not assume plastic incompressibility; see [130] for details. DIC was omitted for HUV and naturally aged material, where the nominal response and nanoindentation results sufficed for comparison among the different types of aging.

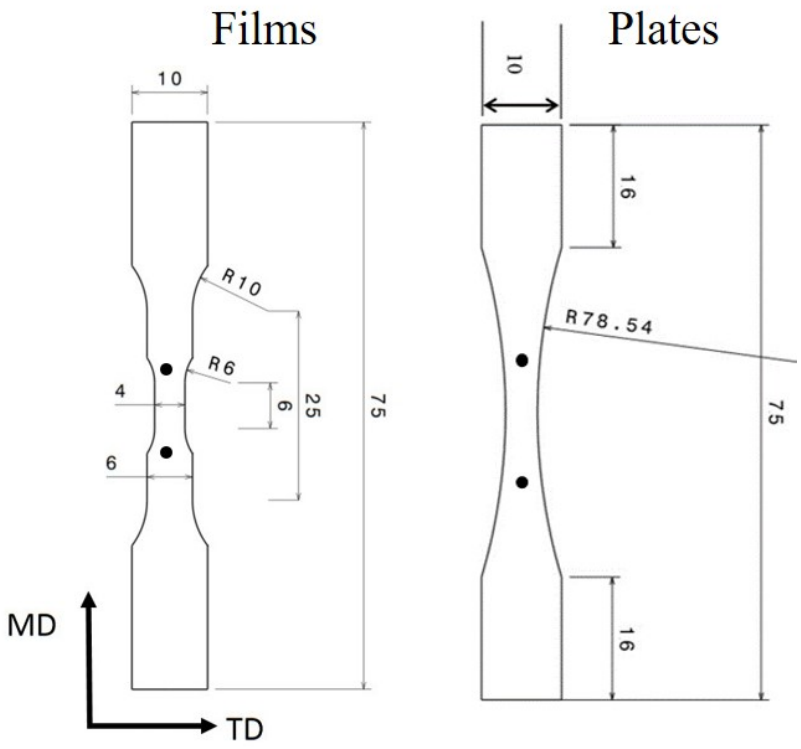

Figure 3.1: Tensile specimen geometries for films and plates (dimensions in mm). The dots mark the locations of the laser extensometer trackers.

3.1.2 Nanoindentation

The stiffness of pristine and aged LDPE was assessed through nanoindentation using a Hysitron TI Premier indenter with a Berkovich tip. The orientation of the indents respect to chemical cracks and tensile loading is shown in Fig. 3.2. For films, 12 indentations were performed in each sample at a constant load of 6500 μN. The load was maintained for 5 seconds before unloading. The constant load was selected to achieve depths that allow us to avoid surface effects, while staying within the 10% of the total thickness of the films (i.e., within 5000 nm). The reduced modulus was obtained from the unloading curves and the elastic modulus estimated using the method by Oliver and Pharr [131]. For the LDPE plates, the specimens were prepared by grinding the through-thickness plane with SiC paper up to 2400 grit. To establish the distance between indents, the average distance between cracks

was calculated for the 240 h UV aged plate with the line intercept method (figure 3.3b), obtaining an average distance of 45 μm. The specimens were indented every (45 μm) / 2= 23 μm across their thickness, covering an area of 0.5 mm for a total of 23 indents per data point in figure 3.11.

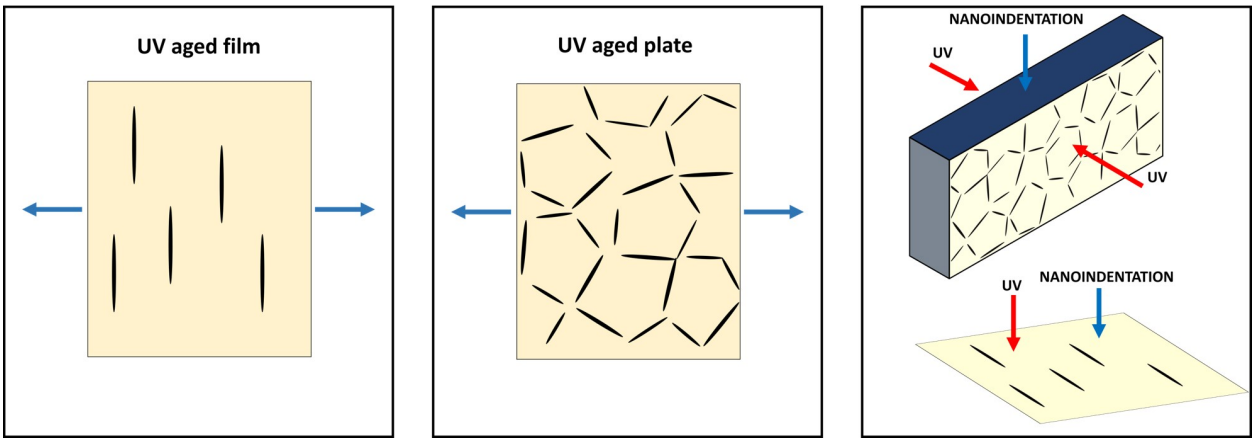

Figure 3.2: Scheme of nanoindentation experiments on aged plates and films, showing relative orientation of chemical cracks, tensile loading and nanoindentation.

3.2 Mechanical Response

3.2.1 UV Aging

3.2.1.1 Tensile Response

Typical nominal stress-strain curves for the as-received and UV aged films are shown in Fig. 3.4a. Specimens cut out of films that were aged up to 192 and 240 hours were too brittle to test, as they prematurely broke during setup, even with most delicate handling. For the as-received film (0 h) the response exhibits a peak load corresponding to neck initiation, followed by a quasi-plateau indicative of neck propagation. At large stretches, the load begins to increase again due to entropic hardening.

UV aging results in three main changes in the tensile response: (i) a steady reduction in the elongation to fracture; (ii) a transient increase in the flow stress; and (iii) a transient

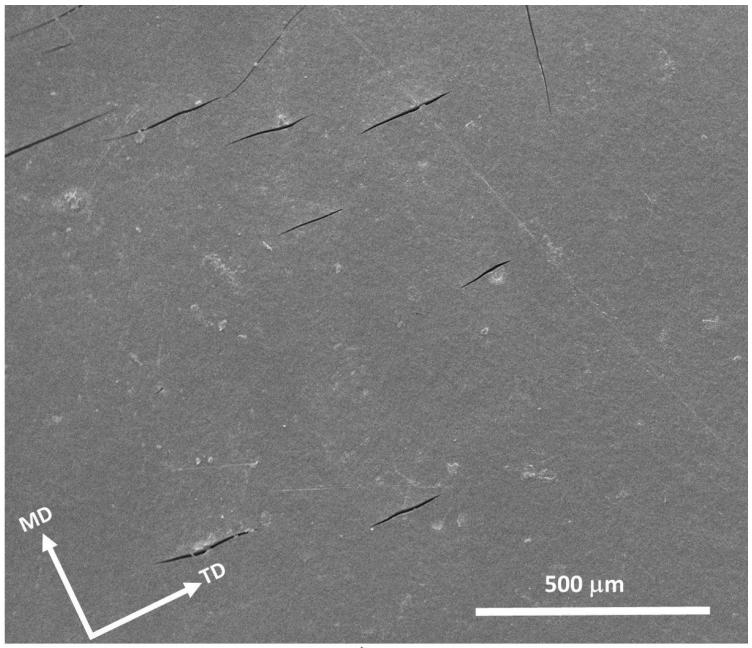

a)

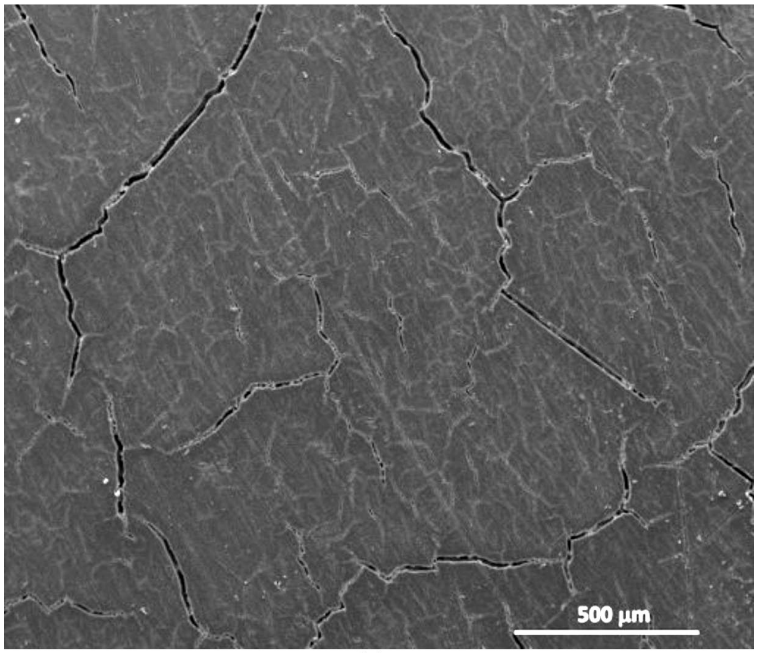

b)

Figure 3.3: Surface of LDPE after 240 hours of UV aging: a) UV-induced cracks perpendicular to the machine direction of the film; b) Polygonal crack pattern formed on UV-aged plates.

increase in strain hardening. In particular, the elongation to fracture is reduced by more than 50% after just 24 h of UV exposure. This trend, which is consistent with the literature [1, 37, 52, 57], is associated with oxidation-induced chain scission. Note that the elongation to fracture in the 96 h specimen is about 1.0, which means that a significant ductility is retained up to this exposure time.

The effect of UV aging on the flow stress of the material is, however, more complex. The true stress–strain responses obtained are shown in Fig. 3.4b. Only strains up to 0.8 are shown, as the pattern distortions at large stretches impeded accurate measurements of local strains. The true stress-strain curves show larger values of stress beyond yielding, due to strain localization. Both the nominal and true responses in Fig. 3.4 reveal a transient strengthening at low UV doses. More importantly, the true stress-strain curves show that the strain hardening rate follows the same trend as the flow stress: it increases with UV aging up to 48 h, and decreases at higher UV exposure times.

To better document the above trends, Fig. 3.5a reports the nominal stress F/A_0 at a strain $\Delta L/L_0 = 0.5$. The stress reaches a maximum between 24 and 48 hours of UV exposure before it decays, suggesting a competition between the various reactions and processes involved in the aging of the polymer. Fig. 3.5b displays the true stress $\sigma_{0.5}$ at a true strain $\varepsilon = 0.5$. When the true stress is considered, the strengthening at intermediate aging times is even more important, with $\sigma_{0.5}$ exceeding 20 MPa for 24 and 48 h. Additionally, Fig. 3.5b shows that even if the initial apparent yield is higher in the 96 h condition (than it is in the 72 h condition), the material degrades further upon straining beyond $\varepsilon \geq 0.5$, with σ reaching values below those of the 72 hour condition.

The loss of ductility induced by UV aging is evident in Fig. 3.4a. This loss is quantified in Fig. 3.6 in terms of a nominal strain to break, $\epsilon_{\mathrm{b}} = \Delta L/L_0\big|_{\mathrm{b}}$, and a true strain to fracture, $\varepsilon_{\mathrm{f}} = 2\ln(w_0/w_{\mathrm{f}})$, measured post mortem ($\sim$ one month) based on width reduction. In all conditions, $\epsilon_b > \varepsilon_{\mathrm{f}}$ due to significant strain recovery after unloading and viscous effects.

The trend of a decreasing strain to fracture indicates profuse chain scission events. It is

consistent with the increase in carbonyl index (Fig. 3.4) and decrease in molecular weight (Fig. 3.5). On the other hand, chain scission alone cannot explain the oxidation-induced strengthening of the polymer in the early stages of exposure to UV radiation (Fig. 3.5). To explain this transient strengthening some other mechanism must be invoked. This is further discussed in Chapter 4.

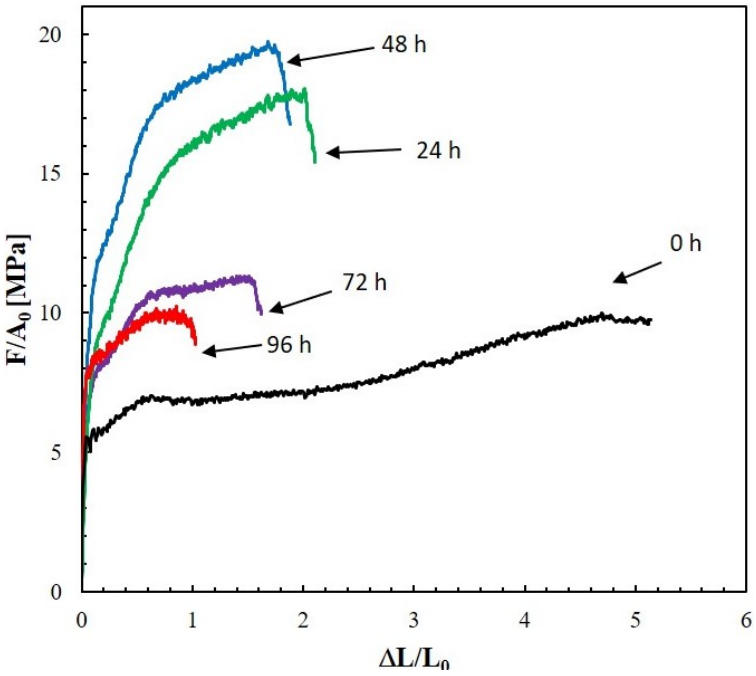

(a)

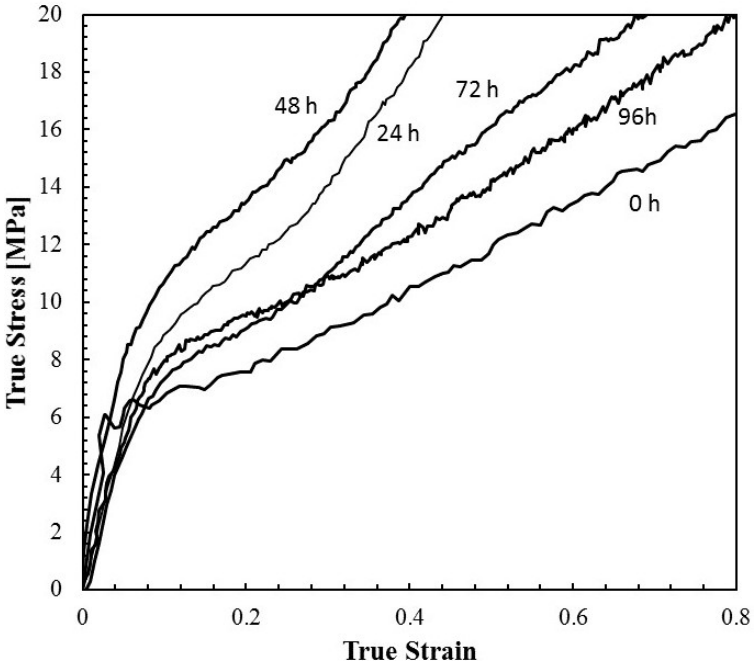

(b)

Figure 3.4: (a) Engineering stress-strain curves for LDPE films UV-aged at various exposure times and tested at room temperature and a true axial strain rate of 0.005 s^{-1}. (b) Corresponding true stress-strain curves.

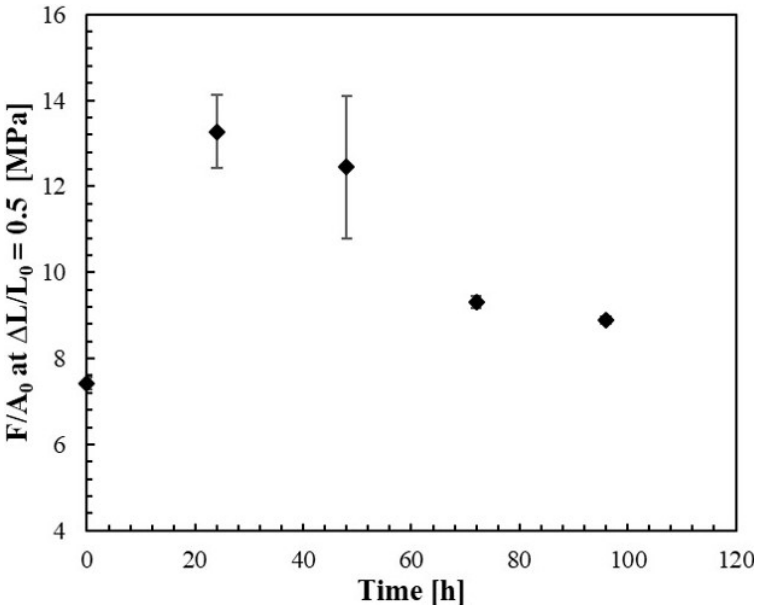

(a)

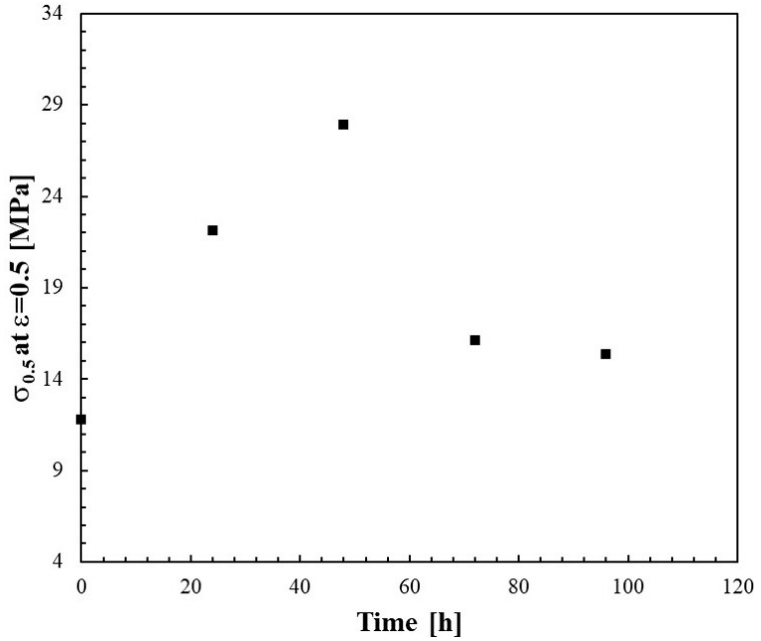

(b)

Figure 3.5: Transient strengthening in the photo-oxidation of LDPE films. (a) F/A_0 at $\Delta L/L_0 = 0.5$ versus aging time; and (b) flow stress at $\epsilon = 0.5$, $\sigma_{0.5}$ versus aging time.

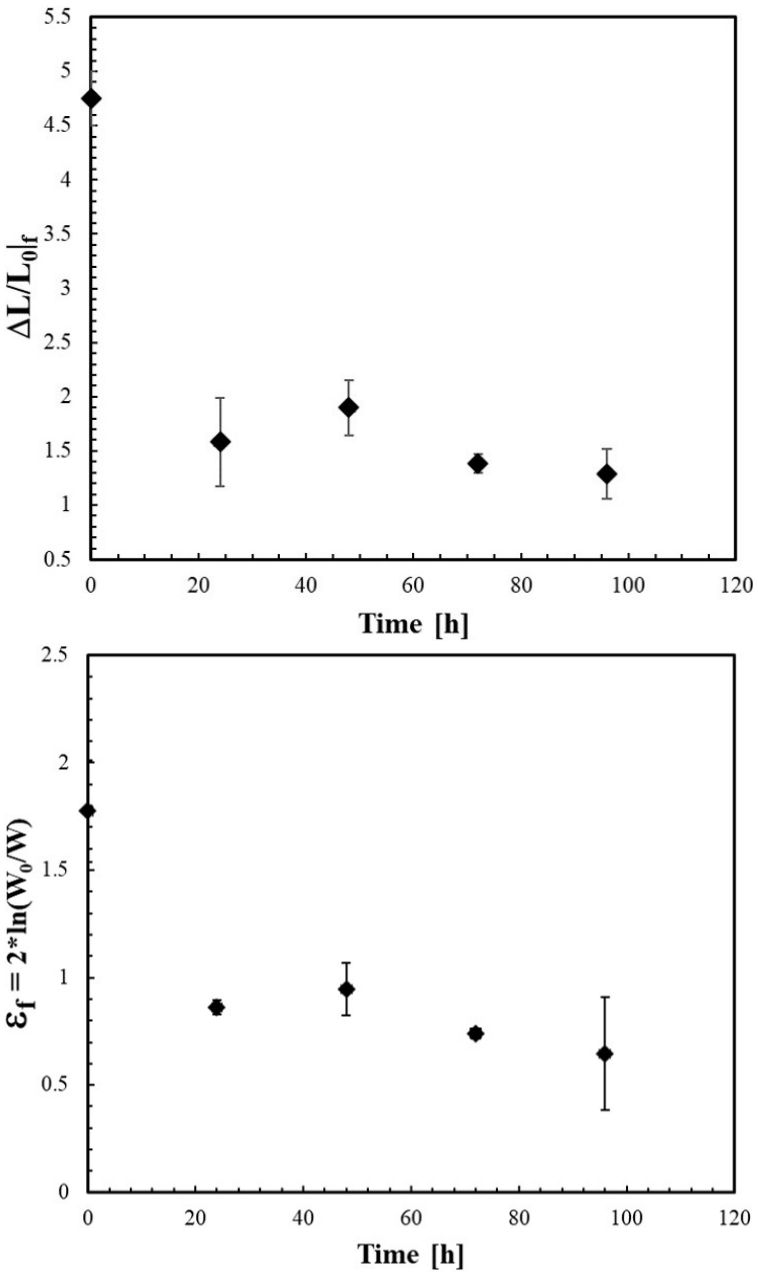

Figure 3.6: (a) Nominal strain at break versus UV aging time for LDPE films; (b) (Post mortem) true strain to fracture versus UV aging time for LDPE films.

Fig. 3.7a shows the typical nominal stress-strain curves for the as-received and UV-aged plates. Unlike the films aged at high UV doses, all aged plates remained in conditions that allowed for tensile testing. The stress strain curve of the as-received plate exhibited a peak load corresponding to neck initiation, followed by a load increase due to entropic

hardening. The as-received plate exhibited higher flow stress than the pristine film. This difference is attributed to the higher lamellar thickness of plates that results from their lower supercooling, as described in Chapter 2.

As observed in the aged films, UV aging resulted in: (i) a reduction in the elongation to fracture; and (ii) a transient increase in the flow stress of the plates. The pristine and 48 h UV-aged plates are the only conditions where strain is large enough to observe post-peak hardening. The strain hardening remained practically unchanged after 48 h of aging.

At low UV doses (0-48 h) the decrease in elongation to fracture is slower in plates than it is in films: it took 48 h of exposure to reduce the elongation to fracture by $\approx 50\%$ in plates, while in films it took 24 h. This difference can be attributed to the effect of thickness in oxygen diffusion and oxidation. As was shown in Chapter 2, photo-oxidation led to the formation of a brittle layer over the ductile core on the plates. During loading, this pristine core is capable to bear further deformation in comparison with the aged films, which aged homogeneously across their thickness, leading to an earlier fracture.

The effect of UV aging on the flow stress of plates was similar to the effect observed in films, i.e., the nominal and true responses (Fig. 3.7) revealed a transient strengthening with aging time. This is noteworthy considering that diffusion effects lead to heterogeneous oxidation and composite like material in plates; while in films, oxidation can be considered homogeneous across its thickness. For plates, the transient strengthening occurs at higher doses than in films (96–192 h for plates *versus* 24–48 h for films). This longer aging time needed to see the strengthening effect on plates is attributed to the aforementioned diffusion effects.

The true stress–strain response of the UV-aged plates is shown in Fig. 3.7b. Only strains up to 1.2 are shown, as the pattern distortions at large stretches impeded accurate measurements of local strains. Up to 192 h of aging, the true stress-strain curves showed larger values of stress beyond yielding due to strain localization and continuous strain hardening. After 240 h of UV aging, the embrittlement was such that a decay on the true stress is observed

after yield, probably due to macro crack initiation.

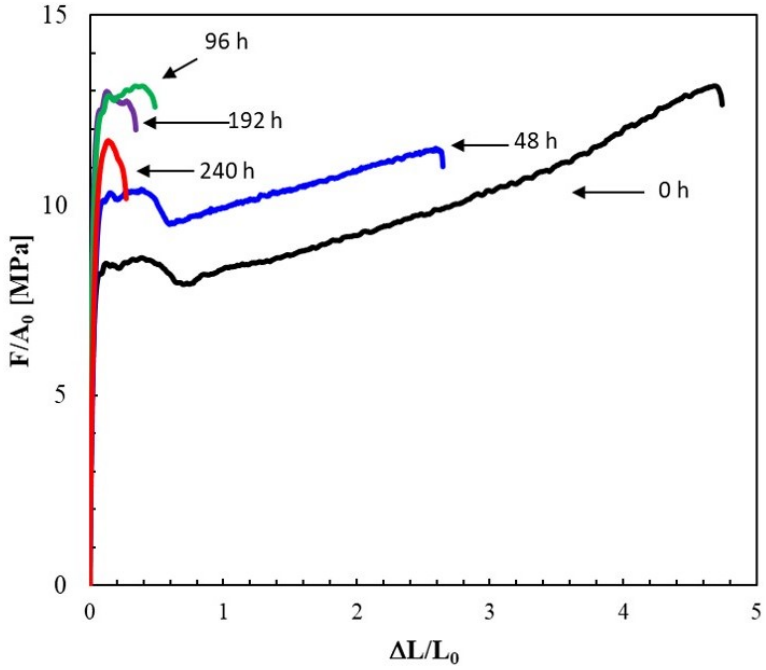

(a)

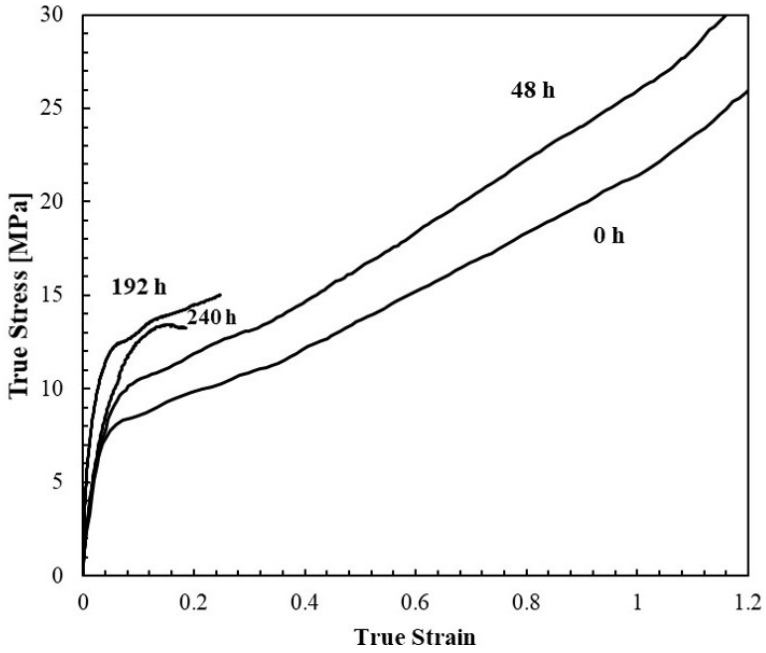

(b)

Figure 3.7: (a) Engineering stress-strain curves for LDPE plates UV-aged at various exposure times and tested at room temperature and a true axial strain rate of 0.005 s^{-1}. (b) Corresponding true stress-strain curves.

Fig. 3.8a reports the nominal stress of the plates, F/A_0, at a strain $\Delta L/L_0 = 0.15$. The stress of the plates reached a maximum between 96 and 192 hours of UV exposure before it decays, reiterating the notion of a competition between the various reactions and processes involved in polymer aging. This is further confirmed in Fig. 3.8b, which displays the true stress $\sigma_{0.15}$ at a true strain $\varepsilon = 0.15$. When true stress is considered, the strengthening at intermediate aging times is slightly higher, with $\sigma_{0.15}$ exceeding 13 MPa for 96 and 192 h.

The UV-induced loss of ductility is quantified in Fig. 3.9 in terms of a nominal strain to break, $\epsilon_\mathrm{b} = \Delta L/L_0\big|_\mathrm{b}$, and a true strain to fracture, $\varepsilon_\mathrm{f} = 2\ln(w_0/w_\mathrm{f})$, measured post mortem based on width reduction. While ϵ_b of the pristine material is significantly larger than that of 48 h UV-aged plate, the ε_f of both conditions are similar. The tensile response in Fig. 3.7a, shows that fracture in these conditions occurs well after neck stabilization. True strain is not expected to change much after neck stabilizes, resulting in a similar ε_f despite having different ϵ_b. It is also noteworthy that at low UV doses $\varepsilon_\mathrm{f} < \epsilon_\mathrm{b}$, while at higher doses $\varepsilon_\mathrm{f} \approx \epsilon_\mathrm{b}$. This might suggest that at high UV aging doses, the extent of oxidation is such that both axial deformation and necking are strongly reduced.

In summary, the overall effect of UV aging on the mechanical response of LDPE plates corresponded with that of UV aging on films, namely, a decreasing strain to fracture and transient strengthening with UV aging time, despite differences due to diffusion effects. The decreasing strain to fracture suggests profuse chain scission, consistent with the physico-chemical changes considered in Chapter 2. However, in line with the observed in UV-aged films, chain scission alone cannot explain the transient oxidation-induced strengthening of the polymer, and other mechanism must be invoked, as is further discussed in Chapter 4.

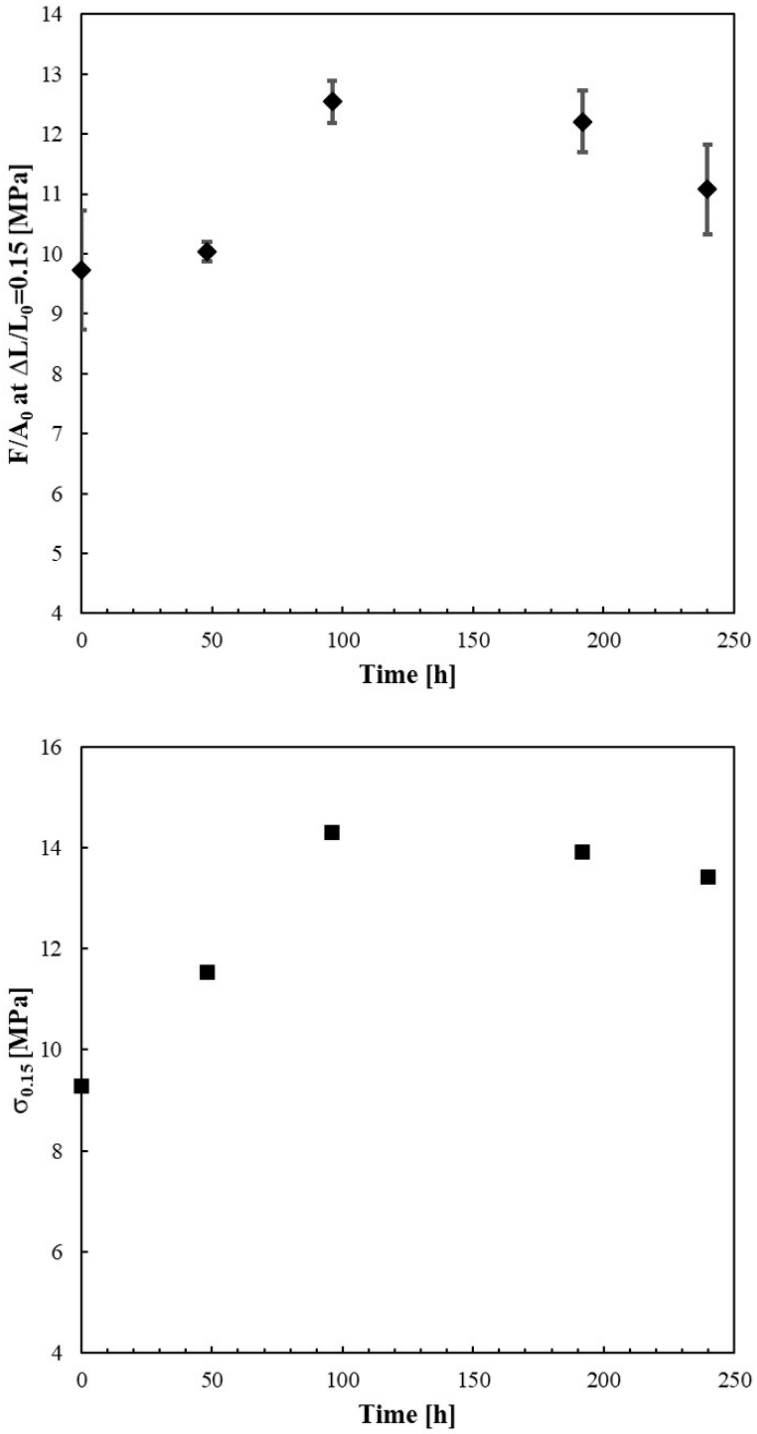

Figure 3.8: Transient strengthening in the photo-oxidation of LDPE plates: F/A_0 at $\Delta L/L_0 = 0.15$ versus aging time; and (b) flow stress at $\epsilon = 0.15$, $\sigma_{0.15}$ versus aging time.

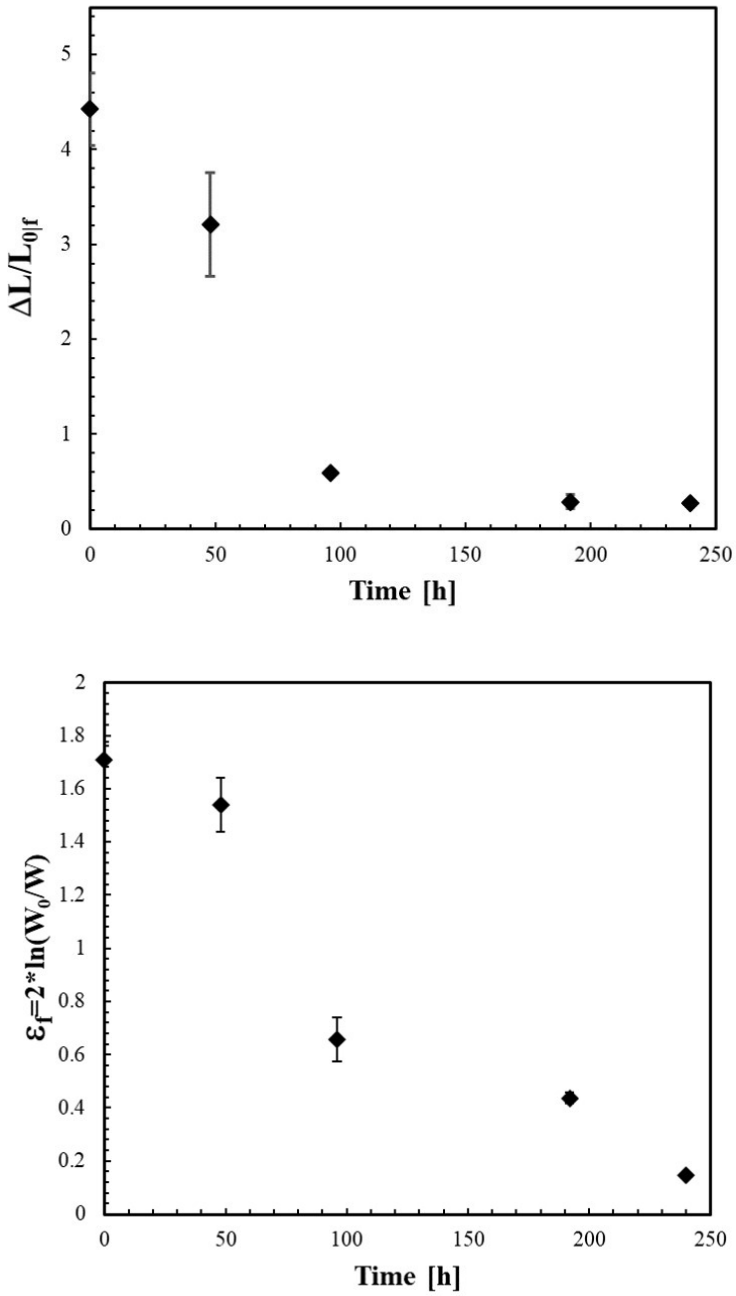

Figure 3.9: (a) Nominal strain at break versus UV aging time for LDPE plates; (b) (Post mortem) true strain to fracture versus aging time for LDPE plates.

3.2.1.2 Nanoindentation

The extreme brittleness of UV-aged films after 192 and 240 h of UV aging impeded their tensile testing. Thanks to nanoindentation, it was possible to estimate the modulus of these specimens. This, in turn, motivated the realization of additional UV exposure experiments (120–216 h) in order to obtain a more complete picture of the evolution of the stiffness with UV dose. The moduli of the aged LDPE films obtained via nanoindentation are shown in figure 3.10.

The stiffness of the film remained unvaried up to 96 h of UV aging. Beyond 96 h of UV exposure the modulus increased proportionally with aging time. The stiffness of semi-crystalline polymers is in part determined by their degree of crystallinity. Additionally, if crosslinking is present, it can also affect the stiffness of the polymer. In fact, the presence of crystals and crosslinks have analogous effects on the elastic deformation of macromolecules: they both act as reticulation points that hinder the movement of chains upon deformation. Indeed, the physico-chemical analysis in Chapter 2 confirmed the oxidation-induced formation of thin crystallites and crosslinking, which could account for the increased stiffness observed.

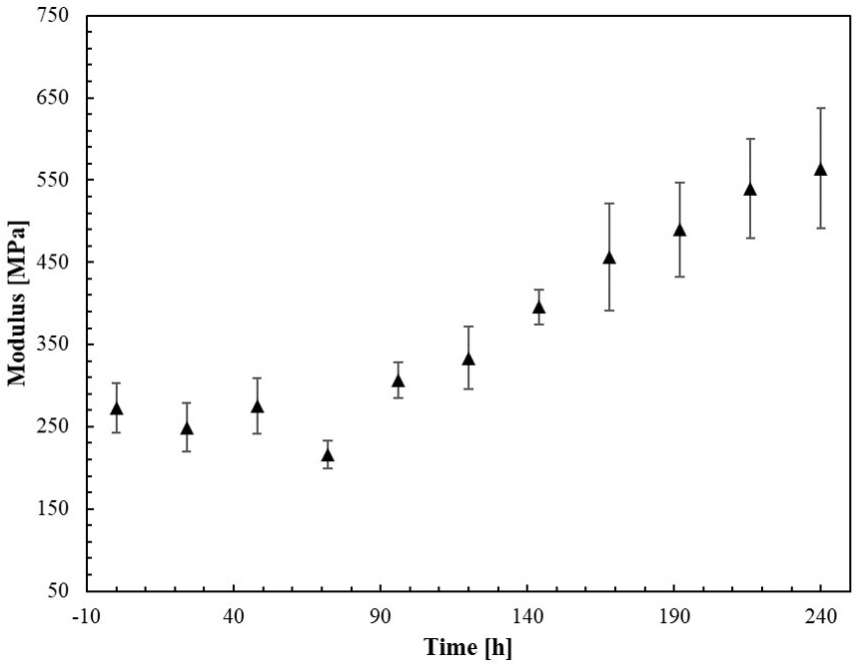

Figure 3.10: Modulus of LDPE films surfaces at various UV aging times, showing increase in stiffness after 96 h of aging.

For bulk specimens, nanoindentation offered the possibility of profiling the advance of oxidation in the material, without the tedious microtoming traditionally used in the study of oxidation of bulk specimens. Figure 3.11 reveals that for the pristine plate (0 h) the modulus is constant across the plate's thickness, with an average value of 0.35 GPa $\pm$ 0.02 GPa, indicating no major effect of the skin-core structure of the plate on stiffness, while only a slight increase is observed on the edges of the plates after 96 h of UV exposure.

A significant difference is observed after 192 and 240 hours of UV aging, where the modulus at the specimen's surface drastically increased: the modulus increased by $\sim$100% after 192 h of aging and by 160 % after 240 h of aging, from 0.35 to 0.9 GPa. As we move into the core of the specimens, the modulus gradually decreases until reaching the values of the pristine material between 250 and 350 μm from the surface.

The gradient in stiffness is likely due to a local increase of crystallinity and crosslinks in the surface of the material, where oxidation is favored due to diffusion effects [132]. As we

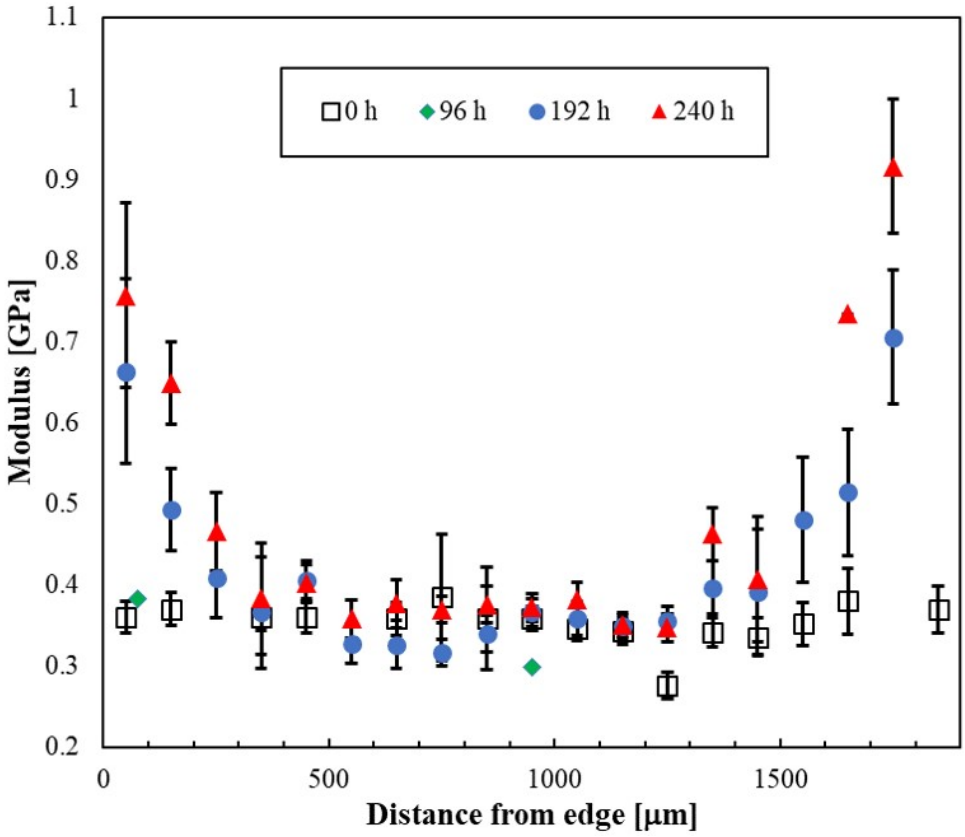

Figure 3.11: Modulus profile across thickness for pristine as well as plates aged for 96, 192 and 240 h, showing a gradual increase on modulus from core to surface after 96 h of aging.

move further into the core of the material, oxygen diffusion becomes more difficult, and with it the processes that lead to stiffening. The nanoindentation results in figure 3.11 suggest an oxidation layer of ~ 250 μm.

Interestingly, at the macro level, i.e., when plates are submitted to simple tension, there is no increase in the modulus, as can be observed in Fig. 3.12, where the evolution of the modulus obtained from tensile tests is compared to the values from nanoindentation on the surface and mid-thickness of the plates. Measurements of absolute modulus using a universal testing machine are not reliable, whereas those obtained from nanoindentation are more reliable, modulo difficulties associated with viscoelasticity. However, one cannot dismiss the relative measurements, i.e. stiffness of an aged specimen relative to the unaged. The tensile data shows a relatively stable stiffness with UV aging, in apparent conflict with the data from nanoindentation: since approximately one quarter of the whole sample (~ 500 μm) has a higher modulus beyond 96 h of aging, one would expect that this would translate into a higher modulus in the macro response, albeit, of smaller magnitude than the one observed on the plate's surface. The discussion of this apparent contradiction is postponed to Chapter 4.

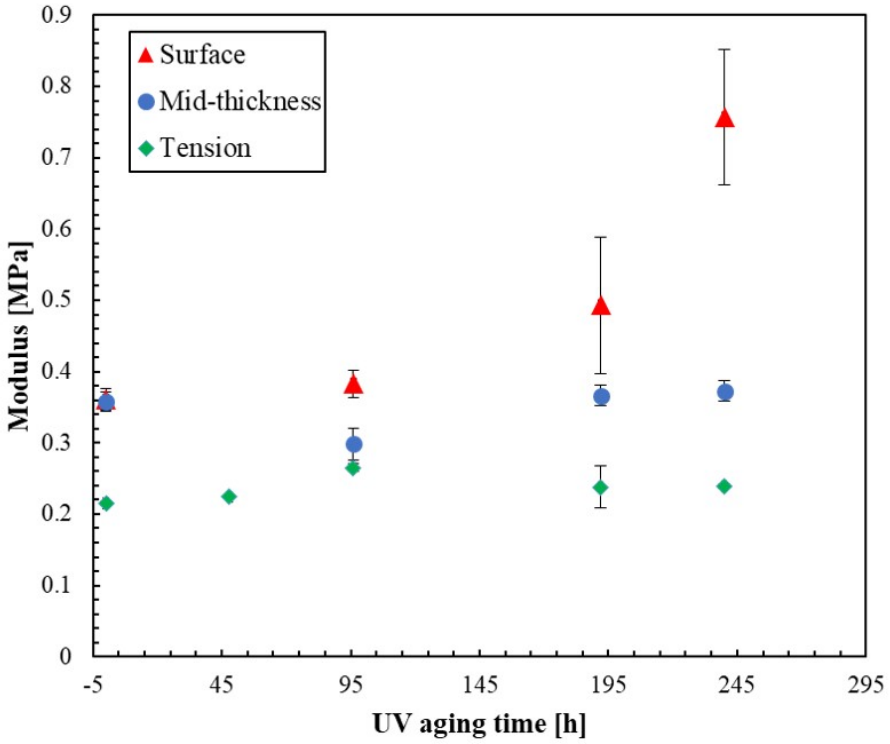

Figure 3.12: Effect of UV aging on stiffness as estimated by simple tension and nanoindentation. Tensile data shows a relatively stable modulus with aging, while nanoindentation data of the plate surface shows a 2-fold increase with aging. The nanoindentation data at mid-thickness remains overall stable, in line with the trend of the tensile modulus.

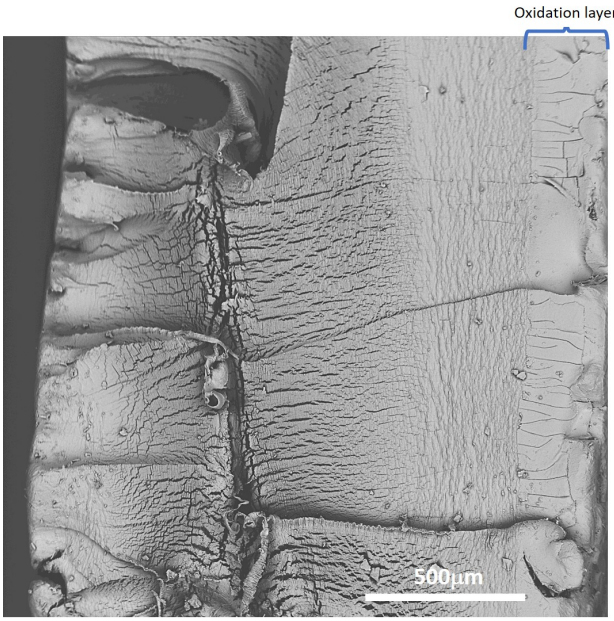

a)

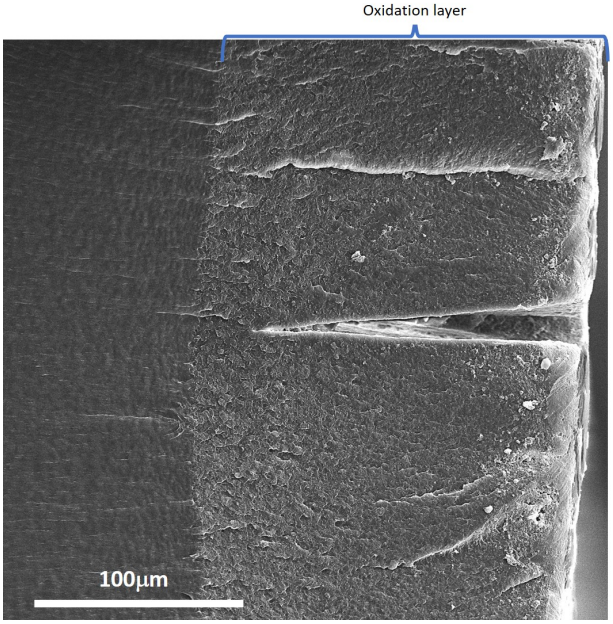

b)

Figure 3.13: a) Fracture surface of LDPE plate after 240 h of UV exposure. An oxidation layer of $\sim$ 200 μm can be distinguished, where cracks perpendicular to the loading direction are arrested. b) A similar oxidation layer can more clearly be observed in the fracture surface of an LDPE plate after 240 h of HUV aging.

3.2.2 HUV Aging

3.2.2.1 Tensile Response

In order to optimize the number of experiments, selected aging conditions were mechanically characterized for HUV aging, namely 48 and 96 h. These aging times were chosen based on the results obtained from UV aging, where they corresponded to transient strengthening and decay in flow stress, respectively.

Typical nominal stress-strain curves for the as-received and HUV-aged films are shown in Fig. 3.14. The mechanical response of the HUV-aged specimens followed a trend similar to that of UV-aged films: a steady reduction in the elongation to fracture; transient strengthening at low UV dose (48 h), and a transient increase in strain hardening. This suggests that in the presence of humidity, a similar competition of reactions and processes is involved in the oxidation of the polymer. This can be observed more clearly in Fig. 3.15, which compares the mechanical response of UV and HUV-aged films. Humidity seems to accelerate the reduction in elongation to fracture at large doses (96 h). This effect was also observed on the true strain at break ε_{f}, which after 96 h of aging is just $\varepsilon_{\mathrm{f}HUV} = 0.15$, while after UV-aging for the same time it was $\varepsilon_{\mathrm{f}UV} = 0.64$.

After 48 h of aging, HUV-aged films show a lower strength than UV-aged films. Recall the results obtained from the physico-chemical characterization, which showed an accelerating effect of HUV on the oxidation reactions. Thus, the lower strength obtained after 48 h in HUV compared to UV can be attributed to an earlier onset of the transient behavior due to the accelerating effect of humidity.

The selected conditions for mechanical characterization of HUV-aged plates were 192 h and 240 h, following the same criteria that was used for the films, i.e., UV doses that marked the rise and decay of the flow stress. The nominal response of the HUV-aged plates (Fig. 3.16) also revealed a transient strengthening after 192 h of aging. The elongation to fracture was reduced with aging and remained practically unchanged after 192 h. Fig. 3.17 compares the

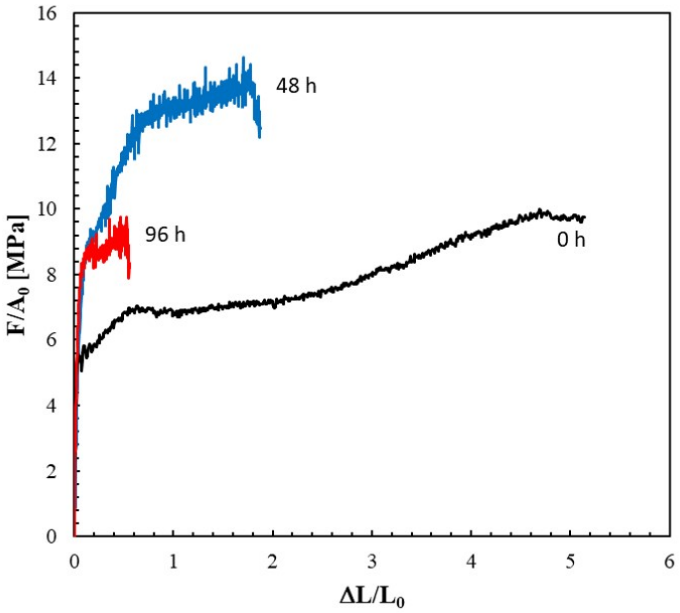

Figure 3.14: Engineering stress-strain curves for LDPE films HUV aged for 48 and 96 h and tested at room temperature and a true axial strain rate of 0.005 s^{-1}.

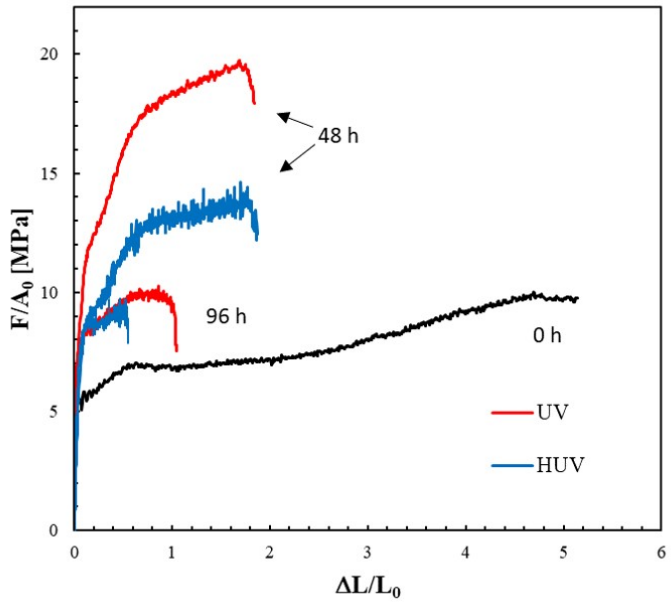

Figure 3.15: Comparison of the engineering stress-strain curves for LDPE films UV and HUV aged for 48 and 96 h and tested at room temperature and a true axial strain rate of 0.005 s^{-1}.

response of UV-aged and HUV-aged plates. HUV-aged plates showed a reduced flow stress compared to UV-aged plates. This reaffirms that humidity accelerates the onset of the UV-induced transient strengthening of the polymer, as observed in the films. The decreasing strain to fracture, indicative of profuse chain scission, is consistent with the increase in carbonyl index revealed in Chapter 2 (Fig. 2.25) However, as in the UV aging case, chain scission alone cannot explain the transient strengthening in the early stages of exposure to UV radiation observed in Fig. 3.14 and 3.16.

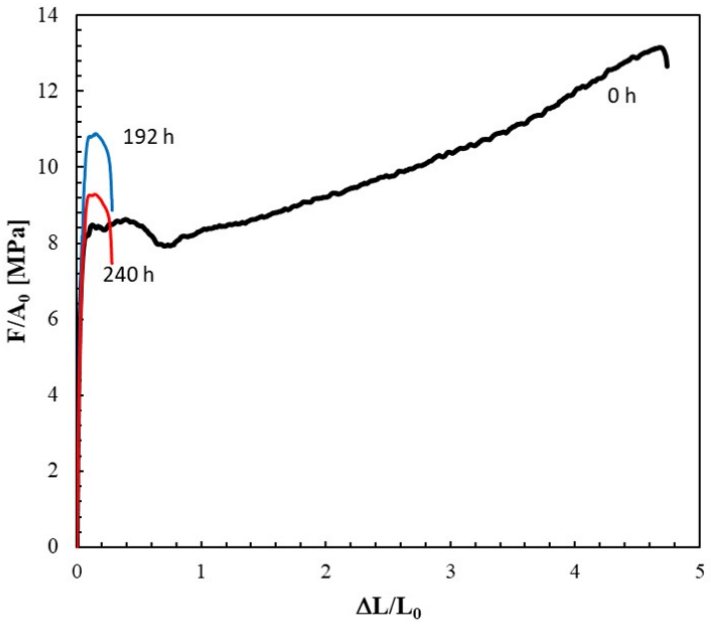

Figure 3.16: Engineering stress-strain curves for LDPE plates HUV aged at various exposure times and tested at room temperature and a true axial strain rate of 0.005 s^{-1}

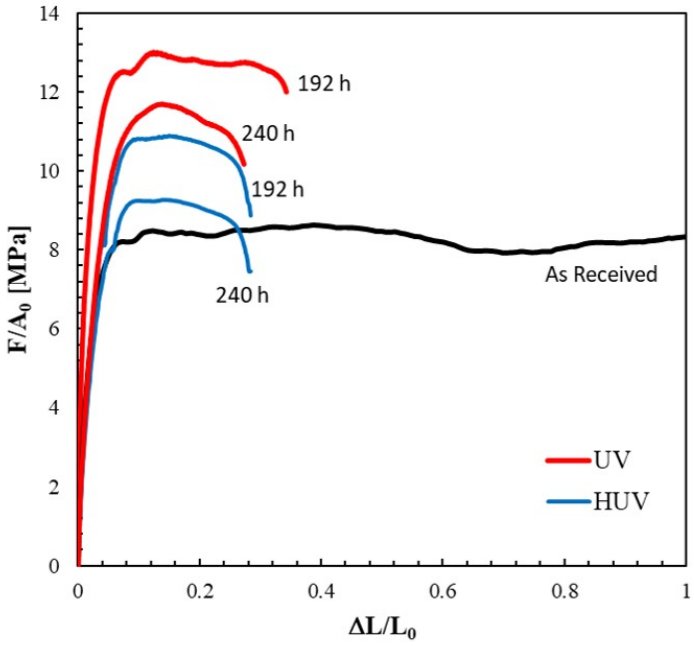

Figure 3.17: Comparison of the engineering stress-strain curves for LDPE plates UV and HUV aged at various exposure times and tested at room temperature and a true axial strain rate of 0.005 s^{-1}

3.2.2.2 Nanoindentation

The moduli of the HUV-aged LDPE films are shown in figure 3.18, where the moduli of UV-aged films are also displayed for comparison. After 48 h of HUV aging, the modulus is slightly higher, but within uncertainty, of that of the 48 h UV-aged film. After 96 h, the effect of humidity is clearer, as HUV aging results in a modulus increase of $\approx 54\%$ with respect to its UV-aged counterpart. In fact, the modulus of the 96 h HUV-aged film (470 ± 20 MPa) coincides with that of 192 h of UV aging (490 ± 60 MPa), illustrating the accelerating effect of humidity in the photo-oxidation of LDPE. Being able to make such comparison with severely aged film specimens highlights the advantage of implementing nanoindentation in the study of polymer films aging. Given the exhaustive nanoindentation campaign carried out for UV plates, and since all UV and HUV aged plates were fit for tensile testing, the nanoindentation of HUV-aged plates was omitted in order to optimize the number of experiments.

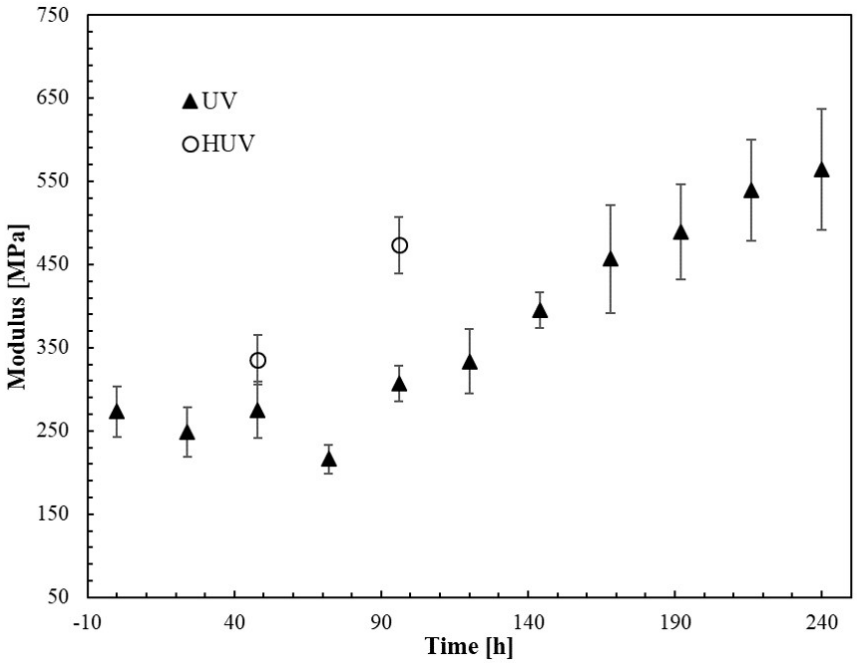

Figure 3.18: Modulus of LDPE films surfaces at various UV and HUV aging times, showing the accelerating effect of HUV on the polymer stiffness.

3.2.3 Natural Aging

3.2.3.1 Tensile Response

Representative nominal stress-strain curves for the as-received and naturally-aged films are shown in Fig. 3.19. Films that were aged beyond 2 months were too brittle to test, as they prematurely broke during removal from the set up. Fig. 3.19a shows elongation to fracture decreasing with aging time. A month of natural aging resulted in a transient strengthening of the film, accompanied with a reduction of $\approx$ 50 % in the elongation to fracture. After 2 months of natural aging the elongation to fracture is reduced further by $\approx$ 80 %. While the elongation to fracture is constant across the 3 samples tested, a scatter in the flow stress of the films is observed. The 2 month specimen with the highest flow stress follows approximately the same path of the 1 month aged film, up to an abrupt load drop. Similarly, the 2 month specimen with the lowest flow stress approximately the same path of the as-received film, up to an abrupt load drop. This scatter in the flow stress could be a

consequence of the transition from strengthening to weakening at this dose.

After comparison with the mechanical responses of UV and HUV-aged films, it was found that the HUV-aged films had a response similar to that of the naturally aged films, as observed in Fig. 3.19b. The 48 h HUV-aged film received a UV dose of 248 J/m^2. The UV dose after 1 month of natural aging is estimated to range between 416.66 J/m^2 and 992 J/m^2, based on various radiation values reported for Doha, Qatar [95, 133, 134]. Similarly, the UV doses for 96 h of HUV aging is 496 J/m^2, while 2 months of natural aging provide between 833.33 J/m^2 and 2012 J/m^2. Thus, the estimated UV doses after 1 and 2 months of natural aging are higher than those of 48 h and 96 h of HUV aging, respectively. One would then expect the response of the naturally aged films to reveal a more advanced oxidation, relative to the HUV specimens. However, after 1 and 2 months of natural aging, the average response is the same as the response after 48 and 96 h of HUV-aging.

To makes sense of this, two aspects related to the uncontrolled nature of outdoor aging can be considered: temperature and "shading". The temperature during the 2 months of natural aging ranged between 22 to 45°C, which is lower than the 60°C used in the lab-controlled experiments. However, one could question if this difference in temperature is enough to compensate the $\approx$ 70%–238% greater UV irradiance in natural aging compared to lab-controlled aging, especially considering the larger exposure time in natural aging. At this point one needs to consider the effect of "shading". A very important factor in photo–voltaic modules technology, shading refers to the blockage of sun's irradiance to the material. Shading in this sense can be divided into 2 types: soft shading which includes air pollution, and hard shading, which refers the accumulation of solids on the surface of the material [135]. As was shown in Chapter 2, indeed significant dust accumulation occurred during the natural aging experiments. While this dust can further erode the material, it also results in hard shading, blocking the UV irradiance from the sun. Thus, the effective irradiance to the material lower than the one calculated based on the total solar irradiance for Qatar. These findings highlight the complexity of correlating lab-controlled to natural

aging experiments and the importance of natural exposure campaigns to contextualize the outcomes of accelerated aging.

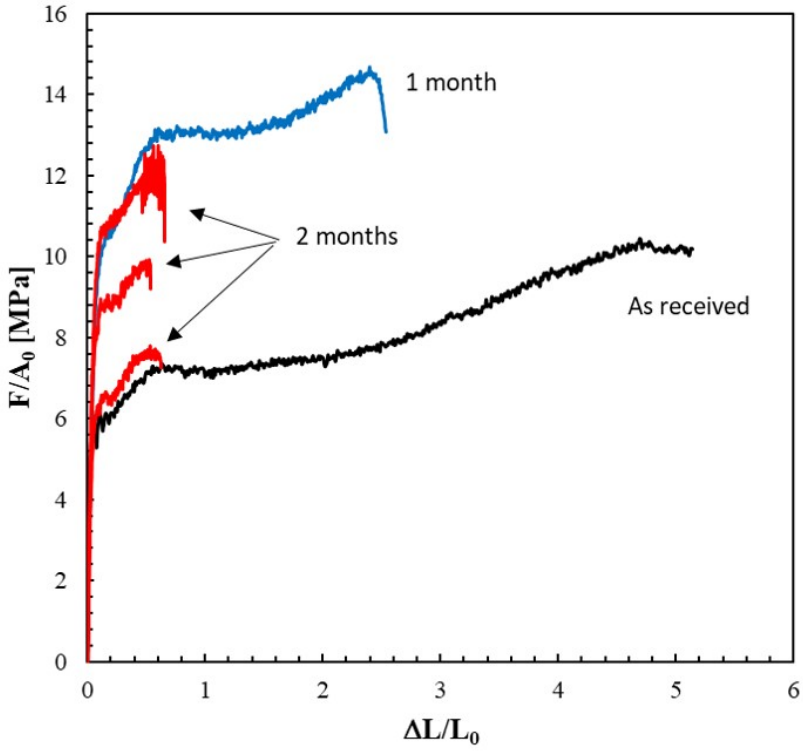

(a)

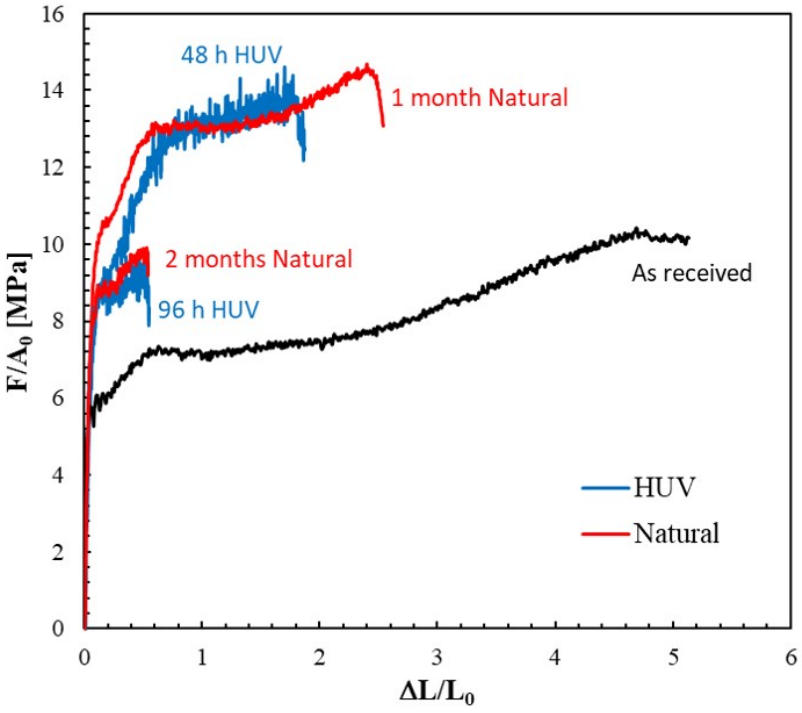

(b)

Figure 3.19: (a) Engineering stress-strain curves for LDPE films naturally aged after 1 and 2 months of exposure and tested at room temperature and a true axial strain rate of 0.005 s^{-1}. (b) Comparison of engineering stress-strain curves for LDPE films naturally and HUV aged.

The mechanical response of naturally aged plates is shown in Fig. 3.20a. Here too, a transient strengthening and a reduction of elongation to fracture with aging time is observed. After 1 month of natural aging the plate shows $\approx 25\%$ higher flow stress and $\approx 33\%$ lower elongation to fracture than the as-received plate, while the strain hardening remains unaltered. After 2 months of natural aging a maximum flow stress is reached, the elongation to fracture was reduced by $\approx 70\%$ and the second yield characteristic of the pristine plate was still present. Beyond 4 months, elongation to fracture and flow stress decreased dramatically. At 8 months, the decrease in flow stress was such that it fell below the levels of the pristine material. This was the only instance among the conditions studied where such a low flow stress was observed. These results confirm that photo-oxidation induces a transient strengthening in LDPE in all aging types studied (UV, HUV, natural) and in both homogeneous (films) and heterogeneous (plates) oxidation. As expected, the time for transient strengthening onset is higher in naturally-aged plates than in films, due to differences in thickness and diffusion limited oxidation.

The responses of naturally and HUV-aged plates are compared in Fig. 3.20b. The curve corresponding to 1 month of aging is omitted for clarity. The 192 h HUV-aged had a stress level similar to the 2 months naturally aged specimen, while only a third of its elongation to fracture. Meanwhile, the 240 h HUV-aged plate provided a close match to the 4 months naturally aged plate. If we compare the UV irradiance in each setting, 4 months of natural aging provided between 1666.5 J/m^2 and 4196 J/m^2, while 240 h of HUV aging provided a radiation of 1240 J/m^2. In this case, higher UV dose from natural aging does result in higher oxidation (as measured by elongation to fracture). This is in contrast with naturally aged films, where apparent lower UV doses led to higher embrittlement. There results reaffirm the complexity of correlating laboratory and natural aging experiments. Besides the hard shading effects aforementioned and that are evidenced in Fig. 3.21, the accelerated nature of lab-controlled experiments could also complicate the correlation for bulk specimens via DLO [40]. When high UV radiations or temperatures are used in accelerated experiments

of bulk specimens, diffusion limited oxidation can occur due to limited influx of oxygen beyond the surface of the material, resulting in an spatially heterogeneous oxidation. In natural aging, by contrast, radiation and temperature are lower, leading to a slower oxygen consumption. Thus, oxygen is not the limiting reactant and oxidation occurs in a more homogeneous way compared to accelerated aging.

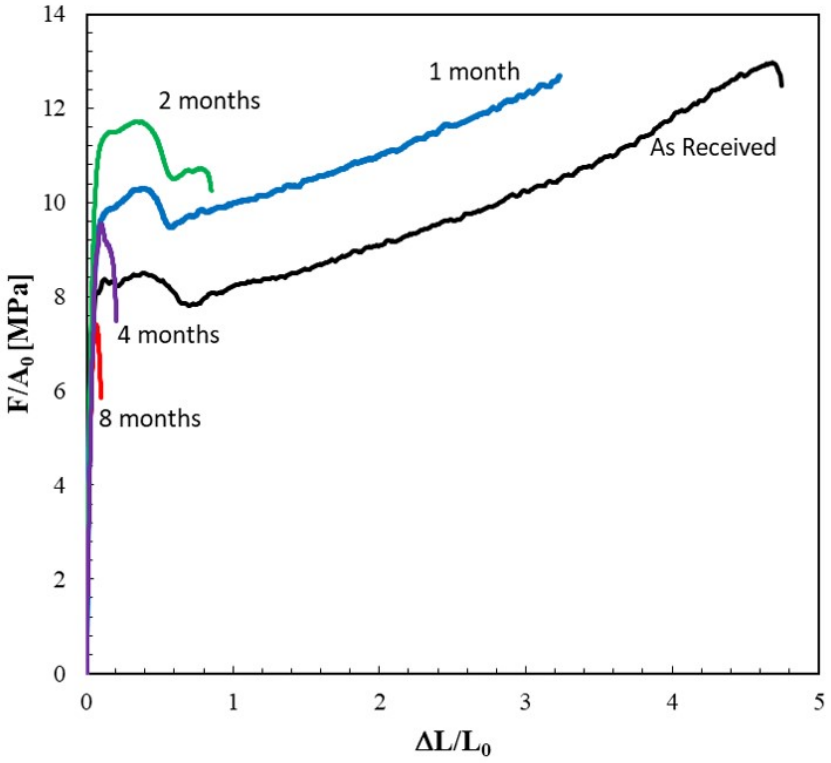

(a)

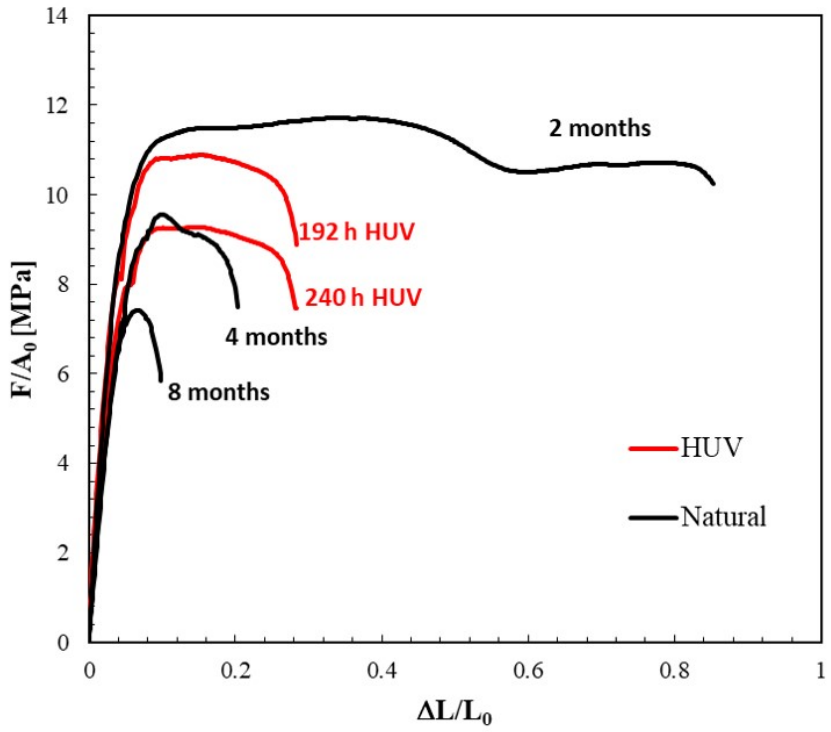

(b)

Figure 3.20: (a)Engineering stress-strain curves for LDPE plates naturally aged at various exposure times and tested at room temperature and a true axial strain rate of 0.005 s^{-1} (b) Comparison of engineering stress-strain curves for LDPE plates naturally and HUV aged.

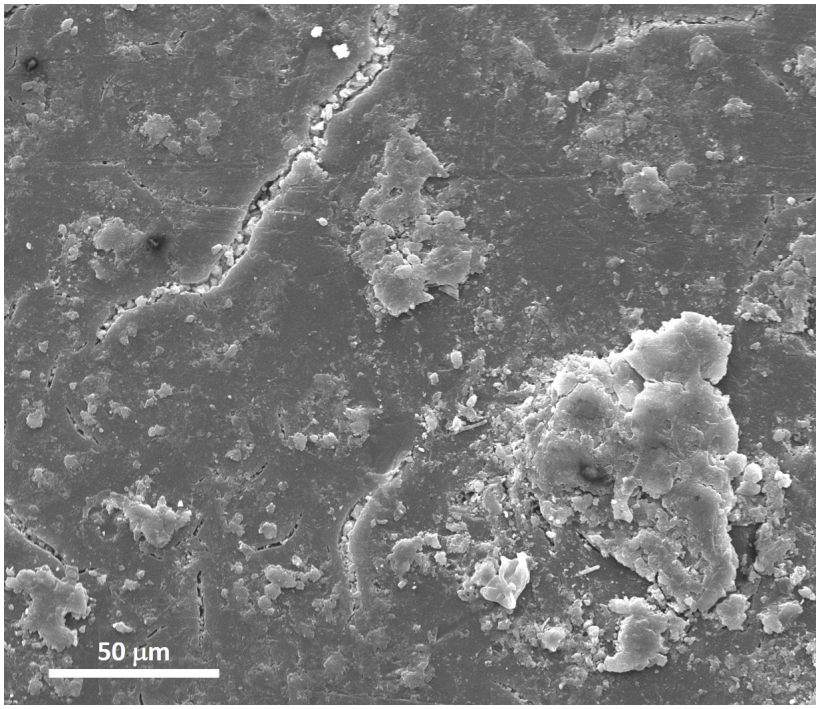

Figure 3.21: "Hard shading" of LDPE plate by accumulation of dust particles during natural oxidation.

3.2.3.2 Nanoindentation

Fig. 3.22 shows the moduli of naturally aged LDPE films in context with the moduli of as-received, UV and HUV aged films. After 1 month of natural aging the stiffness of the film remained unchanged (281 ± 30 MPa *versus* 273 ± 30 MPa of the pristine film). This is in line with the observed in UV aged films, where no change in modulus was observed up to 96 h of accelerated aging. Further natural aging led to a stiffness increase to 340 ± 40 MPa after 2 months of exposure (Fig. 3.22).

Recall that the tensile response of the 1 month naturally aged film roughly corresponded with that of the 48 h HUV-aged film (Fig. 3.19). Comparing the stiffness obtained for these two specimens (Fig. 3.22), it is noted than their moduli are similar (barely within uncertainty). Thus, it appears as both tensile and indentation response of the film naturally aged for 1 month correspond well with the response of the 48 h HUV aged film. This might suggest

that the total energy received by the film naturally-aged for 1 month in terms of effective radiation and temperature (plus any humidity and erosion effects), amount to the energy received in the lab-controlled conditions by the film HUV-aged for 48 h. Recall also that the tensile response of the 2 months naturally-aged film corresponded well with that of the 96 h HUV aged film. Contrasting their moduli in Fig. 3.22, we observe that the stiffness of the naturally aged film is lower than that of the 96 h HUV-aged film. This discrepancy reaffirms the aforementioned difficulty of establishing correlations between laboratory and natural aging conditions, as well as the importance of natural aging experiments as benchmark for results obtained in lab-controlled experiments.

The moduli of the edge and middle section of the plate naturally-aged for 4 months is shown in Fig. 3.23, together with the moduli of pristine and UV-aged plates for comparison. The modulus at the surface of the plate increases by $\sim$130% after 4 months of natural aging, from 0.36 to 0.90 GPa. This average surface stiffness of the naturally-aged plate is higher than the average stiffness of the 192 h and 240 h UV-aged films. This is in accordance with the further oxidation of the 4 months naturally-aged plate evidenced in lower strain to fracture and lower flow stress (Fig 3.20). At the core of the specimen the modulus remains unchanged, due to oxygen diffusion effects. While estimation of the oxidation layer by nanoindentation is not possible without full profiling of the modulus, SEM analysis in Chapter 4 allowed for an measurement of the oxidation depth in naturally aged plates.

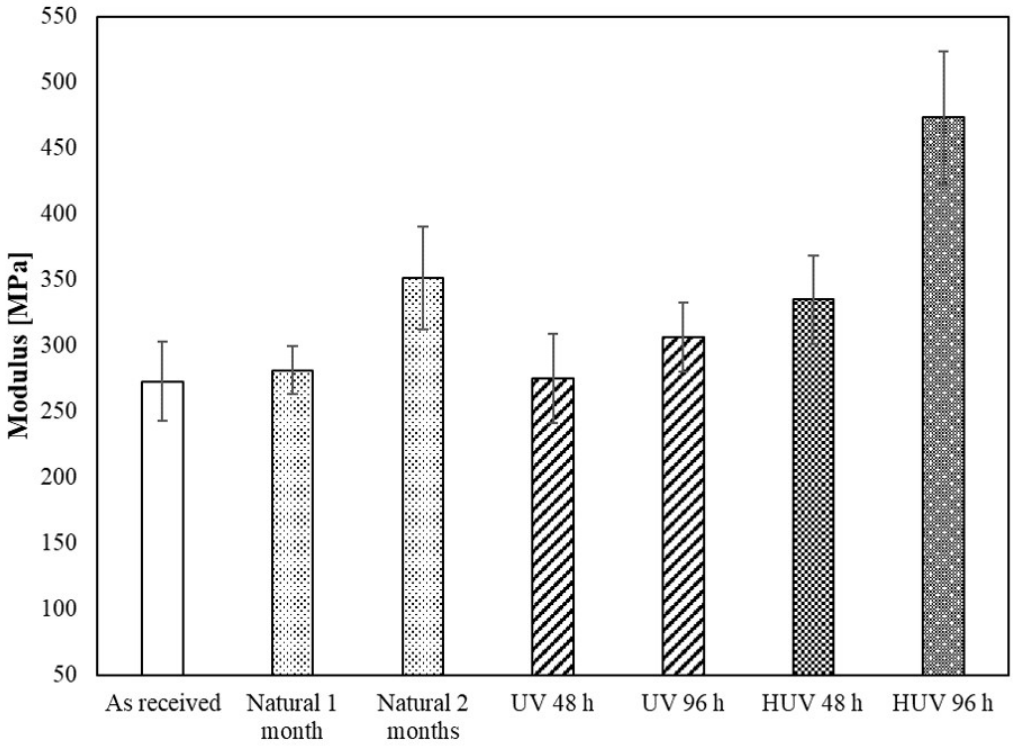

Figure 3.22: Modulus of LDPE films surfaces after 1 and 2 months of natural aging, compared to the moduli of UV and HUV aged specimens.

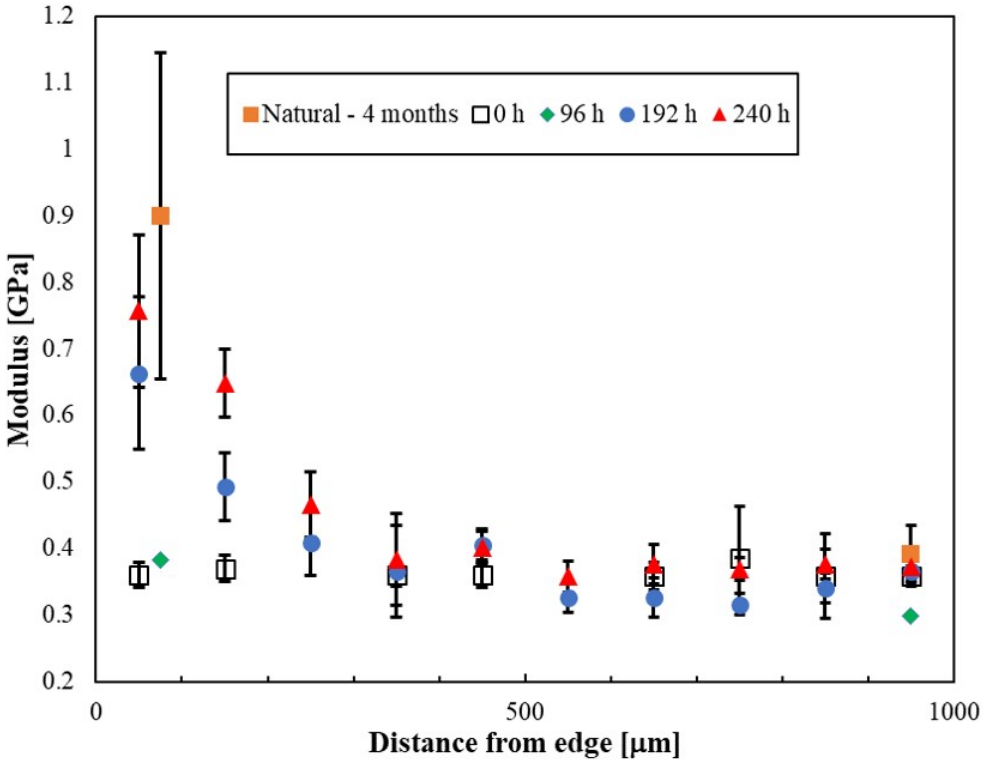

Figure 3.23: Modulus profile across thickness for 4 months naturally-aged plate, in context with pristine and UV-aged plates, showing a gradual increase on modulus from core to surface.

4. DAMAGE CHARACTERIZATION*

In the previous chapters, the UV aging of LDPE films and plates was characterized in terms of phenomena occurring in the nano-scale (chain scission, crosslinking, chemicrystallization, nanoindentation response), mesoscale (oxidation-induced cracking in the absence of mechanical load), and macro-scale (tensile response, embrittlement, and fracture). In this chapter, we examine some of the key findings obtained so far, with emphasis on the transient UV-induced strengthening. In this context, we attempt to link the macroscopically observed behavior with microscopic information. However, to complete the picture at the mesoscale, it is necessary to examine the mechanical damage process.

Interestingly, mechanical damage remains mostly unexplored in aged polymers (for a noteworthy exception, see Qayyum [38, 39]). Thus, in this chapter, we investigate the propensity to cavitation in pristine and oxidized semicrystalline polymer through fractography. With this, we hope to better understand how oxidation affects changes in the internal state, which ultimately affects how damage progression occurs under loading. The results provide an insight into the role of cavitation in the oxidative embrittlement of semicrystalline polymers.

The first part of this chapter focuses on the *post mortem* fractography of mechanically loaded specimens that were UV, HUV, and naturally aged, thus covering oxidation and hydrolysis. Then, the results obtained in this first section, together with the major results from previous chapters, are discussed in light of the state of the art, emphasizing aspects that remain largely unexplained in the literature and pointing, where appropriate, to further avenues of investigation.

*Part of the data reported in this chapter is reprinted with permission from "Effect of UV-aging on the mechanical and fracture behavior of low density polyethylene" by A.K. Rodriguez, B. Mansoor, G. Ayoub, X. Colin, and A.A. Benzerga. *Polymer Degradation and Stability*, vol. 180, pp. 109185, 2020. Copyright [2020] by Elsevier [96]

4.1 Damage Mechanisms

4.1.1 Microscopy

Selected tensile film and plates specimens were observed *post mortem* in scanning electron microscopy (SEM) for detection of "mechanical damage." For each specimen, the surface was first prepared by removing any residual paint (used for DIC) that did not come off after large stretching of the films. The excess paint was carefully removed using the rounded backend of a pair of laboratory tweezers. The paint was dry and came off rather easily. The parts that did not were left to avoid damage to the samples. Then each specimen was gold coated and observed in a FEI model Quanta 400 SEM with 15 kV voltage and a spot size of 3.5. All observations were made in the MD-TD plane for films, while plates observations where made both in the MD-TD and on the fracture surface (Fig. 3.1).

4.1.2 Damage in UV Aging

4.1.2.1 Films

Slant fracture was observed in all film specimens, aged or unaged, as illustrated in Fig. 4.1 (note the residual DIC paint in (b); see Section 4.1.2). The slant mode of fracture suggests that failure occurs by plastic instability, namely that the terminal event is a (macroscopic) shear band. In the unaged specimen (Fig. 4.1a) there was no indication of damage beneath the fracture surface. On the other hand, aged specimens exhibited various sorts of cavitation-mediated damage. First, consider the 48 h aged film of Fig. 4.1b. Further fractographic details are provided in Fig. 4.2. Elongated void-like features are found to form parallel to the tensile MD orientation, Fig. 4.2b. The propensity for these voids is higher in the central region of the specimen where the necking-induced hydrostatic tension is highest, at least before complete drawing. These elongated voids coalesce in the direction of loading to form very long cracks (the central one is over 2 mm long), possibly leading to splitting (see Fig. 4.2a). The voids have an internal structure reminiscent of crazing with lateral void surfaces constrained by residual fibrils that do not fully break, Fig. 4.2c. The thickness of the

fibrillar ligaments in Fig. 4.2c is between 3 and 5 microns, comparable with measurements reported elsewhere for bulk unaged polyamide 6 [32]. At a much lower scale (Fig. 4.2d), even smaller voids are observed in the vicinity of big ones. The small voids appear as precursors to the bigger craze-like voids and suggest a continuous damage process.

Next, consider the 96 h aged film of Fig. 4.1c with details as provided in Fig. 4.3. A more evident combination of mechanical damage and chemical degradation may be observed in this specimen. Just like in the 48 h exposed film, elongated voids are observed at a higher density, although individual voids may be shorter. A direct comparison of void sizes would be difficult since the strains to break for these two conditions are different: $\epsilon_b = 1.95$ versus $\epsilon_b = 1.47$ for the 48 h and 96 h conditions, respectively. Also, the voids are spread all over the specimen and not highly concentrated in the central region. Furthermore, traces of such elongated voids are seen deep below the fracture surface, Fig. 4.3b.

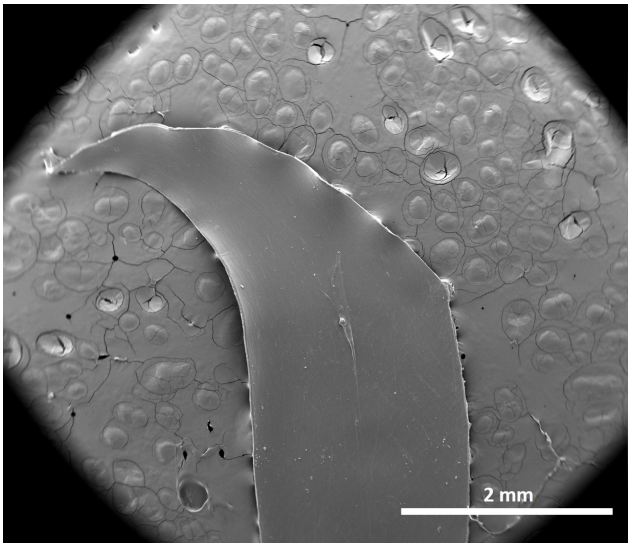

(a) 0 hours

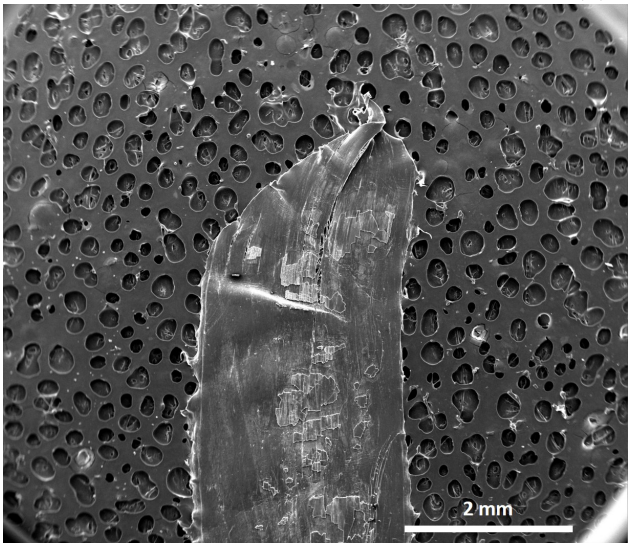

(b) 48 hours

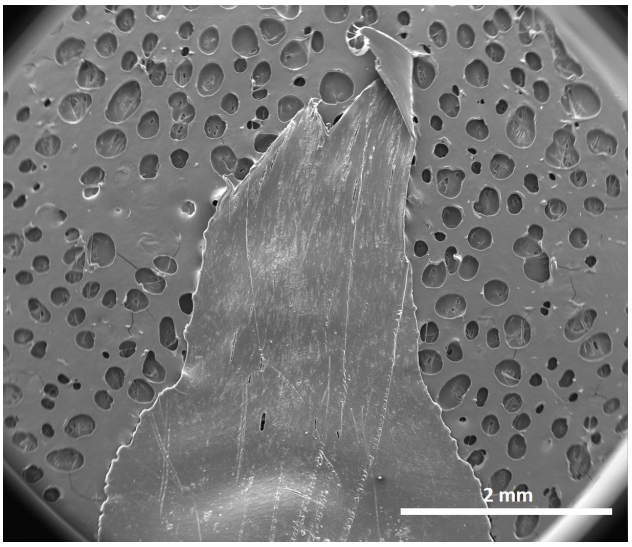

(c) 96 hours

Figure 4.1: Overall fracture mode in tension of LDPE films: (a) pristine material; (b) after 48 h of UV aging; and (c) after 96 h of UV aging.

In some isolated areas, a different type of damage is observed, as illustrated in Fig. 4.3c. This type has previously been reported for various semicrystalline polymers [39]. It suggests an advanced stage of surface degradation, and it is not possible to apportion the chemical and mechanical contributions in reconstructing the genesis of the stage shown in Fig. 4.3c. Some details elsewhere do exhibit some of the elongated voids but with more lateral opening,

Fig. 4.3d; also note the large void at the bottom of Fig. 4.3b. Additional micrographs are presented in Appendix A.

As it will become apparent from this and the following sections, the reported observations of both chemical damage and (chemo-)mechanical damage are quite complex. Some discussion of that is included in the second part of this chapter.

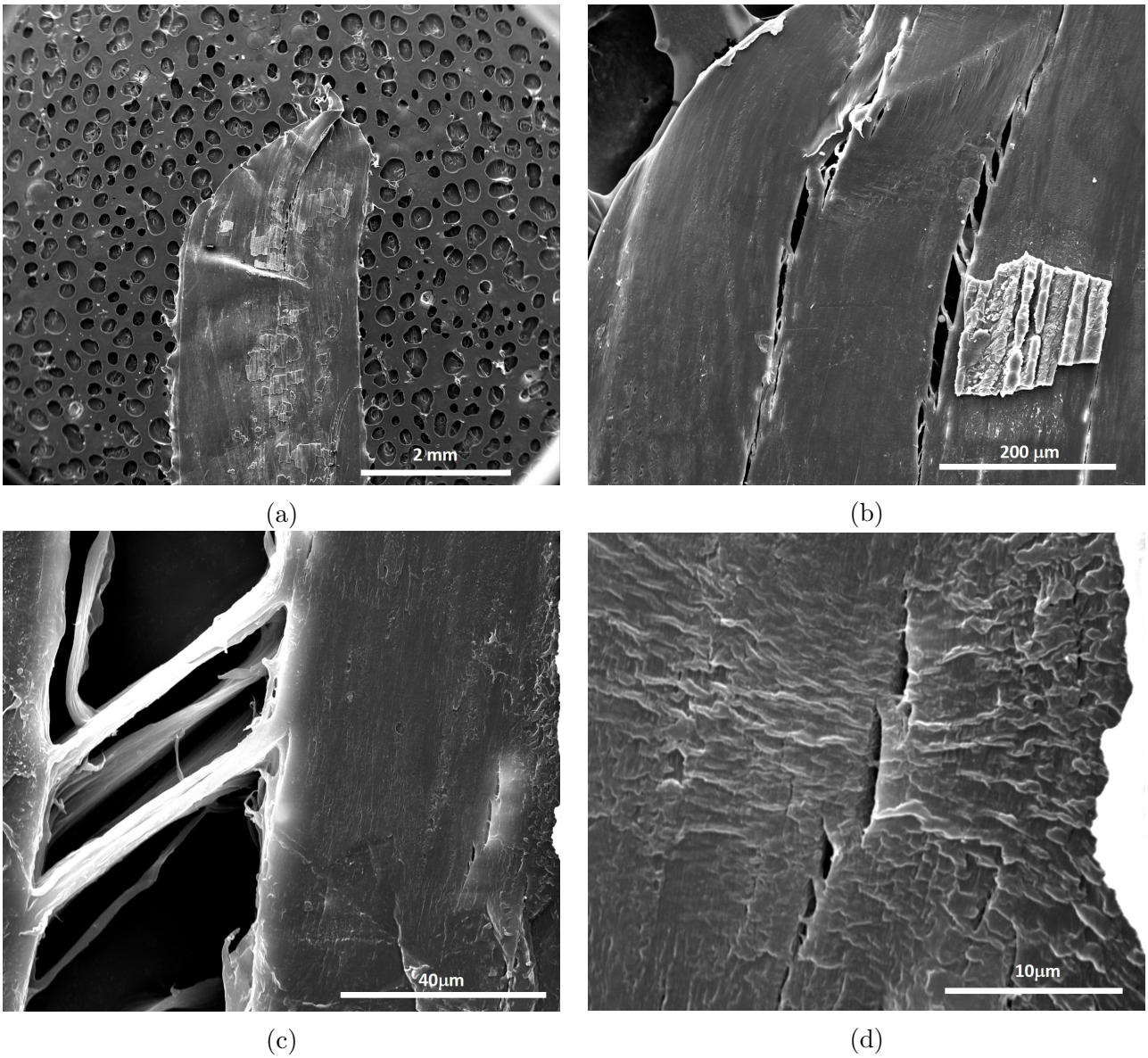

(a) (b)

(c) (d)

Figure 4.2: Fractography of 48 h UV-aged LDPE film. (a) Overall slant fracture. (b) Elongated craze-like voids in a "necklace coalescence" mode. (c) Fine fibril structure of large void. (d) Smaller voids. SEM observations with secondary electrons.

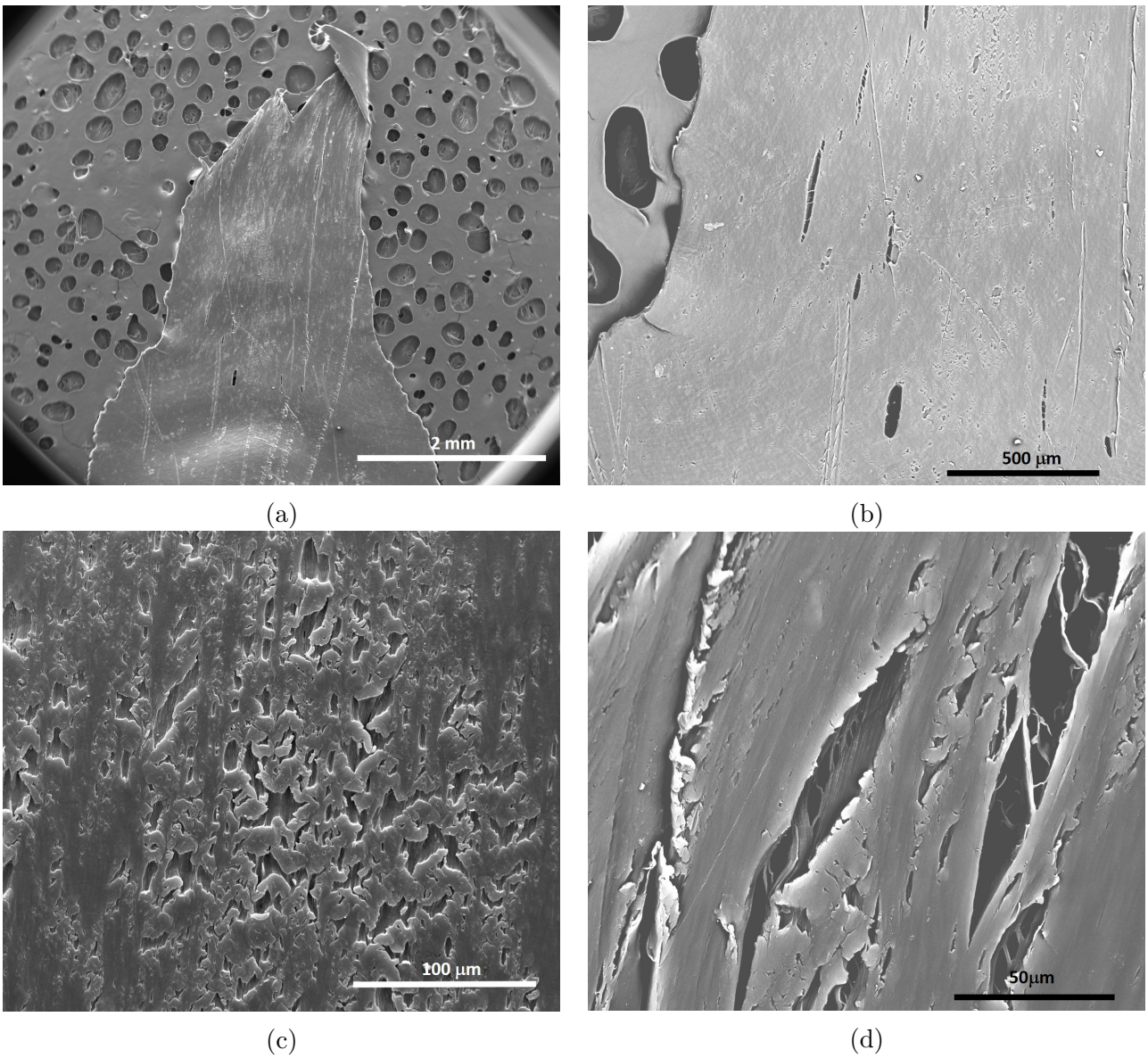

(a) (b)

(c) (d)

Figure 4.3: Fractography of 96 h UV-aged LDPE film. (a) Overall slant fracture. (b) Voids of various sizes and shapes. (c) Area with chemical degradation. (d) Large voids beneath the surface. SEM observations with backscattered electrons in Z-contrast mode, except for (c).

4.1.2.2 Plates

The fractographs of the mechanically loaded plates are shown in Fig 4.4. The pristine plate showed slanted mode fracture with profuse cold drawing (Fig 4.4a). At high UV doses (192 h and 240 h), the specimens seem to exhibit a fracture flat on the plane of the plate

(Fig 4.4b and c). However, cold drawing occurs at the core of the aged specimens due to heterogeneous oxidation, a point that is discussed further below in this section. Besides the fracture mode difference, pristine and aged specimens are also distinguished by their damage under the fracture surface. The surface of the pristine plate looks smooth to the naked eye, but closer examination in Fig. 4.5 reveals fine microvoids under the fracture surface. Nevertheless, it is evident to the naked eye that UV aging induced greater damage in the 192 and 240 h plates. The aged plates exhibited the polygonal cracks that originated during UV aging (Fig 4.4 b and c), with some cracks appearing wider due to deformation. These features are further discussed below. The specimens aged at intermediate UV doses (48 and 96 h) were not observed under SEM, but visual examination revealed: i) a slanted mode of fracture after 48 h of aging, and; ii) a mixed-mode with flat edges and cold drawing at the core after 96 h. The latter can be assumed to be a more ductile version of the fracture mode observed after 192 and 240 h of UV aging.

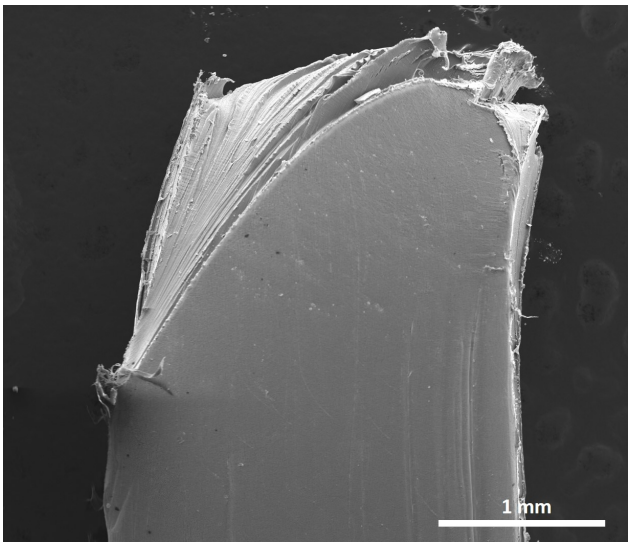

(a) 0 hours

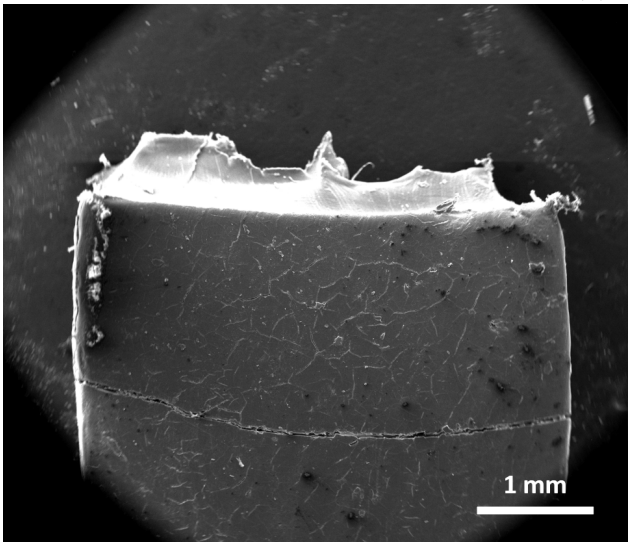

(b) 192 hours

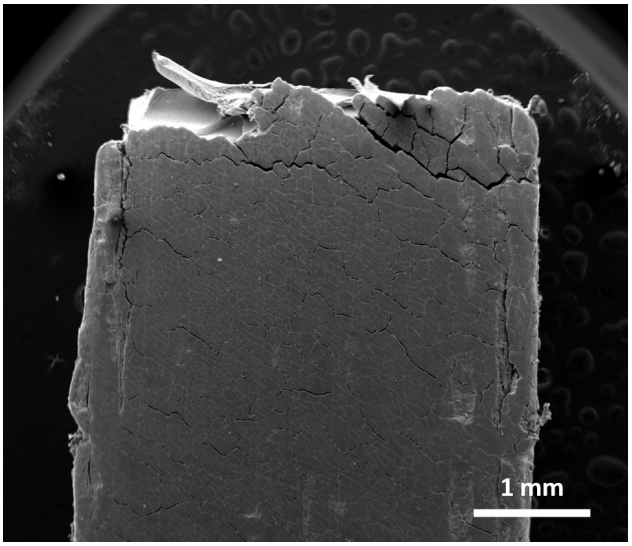

(c) 240 hours

Figure 4.4: Overall fracture mode in tension of LDPE plates: (a) pristine material; (b) after 192 h of UV aging; and (c) after 240 h of UV aging.

Some details of the fracture of the pristine plate are displayed in Fig. 4.5. Fig. 4.5a, reveals a slanted fracture mode, suggesting that failure occurs by plastic instability, namely, a shear band. The prismatic geometry of the tensile specimen used could have played a role in favoring shear-like fracture [136]. Further examination of the pristine specimen at higher magnification (Fig. 4.5b,c) showed microcracks and a ridged texture beneath the fracture

surface. Far from the fracture surface, the ridges are elongated perpendicular to the loading direction (Fig. 4.6a) while under the fracture surface they are oriented perpendicular to the shear band (Fig. 4.6b), suggesting that they are deformation-induced. The thickness of the ridges ranges from 0.5 to 1.0 μm, while the cracks that cut through some of these ridges are 4-10 μm in length. Similar features were observed on the fracture surface of the 240 h UV-aged plate, as shown in Fig. 4.6c. In this case, the ridges reached thicknesses up to 90 μm, and crack lengths up to 20 μm. In the 240 h aged plate, the features were restricted to the core of the specimen, suggesting that they are a characteristic of the pristine material.

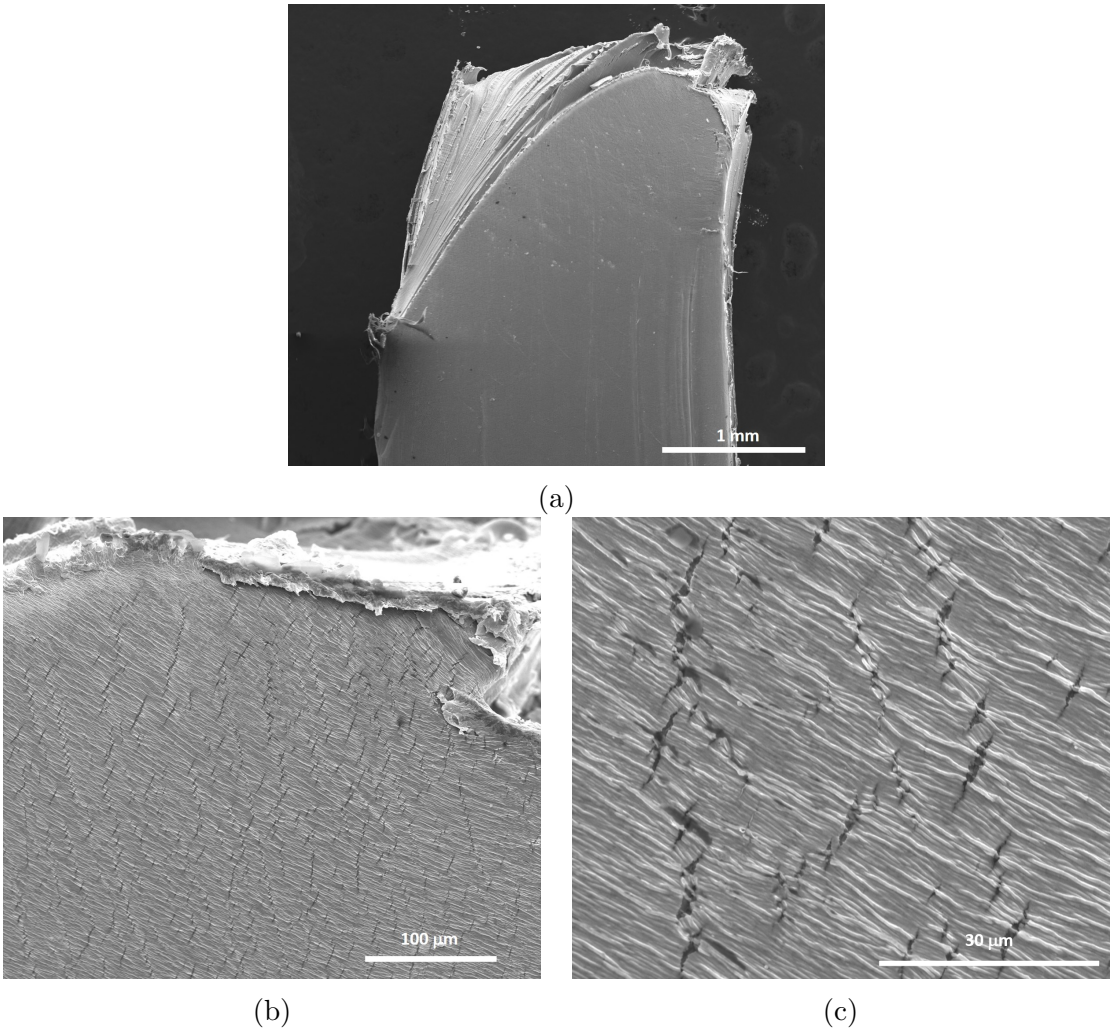

(a)

(b)

(c)

Figure 4.5: Fractography of pristine LDPE plate. (a) Overall slant fracture. (b) Microcracks under fracture surface. (c) Detail of microcracks in (b).

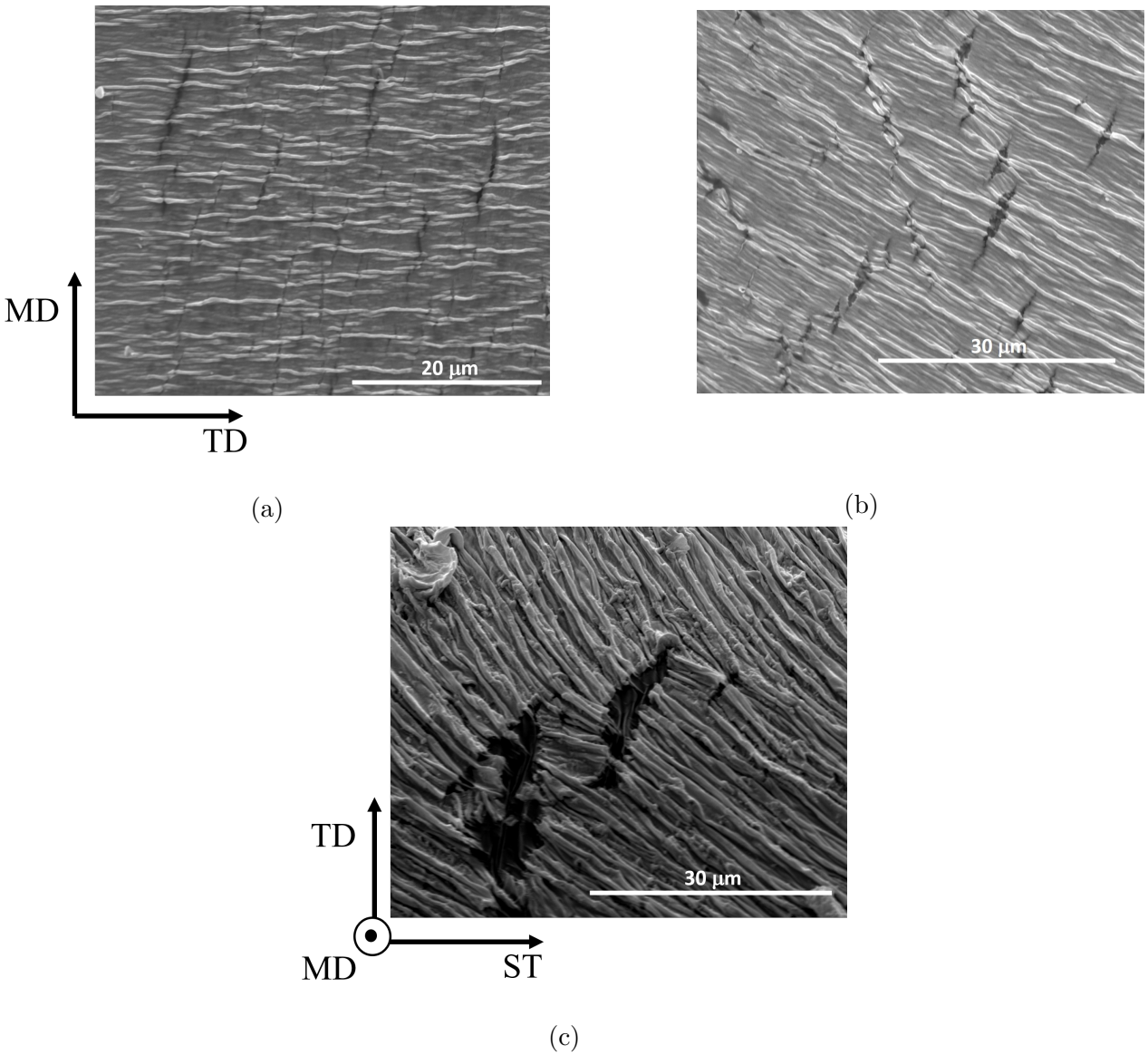

Figure 4.6: SEM micrographs of fibrillar texture on pristine and 240 h UV-aged plate: (a) on the plane of the pristine plate, far from the fracture surface and perpendicular to the loading direction MD, (b) on the plane of the pristine plate, close to the fracture surface and perpendicular to the shear fracture surface, (c) on the fracture surface of the 240 h UV-aged plate.

With the available data, it is challenging to elucidate the origin of these cracks and texture. One option is that the cracks observed are a defect of the applied Au-Pd coating. However, the features in Fig. 4.6c seem to contradict this hypothesis. Moreover, since Fig. 4.6a and b suggest that the ridges can rotate due to deformation, one might think

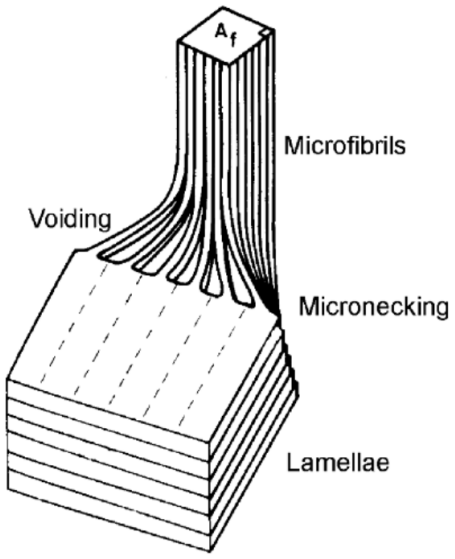

Figure 4.7: Sketch of the transformation of stacks of lamellae into microfibrils upon further deformation. Reprinted by permission from Springer Nature [10], Copyright 1972.

that they are created by the transition from a spherulitic to a fibrillar structure that some semicrystalline polymers undergo after high strains [10, 137, 138]. This transformation is sketched in Fig. 4.7. However, for the fibrils to end up oriented normal to the loading direction, it would require an unlikely fibril rotation of more than 90° with further deformation. Lastly, the ridges and cracks might be a result of voiding within the spherulites: during tensile deformation of spherulites, voiding can occur in the polar and equatorial regions of the spherulites, (see sketch in Fig. 4.8) [11, 139]. The observed ridges might result from the combination of voiding along the polar parts of the spherulites ("polar fans") and large deformations (recall for the as-received plate $\Delta L/L_0 \sim 4.5$). The microcracks observed in Fig. 4.6 would result from the coalescence of several equatorial microcracks in the spherulites. Further investigation is needed to determine the origin of the ridged texture observed.

The fracture surface of the pristine plate is shown in Fig. 4.9a, displaying profuse material drawing product of high plastic deformation and ductility. The drawing of the material results in some ribbon-like features, which in turn exhibits profuse striation (Fig. 4.9b). The wrinkled aspect of these ribbons may indicate a fast release after drawing under tension [140].

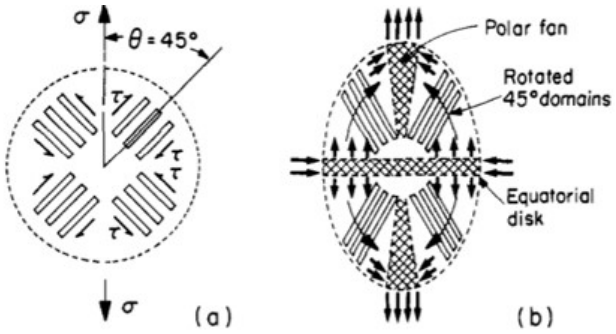

Figure 4.8: Sketch of a spherulite deformed in tension and definition of regions according to their orientation relative to the applied load: equatorial, polar, and diagonal regions. Reprinted by permission from American Chemical Society [11], Copyright 1988.

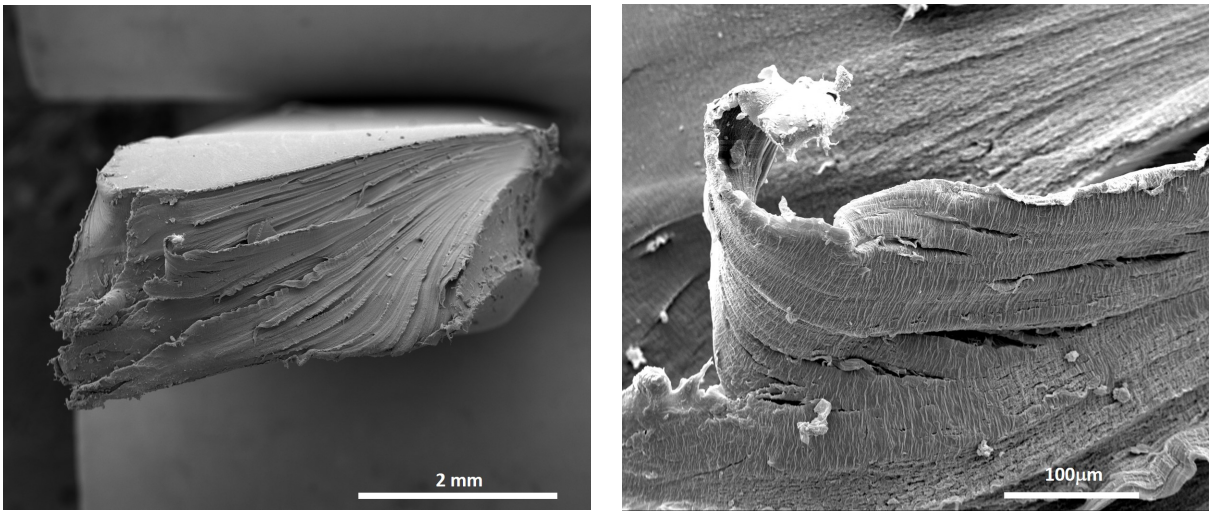

(a) (b)

Figure 4.9: Fractography of pristine LDPE plate. (a) Fracture surface showing profuse material drawing. (b) Ribbon-like feature showing microstriation.

Details of the fracture of the 192 h UV-aged plate are shown in Fig. 4.10. Fig. 4.10a shows a crack that percolates through the whole width of the specimen, approximately 2 mm below the fracture area. Higher magnification of this crack is shown in Fig. 4.10b. The origin of this percolating crack remains to be elucidated. Fig. 4.10c and d compare the crack pattern of the 192 h UV-aged specimen before deformation and after deformation to fracture. We can see that the deformation, in this case of $\sim$ 30 %, caused the cracks to open up, growth, and coalesce, forming a larger crack pattern in the deformed specimen.

The fracture surface after 192 h of UV aging in Fig. 4.11 displayed flat edges and material drawing in the core of the specimen. Cracks on the UV-exposed face were arrested within the oxidation layer (Fig. 4.11b and c). The transition between the oxidized area and the drawing area exhibited some voids of various sizes (Fig. 4.11d), where two main voids of $\sim$ 80 μm and $\sim$ 50 μm are accompanied by some smaller voids of $\sim$ 8 μm. These voids seem to originate at the chemical-cracks on the exposed surface of the plates (upper side of specimen in Fig. 4.11). The smaller voids appear as precursors to the bigger voids and suggest a continuous damage process.

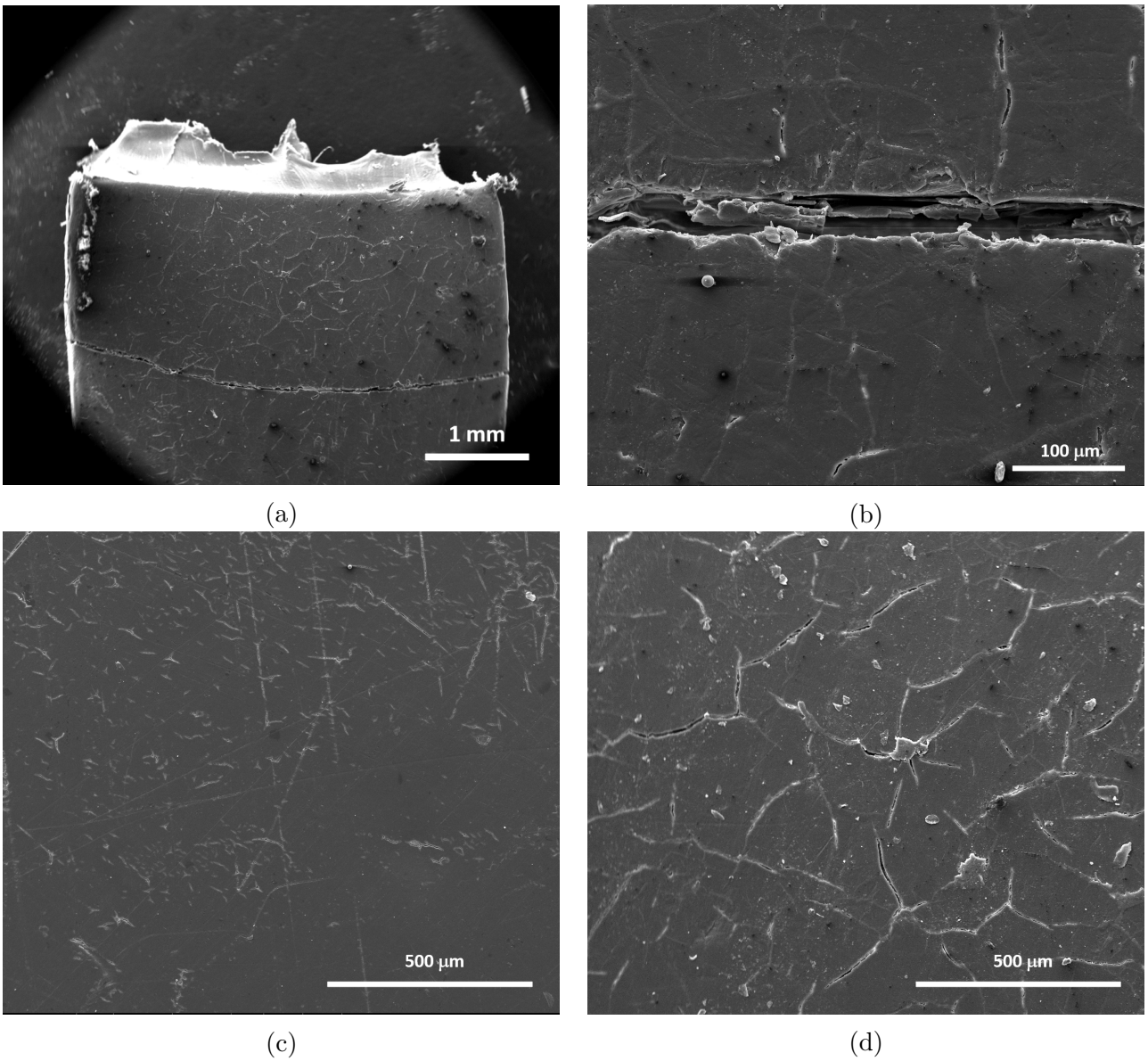

Figure 4.10: Fractography of 192 h UV-aged LDPE plate. (a) Fracture mode of LDPE plate after 192 h of HUV aging, and; (b) Detail of percolating crack. (c) Microcracks formed post-aging in absence of external loads. (d) Crack network formed after fracture.

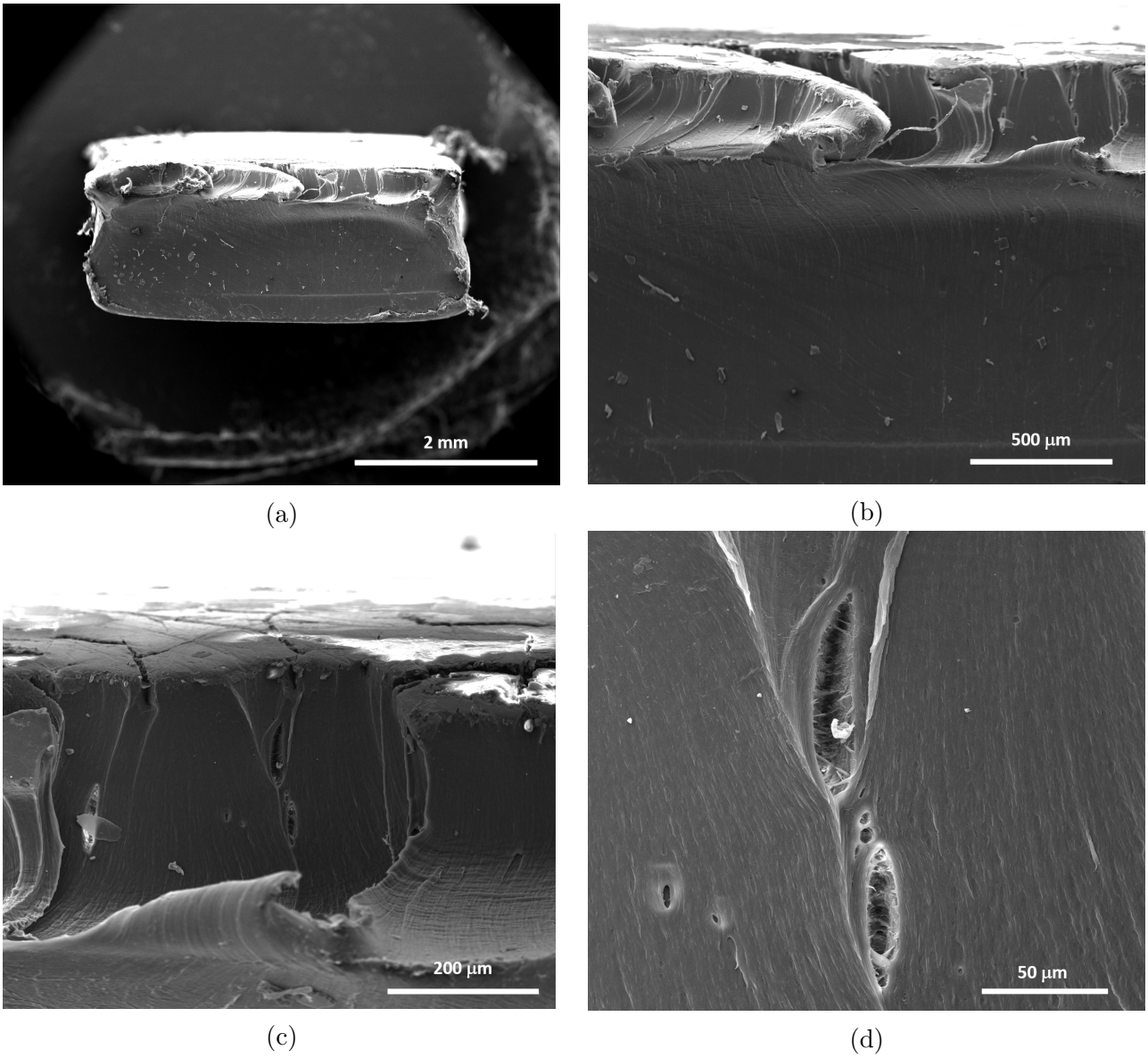

Figure 4.11: Fractography of 192 h UV-aged LDPE plate: (a) Fracture surface. (b) Oxidized layer with material drawing. (c) Detail of cracks and voids in the oxidation layer. (d) Voids in oxidation layer.

Fractography of the 240 h UV-aged plate is shown in Fig. 4.12 and 4.13. Comparison of the damage state before (Fig. 4.12a) and after deformation (Fig. 4.12b) shows that several more cracks open up after a deformation of $\sim$ 20 %. After 240 h of UV aging, the fracture surface is more irregular than that of the 192 h plate. (Fig. 4.13b,c and d). The flat

oxidation layer is followed by a transition zone characterized by a microfibrillar texture (Fig. 4.13b and c) that was previously discussed. Towards the drawing zone, microcracks along the thickness are observed, ranging from ∼5 to ∼80 μm in length (Fig. 4.13 b and d). Fig. 4.13d shows details of these cracks, which seemed to originate in the rupture of the highly oriented polymer fibrils. The microcracks resemble the "diamond" shaped cavities previously reported for some pristine polymers as results of deliberately included defects or in aged polymers such as PA6, PVC, and PC after aging [39]. Interestingly, the diamond cavities previously reported in the literature appeared on the exposed face of the material, unlike the present case where the diamond cracks appeared on the fracture surface of the specimen. Among the fracture surfaces analyzed, only 240 h UV exhibited this profuse cracking on the fracture surface.

The fracture surfaces of the 192 and 240 h UV-aged plates in Fig. 4.11a and 4.13a were flat on the edges while the core exhibited material drawing, in contrast with the pristine plate, where the fracture surface was homogeneous across thickness (Fig. 4.5). These features illustrate the heterogeneous nature of the oxidative-aging on bulk polymers: since oxidation is a diffusion-controlled process, an oxidation gradient arises where the outer region of the plate oxidizes to a greater degree since oxygen is more readily available, forming an oxidation layer. Towards the core of the plate, oxygen diffusion is limited, thus oxidation occurs to a lesser degree (or not at all) depending on the specimen's thickness. This explain why UV-aged plates are able to retain more ductility compared to UV-aged films (Chapter 3), even at higher UV-doses: in plates, even if the outer layers have embrittled to the point of no longer withstand load, the core of the plate is still intact enough to bear load and undergo considerable plastic deformation. Assessment of the SEM micrographs in Fig. 4.11 and 4.13 reveal an average thickness of the oxidation layer (TOL) of 180 $\pm$ 50 μm after 192 and 240 h of UV aging. The measurement of TOL on SEM must be taken with caution as it depends on how distinguishable the layer is in a specific condition is. More importantly, the inability to distinguish color on SEM is the main challenge when determining TOL in this way. In

the 192 h sample (Fig. 4.11), for example, the proximity of the ductile material drawing to the edge of the specimen makes it difficult to assess where the flat, oxidized layer ends and the pristine core begins. At the same time, the micrograph does not allow for distinction between the other oxidized edge of the specimen and the pristine core. For other conditions (Fig. 4.13, 4.16, 4.19), the assessment of TOL was more straightforward. This value of TOL is validated via the nanoindentation data described in Chapter 3 (Figure 3.11), where the onset of modulus increase suggested a similar value of TOL.

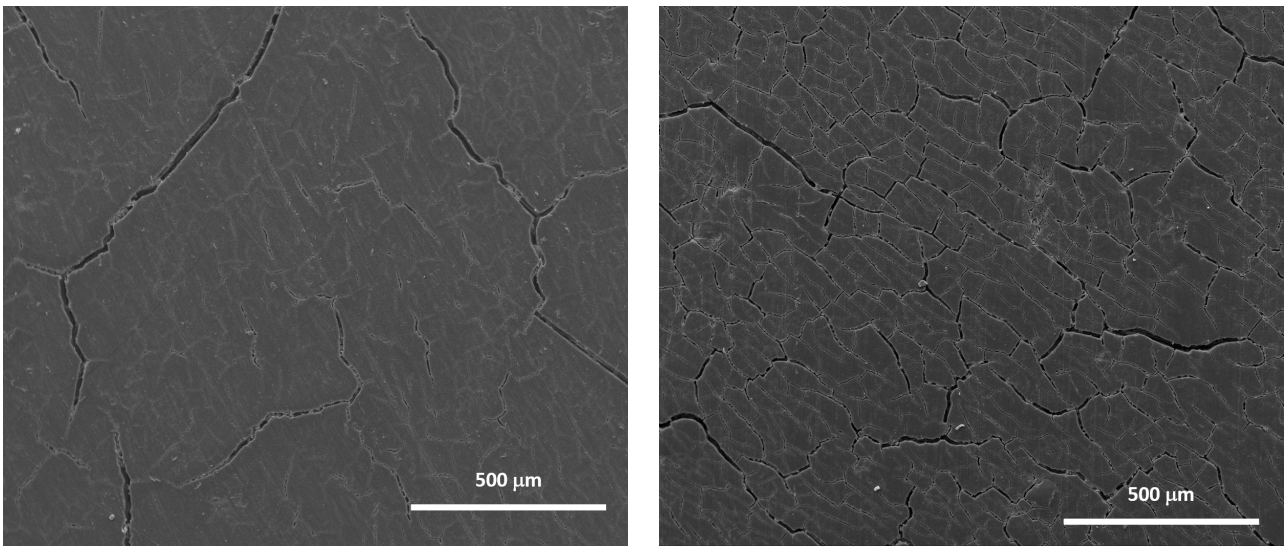

(a) (b)

Figure 4.12: Details of the plane of the plate for the 240 h UV=aged specimen:(a) Crack network formed post-aging in absence of external loads, and; (b) crack network after fracture.

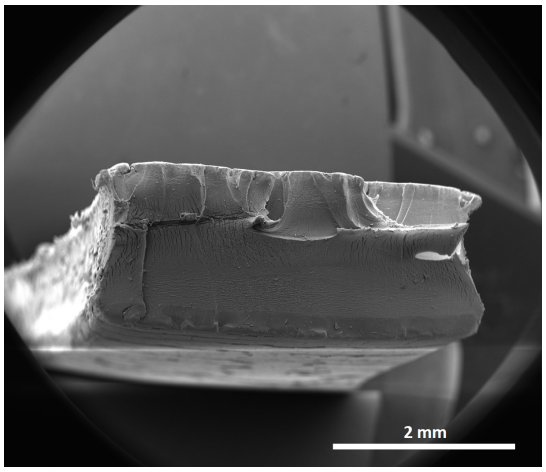

(a)

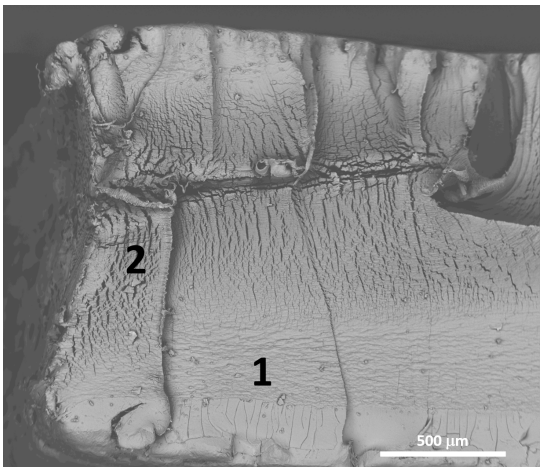

(b)

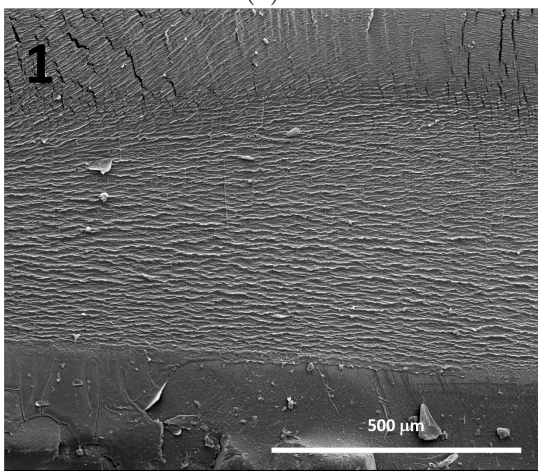

(c)

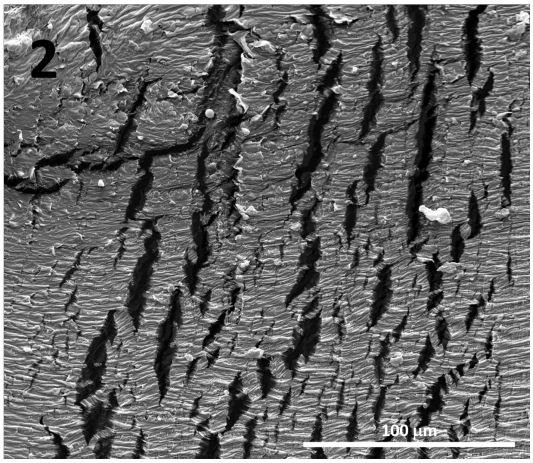

(d) Cracks

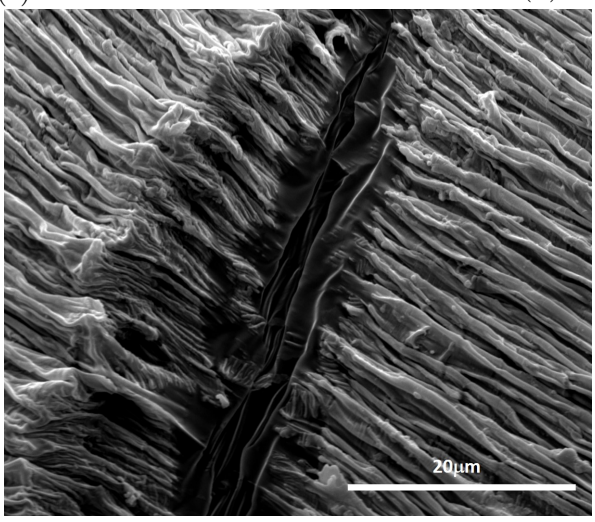

(e)

Figure 4.13: Fractography of 240 h UV-aged LDPE plate.: (a) Fracture surface. (b) Oxidized layer with material drawing from pristine core. (c) Microstriations in transition zone. (d) Microcracks near material drawing zone. (d) Detail of microcracks.

4.1.3 Damage in HUV Aging

4.1.3.1 Films

As was demonstrated in Chapters 2 and 3, humidity had an accelerating effect on the physico-chemical and macro mechanical aspects of UV aging of LDPE, in spite of the hydrophobic nature that renders the polymer resistant to hydrolytic decomposition. It was also shown in the previous chapters that humidity cycles affected the UV-induced chemical damage, resulting in increased surface irregularity on the HUV-aged films and modified crack patterns on the HUV-aged plates. In this section, we assess whether humidity also affects the mechanical damage of UV-aged LDPE and if so, how it relates to the observed physico-chemical and mechanical aspects of oxidation studied so far.

Fractography of the 96 h HUV-aged film is displayed in Fig 4.14, together with its UV-aged counterpart for comparison. The fracture mode in 96 h HUV-aged is overall flat mode, unlike pristine and UV-aged films, which all showed a slanted fracture mode (Fig. 4.14a and b). This is in accordance with the lower ductility exhibited in the tensile response of 96 h HUV film in Chapter 3. Recall that while 96 h HUV film had a flow stress similar to that of the UV film, the elongation to fracture was reduced by $\sim 50\%$. Another main difference between UV and HUV-aged films observed in Fig. 4.14c and d is the absence of elongated void-like features parallel to the tensile MD orientation that were common in the UV-aged films (Fig. 4.2 and 4.3).

Instead, the HUV-aged film shows microcracks oriented exclusively perpendicular to the tensile MD orientation, as observed in Fig. 4.15. The propensity for these cracks is higher in the central region near the fracture surface (Fig. 4.15 b and c), while away from the fracture surface the density of cracks decreases (Fig. 4.15 d). It can be assumed that the origin of the overall flat fracture mode is the linking of these horizontal cracks. It is worth highlighting that despite HUV inducing just a barely perceptible chemical-damage (Fig. 2.31), it had a significant impact on damage upon deformation.

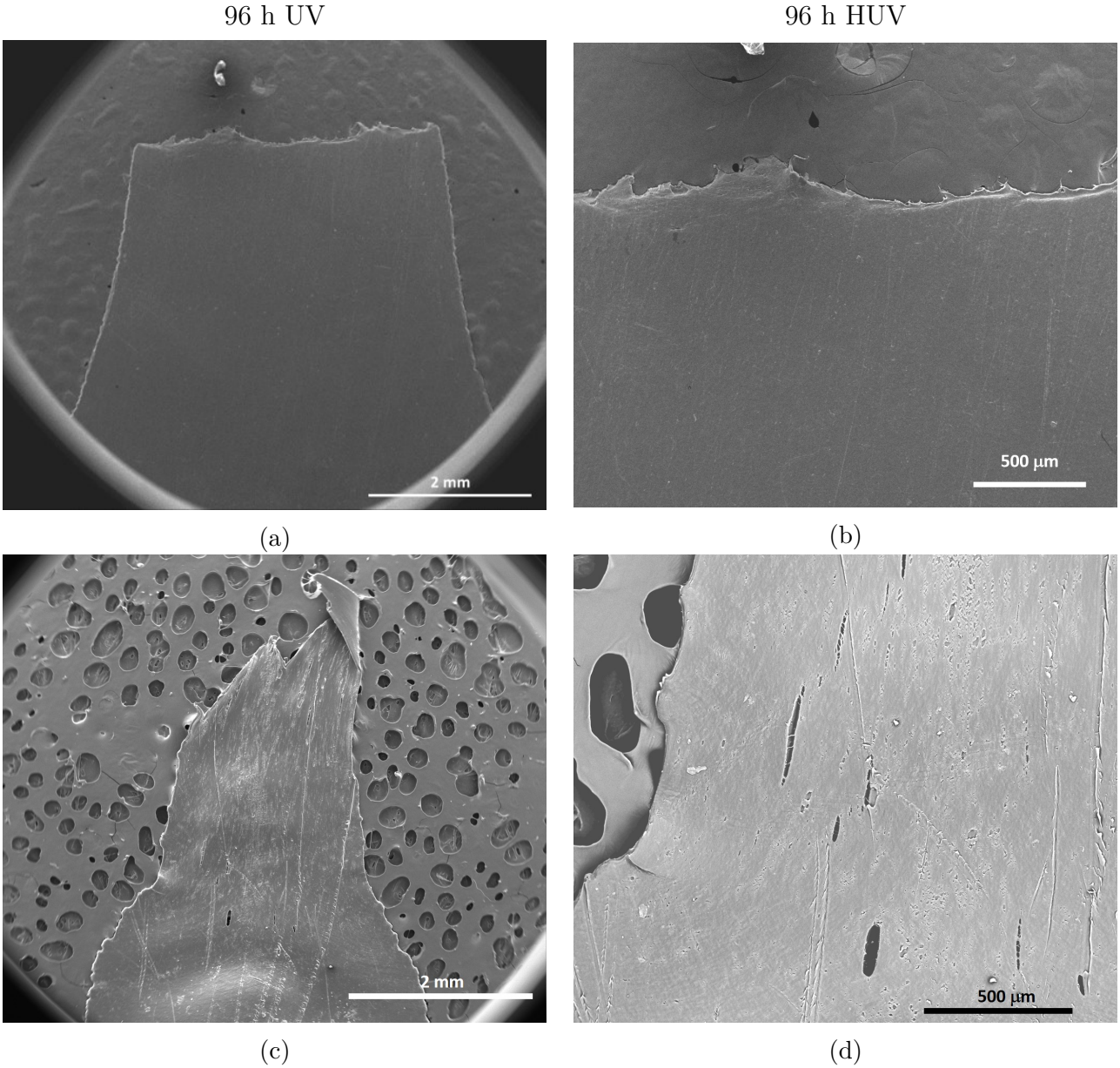

Figure 4.14: Fractography of LDPE film after 96 h of HUV aging. (a) Fracture mode, and; (b) detail of area under the fracture surface. For comparison, also shown: (c) the fracture mode of LDPE film after 96 h of UV aging, and; (d) the damage under its surface.

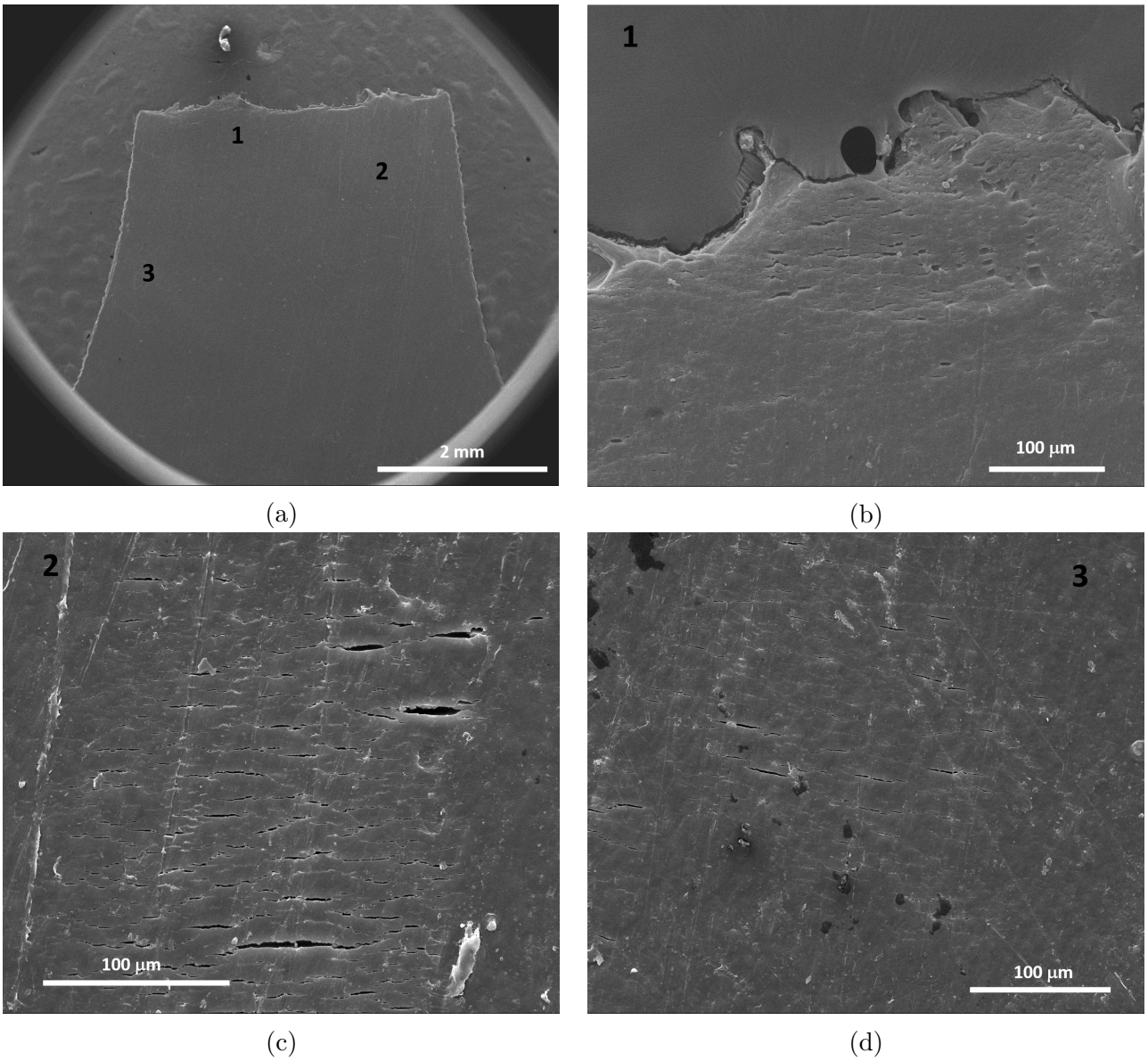

Figure 4.15: Fractography of LDPE film after 96 h of HUV aging. (a) Fracture mode. (b) Area under the fracture surface. (c) Cracks perpendicular to the MD loading direction, in the central region of the specimen. (d) Lower density of cracks away from fracture surface.

4.1.3.2 Plates

Next, consider the 240 h HUV-aged plate in Fig. 4.16. The plate had a slightly slanted fracture mode with material drawing from the core, similar to the drawing displayed by the UV-aged plates. Like its UV counterparts, the exposed surface of the HUV plate shows the

crack pattern that emerged during aging, with some cracks apparently becoming wider due to deformation (Fig. 4.16b and c).

The 240 h HUV specimen displayed more clearly the oxidation layer, as indicated in Fig. 4.17. The micrographs also show how cracks formed in the exposed surface are arrested in the oxidation layer of the material (Fig. 4.17 b and c). The average thickness of the oxidation layer (TOL) on Fig. 4.17b was 177±3 μm. This value is similar to that obtained from SEM fractography of the 192 and 240 h UV-aged plate (190±70 μm and 170±50 μm, respectively). In fact, since the TOL value remained unchanged between 192 h and 240 h of UV aging, an even across different aging types (240 h UV vs 240 h HUV), it seems to suggest that a steady-state TOL has been reached after 192 h of accelerated weathering.

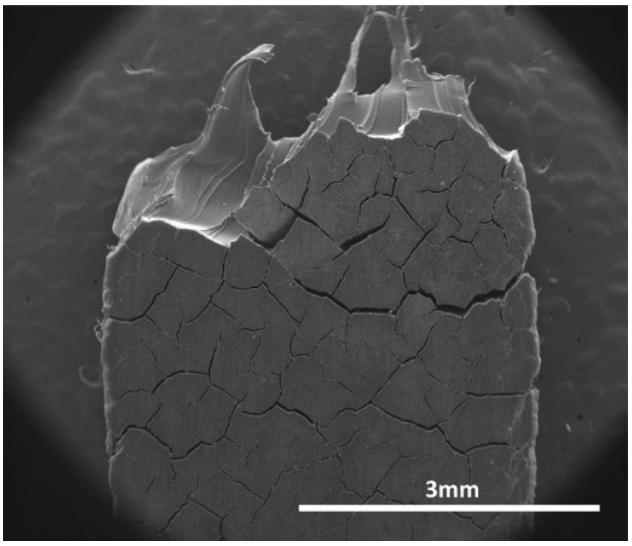

(a) 240 h HUV: Fracture

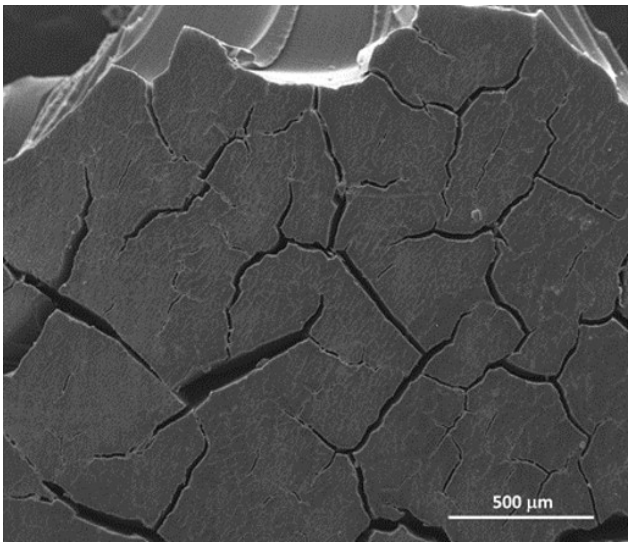

(b) 240 h HUV: Fracture detail.

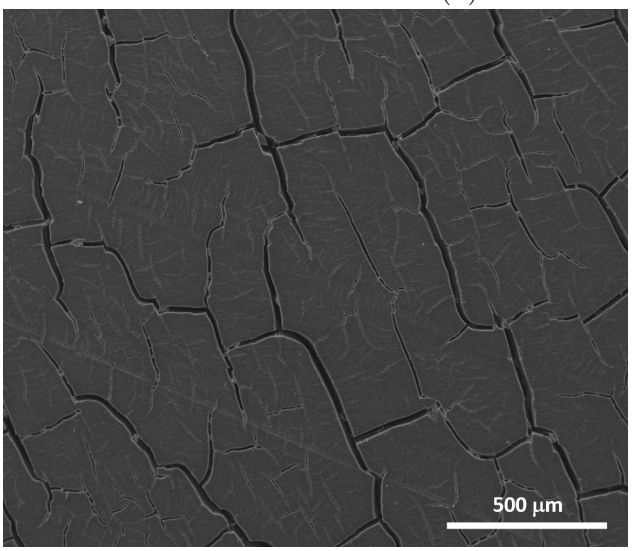

(c) 240 h HUV: Surface post-aging, in absence of loading.

Figure 4.16: (a) Fracture mode of LDPE plate after 240 h of HUV aging. (b) Detail of widened cracks after deformation. (c) Detail of surface after HUV aging, prior to mechanical loading.

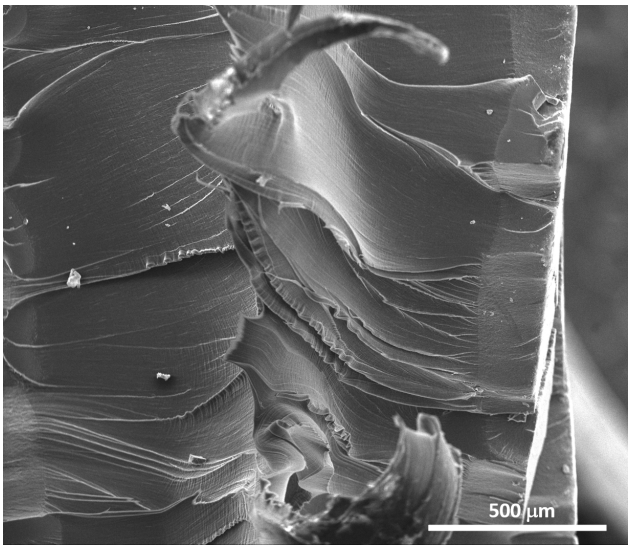

(a)

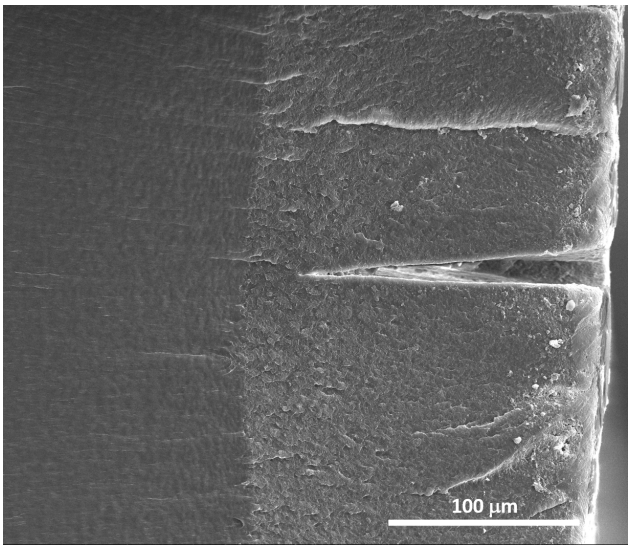

(b)

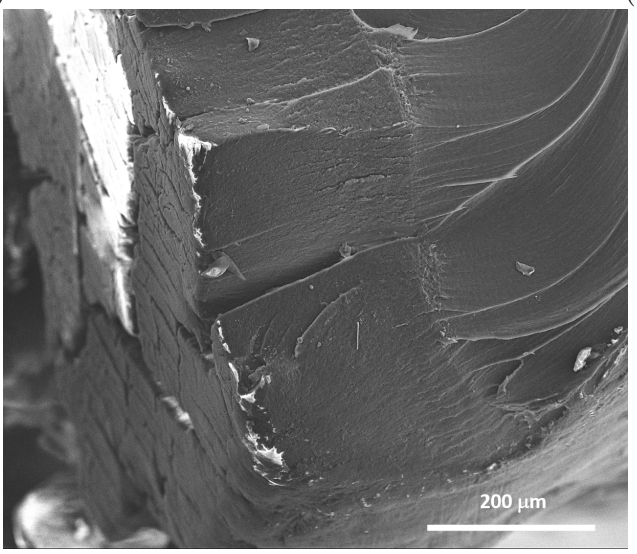

(c)

Figure 4.17: (a) Fracture surface of LDPE plate after 240 h of HUV aging. (b) An oxidation layer of $\sim$ 180 μm can clearly be observed in the fracture surface. (c) Detail showing how cracks originated in the surface are arrested within the oxidation layer.

4.1.4 Damage in Natural Aging

4.1.4.1 Films

The *post mortem* fractography of the 2 months naturally-aged film is provided in Fig. 4.18. Similar to the HUV-aged film, the fracture mode of the naturally-aged film was overall flat, distinguishing it from the pristine and UV-aged films with their slanted fracture mode. Fig. 4.18 shows the overall erosion of the film and the presence of artifacts on its surface resulting from the exposure of the sample to wind, sand and dust [127]. A detail of the region under the fracture surface in Fig. 4.18b revealed that the mechanical damage consisted mostly of cracks perpendicular to the loading direction MD. A detail of these cracks is displayed in in Fig. 4.18c, highlighting the bifurcation of one crack, as well as very fine fibers between the cracks, oriented along the MD tensile direction. Another parallel with the HUV-aged film is the absence of elongated voids parallel to the MD tensile direction, a feature observed in the UV-aged films (Fig. 4.2 and 4.3).

4.1.4.2 Plates

For the damage in naturally aged bulk specimens consider the 8 months aged plate in Fig. 4.19. The overall fracture mode is slanted, and, like all the plates previously examined in this chapter, it shows material drawing on the core of the specimen (Fig. 4.19a). The cracks in the exposed surface of the plate appeared less wide and deep than those in the post-mortem HUV-aged plates (Fig. 4.16), probably due to the lesser total deformation and the effect of the dust particles filling in the cracks of the naturally aged plate. A salient feature on this specimen is the crack perpendicular to the MD loading direction in Fig. 4.19b, akin to delamination in composite materials.

The fracture surface is shown in Fig. 4.19c, with details in Fig. 4.19d. No cracks where observed in the transition between the oxidation layer and the pristine core of the specimen. An oxidation layer appears to be distinguishable in Fig. 4.19d, where the cracks of exposed surface seem to be arrested. The thickness of the oxidation layer (TOL) based on Fig. 4.19d

is estimated to be $\sim$ 350$\pm$120 μm. This value is higher than the TOL estimated from SEM fractography on the accelerated aged specimens (average TOL for lab-controlled conditions $\sim$ 180$\pm$40 μm). Based on the nanoindentation data presented in Chapter 3 (Fig. 3.11), we can establish an upper limit for TOL of $\sim$ 300 μm. Thus, the discrepancy between the measured TOL's on accelerated and naturally aged specimens might be indicative of one of the following: (i) steady state has not been reached in 192-240 h of accelerated aging, so further aging would lead to a larger TOL; (ii) TOL of 192 and 240 h plate is indeed closer to 300 μm, but SEM is not reliable tool to measure TOL; (iii) steady state has been reached in both accelerated and natural aging but the slower oxidation rate in natural aging allows, on the long run, a deeper oxygen diffusion, thus a thicker TOL [99]. With the data at hand, it is not possible to completely discern among these options. For example, the measurement of TOL on SEM depends on how distinguishable the layer is in a given specimen and condition, and how straight (i.e., parallel to the plane of view) the surface of a sample is, so point (i) cannot be fully discarded. At any rate, considering all the data available from SEM and nanoindentation, an upper bound limit of 300–350 μm can be established for the TOL of bulk LDPE specimen under the conditions studied in this work.

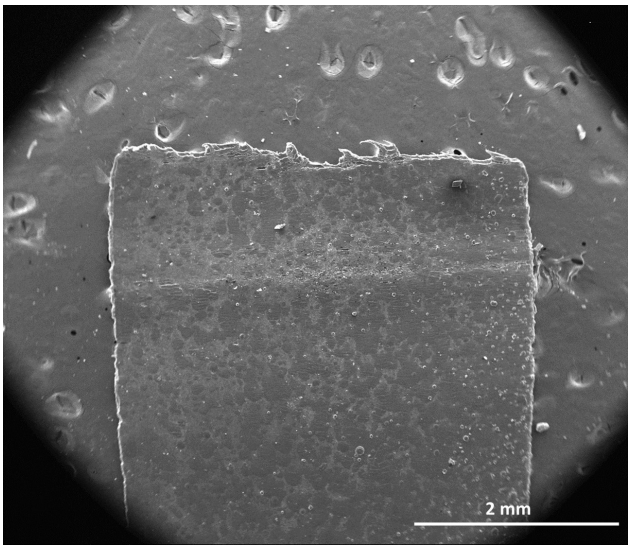

(a)

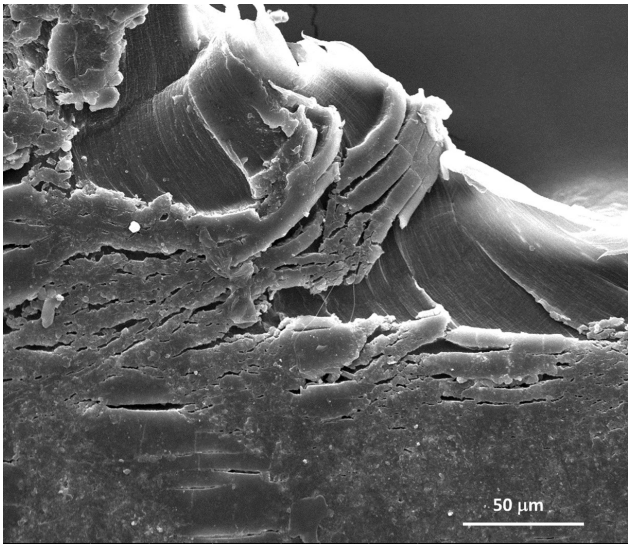

(b)

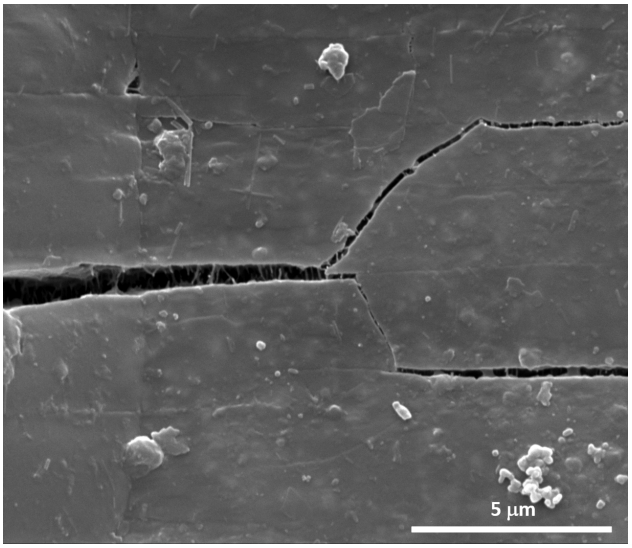

(c)

Figure 4.18: Fractography of LDPE film after 2 months of natural aging. (a) Flat fracture mode. (b) Microcracks perpendicular to the MD loading direction under the fracture surface, together with some material drawing. (c) Detail of bifurcation of microcracks and fibers along the MD loading direction.

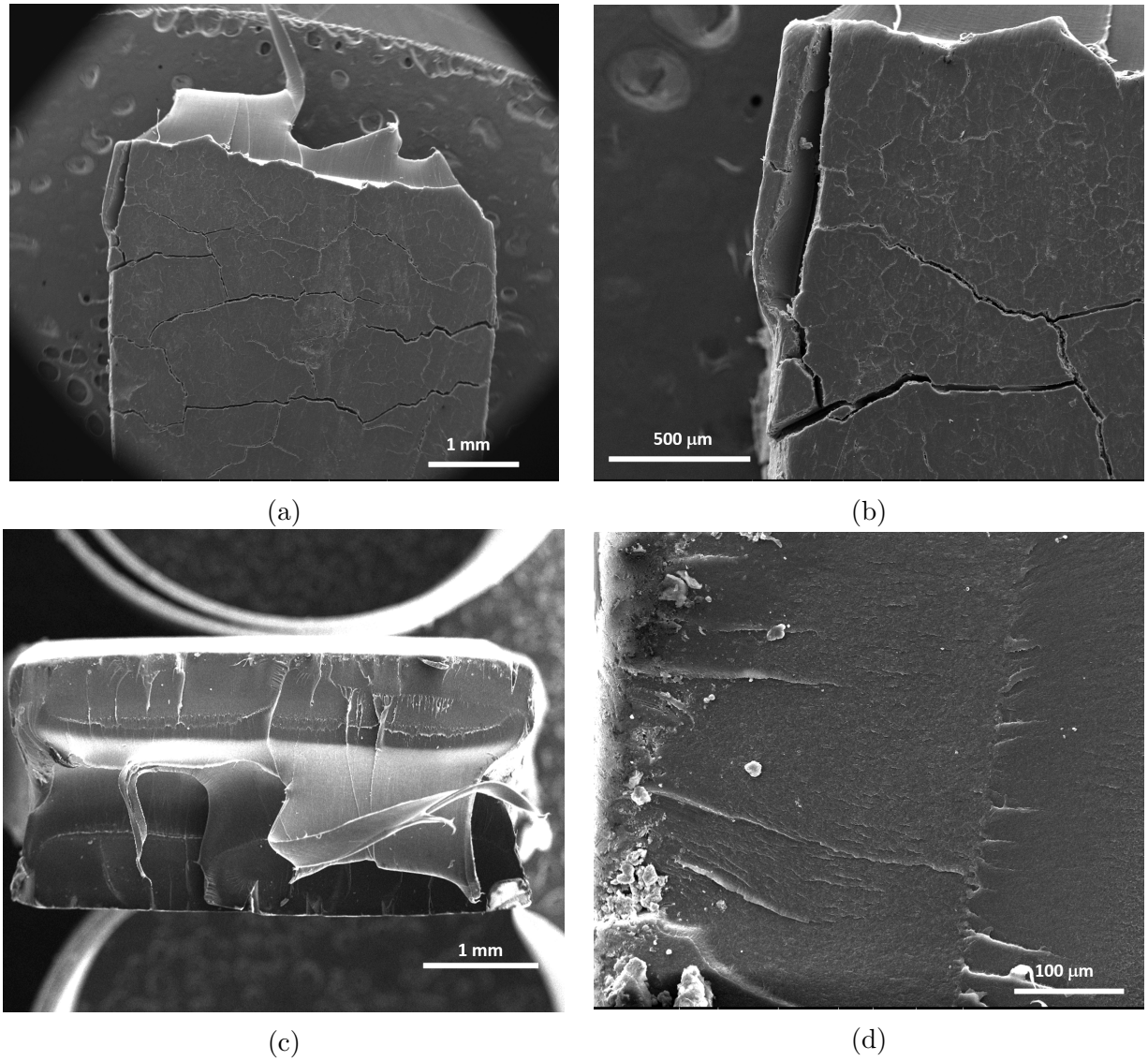

Figure 4.19: Fractography of LDPE plate after 8 months of natural aging. (a) Fracture mode. (b) Crack opening akin to delamination. (c) Fracture surface showing flat edges and drawing from the pristine core. (d) Detail of apparent oxidation layer of ∼300 μm thickness.

4.2 Discussion

The key findings of Chapters 2, 3 and the present chapter can be summarized as follows: (i) the oxidation-induced transient strengthening regardless of aging type (lab-controlled UV and HUV aging, natural aging) and type of oxidation (homogeneous and heterogeneous oxidation); (ii) the indirect evidence of secondary crystals formed because of UV and HUV

aging (Fig. 2.16); (iii) the observation of "chemical damage" prior to any mechanical testing (Fig. 2.18); (iv) the oxidation-induced cavitation upon mechanical loading (Figs. 4.2 and 4.3); These results are discussed in light of the state of the art, laying emphasis on aspects that remain largely unexplained in the literature and pointing, where appropriate, to further avenues of investigation.

In the following discussion we refer to the physico-chemical characterization of LDPE. This was performed exclusively on films, where oxidation is nominally homogeneous. We extend some of the observations from this physico-chemical characterization to the plates, since they were made out of the same LDPE FB3003 pellets and shared with films the same trends in terms of the effect of aging on mechanical response. Nevertheless, structural effects and diffusion limited oxidation, which are characteristics of oxidation in bulk specimens will be invoked during the discussion when relevant.

4.2.1 Chain Scission versus Crosslinking

The loss of ductility induced by photo-oxidation during UV, HUV and natural aging was evident in Chapter 3. This loss is quantified in Fig. 4.20 for the UV-aged films and 4.21 for the UV-aged plates in terms of a nominal strain to break, $\epsilon_{\mathrm{b}} = \Delta L/L_0\big|_{\mathrm{b}}$, and a true strain to fracture, $\varepsilon_{\mathrm{f}} = 2\ln(w_0/w_{\mathrm{f}})$, measured post mortem ($\sim$ one month) based on width reduction.

The trend of a decreasing strain to fracture indicates profuse chain scission events. It is consistent with the increase in carbonyl index (Fig. 2.13) and decrease in molecular weight (Fig. 2.14) discussed in Chapter 2. On the other hand, chain scission alone cannot explain the oxidation-induced strengthening of the polymer in the early stages of exposure to UV radiation (Fig. 3.5, 3.8, 3.14, 3.16, 3.19, 3.20). To explain this transient strengthening some other mechanism must be invoked.

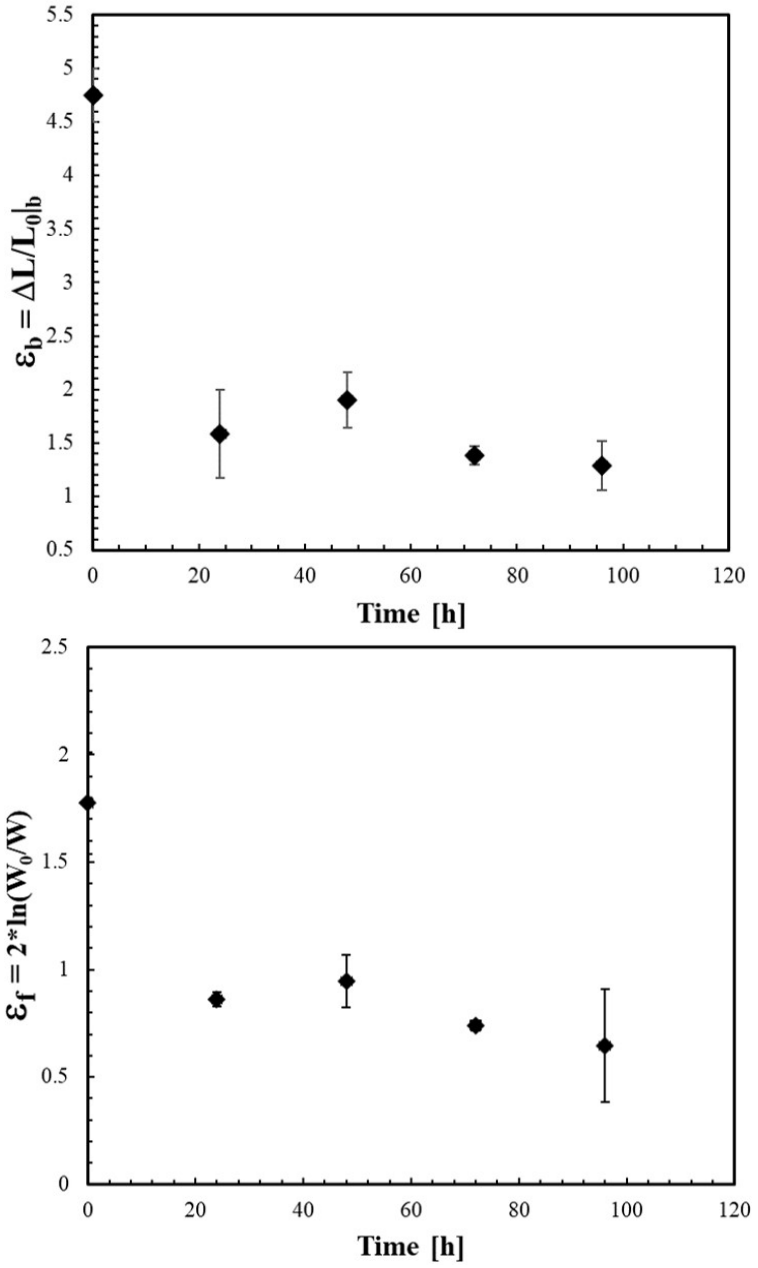

Figure 4.20: Effect of UV aging on strain of LDPE films: (a) Nominal strain at break versus aging time; (b) (Post mortem) true strain to fracture versus aging time.

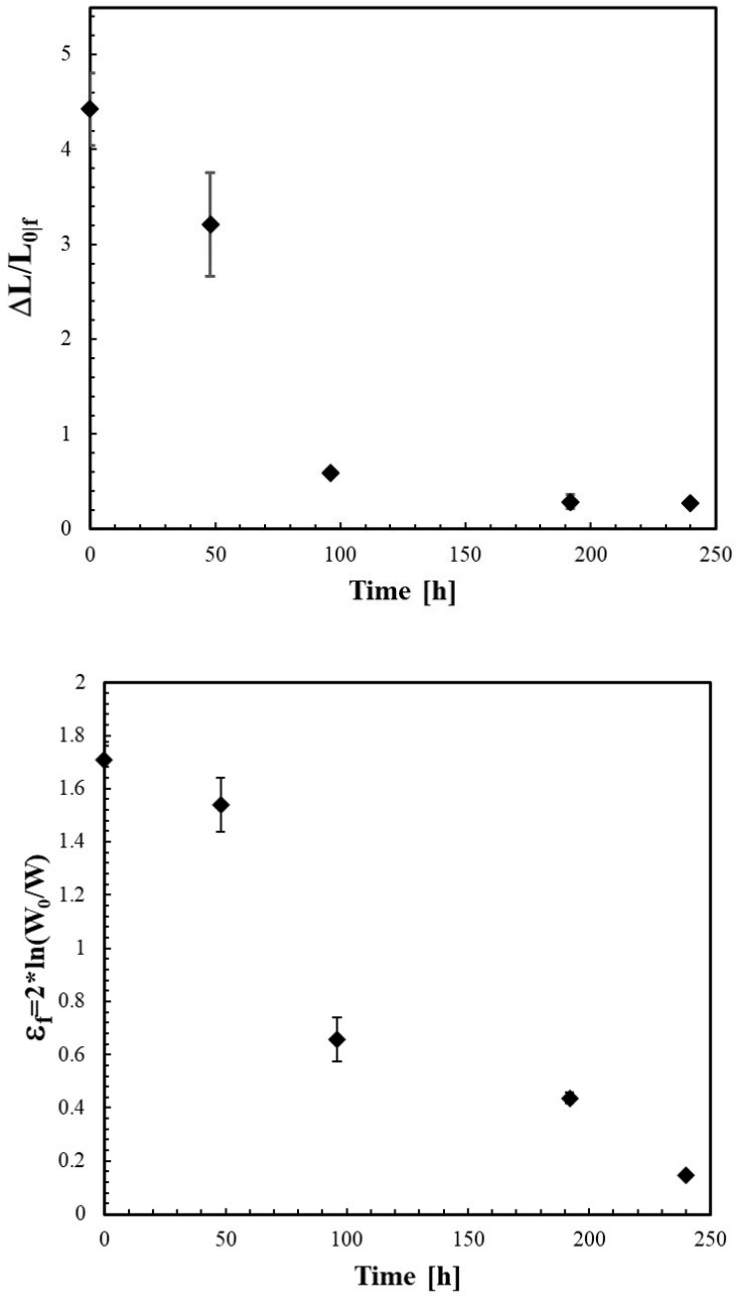

Figure 4.21: Effect of UV aging on strain of LDPE plates: (a) Nominal strain at break versus aging time for LDPE plates; (b) (Post mortem) true strain to fracture versus aging time for LDPE plates.

The transient behavior suggests a competition among the various radiation-mediated mechanisms, but their interplay is rather intricate. Indeed, the molecular weight decreases

from the outset of radiation (Fig. 2.14) whereas other physico-chemical characteristics undergo an incubation period and remain unchanged below 48 hours of aging; see Fig. 2.13 for CI and VI and Fig. 2.15b for crystallinity. Correspondingly, there are two regimes over which the strain to break ϵ_b decreases. In the first (roughly up to 48 h of radiation for films, 96 h for plates), ϵ_b goes from $\sim$5 down to $\sim$2 (films) or $\sim$0.5 (plates) without any noticeable change in crystallinity or reaction products, as measured by CI and VI. In the second regime (beyond 48 h of aging), ϵ_b continues to decrease, albeit less abruptly, while CI and VI undergo a significant increase.

The delayed onset of ductility loss in plates respect to aged films is a consequence of chemical damage and diffusion limited oxidation (DLO) on bulk specimens, as discussed in section 3.2.1.1. UV aging resulted in chemical damage (irregularities, voids and cracks) in both films and plates without any external mechanical loading (Chapter 2). The effect of this chemical damage upon deformation is more critical in films, where oxidation is homogeneous across thickness, meaning that the whole specimen is compromised. In plates, however, the effect of oxidation is constrained to the outer layer (which can reach up to $\sim$ 300 μm into the material), leaving a core of pristine material that is capable of bearing load even after the failure of the oxidized layer. This effect is illustrated in Fig. 4.22.

To gain insight into the transient strengthening, our first attempt is to invoke radiation-induced crosslinking and its effect in counteracting chain scission. Indeed, crosslinking generally increases the strength of a semicrystalline polymer by improving the cohesive strength of the amorphous phase due to a higher molar mass [20], or by way of branching and its deterrent effect on chain mobility and disentanglement [37].

A method to estimate the average molecular weight between crosslinks is from mechanical tests above the glass transition temperature. In particular, the evolution of hardening provides great insight. It is worth emphasizing, at this juncture, the importance of obtaining true stress–strain responses in order to make robust estimates of hardening rates. Close examination of Fig. 3.4b and 3.7 shows a significant increase in hardening rate between the

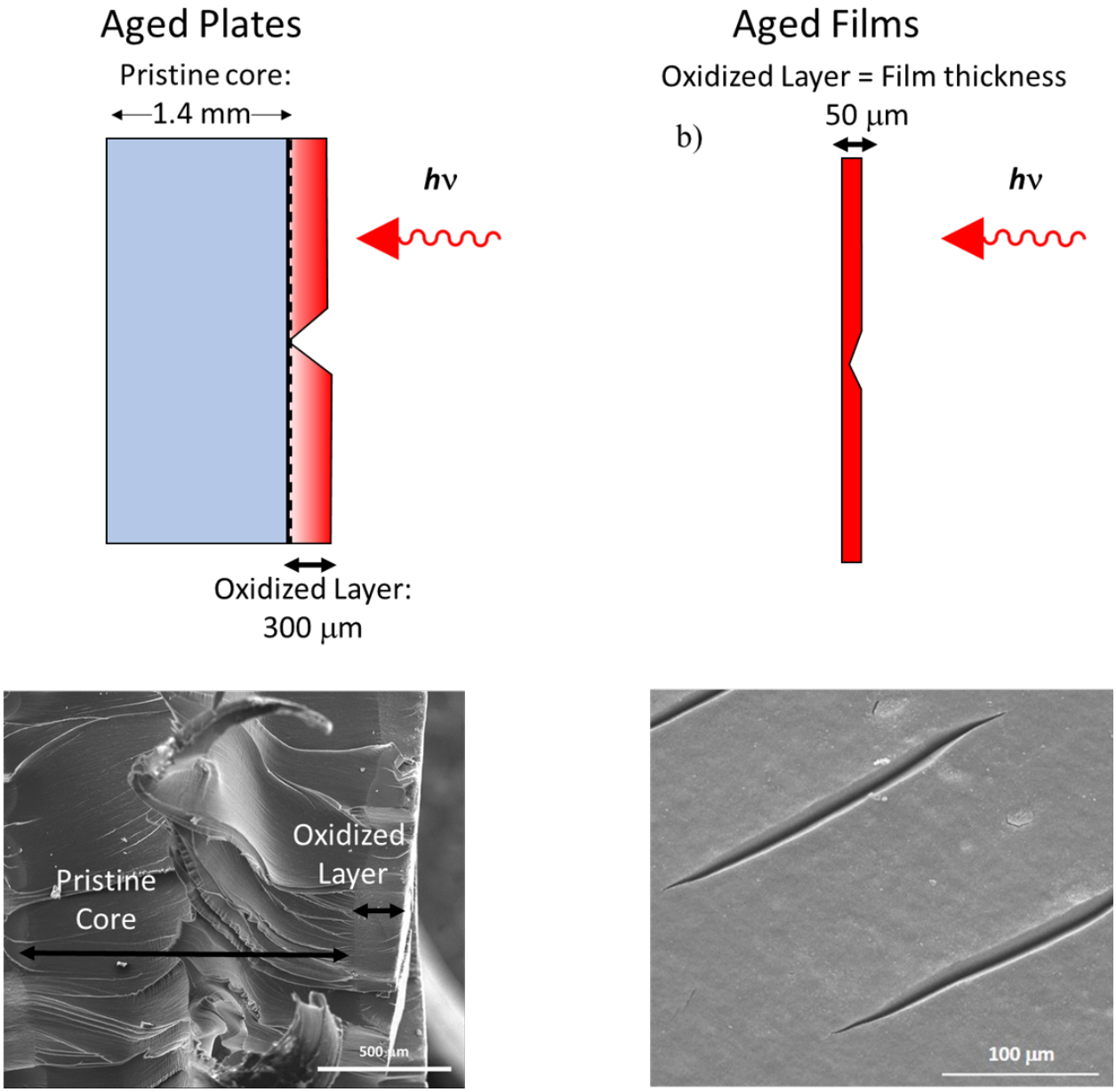

Figure 4.22: Illustration of the effect of crack channeling on UV-aged plates and films: In plates (left), oxidation and chemical cracks are limited to the oxidized layer, leaving enough pristine material in the core to bear additional load. in films (right), oxidation is homogeneous and presence of cracks has a more catastrophic effect.

unaged condition and the specimens aged under 48 h for films, and 192 h for plates. This type of hardening is usually attributed to an increase in crosslinking.

In order to test this hypothesis, the concentrations of chain scissions and crosslink nodes were estimated for each UV and HUV aging condition using GPC measurements as input: knowing M_n and M_w for each aging time, the corresponding numbers of chain scissions n and crosslink nodes x per unit mass were deduced from Saito's equations as reported in reference [37]:

$$\Delta_n = \frac{1}{M_n} - \frac{1}{M_{n0}} \quad \text{and} \quad \Delta_w = \frac{1}{M_w} - \frac{1}{M_{w0}} \tag{4.1}$$

$$n = \frac{2}{3}(2\Delta_n - \Delta_w) \quad \text{and} \quad x = \frac{1}{3}(\Delta_n - 2\Delta_w) \tag{4.2}$$

The results reported in Fig. 4.23 clearly show that in the 0 h–192 h range, chain scission dominates over crosslinking.

Difficulties in extracting information about the molecular weight between crosslinks is documented in the literature and the results in Fig. 4.23 should be interpreted with care. Additionally, the insolubility of sufficiently large, crosslinked structures can impede their analysis with GPC and would not be included in the molecular weight distribution curves, which may also lead to lower estimates of molecular weight averages despite the crosslinking reactions [56].

4.2.2 Chemi-crystallization

Two distinct scenarios of oxidative embrittlement are found in the literature. In the case of a largely predominant chain scission process, the destruction of the entanglement network leads to ductility loss. However, since small macromolecular fragments are also very mobile in a rubbery amorphous phase, they migrate rapidly up to the surface of crystalline lamellae to integrate and thicken them. The increase in both lamellar thickness and crystallinity ratio then explain the increase in yield stress [1]. In the case of a pure crosslinking process, for

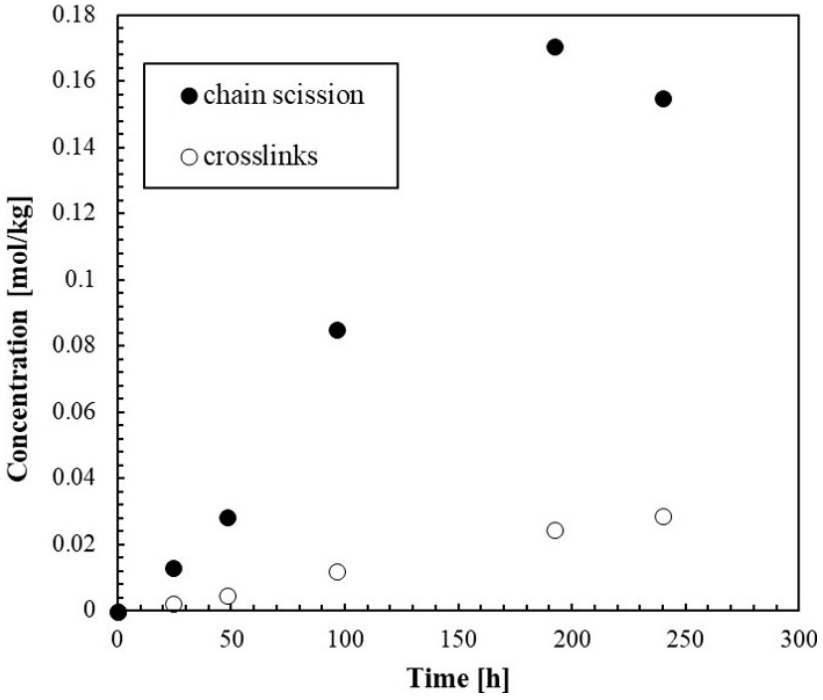

(a) UV

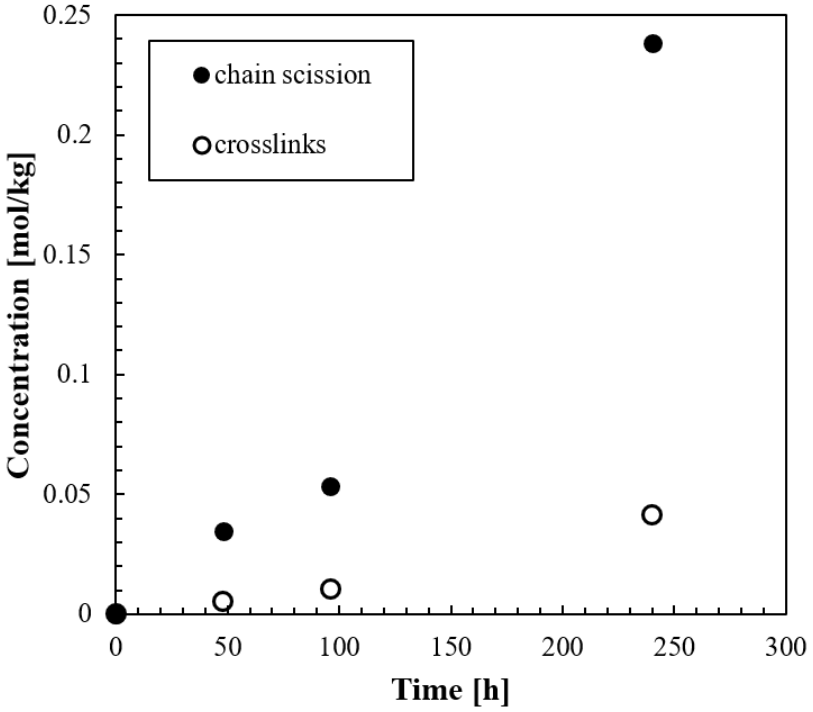

(b) HUV

Figure 4.23: Number of chain scissions and crosslinks per unit mass as a function of UV aging time for: (a) UV-aged, and; (b) HUV-aged LDPE.

instance by gamma irradiation in the case of PE, the same mechanical trends are typically observed [102], but with a totally different physico-chemical scenario. Indeed, it appears clearly that branching disfavors cavitation during yielding and is not favorable to ductility. It should be emphasized the strong increase in yield stress (+25%) for a small concentration of chemical crosslinks $\approx 10^{-2}$mol/kg, in comparison with the concentration of entanglement crosslinks $\approx 40x10^{-2}$mol/kg (see Fig. 2 in [102]).

Neither of these scenarios is applicable to the low density polyethylene studied here. Although a chain scission process is predominant, it causes practically no change in the crystallinity ratio or in the thickness of primary lamellae in the early hours of aging (see Fig. 2.15, 2.16 and 2.29). As a consequence, the first scenario cannot be retained. However, crosslinking is not totally negligible because it prevents chemi-crystallization. Indeed, instead of an increase in the thickness of primary lamellae, we observe clearly the formation of secondary lamellae (see Fig. 2.15 and 4.24). It should be emphasized that, due to its low sensitivity, DSC allows to detect only the largest secondary lamellae. The melting endotherms of thinner lamellae are probably hidden in the decreasing baseline of DSC endotherms (between 20 and 50 °C). Therefore, the population of these new small crystals should be far from negligible.

Recall the evolution of lamellar thickness with aging shown in Fig. 2.16. The thickness of primary crystals remains overall constant during aging while that of secondary crystals, l_c, reaches a local maximum at 48 h. This results in a higher reduction of the interlamellar space, further restraining chain mobility. When l_c reaches a maximum at 48 h so does the flow stress in films (Fig. 3.4a), thus, supporting the premise that the transient UV-induced strengthening is a consequence of chemi-crystallization.

In the plates, the increase in l_c at 48 h leads to an increase in flow stress (Fig. 3.7), but this does not correspond to the maximum flow stress observed, which occurred between 96 and 192 h. This delay on the transient strengthening in aged plates is presumably due to the thickness of the oxidation layer (TOL) not being large enough after 48 h of aging to produce such a strengthening effect on the response of the whole plate. Instead, the

maximum was observed between 96 and 192 h where the TOL is probably large enough to increase the strength on the overall response of the plate, accompanied, additionally, by the overall increase in crystallinity observed at this aging times (as shown in Fig. 2.29).

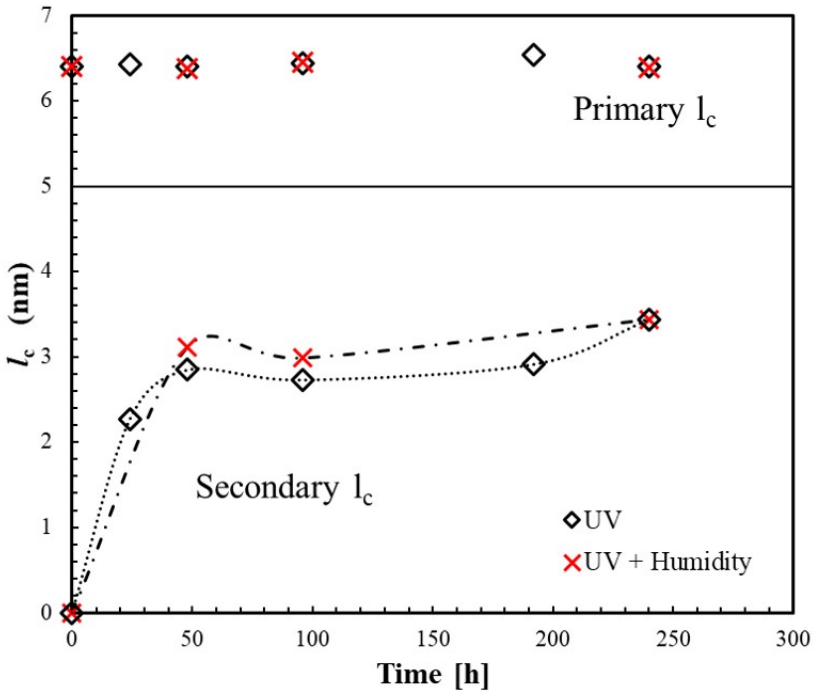

Figure 4.24: Lamellar thickness of primary and secondary crystals versus aging time for UV and HUV aging; see equation (2.3). Dashed lines are included to guide the eye.

Given that crosslinking has an important impact on mechanical properties, a new scenario is advanced whereby new small crystals act as chemical crosslinks. The free chain segments generated by chain scission are presumed to crystallize instantly, thus, the expected adverse effect of chain scission on the mechanical response of the material is not observed in the 24-48 h aging range for films, or in the 96-192 h range in plates, as expected due to DLO. The crystallites resulting from chain scission and its consequent chemi-crystallization behave like crosslinks, resulting in the observed strengthening at intermediate UV doses. Since the effect of the thin crystallites is similar to an increased entanglement density, they also affect

the large strain response of the material [141], as observed in Fig. 3.4 and 3.8, where the strain hardening increases at intermediate UV doses. The effect of secondary crystals can be synergistic with the concurrent oxidation-induced crosslinking, as estimated in Fig. 4.23.

Evidently, the translation of the resulting small increase in crystallinity ratio into an equivalent concentration in chemical crosslinks remains a conceptual issue. One way to investigate the validity of this scenario would consist of conducting mechanical tests above the melting point of secondary lamellae. Indeed, the mechanical behavior should remain unchanged between the pristine and aged materials.

As UV radiation increases further (48-96 h range in films, 96-192 h in plates), the chemi-crystallization stops, and thus, the adverse effect of chain scission becomes evident, as it becomes all the more dominant (Fig. 4.23). The overall decrease in the molecular weight (Fig. 2.14) is such that after 96 hours of exposure it has already decreased by $\sim 70\%$, from $M_w = 164.500\ g/mol$ to just $M_w = 47.000\ g/mol$. This effectively counteracts any strengthening effect of chain scission (by way of chemi-crystallization) or crosslinking in films, contributing to the weakening observed in Fig. 3.4 and Fig. 3.5. The decrease in strain hardening observed beyond 96 h of aging is attributed to the lower density of network entanglements [141] that results from a lower molecular weight. Moreover, the predominance of chain scission on the later stages of oxidation lead to formation of what we have referred to as "chemical cracks" (see section 2.3.2), further contributing to the weakening of the material.

In the specific case of the plates, consider again the role of diffusion limited oxidation and TOL: recall that in plates, the strong decrease in M_w at 96 h noted above is constrained to the oxidation layer and combined with the presence of the pristine core as well as an increased percent crystallinity (Fig. 2.15b) that leads to strengthening between 96 and 192 h. Beyond 192 h, the even higher chain scission, which now affects a presumably larger portion of the plate, summed to the increased chemical damage (highly cracked surface of Fig. 2.20) is such that results in weakening of the plates.

4.2.3 Chemical Stress Model

The transient strengthening effect due to chemi-crystallization contrasts with other phenomena that weaken the polymer response, namely chemical cracking and cavitation. In section 2.3.2 we showed that photo-oxidation results in cracking in the absence of mechanical loading, with chemical cracks occurring along the transverse direction (TD) in films (Fig. 2.17, 2.18), and in an polygonal array in plates (Fig. 2.20, 2.32, 2.35).

In Chapter 2 the appearance of "chemical cracks" in the absence of mechanical loading was attributed to a "chemical stress" [115], which is a residual stress related to the chemical reactions of oxidation. This residual stress may originate on volume change that is concurrent with the thickening of the oxidized layer, or in density gradients due to chemi-crystallization. The pattern of these chemical cracks in films and plates is related to their macromolecular orientation and the changes in their morphology. The estimated critical chemical stress for surface cracking and channeling in LDPE films, are ∼110 MPa and ∼150 MPa, respectively. Compared with the flow stress of LDPE films, the estimated value for surface cracking is large enough to produce local cracking. For plates, the estimated critical chemical stress for surface cracking was ∼65 MPa, also sufficient to produce local cracking if we compare it with the flow stress of the plates. The observed chemical cracks, together with the results from DSC for lamellar thickness of primary and secondary crystalline regions (Fig. 2.16) lead us to presume that the new interlamellar thickness l_{a1} (Fig. 2.19b), falls below the critical interlamellar thickness established by Fayolle et al. for polyethylene $l_{ac} = 6\ \mu$m [1,37], below which a sharp ductile to brittle transition occurs. Finally, these oxidation-induced cracks contribute to the weakening observed at larger UV doses and the observed lower ductility.

4.2.4 Chemo-mechanical Aspects

In Chapter 2 and the previous section the formation of chemical cracks was rationalized on the basis of a chemical stress concept and their pattern based on processing history combined with radiation induced morphological changes.

In addition, the type of damage observed in mechanically loaded specimens post aging demonstrates other aspects of coupling between chemistry and mechanics in oxidative embrittlement. While extensive damage and cracking were observed in aged film and plates specimens (Figs. 4.2, 4.3, 4.11, 4.13, 4.16 and 4.19), no trace of damage was seen in the highly ductile unaged films (see Fig. 4.1a), and just a small amount was observed on the equally ductile pristine plates.

That no cavitation is observed in the tensile deformation of LDPE is certainly in keeping with the literature [30]. However, the present investigation clearly shows that UV irradiation activates the cavitation process. To our knowledge, this is the first report of cavitation in UV-exposed LDPE.

The formation of cavities upon deformation in semicrystalline polymers is believed to depend on the relationship between the strength of the crystalline phase and the strength of the amorphous phase: a strong crystalline region and/or weak amorphous phases promote cavitation since these conditions favor the deformation of the amorphous phase over the plastic deformation of crystalline regions [29]. Taking this into account, photo-oxidation presumably promotes the observed cavitation by: i) providing nucleation sites for voids since it creates surface defects and chemical cracks as observed in the post-aging micrographs (Fig. 2.17, 2.18, 2.20, 2.32, 2.35); ii) forming secondary crystals which increase the stress necessary for the deformation of crystalline regions (Fig. 2.16 and 4.24), and; iii) reducing the molecular weight, thus weakening the amorphous region by decreasing its density of entanglements (Fig. 2.14 and 2.27).

Our observations in UV irradiated LDPE reveal the formation of cavities at multiple scales and in various shapes. Some rather large elongated, probably coalesced microcracks were shown in Figs. 4.2 and 4.3. Fig.4.25 shows instances of smaller craze-like voids in the 96 h UV-aged specimen. The presence of various void sizes hints at a continuous void formation process.

In films, interestingly, the “chemical cracks” observed in heavily irradiated specimens are

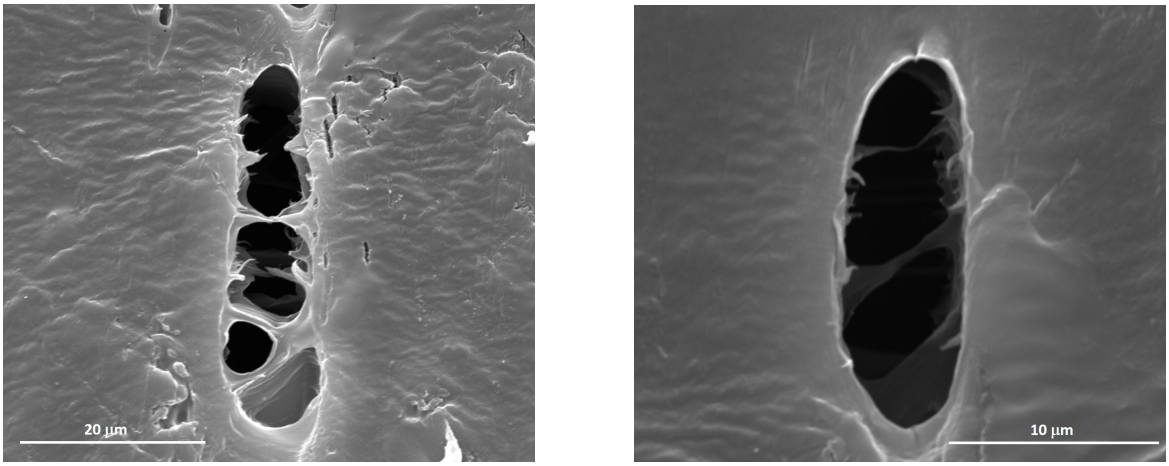

(a) (b)

Figure 4.25: SEM micrographs of well developed craze-like voids beneath the fracture of a 96 h specimen.

oriented along the transverse direction (Fig. 2.18) whereas the mechanically induced ones are mostly parallel to the loading (machine) direction (Figs. 4.2 and 4.3). Recall that films with the type of chemical cracks in Fig. 2.18 had essentially zero ductility. On the other hand, for moderately irradiated films, cavities are favored by profuse chain scissions then grow plastically upon further drawing and align themselves with the loading direction. Some of the elongated cavities are several hundreds of microns long as a result of coalescence in "columns".

The absence of cavitation damage does not prevent failure in the pristine material, but the latter is induced by some macroscopic shear band, as manifested in the slant fracture mode in Fig. 4.1 and 4.4. In aged films specimens, the terminal event also seems to be a (macro) shear band although both chemical and mechanical damage must play a role in causing premature instability.

The chemo-mechanical coupling in oxidative embrittlement is also demonstrated by the disparity of the stiffness measured by nanoindentation and tensile tests. Recall that the tensile data showed a relatively stable stiffness of the plates with UV aging, in apparent conflict with the data from nanoindentation, which indicated that at least one quarter of the

whole sample ($\sim$ 500 μm) has a higher modulus after 96 h of aging. One would expect this to result in a higher modulus in the macro response, albeit of smaller magnitude than the one observed on the plate's surface.

Assessment of the structural integrity of the plates post-aging via fractography (Figure 3.13) revealed an oxidation layer of similar magnitude to that suggested by the onset of modulus increase in the nanoindentation results (Figure 3.11). In this layer, we can distinguish how the cracks in the surface propagate into the material until they seem to be arrested within the oxidized region. These cracks revealed in SEM negatively affect the mechanical response of the material, compromising its load capacity and stiffness. Hence, the apparent discrepancy between the stiffness variation with UV in tension and nanoindentation can be interpreted as follows: In nanoindentation, the probed volume is small, falling in between the microcracks; thus, the increased modulus observed in nanoindentation may be due to oxidation-induced crosslinking and chemi-crystallization. When these results are compared to those obtained by tensile testing, one must consider that in tensile testing, the modulus measurement delivers a net value that is affected by the profuse microcracking observed, which is also a product of the oxidation. One could then conclude that the observed difference between the macro and nano response is basically a size effect.

It is worth noting in closing that the chemically induced damage leads, through cavitation, to dilatation and probably pressure sensitivity of plastic flow. Indeed, the tensile deformation of aged LDPE films is not volume-preserving, contrary to what has been claimed in the literature for LDPE and other low crystallinity polymers [30].

4.2.5 Correlation between Natural and Accelerated Aging

Accelerated aging experiments are commonplace in oxidation studies of polymers. However, whether oxidation chemistry can be accelerated without additional complexities (e.g., DLO) and predictions can directly be made from accelerated experiments is not yet settled [40, 99]. Thus, when studying accelerated aging, it is necessary to consider all relevant aspects that can indicate an alteration of the aging pathways.

In this context, we look at the results obtained from natural aging and compare them with the accelerated aging results. The comparison of the mechanical response of these materials was made in Chapter 3, and the results are summarized in Fig. 4.26. We observed that a connection can be made between certain HUV and natural aging conditions, namely: the response of the 48 h HUV film corresponded to the response of the 1 month naturally aged film, while the 96 h HUV-aged film corresponded to the average response of the 2 month naturally-aged specimen. In plates, an equivalence was observed between the responses of the 240 h HUV and the 4 months naturally aged plates. The results highlighted the challenge of connecting accelerated and natural aging based solely on estimations of energy received, being the ever-changing natural aging conditions and it associated complexities, the main reason impeding a direct correlation.

Thus, it would be interesting to see if the correlation observed at the macroscopic, mechanical behavior also implies an correlation on the damage process. For this, consider the compared fractography of 96 h HUV and 2 months naturally-aged films in Fig. 4.27 and 4.28. A more thorough analysis would involve damage comparison for all the natural aging conditions that matched an accelerated aging condition; however, not all the cases involved were observed under SEM. The overview of the fracture area in Fig. 4.27 shows that 96 h HUV and 2 months naturally aged films share the same flat fracture mode, which indeed distinguishes them from the 48 h and 96 h UV films, which had a slant fracture (Fig. 4.1). Fig. 4.28a and b show that in both conditions, there is profuse damage under the fracture surface, which in both cases consists of flat cracks perpendicular to the loading direction. A comparison at higher magnification of the area under the fracture surface is made in Fig. 4.28c and d. Compared to its natural-aged counterpart, the cracks in the 96 h HUV condition are more numerous, shorter, and have blunter tips, and more cracks opened up along the deformation direction. Some of these cracks coalesce diagonally. Meanwhile, the cracks of the naturally-aged films are longer, thinner, and have sharper tips. The naturally-aged specimen also exhibits some cracks parallel to the loading direction, connecting horizontal

cracks. Lastly, damage far from the fracture surface is detailed in Fig. 4.28e and f. In this area, the HUV-aged specimen has cracks that are sharper than those close to the fracture surface of Fig. 4.28c and all cracks are perpendicular to the loading direction. The natural counterpart (Fig. 4.28f) exhibits more crack channeling, as indicated by the cracks parallel to the loading direction, leading to coalescence in 90° angles. The blunt, more open cracks near the fracture surface of the 96 h HUV film suggest a slightly more ductile deformation, while in the naturally-aged specimen, the sharper cracks and larger crack channeling suggests a more brittle deformation.

In conclusion, a correlation was observed between 96 h of HUV and 2 months of natural aging. Specimens aged under these conditions showed the same mechanical response and shared similar damage after fracture. Ultimately, these results highlight the importance of humidity in replication natural aging in laboratory accelerated experiments.

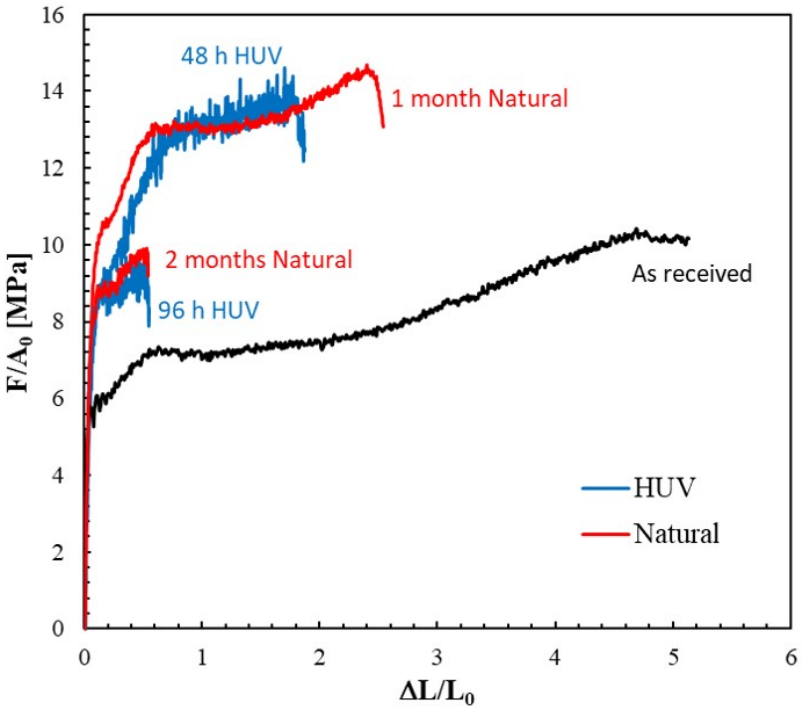

(a)

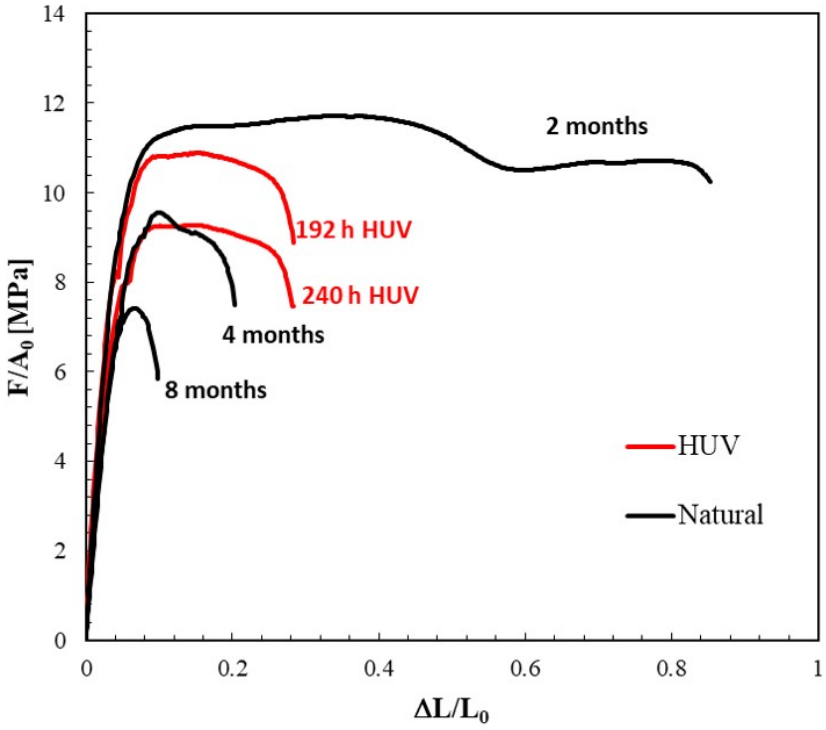

(b)

Figure 4.26: (a) Comparison of engineering stress-strain curves for LDPE films naturally and HUV-aged. (b) Comparison of engineering stress-strain curves for LDPE plates naturally and HUV-aged. All test room temperature and a true axial strain rate of 0.005 s^{-1}.

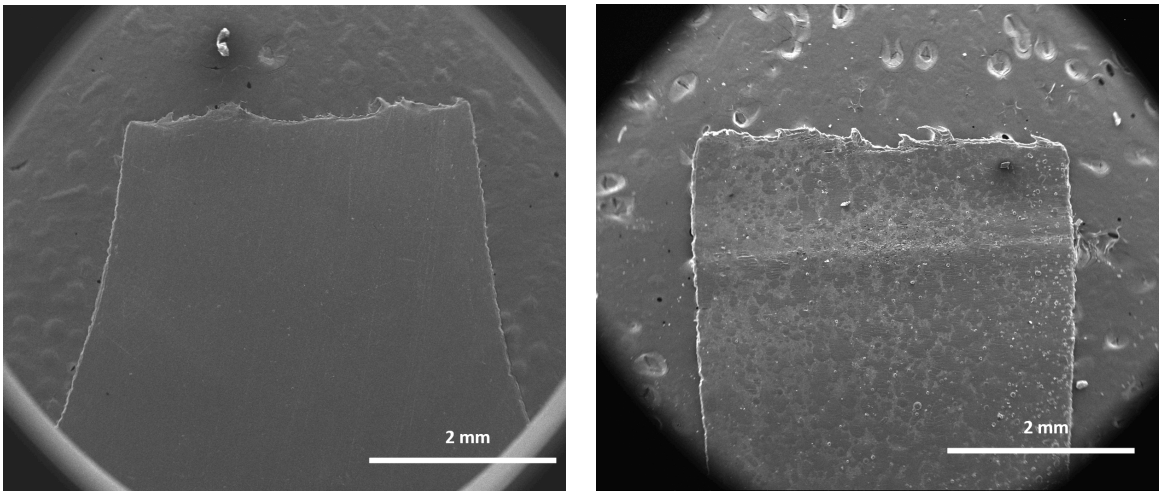

(a) 96h HUV (b) 2 months natural

Figure 4.27: Comparison of the fracture modes of the 96 h HUV-aged films (a) and the 2 months naturally-aged film (b).

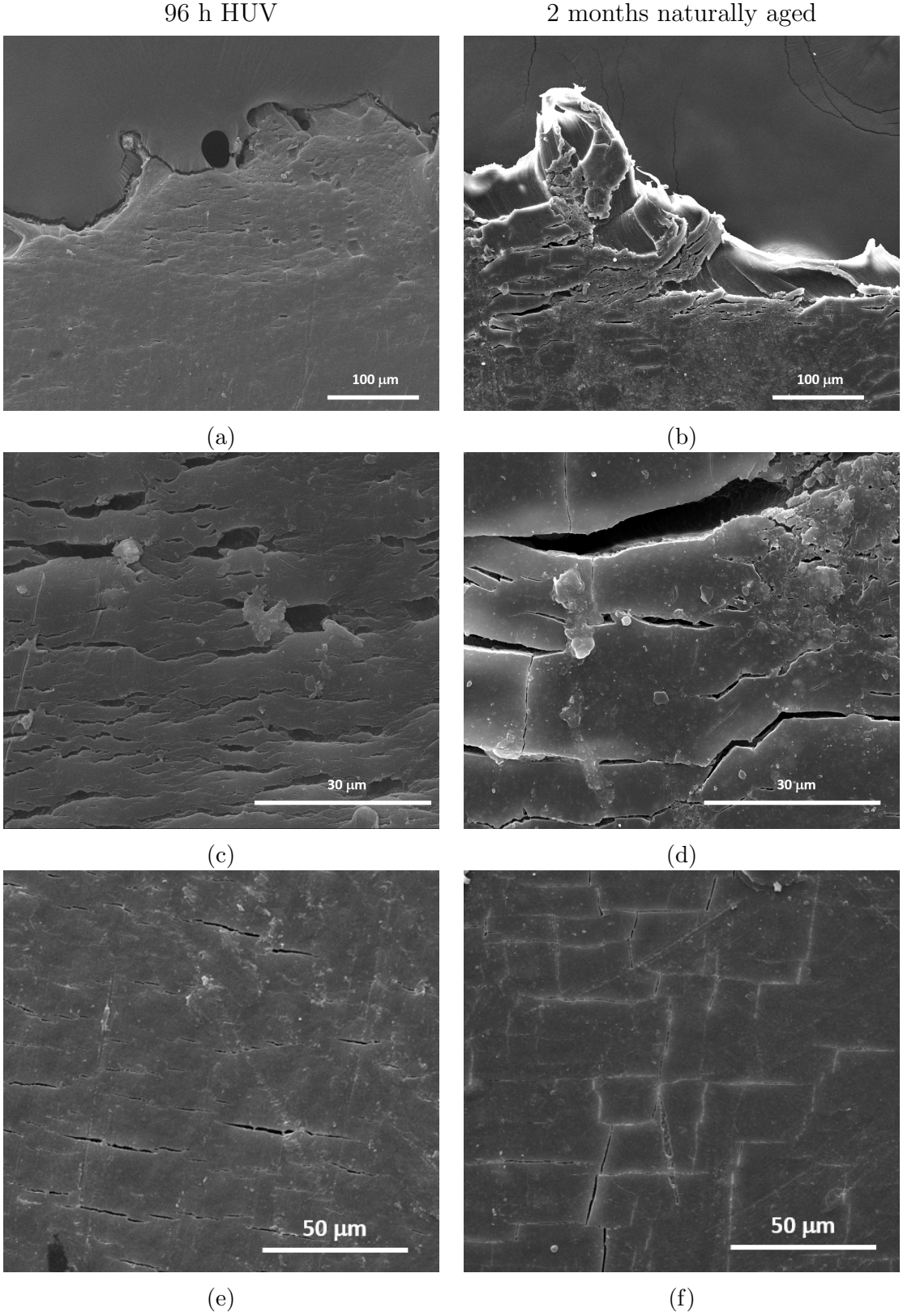

Figure 4.28: Comparison of damage after tensile fracture of films after 96 h of HUV aging and 2 months of natural aging: (a),(b): area under the fracture surface; (c),(d): damage under fracture surface, and; (e),(f) damage away from fracture surface.

5. MODELING

In the previous chapters, the photo-oxidation of a semicrystalline polymer was characterized across various scales. Results indicated that the superficial crack pattern depends on the depth of the oxidation layer relative to the substrate. The extent of the oxidation clearly determines the degree of embrittlement, in addition to the newly discovered phenomenon of transient strengthening.

With this in mind, a modeling strategy is developed here for inverse identification of the thickness of the oxidation layer (TOL). This is attempted by considering an aged plate as a bilayer system whereby: (i) the core is modeled as a pristine plate specimen, and; (ii) TOL is a layer of unknown thickness modeled as an aged film. To model pristine and aged materials, we use the Boyce-Parks-Argon polymer constitutive model modified by Chowdhury et al. [142] to better account for the small strain behavior. The model has many material parameters. The first step consists of identifying these parameters for pristine and aged materials through "inverse identification". In this process, the experimental specimens (see Chapter 3 are modeled by means of the finite element method and an advanced constitutive polymer model. The mechanical response of each specimen is then simulated, the response obtained is compared with the experimental one, and the material parameters are updated accordingly. This process is repeated until the best fit is achieved.

The results obtained are discussed in light of the experimental observations, and an assessment is made of the effectiveness of both the modeling strategy and the experimental methods for determining TOL in oxidized bulk polymers. In passing, we examine possible structural effects on the unaged films and plates through modeling.

5.1 Experimental Data

The calibration of the macromolecular model requires experimental data under several loading conditions. Calibration of rate sensitivity is particularly important for modeling

semicrystalline polymers as their flow stress, low strain hardening, and the initial modulus are highly dependent on deformation rate [143, 144]. For the rate sensitivity experiments, tensile specimens of as-received films and plates were cut out according to the geometries displayed in Fig. 5.1. Tensile tests were conducted at room temperature and a *true* axial strain rate of 0.1, 0.01, 0.005 and 0.001 s^{-1}.

Fig. 5.2 shows the effect of strain rate on film and plate specimens. The increase in flow stress with increasing strain rate occurs because faster rates provide lesser time to the polymeric chains to accommodate deformation at the molecular level, resulting in stiffer macromolecules [145]. Additionally, the post-yield softening becomes more pronounced with increasing strain rate. This effect is exacerbated in the plates. This can be related to the "self-heating" effect at high strain rate which is well documented to occur on polymers. Adiabatic conditions are reached at strain rates >0.01 s^{-1}, resulting in important thermal softening [146, 147]. The self-heating effect is more evident in bulk than in films because the strain rate at which the transition from isothermal to adiabatic conditions occurs in polymers decreases with increasing thickness [148].

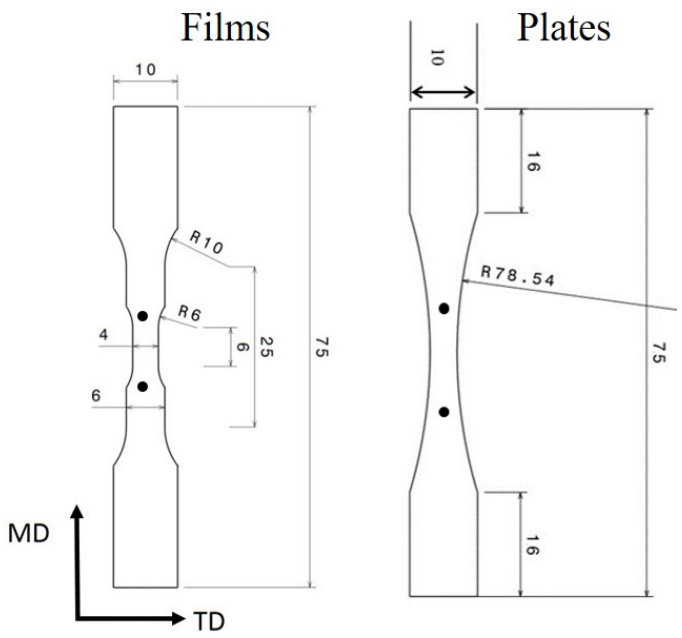

Figure 5.1: Tensile specimen geometries for films and plates (dimensions in mm). The dots mark the locations of the laser extensometer trackers.

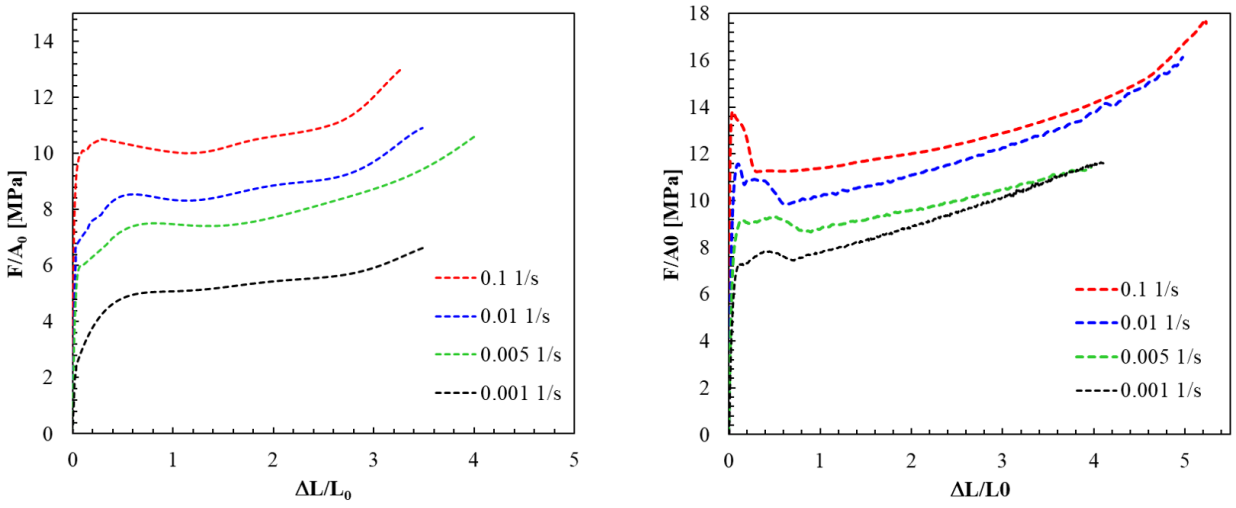

Figure 5.2: Nominal stress-strain curves for LDPE (a) films, and; (b) plates at room temperature and various true axial strain rates.

5.2 Inverse Identification of Oxidation Layer

The methodology proposed consists in modeling the plate aged after "H" hours as a bilayer system whereby the core is modeled as the pristine plate specimen, and a layer of an unknown thickness (i.e., TOL) is modeled as a UV-aged film, as sketched in Fig. 5.3. The conditions of 192 h and 240 h, for which TOL was experimentally inferred, are used to asses the methodology developed.

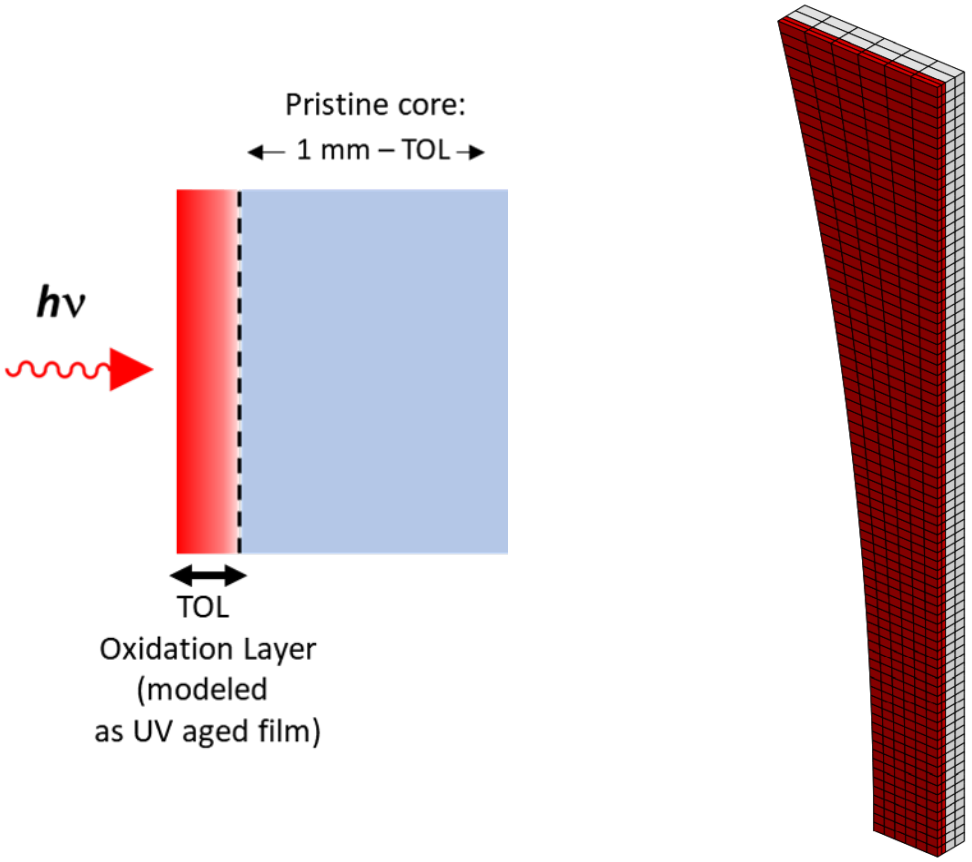

Figure 5.3: (a) Scheme of bilayer system used to model UV-aged plates, where the core is modeled as a pristine plate specimen, and the oxidation layer of an unknown thickness (TOL) is modeled as an aged film. (b) Mesh of the bilayer tensile model, with the oxidation layer in red. In this example, TOL = 0.1 mm and pristine core is 0.9 mm thick.

An initial approach was attempted in which a plate aged for H hours was modeled as a

bilayer system of a pristine core and layer of unknown thickness (TOL) modeled as a film also aged for H hours. This approach implied the following assumptions: (i) the plate material is the same as the film material; (ii) the response of film aged H hours is independent of its thickness, and; (iii) the response of the free-standing film is the same as that of the film on a substrate (core). This method worked well for the 48 h UV-aged plate. However, it did not work for any other plate aged for $H > 48$ h, as the rapid degradation of films aged for $H > 48$ h, results in a weak response that does not correspond to the hardening observed in UV-aged plates at $H = 48$ h–192 h.

At any rate, a second approach is proposed whereby a plate aged for H hours is modeled as a bilayer system of a pristine core and layer of unknown thickness modeled as the film also aged for 48 h. The 48 h aged film can be assumed to better represent the plasticity of the oxidation layers of all the aged plates since the effective response of films at $H >$48 h is affected by profuse damage-induced weakening, which the constitutive model used does not account for. Additional assumptions are: (i) the plate material is the same as the film material, and; (ii) the response of the free-standing film is the same as that of the film on a substrate. Note that the tensile model of Fig. 5.3 remains valid for this approach.

5.2.1 Constitutive Model

The macromolecular model implemented by Kweon and Benzerga [72] is employed here to depict the mechanical behavior of pristine and aged LDPE films and plates. The same is based on the Boyce-Arruda model, which combines the viscoplastic law based on the double-kink theory proposed by Argon [68] with a full chain network model based on rubber elasticity aimed at modeling the large strain hardening of glassy polymers [22, 149]. A back stress is typically introduced that represents the plastic resistance caused by molecular orientation during stretching. Enhanced orientation hardening was introduced by Wu and Van Der Giessen. [70] by combining both the 3-chain and 8-chain models from [22, 149]. Chowdhury et al. [142] modified the model to better account for the small strain behavior by implementing an implicit update of the back stress to independently model pre-peak

hardening and post-peak softening, characteristic of glassy polymers[1].

5.2.1.1 Constitutive Equations and Evolution Laws

The model assumes the following multiplicative decomposition of the deformation gradient, which is represented in the sketch of Fig. 5.4:

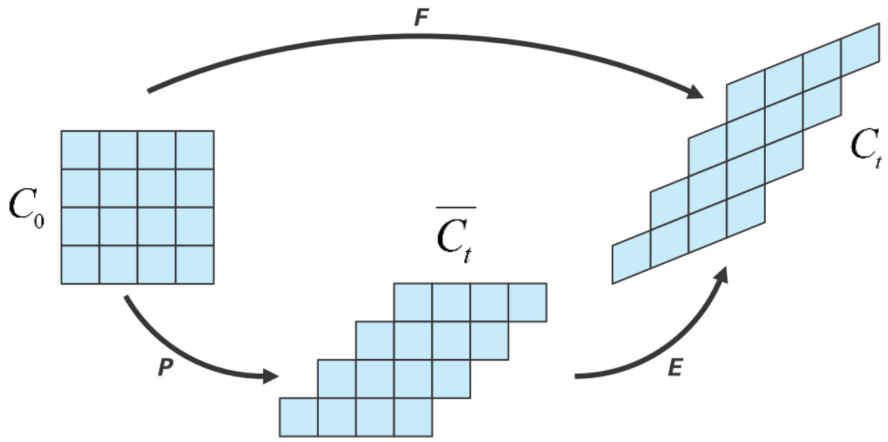

Figure 5.4: Multiplicative decomposition of the deformation gradient

$$\boldsymbol{F} = \boldsymbol{E}\boldsymbol{P} \tag{5.1}$$

The velocity gradient $\boldsymbol{L}$ is given by:

$$\boldsymbol{L} = \dot{\boldsymbol{F}}\boldsymbol{F}^{-1} = \boldsymbol{L}^e + \boldsymbol{E}\boldsymbol{L}^p\boldsymbol{E}^{-1} \tag{5.2}$$

with

$$\boldsymbol{L}^e = \dot{\boldsymbol{E}}\boldsymbol{E}^{-1} \quad \text{and} \quad \boldsymbol{L}^p = \dot{\boldsymbol{P}}\boldsymbol{P}^{-1} \tag{5.3}$$

[1]Here, the constitutive model is reformulated so as to resolve an objectivity issue with the implementation in [72], which resulted from the constraints of the user-defined routine the authors employed.

so that

$$\dot{\boldsymbol{E}} = \boldsymbol{L}\boldsymbol{E} - \boldsymbol{E}\boldsymbol{L}^{p}$$

The second Piola-Kirchhoff stress tensor $\boldsymbol{\Pi}^{\boldsymbol{e}}$ defined with respect to the intermediate configuration $\overline{C}_t$:

$$\boldsymbol{\Pi}^{\boldsymbol{e}} = J_e \boldsymbol{E}^{-\mathbf{1}} \boldsymbol{\sigma} \boldsymbol{E}^{-T} \tag{5.4}$$

where $J^e = \det \boldsymbol{E}$ and $\boldsymbol{\sigma}$ the Cauchy stress.

The Mandel stress tensor is expressed as:

$$\boldsymbol{M} = J^e \boldsymbol{E}^T \boldsymbol{\sigma} \boldsymbol{E}^{-T} = \boldsymbol{E}^T \boldsymbol{E} \boldsymbol{\Pi}^e \tag{5.5}$$

Defining a projector $\mathbb{P}^{\mu}$ such that $\boldsymbol{M}^{\mu} = \mathbb{P}^{\mu} : \boldsymbol{M}$ with

$$\mathbb{P}^{\mu} = \mathbb{P}^{s} + \mu \mathbb{P}^{ss} \tag{5.6}$$

$\mathbb{P}^s$ and $\mathbb{P}^{ss}$ are projectors linking a tensor to its symmetric and skew-symmetric parts, respectively. Let $\boldsymbol{b}$ be the back-stress and:

$$\boldsymbol{X} = \operatorname{dev}\left(\boldsymbol{M}^{\mu} - \boldsymbol{b}\right) \tag{5.7}$$

where dev indicates the deviatoric part. In Kweon and Benzerga the evolution of $\boldsymbol{b}$, which dictates orientation hardening is expressed as:

$$\overset{\triangledown}{\boldsymbol{b}} = \mathbb{R} : \boldsymbol{D}^{p} \tag{5.8}$$

where $\mathbb{R}$ is expressed as a function of the Cauchy–Green tensor $\boldsymbol{B} = \boldsymbol{F}\boldsymbol{F}^T$.

Here, a convected $\boldsymbol{B}$ is used to express $\mathbb{R}$, leading to:

$$\boldsymbol{B}^e = J^e \boldsymbol{E}^{-1} \boldsymbol{B} \boldsymbol{E}^{-T} = J^e \boldsymbol{E}^{-1} \left(\boldsymbol{E} \boldsymbol{P} \boldsymbol{P}^T \boldsymbol{E}^T \right) \boldsymbol{E}^{-T} = J^e \boldsymbol{P} \boldsymbol{P}^T \tag{5.9}$$

Considering the normality rule with respect to equipotentials such that $X_{eq} = \text{constant}$, One notes that $\boldsymbol{L}^p$ becomes symmetric for $\mu = 0$. The flow rule is defined such that there is incompressible plastic deformation:

$$\boldsymbol{D}^p = \dot{p} \frac{\partial X_{eq}}{\partial \boldsymbol{M}} = \frac{3}{2} \dot{p} \frac{\partial \boldsymbol{X}}{\partial X_{eq}} : \mathbb{P}^{\mu} \tag{5.10}$$

where the subscript "$_{eq}$" denotes the von Mises invariant. A viscoplastic law accounts for the effects of strain rate by defining the effective plastic strain rate as:

$$\dot{p} = \dot{p}_0 \exp \left[-\frac{A(s - 3\alpha M_m)}{T} \left(1 - \left(\frac{X_{\text{eq}}}{s - 3\alpha M_m} \right)^m \right) \right] \tag{5.11}$$

In order to avoid a strain rate "jump" at $X_{\text{eq}} = 0$ the previous equation was replaced by:

$$\dot{p} = \dot{p}_0 \exp \left(-\frac{A(s - 3\alpha M_m)}{T} \right) \sinh \left(\frac{A(s - 3\alpha M_m)}{T} \left(\frac{X_{\text{eq}}}{s - 3\alpha M_m} \right)^m \right) \tag{5.12}$$

with A, $\dot{p}_0$ and m being material parameters that control the rate dependence, α accounts for the pressure sensitivity, T is the absolute temperature, and $M_m = \frac{1}{3}\text{tr}(\boldsymbol{M})$. While the exponent m is taken in the original macromolecular model proposed by Boyce and Arruda [22] as $m = 5/6$ (following Argon's derivation [68]); it is taken here as a free material parameter in accordance with Kweon and Benzerga's approach [72].

Strain softening is included by the state variable s, a micro-scale athermal shear strength. In the original macromolecular model by Boyce et al. [22], the evolution of s led to a sharp yield. Chowdhury et al. [71] modified the evolution of s to better account for the small strain behavior and to independently model pre-peak hardening and post-peak softening of polymers. Thus, the evolution law of s is:

$$\dot{s} = \left(H_1 \left(1 - \frac{s}{s_1} \right) + H_2 \left(1 - \frac{s}{s_2} \right) \right) \dot{p} \tag{5.13}$$

with s_1 and s_2 being adjustable parameters and H_1 and H_2 functions given by:

$$H_1 = -h_1(\tanh((p - \overline{p})/(f\overline{p})) - 1) \tag{5.14}$$

$$H_2 = \quad h_2(\tanh((p - \overline{p})/(f\overline{p})) + 1) \tag{5.15}$$

Recall that the evolution of the back-stress $\boldsymbol{b}$ was given by $\overset{\nabla}{\boldsymbol{b}} = \mathbb{R} : \boldsymbol{D}^p$. The $\mathbb{R}$ tensor is a fourth order tensor specified by a non-Gaussian network model [150] that includes both the three-chain rubber elasticity model [22] and the eight-chain model [69]:

$$\mathbb{R} = (1 - \kappa)\mathbb{R}^3 + \kappa\mathbb{R}^8 \tag{5.16}$$

with

$$\kappa = 0.85\overline{\lambda}/\sqrt{N} \text{ and } \overline{\lambda} = \max_{I=1,2,3} \lambda_I.$$

N is a material constant that represents the average number of links between entanglements, and is related to the molecular weight of the material. $\overline{\lambda}$ is the maximum principal stretch. $\mathbb{R}^8$ and $\mathbb{R}^3$ are given by:

$$\mathbb{R}^8 = \frac{1}{3} C_R \sqrt{N} \left[\frac{1}{B_{kk}} \left(\frac{\xi_c}{\sqrt{N}} - \frac{\beta_c}{\lambda_c} \right) \boldsymbol{B} \otimes \boldsymbol{B} + \frac{\beta_c}{\lambda_c} \left(\boldsymbol{I} \overline{\otimes} \boldsymbol{B} + \boldsymbol{B} \overline{\otimes} \boldsymbol{I} \right) \right] \tag{5.17}$$

where C^R is the rubbery modulus, a material constant and:

$$\lambda_c^2 = \frac{1}{3} \mathrm{tr} \boldsymbol{B} \tag{5.18}$$

$$\beta_c = \mathcal{L}^{-1} \left(\frac{\lambda_c}{\sqrt{N}} \right) \tag{5.19}$$

$$\xi_c = \frac{\beta_c^2}{1 - \beta_c^2 / \sinh^2(\beta_c)} \tag{5.20}$$

with $\mathcal{L}^{-1}$ being the inverse of the Langevin function, which is estimated using a Padé approximation.

The calculation of $\mathbb{R}^3$ is less straightforward. Let $\lambda_{I=1,2,3}$ be the eigenvalues of $\boldsymbol{B}^{1/2}$ and $\vec{e}_{I=1,2,3}$ the corresponding eigenvectors. $\mathbb{R}^3$ is computed as:

$$\mathbb{R}^3_{IJKL} = \mathcal{K}(\lambda_I, \lambda_J)\left(\delta_{IK}\delta_{JL} + \delta_{IL}\delta_{JK}\right) \tag{5.21}$$

By using this definition, $\mathbb{R}^3$ is expressed in the eigenframe. Therefore it needs to be rotated as: $(\boldsymbol{R}\otimes\boldsymbol{R}) : \mathbb{R}^3 : (\boldsymbol{R}^T\otimes\boldsymbol{R}^T)$ where $\boldsymbol{R}$ is the rotation tensor between the eigenframe and the reference frame.

If $\lambda_I \neq \lambda_J$, $\mathcal{K}(\lambda_I, \lambda_J)$ is given by :

$$\mathcal{K}(\lambda_I, \lambda_J) = \frac{1}{6}C_R\sqrt{N}\frac{\lambda_I^2 + \lambda_J^2}{\lambda_I^2 - \lambda_J^2}(\lambda_I\beta_I - \lambda_J\beta_J) \tag{5.22}$$

If $\lambda_I = \lambda_J = \lambda$, $\mathcal{K}(\lambda_I, \lambda_J)$ is given by :

$$\mathcal{K}(\lambda_I, \lambda_J) = \frac{1}{6}C_R\sqrt{N}\lambda^2\left(\frac{\xi}{\sqrt{N}} + \frac{\beta}{\lambda}\right) \tag{5.23}$$

with

$$\beta = \mathcal{L}^{-1}\left(\frac{\lambda}{\sqrt{N}}\right) \quad \text{and} \quad \xi = \frac{\beta^2}{1 - \beta^2/\sinh^2(\beta)} \tag{5.24}$$

5.2.1.2 Implicit Time Integration

The constitutive model described in the previous section was implemented in the FEM software Z-set. The state variables to be integrated are: $\boldsymbol{E}$, $\boldsymbol{b}$, p and s. Their evolution laws

are given by:

$$\dot{\boldsymbol{E}} = \boldsymbol{L}F - \dot{p}F\boldsymbol{n}^{\mu} \tag{5.25}$$

$$\dot{\boldsymbol{b}} = \mathbb{R} : \boldsymbol{D}^{p} = \dot{p}\mathbb{R} : \boldsymbol{n}^{\mu} \tag{5.26}$$

$$\dot{p} = E(s, M_m)G(s, M_m, X_{\text{eq}}) \tag{5.27}$$

$$\dot{s} = \left(H_1\left(1 - \frac{s}{s_1}\right) + H_2\left(1 - \frac{s}{s_2}\right)\right)\dot{p} \tag{5.28}$$

with

$$G(s, M_m) = \dot{p}_0 \exp\left(-\frac{A(s - 3\alpha M_m)}{T}\right)$$

and

$$F(s, M_m, X_{\text{eq}}) = F_x\left(\frac{A(s - 3\alpha M_m)}{T}\left(\frac{X_{\text{eq}}}{s - 3\alpha M_m}\right)^{m}\right)$$

with $F_x(.) = \sinh(.)$ or $G_x(.) = \exp(.)$. H_1 and H_2 are given by:

$$H_1 = -h_1(\tanh((p - \overline{p})/(f\overline{p})) - 1) \tag{5.29}$$

$$H_2 = h_2(\tanh((p - \overline{p})/(f\overline{p})) + 1) \tag{5.30}$$

The derivatives used are detailed in Appendix B. Time discretization leads to the following sets of equations which are solved with respect to the increments ($\mathbf{V}_S = \Delta\boldsymbol{E}$, $\Delta\boldsymbol{b}$, Δp and Δs) of the state variables over a time step Δt using the Newton-Raphson method:

$$\mathbb{R}_E = \Delta\boldsymbol{E} - \Delta F\boldsymbol{F}^{-1}E + \Delta p\boldsymbol{E}\boldsymbol{n}^{\mu} \tag{5.31}$$

$$\mathbb{R}_b = \Delta\boldsymbol{b} - \Delta p\mathbb{R} : \boldsymbol{n}^{\mu} \tag{5.32}$$

$$R_p = \Delta p - E(s, M_m)F(s, M_m, X_{\text{eq}})\Delta t \tag{5.33}$$

$$R_s = \Delta s - \left(H_1\left(1 - \frac{s}{s_1}\right) + H_2\left(1 - \frac{s}{s_2}\right)\right)\Delta p \tag{5.34}$$

Finally, the consistent tangent matrix is calculated to improve convergence:

$$\underline{\mathbb{L}^c} = \partial\boldsymbol{\sigma}/\partial\boldsymbol{E} \tag{5.35}$$

More details of the matrix calculation are presented in Appendix B.

5.2.2 Finite Element Models

The macromolecular model described in the previous section was implemented on Z-Set, a FEM software developed by ONERA and MINES ParisTech. The tensile specimen geometries used for film and plates were replicated as finite element models and are described below.

5.2.2.1 Film Tensile Model

Fig. 5.5 shows the finite element mesh and boundary conditions utilized to model the tensile deformation of the film specimens. One quarter of the tensile specimen is modeled, taking advantage of the two planes of symmetry to reduce computational cost. Additionally, the grip area of the specimen is also omitted for the same purpose. Since only one half of the total length is modeled, the displacement rate applied to the model is one half ($\dot{\delta}/2$) of the axial displacement rate applied on experiments ($\dot{\delta}$), as shown in Fig. 5.5. The mesh is composed of C3D20R elements, which are quadratic brick elements with reduced integration. The latter was preferred over full integration elements to avoid possible volume locking issues [151]. The mesh, selected after a mesh convergence study, has 208 elements and 1739 nodes and is refined in the gauge section. In order to emulate the experimental conditions, the deformation output is measured at the same height where the laser extensometer reflective tape was placed during the experiments. The force was taken as the sum of the reaction forces across the top nodes. Lastly, nominal stress (F/A_0) and strain ($\Delta L/L_0$) curves were used to compare modeling and experimental data.

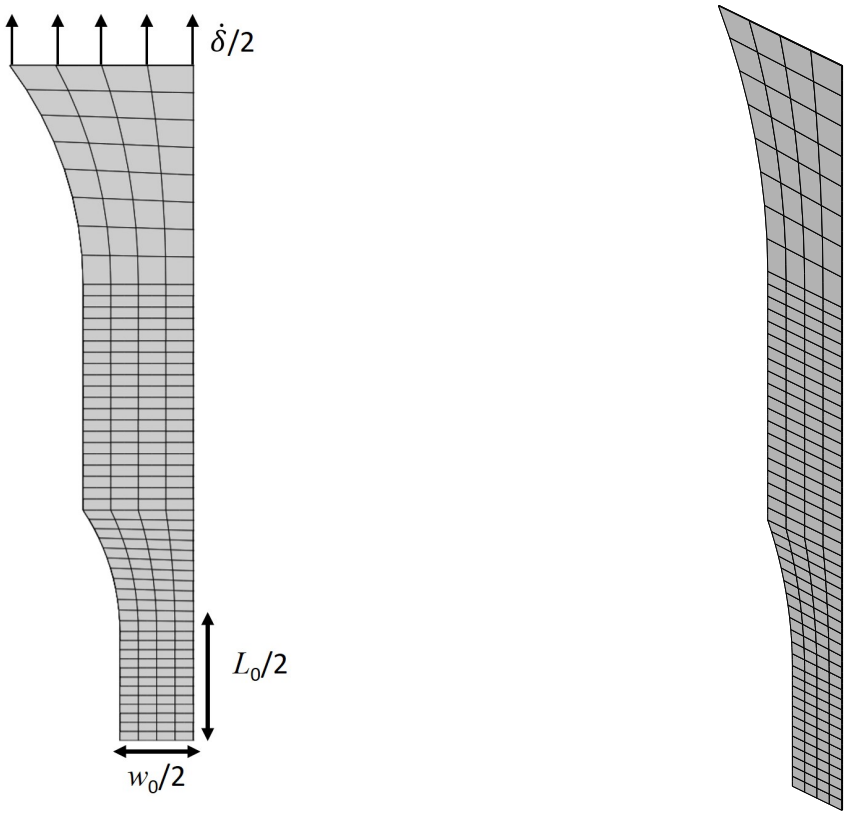

Figure 5.5: Finite element mesh of the film tensile model used for optimization and boundary conditions applied.

5.2.2.2 Plate Tensile Model

The finite element mesh and boundary conditions used to model the tensile deformation of the plates are shown in Fig. 5.6. Only one quarter of the specimen geometry is modeled, and the grip section is not included to reduce computational cost. The displacement rate applied to the model is one half ($\dot{\delta}/2$) of the axial displacement rate applied during the experiments ($\dot{\delta}$). The mesh was selected after a mesh convergence study and is composed of 1920 C3D20R elements and 10333 nodes. The mesh is refined in the gauge section. The deformation output is calculated at the same height where the laser extensometer reflective tape was placed during the experiments in order to replicate the experimental conditions. The force was taken as the sum of the reaction forces across the top nodes. Nominal stress (F/A_0) and strain ($\Delta L/L_0$) curves were used to compare modeling and experimental data.

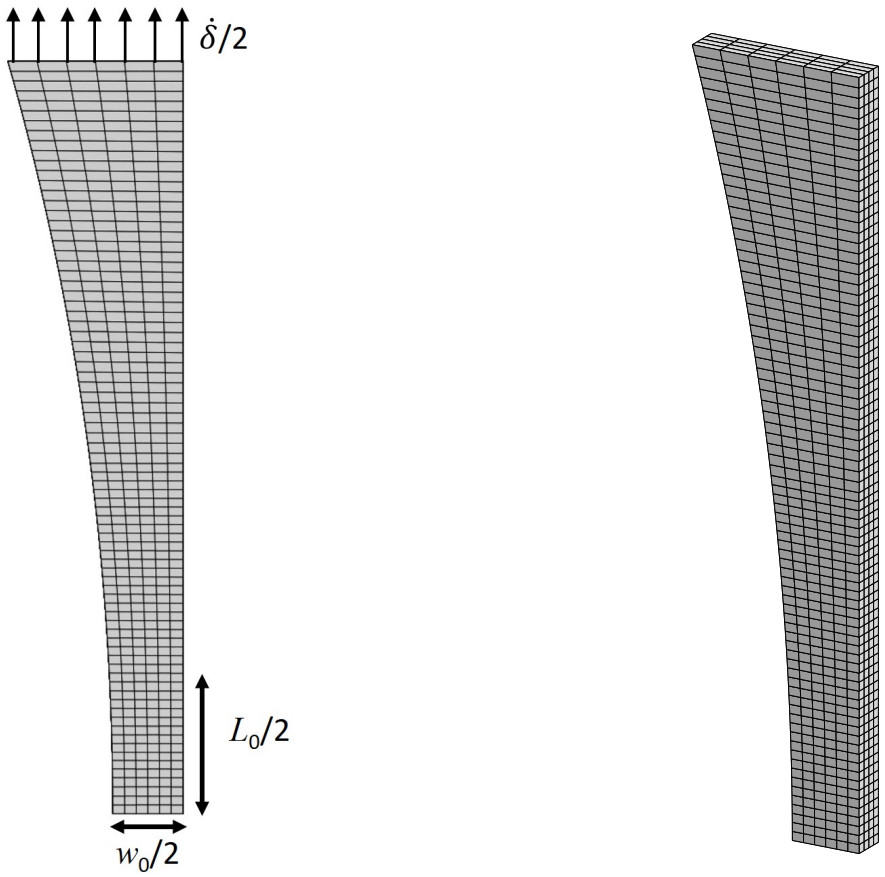

Figure 5.6: Finite element mesh of the plate tensile model used for optimization and boundary conditions applied.

5.2.3 Model Calibration

Fourteen material parameters enter the macromolecular model described in section 5.2.1. These parameters account for the various features of the mechanical behavior of a polymer: the elastic constants E and ν; small-strain hardening/softening parameters s_0, s_1, s_2 and h_1, h_2, f, $\bar{p}$, rate-sensitivity parameters A, m and $\dot{p_0}$; pressure-sensitivity parameter α; rubbery modulus C^R and number of links between entanglements N.

Consider that pristine and aged LDPE are, technically, no longer the same material, i.e., while they still share the main chemical structure of PE, their molecular weight, crystallinity, morphology, surface finish, and by consequence, their mechanical behavior, are no longer the

same due to aging. Therefore, and given that the macromolecular model as it stands, does not take aging damage into account, different sets of material parameters are necessary to describe pristine and aged materials. Accordingly, two main model calibrations were performed: (i) a first calibration where the material parameters of pristine films and plates are identified, and; (ii) a second calibration concerned with the material parameters of the UV-aged-films.

The calibrations were done through optimization or inverse parameter identification, using the optimization module of the Z-Set FEM software. Specifically, we used the Nelder-Mead optimization algorithm available in Z-set. The optimizer works by evaluating and minimizing an error function defined as the weighted sum of objective functions, which are given by comparing simulation results and a reference. In this case, the optimizer takes an initial set of parameters and simulates the mechanical response of the material using the macromolecular model. This response is compared with the experimental data recorded for the same loading conditions. This is done iteratively until convergence is achieved. The set of parameters that produces the best fit between simulation and experiments, i.e., the one resulting in the minimum error function value, is taken to represent the behavior of the material. A diagram of this process is shown in Fig. 5.7.

In order to reduce the number of parameters that enter the calibration process by optimization, and thus, decrease the computational cost of the same, some parameters were fixed. An effective modulus was obtained from the initial slope of the experimental tensile results. For pristine films an effective $E_{films} = 150.0$ MPa was used. On the other hand, the effective modulus of plates was affected by strain rate, so different effective modulus were used for different strain rate condition, as listed in Table 5.2. The Poisson's ratio for LDPE, ν, was taken as 0.4 [152]. For the determination of the pressure sensitivity parameter, the tension-compression asymmetry of the material is invoked. Since the study of different loading modes was out of the scope of the experimental campaign, the value of the pressure sensitivity parameter was determined using equation 5.36 [18] and values of σ_y for tension

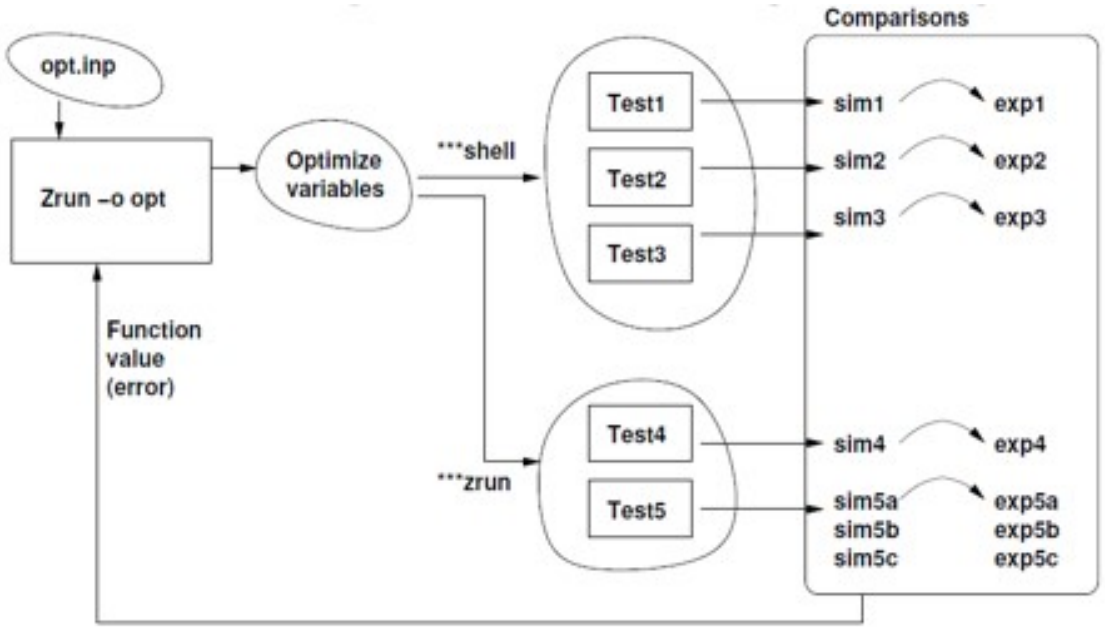

Figure 5.7: Diagram of the interaction between the optimizer and sub-simulations which generate the data to be compared with experimental results.

and compression reported for three different LDPE's in [153].

$$|\sigma_y| = \sigma_{e|yield} = (s - \alpha\sigma_h)|_{yield} \tag{5.36}$$

The pressure sensitivity was approximated as the average over the three LDPE's presented in [153], resulting in α =0.036.

In the model, the rate sensitivity is controlled by A, m and $\dot{p}_0$. For the pristine material, the calibration of these parameters was done through optimization with the mechanical response of the experiments at various strain rates. For calibration, data at strain rates of 0.1, 0.005 and 0.001 s^{-1} was used, while the data at 0.01 s^{-1} was reserved for validation of the calibration results. Since the test matrix of the aged-material did not comprise testing at various strain rates, a simplifying assumption is made that the rate sensitivity parameters remain constant post-aging. Thus, A, m, and $\dot{p}_0$ became fixed parameters on the calibration of UV-aged films, their values being those obtained from the optimization of pristine films.

Lastly, the optimization procedure requires an initial value for each parameter. For this,

an initial estimation was made by following, as much as possible, the procedure developed by Poulain et al. [73]. For convenience, a unique initial set was determined for both films as a plate, and they are shown in Table 5.1.

For all conditions, calibration was first attempted with a single element. In the cases where this was successful, these parameters were then used for calculations with the tensile specimens models depicted in Fig. 5.5 and 5.6 for corroboration. In the cases were single element calibration was not appropriate (either due to structural effects or heterogeneous deformation), calibration was attempted a second time using the tensile specimen models.

The optimization algorithm allows for the designation of different weights to the conditions used in the error function calculation. During the calibration of pristine material, an additional was assigned to the 0.005 s^{-1} condition, which was of special interest since it was the rate used in the experiments with aged specimens.

5.2.3.1 As-Received Material

Films

The results obtained after optimization with a single element for the pristine film are shown in Fig. 5.8a, and the corresponding material parameters in Table 5.1. Overall, we found a good agreement between the simulation and the experimental data. In fact, the validation set at 0.01 s^{-1}, which was not included in the optimization procedure, seemed to show an even better fit during yield than the conditions included on the calibration. On the other hand, the model predicted a later yield and shallower softening for the 0.1 s^{-1} condition compared with the experimental data. This can be attributed, in part, to the self-heating effects described by G'sell [146], by which the deformation of the polymer cannot be considered isothermal at strain rates above 0.01 s^{-1}, and adiabatic effects result in an increased softening after yield. Since the deformation is assumed to be isothermal in the model, adiabatic effects are not taken into account; thus, it cannot reproduce this additional softening. One also notes that at the lowest strain studied of 0.001 s^{-1}, the large strain hardening predicted by the model is considerably larger than in the experiments.

Parameter	Units	Min	Max	Initial	1st calibration (single element)	2nd calibration (tensile model)
E (fixed)	MPa	150.0	-	-	-	-
ν (fixed)	-	-	-	0.4	-	-
T (fixed)	K	-	-	298.0	-	-
α (fixed)	-	-	-	0.036	-	-
s_0	MPa	0.5	30.0	16.0	2.12	1.92
s_1	MPa	0.5	50.0	40.0	2.33	2.01
s_2	MPa	0.5	50.0	12.8	17.04	32.98
h_1	MPa	0.0	35000.0	1276.82	14000.0	542.28
h_2	MPa	0.0	1500.0	66.59	3.90	4.66
m	-	0.05	-	0.83	2.55	2.20
$\dot{p_0}$	s^{-1}	0.001	-	0.0054	0.00189	0.00115
A	K/MPa	10.0	1000	335.0	16.23	22.53
C^R	MPa	0.05	20.0	15.0	0.99	0.88
N	-	0.5	50.0	7.75	8.98	10.54
$\bar{p}$	-	0.0004	0.5		0.00648	
f	-	0.001	100	0.01	0.147	0.207
Final error function value					0.3062	0.0527

Table 5.1: Values of the material parameters obtained at each optimization for the pristine film model. Initial estimation, minimum and maximum values of LDPE material parameters are also displayed.

Fig. 5.8a also seems to show that the response of the LDPE films can be modeled with a single element, which would suggest that the deformation of the films is homogeneous and structural effects are negligible. In order to corroborate this, calculations were made using the parameters obtained by single element calibration and the tensile film model depicted in Fig. 5.5. The results in Fig. 5.8b reveal that the material parameters determined with a single element allow replicating the response of the films up to yield, but result in higher predicted stresses at large strains, especially for the 0.005 and 0.001 s^{-1} strain rates. Therefore, a second optimization for the pristine film was performed, using, in this occasion, the tensile model of Fig. 5.5, and the parameters obtained in the first optimization as initial input for the calibration. The results of this second optimization are shown in Fig. 5.9 and the corresponding material parameters in Table 5.1. An improved agreement between experiments and simulations was obtained, as reflected as well in the smaller final error function

value (see Table 5.1); however, the softening and large strain hardening of the 0.001 s^{-1} condition remained elusive to replicate. The calibrations results were validated by modeling the response at 0.01 s^{-1}, which showed a good agreement between experiments and model.

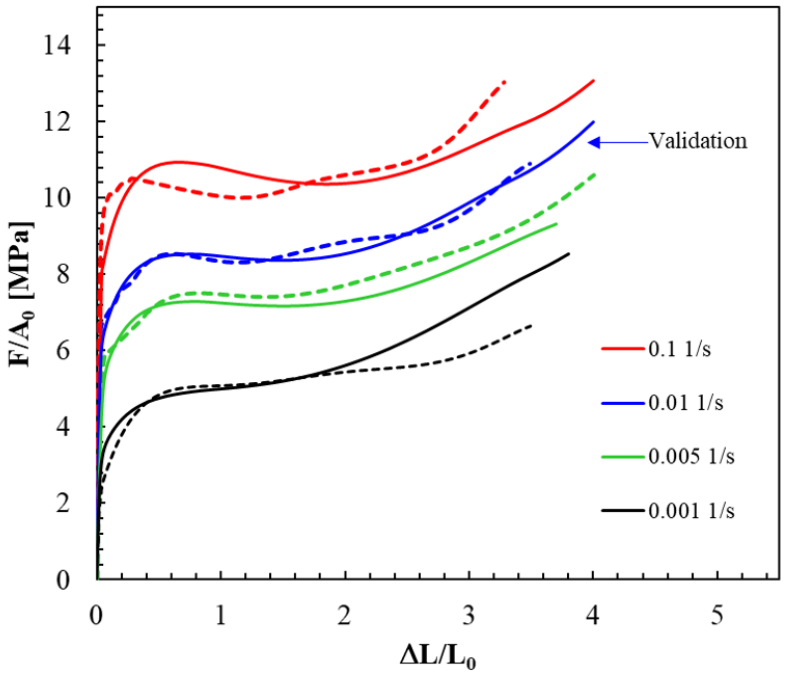

(a)

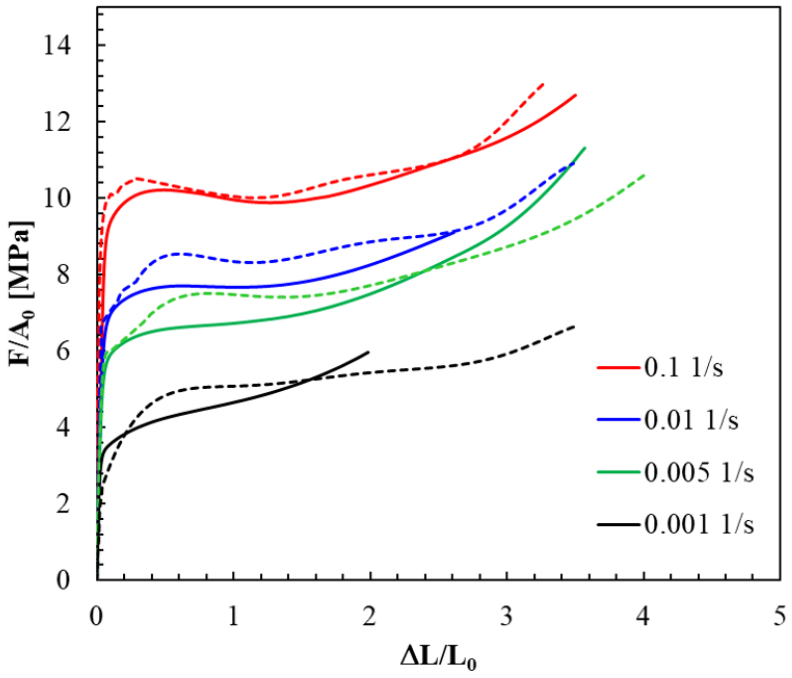

(b)

Figure 5.8: Computed (solid lines) versus experimental (dashed lines) nominal stress–strain responses of LDPE films at various strain rates. (a) calibration with a single element. Curves corresponding to 0.01 s^{-1} were not included in the calibration and were used only as validation for the calibration procedure. (b) Simulations with tensile model and material parameters obtained from single element calibration.

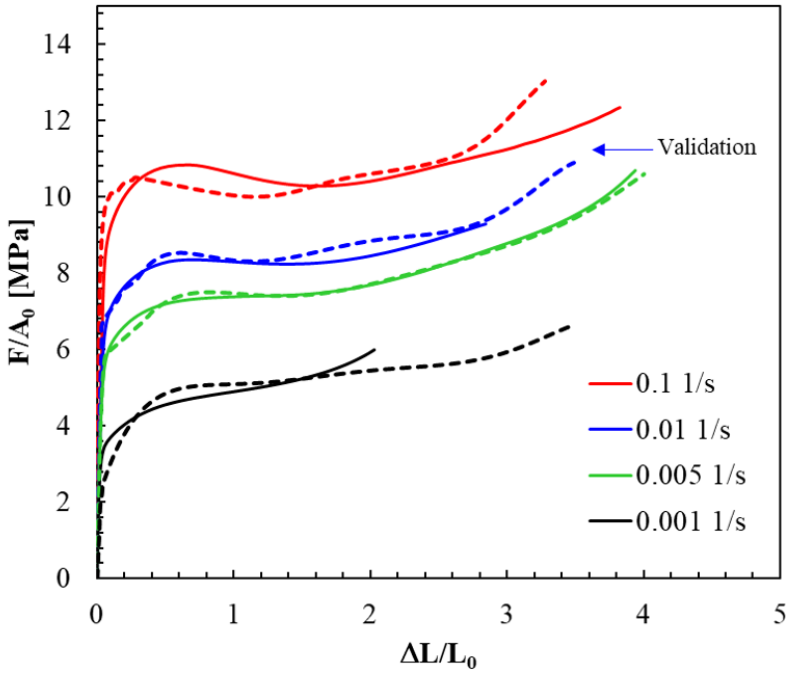

Figure 5.9: Computed (solid lines) versus experimental (dashed lines) nominal stress–strain responses of LDPE films at various strain rates calibrated using the tensile model. Curves corresponding to 0.01 s^{-1} were not included in the calibration and were used only as validation for the calibration procedure.

Plates

In contrast to films, the deformation of the bulk specimens could not be captured with single element calculations, as the optimization results show in Fig. 5.10a. This is probably due to the heterogeneous nature of the tensile deformation of the plates, where strain localization occurs. Therefore, a second optimization of the pristine plates was performed, this time using the tensile model (Fig. 5.6) instead of a single element. Fig. 5.10b shows that a significantly improved agreement between experiment and simulations is obtained with the tensile mesh. This is captured as well in the decreased error value function in Table 5.2, where the material parameters obtained for each calibration are also displayed. The ability to model the response of the LDPE plates by using the tensile mesh, in contrast with the single element, confirms that the deformation of the plates is heterogeneous and that struc-

tural effects are non-negligible in this case. Despite the improved fit obtained in the second optimization, an even better fit was desired for the 0.005 s^{-1} since it is the strain rate used with the UV-aged plates. Thus, a third optimization was performed, this time using only the 0.005 s^{-1} condition, and leaving the other strain rates as validating set. The results obtained in Fig. 5.11 showed an improved agreement on the yield and small strain softening of all strain rates except 0.1 s^{-1}, which can be related to the adiabatic effects aforementioned. The improvement in small strain behavior, however, came at the expense of the large strain hardening leading, ultimately leading to a higher error function value.

Overall, the results in Fig. 5.8-5.10 also proved that the macromolecular model works for describing the deformation of semicrystalline polymers, even if it was formulated for amorphous polymers. This is due, in part, to the fact that the mechanical response of semicrystalline polymers is, phenomenologically, very similar to the response of glassy polymers, i.e., both exhibit temperature and strain rate sensitivity, post-yield softening, and strain hardening. This is exemplified in the model on the viscoplastic law [147]. For glassy polymer chains, this is modeled by an Arrhenius-like equation [68]. But it happens that in a polymeric crystalline phase, the plastic flow can also be represented by an Arrhenius equation [77]. Thus, it is reasonable that the model, as it stands, is able to replicate the response of a semicrystalline polymer specimen.

Parameter		Units	1st calibration (single element)	2nd calibration (tensile model)	3rd calibration (tensile model, 0.005 s^{-1})
E (fixed)	0.001 s^{-1}	MPa	230.0	-	-
	0.005 s^{-1}	MPa	230.0	-	-
	0.01 s^{-1}	MPa	360.0	-	-
	0.1 s^{-1}	MPa	660.0	-	-
ν (fixed)		-	0.4	-	-
T (fixed)		K	298.0	-	-
α (fixed)		-	0.036	-	-
s_0		MPa	3.87	3.51	8.39
s_1		MPa	0.68	0.65	10.73
s_2		MPa	5.74	4.89	15.35
h_1		MPa	41.60	44.11	16640.4
h_2		MPa	8.05	8.13	22.49
m		-	3.07	2.87	1.0
$\dot{p_0}$		s^{-1}	0.0010	0.00115	0.0064
A		K/MPa	10.0	12.05	193.85
C^R		MPa	2.39	1.85	1.58
N		-	49.31	44.64	19.73
$\bar{p}$		-	0.000109	0.00012	0.0062
f		-	0.00172	0.00196	0.063
Final error function value			0.2317	0.3189	3.191

Table 5.2: Values of the material parameters obtained at each optimization for the pristine plate model. Initial, minimum and maximum values are same as in Table 5.1, except for E.

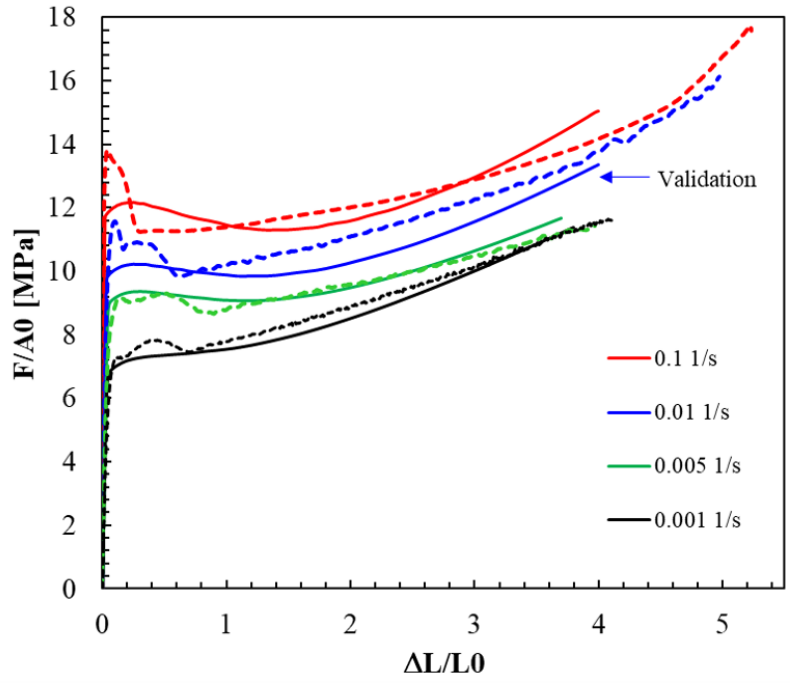

(a)

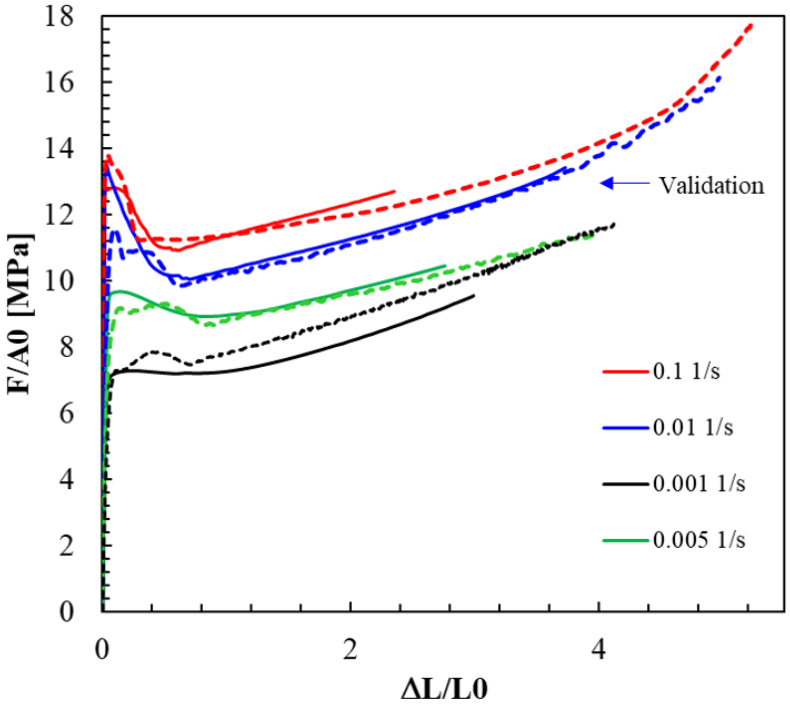

(b)

Figure 5.10: Computed (solid lines) versus experimental (dashed lines) nominal stress–strain responses of LDPE plates at various strain rates: (a) calibration with a single elements, and; (b) calibration with tensile model. Curves corresponding to 0.01 /s were not included in the calibration and were used only as validation for the calibration procedure.

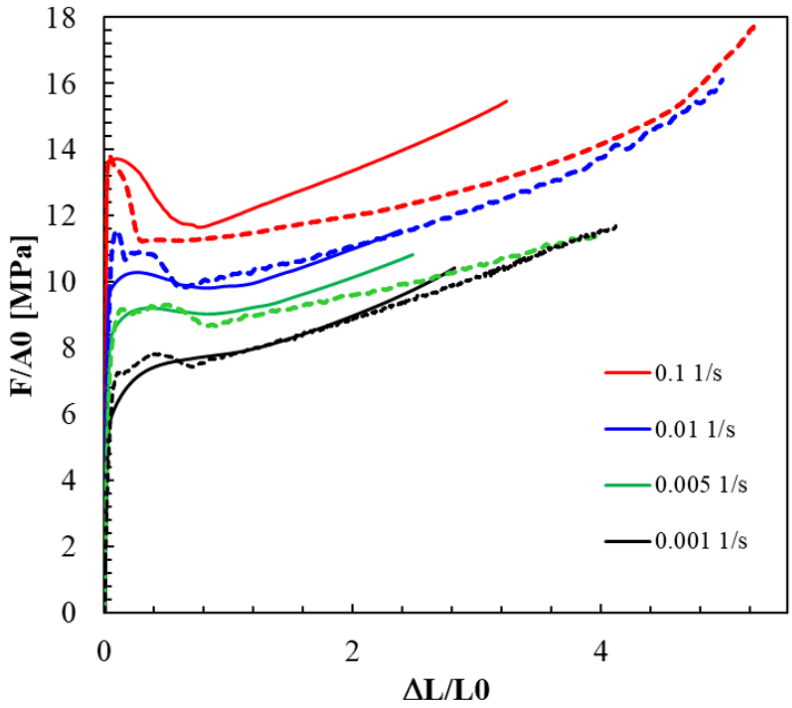

Figure 5.11: Computed (solid lines) versus experimental (dashed lines) nominal stress–strain responses of LDPE plate at various strain rates calibrated using the tensile model. Only the 0.005 s^{-1} condition was used for optimization. All other curves were used only as validation for the calibration procedure.

5.2.3.2 UV-Aged Films

In Chapters 2-4, we showed that LDPE UV-aged to various aging times exhibited different material properties. Thus, specimens aged to various aging times cannot be considered the same material, each of them requiring their own set of parameters to describe their mechanical behavior. Accordingly, individual fits were made for each UV aging condition between 24 to 96 h. Since all test for aged films were made at 0.005 s^{-1} and room temperature, the parameters found through optimization are not unique. To decrease the number of parameters to determine, the rate sensitivity parameters A, m, and $\dot{p}_0$ were assumed to remain unchanged during aging, so their values were taken to be equal to the A, m, and $\dot{p}_0$ obtained for the as-received film in the previous section. For some UV aging conditions, one calibration with a single element was enough to obtain a good agreement between ex-

periments and the model. In others, a second calibration using the film tensile mesh was necessary.

The results of the calibrations of UV-aged films, together with the pristine (0 h) film at the strain rate of $0.005s^{-1}$ obtained in section 5.2.3.1, are shown in Fig. 5.12. All calculations shown were made using the tensile mesh. As expected, the model was able to replicate each individual response. The parameters obtained for each UV aging time are shown in Table 5.3. Since no large strain hardening was observed for the aged films, the values of C^R and N should be taken with caution. These parameters are employed in section 5.3.1 for the estimation of the thickness of the oxidation layer in bulk specimens.

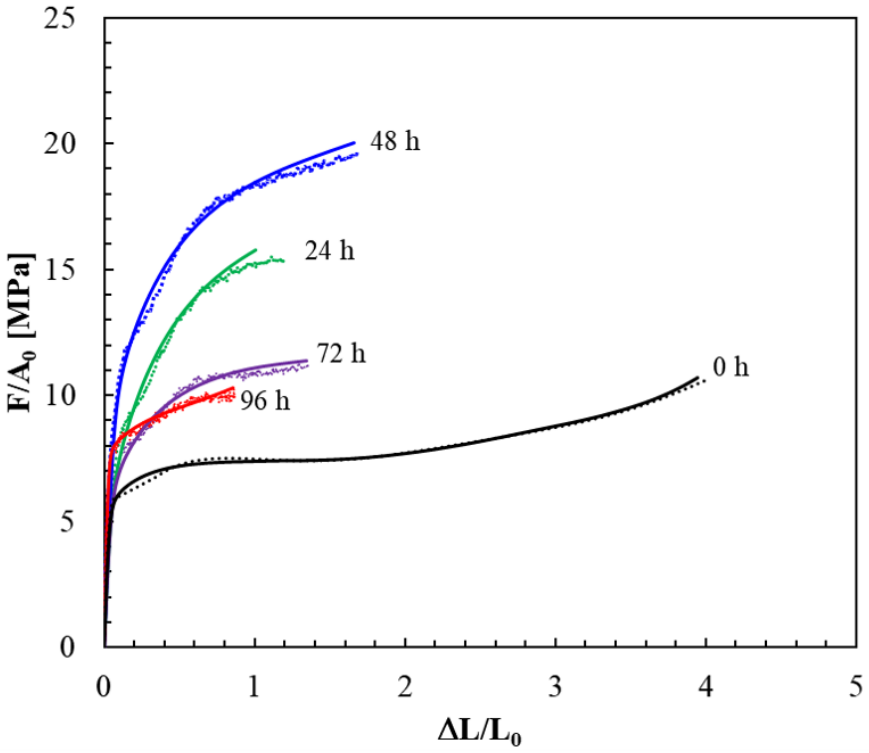

Figure 5.12: Computed (solid lines) versus experimental (dotted lines) nominal stress–strain responses of UV-aged LDPE films. Experimental and computed curves of the pristine plate are shown for comparison. All calculations were made with the tensile mesh and a strain rate of 0.005 s^{-1}.

Parameter	Units	24 h	48 h	72 h	96 h
E (fixed)	MPa	116.4	135.0	116.35	240.0
ν (fixed)	-		0.4		
T (fixed)	K		298.0		
α (fixed)	-		0.036		
m (fixed)	-		2.55		
$\dot{p_0}$ (fixed)	s^{-1}		0.00189		
A (fixed)	K/MPa		16.23		
s_0	MPa	2.65	6.08	2.60	3.74
s_1	MPa	1.53	0.00013	3.23	4.88
s_2	MPa	213.50	354.72	191.55	131.11
h_1	MPa	162.23	0.05	0.16	183.96
h_2	MPa	15.15	17.63	9.28	4.90
C^R	MPa	2.97	2.88	1.59	1.34
N	-	8.09	10.58	15.17	4.08
$\bar{p}$	-	0.0002	0.5	0.0004	0.0006
f	-	0.186	0.00010	0.002	0.002

Table 5.3: Values of the material parameters obtained at each optimization for the pristine film model. Initial estimation, minimum and maximum values of LDPE material parameters are also displayed.

5.3 Results

5.3.1 Estimation of Thickness of Oxidation Layer

The results of the estimation of TOL by this method are shown in Fig. 5.13. Recall that from experimental observations on 192 h and 240 h UV-aged plates deformed to fracture (chapters 3 and 4) a thicknesses of oxidation layer TOL_{exp} ~200 μm was inferred. For the 48 h UV-aged plate (Fig. 5.13a), the proposed methodology estimates a TOL in the 0.05–0.15 mm range. The flow stress of the UV-aged plate seems to be better represented by a system with a TOL = 0.15 mm, but after softening, the mechanical response is clearly better captured by a TOL of 0.05 mm. These values are in line with the TOL estimated from experimental observations at higher UV-doses: due to diffusion limited oxidation, TOL at 48 h is expected to be smaller than TOL at high UV doses (TOL_{exp} ~0.18 mm) where the steady state has presumably been reached. Lastly, one notices that while the bilayer model can make a reasonable estimation of $\text{TOL}_{48\text{h}}$, it is not able to reproduce the deep softening

observed in the 48 h UV-aged plate.

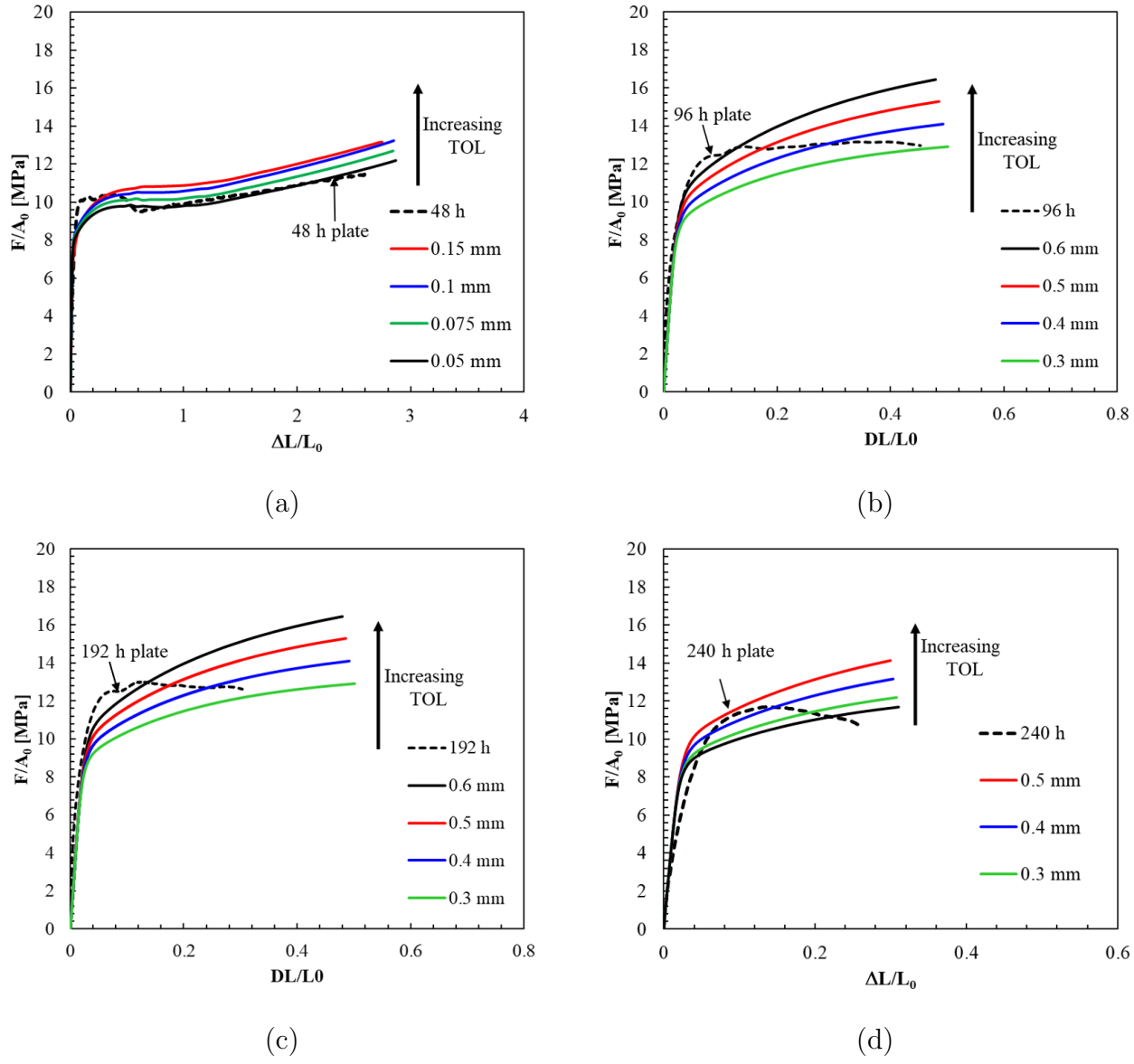

Figure 5.13: Estimation of the thickness of oxidation layer (TOL): Computed (solid lines) and experimental (dashed lines) nominal stress-strain responses of UV-aged LDPE plates: (a) 48 h, (b) 96 h, (c) 192 h, and; (d) 240 h. Plates were modeled as bilayer systems of various TOL's.

Based on the 48 h condition results and the TOL estimates from experiments, it would be reasonable to expect a TOL between 0.75 and 0.2 mm for the 96 h condition. Fig. 5.13b compares the 96 h UV-aged plate experimental response with the bilayer model results, suggesting a TOL_{96h} ∼0.3–0.6 mm. While the trend of TOL respect to aging time is correct, i.e., $TOL_{96h} > TOL_{48h}$, the model estimates are higher than the TOL inferred from experimental observations. The same occurs for the 192 h UV-aged plate depicted in Fig. 5.13c. Lastly, Fig. 5.13d shows that at 240 h of UV aging, the problem is inverted: at such high UV dose, the response of the bulk is weakened to the point that the bilayer model approach estimates a TOL decreasing with time such that $TOL_{240h} < TOL_{96,192h}$.

The proposed bilayer model methodology allowed us to estimate lower and upper bounds for the TOL of a UV-aged polymer. Some of the estimates are larger than what we inferred from SEM observations, suggesting that the effect of oxidation can indeed go as deep as 0.6 mm into the material. In fact, while some reports in the literature suggest a maximum oxidation depth of 0.1 mm for LDPE in similar aging conditions [49,50], others have observed oxidation depths beyond 0.1 mm and up to 1.5 mm [132, 154]. The latter values are high compared to other semicrystalline polymers such as HDPE, a difference that is attributed to the high oxygen diffusion rate of LDPE compared to HDPE due to its lower crystallinity [132]. In any case, if TOL at high UV-doses is indeed ∼0.6 mm or more, this suggests that what was observed experimentally was, at most, the minimum oxidation layer and that SEM cannot capture the oxidation layer in its totality. The measurement of TOL on SEM depends on how distinguishable the layer is in a specific condition. The inability to distinguish colors in SEM is likely what most greatly affects an accurate determination of the TOL.

Finally, the supposedly decrease in TOL after 240 h estimated by the bilayer model can be attributed to the profuse cracking that occurs on the plate at this dose, which affects the plate's effective response. In fact, considering the degree of mechanical degradation that the film specimens exhibited after very high UV doses, it could be assumed that the outer part of the oxidation layer at this point is rendered unable to bear any load, a fact that cannot

be captured by the approach and the model as they stand.

5.3.2 Critical Assessment of Modeling Approach

In order to critically asses the modeling approach used, recall the assumptions made, in particular, the disregard of material variability between films and plates. In fact, when the experimental responses of pristine films and plates are compared (Fig. 5.14) we observed that the plate exhibited a higher flow stress than the film. This difference can be attributed to the difference in processing, i.e., film extrusion *versus* compression molding, which leads to distinct chain orientations and crystalline morphologies. Specifically, the lower cooling rate of the plates after processing presumably leads to higher lammelar thickness, and thus higher flow stress. Here, the film and plate tensile specimen geometries were modeled using the same set of material parameters in order to explore further this difference in responses.

The results obtained, using the material parameters of the pristine plate and a strain rate of 0.005 s^{-1}, are shown in Fig. 5.15. It reveals that, in fact, even when modeling films and plates as having the same intrinsic material properties, the plate has a higher flow stress than the films. What is observed in Fig. 5.15 is an effect of pressure: the plate is in a state of plane strain, while the film is in a state of plane stress. This effect of pressure is accounted for in the model by the material parameter α. The results of Fig. 5.15 show that difference observed in the mechanical response of pristine films and plates is, at least in part, due to pressure effects. Additionally, these results do not negate the assumption that films and plates are inherently the same material.

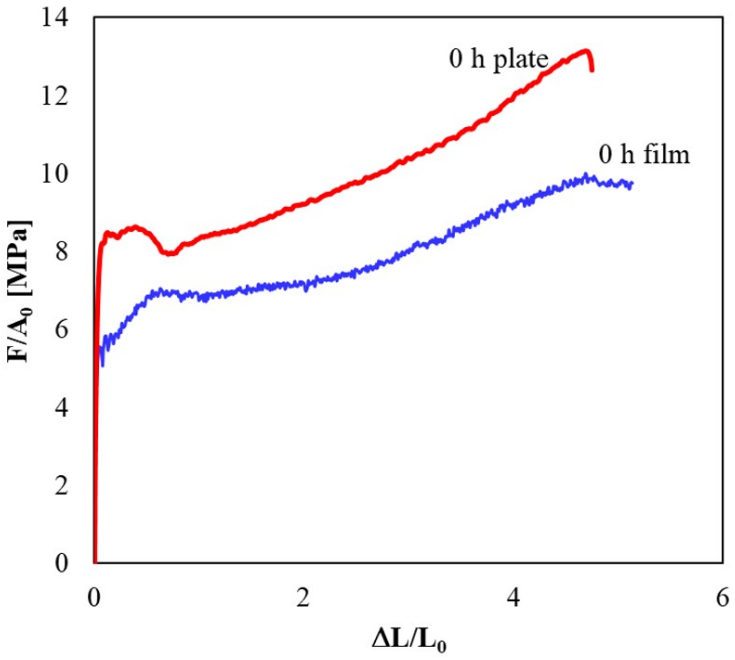

Figure 5.14: Experimental nominal stress–strain responses of pristine LDPE plate and film evidencing difference in tensile response. Experiments done at 0.005 s^{-1}.

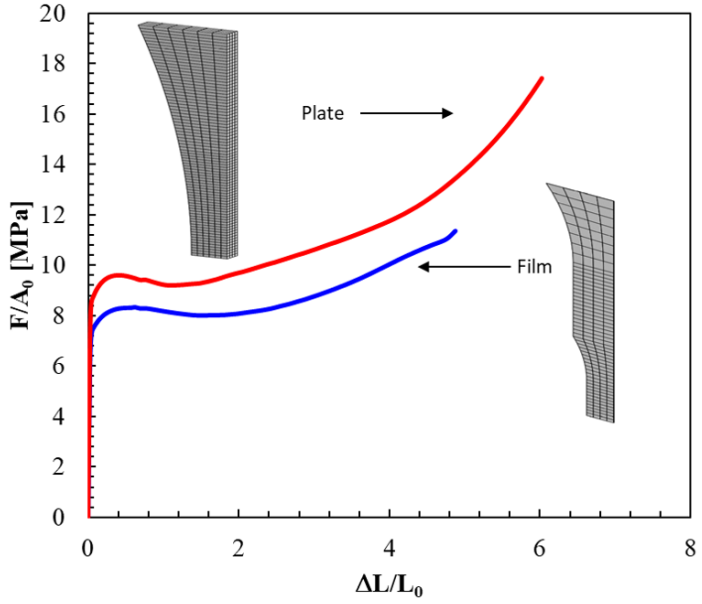

Figure 5.15: Computed nominal stress–strain responses of LDPE plate and film evidencing pressure effects. Both calculations were made with the same set of material parameters, changing only the specimen geometry. Calculations done at 0.005 s^{-1}.

6. CONCLUSIONS

This research aimed to characterize the photo-oxidation of semicrystalline polymers and investigate the role of aging-induced damage in oxidative embrittlement. The main research objectives of this study were: (i) to investigate the chemo-mechanical aspects of UV aging prior to loading; (ii) to examine the effects of UV aging on the mechanical behavior and damage progression; (iii) to establish a connection between accelerated aging and natural aging, and; (iv) to estimate the extent of diffusion-limited oxidation through inverse modeling. These goals were achieved in varying degrees, and the pertaining conclusions are as follows:

- The characterization of the chemo-mechanical aspects of UV aging before loading showed that photo-oxidation led to the formation of micro-cracks in the absence of any mechanical loads. The pattern of these chemical cracks was determined by the supramolecular orientation of the polymer (e.g., row-nucleated or spherulitic), with the cracks oriented along the transverse direction of the films. In plates, the cracks formed a polygonal array on the exposed surface. A superficial layer embrittlement model was invoked to rationalize these "chemical cracks" through a residual stress termed "chemical stress" akin the thermal stress in multi-layered systems. Chemical cracking was observed regardless of the thickness of the specimen (film and bulk) and the aging considered (UV, HUV, and natural aging.). Additionally, humidity lead to an acceleration of the UV aging effects observed on the polymer.

- Transient strengthening manifests in the increase in the flow stress and strain hardening capacity of the polymer at low to moderate radiation doses. This was explained by chemi-crystallization, which led to the formation of thin crystallites that play the role of chemical crosslinks. At higher radiation doses, chain scission dominated, and the usual weakening ensued. In plates, the effect of diffusion limited oxidation (DLO) resulted

in a shifting of the transient strengthening to slightly higher UV doses compared to films. Transient strengthening occurred in all the considered aging types. Humidity lead to an acceleration of the UV aging effects on the of the polymer.

- Examination of the effects of UV aging on the mechanical response and damage progression showed that the tensile deformation of aged films led to the formation of voids and long cracks parallel to the loading direction, in contrast with the behavior of pristine LDPE films. Photo-oxidation presumably promotes cavitation by providing nucleation sites generated by chain scission events. In bulk specimens, tensile deformation opened up more cracks and widened the existing ones.

- The processes involved in the (photon-mediated) oxidative embrittlement of semicrystalline polymers are likely to borrow many aspects of the specific mechanisms pertaining to LPDE, as uncovered in this investigation. Cavitation, for instance, is expected to play an even bigger role in materials with higher crystallinity.

- A correlation was found between accelerated aging (HUV) and natural aging. Details aside, it was found that 96 h of HUV aging roughly corresponded to 2 months of natural aging in films in terms of mechanical tensile behavior. Closer inspection of damage as characterized using SEM, showed similar damage process. These results highlighted the role of humidity in replicating natural aging conditions in laboratory accelerated aging experiments.

- A strategy was developed to estimate the thickness of the oxidation layer through inverse modeling. It consisted of modeling an aged plate as a bilayer system of a pristine core and an oxidized layer of unknown thickness. The responses of modeled plates with oxidation layers of various thicknesses were compared to the experimental ones, with a matching response indicating the appropriate thickness. The approach allowed to estimate lower and upper bounds of thickness of the oxidation layer.

A few directions for future work:

- Although the initial intent was to explore a range of crystallinities in PE for instance using LDPE, LLDPE, HDPE, UHMPE, the thesis concentrated on a single crystallinity level, i.e., that of LDPE. This choice emerged en force with discoveries made thanks to microscopic examinations of damage. Clearly, one direction for future work consist of extending the present work for various degrees of crystallinity. This would be important from a number of perspectives. For example, pristine LDPE is reported not to cavitate. In this study we have shown that (i)LDPE cavitates under relatively small UV doses; and (ii) LDPE plates exhibited an unusual type of superficial void nucleation in the unaged state. Whether such findings remain valid for other crystallinities remains to be investigated.

- It has been reported in the literature that the damage distribution in semicrystalline polymers such as PA6 is affected by the triaxiality state [155]. Recently, the work by Cundiff [147] has explored the effect of triaxiality on the mechanical behavior of aged PA6. However, the effects of triaxiality on the damage process of aged PE remains unexplored. Thus, a venue for future work is to investigate how triaxiality affects the damage process on aged PE.

- The viscoplastic constitutive model used in this work does not account for UV-induced damage. Future work could be dedicated to improve the coupling between fine scale aging chemical kinetic models (such as those developed by Colin et al. [4]) with the micromechanical damage models as developed in [147].

REFERENCES

[1] B. Fayolle, E. Richaud, X. Colin, and J. Verdu, "Review: Degradation-induced embrittlement in semi-crystalline polymers having their amorphous phase in rubbery state," *J. Mater. Sci.*, vol. 43, no. 22, pp. 6999–7012, 2008.

[2] M. Gardette, A. Perthue, J. L. Gardette, T. Janecska, E. Földes, B. Pukánszky, and S. Therias, "Photo- and thermal-oxidation of polyethylene: Comparison of mechanisms and influence of unsaturation content," *Polym. Degrad. Stab.*, vol. 98, no. 11, pp. 2383–2390, 2013.

[3] I. Grigoriadou, K. M. Paraskevopoulos, K. Chrissafis, E. Pavlidou, T. G. Stamkopoulos, and D. Bikiaris, "Effect of different nanoparticles on HDPE UV stability," *Polym. Degrad. Stab.*, vol. 96, no. 1, pp. 151–163, 2011.

[4] X. Colin, B. Fayolle, L. Audouin, and J. Verdu, "The classical kinetic model for radical chain oxidation of hydrocarbon substrates initiated by bimolecular hydroperoxide decomposition," *International Journal of Chemical Kinetics*, vol. 38, pp. 666–676, nov 2006.

[5] L. Lin and A. S. Argon, "Structure and plastic deformation of polyethylene," 1994.

[6] G. Michler, *Electron Microscopy of Polymers*. Springer Laboratory, Springer Berlin Heidelberg, 2008.

[7] P. J. Brennan, "Uva-340 exposure of automotive materials: A status report," *Journal of Vinyl Technology*, vol. 12, no. 2, pp. 73–77, 1990.

[8] E. Grau, *Polymerization of ethylene : from free radical homopolymerization to hybrid radical / catalytic copolymerization*. PhD thesis, nov 2010.

[9] C. H. M. Weber, A. Chiche, G. Krausch, S. Rosenfeldt, M. Ballauff, L. Harnau, I. Göttker-Schnetmann, Q. Tong, and S. Mecking, "Single Lamella Nanoparticles of

Polyethylene," *Nano Lett.*, vol. 7, pp. 2024–2029, jul 2007.

[10] A. Peterlin, "Plastic deformation of unoriented crystalline polymers under tensile load," in *Advances in polymer science and engineering*, pp. 1–19, Springer, 1972.

[11] A. Galeski, A. Argon, and R. E. Cohen, "Changes in the morphology of bulk spherulitic nylon 6 due to plastic deformation," *Macromolecules*, vol. 21, no. 9, pp. 2761–2770, 1988.

[12] J. M. Hutchinson, "Physical aging of polymers," *Progress in Polymer Science*, vol. 20, pp. 703–760, jan 1995.

[13] G. M. Odegard and A. Bandyopadhyay, "Physical aging of epoxy polymers and their composites," *Journal of Polymer Science Part B: Polymer Physics*, vol. 49, pp. 1695–1716, dec 2011.

[14] W. L. Hawkins, *Polymer Degradation and Stabilization*, vol. 8 of *Polymers Properties and Applications*. Berlin, Heidelberg: Springer Berlin Heidelberg, 1984.

[15] United States Environmental Protection Agency, "Sources of Aquatic Trash."

[16] European Commission, "Press release - Closing the loop: Commission adopts ambitious new Circular Economy Package to boost competitiveness, create jobs and generate sustainable growth," *NewEurope*, no. December, pp. 13–15, 2015.

[17] A. L. Andrady, A. Torikai, H. H. Redhwi, K. K. Pandey, and P. Gies, "Consequences of stratospheric ozone depletion and climate change on the use of materials.," *Photochem. Photobiol. Sci. Off. J. Eur.*, vol. 14, no. 1, pp. 170–184, 2014.

[18] X. Marc and N. Poulain, "On the Thermomechanical Behavior of Epoxy Polymers: Experiments and Modeling," no. December, p. 259, 2010.

[19] C. Bawn, "Encyclopedia of polymer science and engineering," *Polymer (Guildf).*, vol. 28, no. 7, p. 1234, 1987.

[20] G. H. Michler and F. B. Calleja, *Mechanical Properties of Polymers Based on Nanostructure and Morphology*. Taylor & Francis, 2005.

[21] C. G'sell and A. Dahoun, "Evolution of microstructure in semi-crystalline polymers under large plastic deformation," *Mater. Sci. Eng. A*, vol. 175, no. 1-2, pp. 183–199, 1994.

[22] M. C. Boyce, D. M. Parks, and A. S. Argon, "Large inelastic deformation of glassy polymers. part I: rate dependent constitutive model," *Mech. Mater.*, vol. 7, no. 1, pp. 15–33, 1988.

[23] W. A. Spitzig and O. Richmond, "Effect of hydrostatic pressure on the deformation behavior of polyethylene and polycarbonate in tension and in compression," *Polymer Engineering & Science*, vol. 19, pp. 1129–1139, dec 1979.

[24] S. Rabinowitz, I. Ward, and J. Parry, "The effect of hydrostatic pressure on the shear yield behaviour of polymers," *Journal of materials Science*, vol. 5, no. 1, pp. 29–39, 1970.

[25] J. Sauer, K. Pae, and S. Bhateja, "Influence of pressure on yield and fracture in polymers," *Journal of Macromolecular Science, Part B*, vol. 8, no. 3-4, pp. 631–654, 1973.

[26] C. G'Sell, "PLASTIC DEFORMATION OF GLASSY POLYMERS: CONSTITUTIVE EQUATIONS AND MACROMOLECULAR MECHANISMS.," vol. 3, pp. 1943–1982, Pergamon Press (International Series on the Strength and Fracture of Materials and Structures), jan 1986.

[27] S. Humbert, O. Lame, J. M. Chenal, C. Rochas, and G. Vigier, "New insight on initiation of cavitation in semicrystalline polymers: In-situ SAXS measurements," *Macromolecules*, vol. 43, no. 17, pp. 7212–7221, 2010.

[28] O. Redakcji, A. Pawlak, and A. Galeski, "Cavitation during tensile drawing of semicrystalline polymers," *Polimery*, vol. 56, no. 9, pp. 627–636, 2011.

[29] A. Pawlak, A. Galeski, and A. Rozanski, "Cavitation during deformation of semicrystalline polymers," *Prog. Polym. Sci.*, vol. 39, no. 5, pp. 921–958, 2014.

[30] A. Pawlak, "Cavitation during tensile deformation of high-density polyethylene," *Polymer*, vol. 291, no. 48, pp. 1397–1409, 2007.

[31] A. Galeski and A. Rozanski, "Cavitation during Drawing of Crystalline Polymers," *Macromol. Symp.*, vol. 298, no. 1, pp. 1–9, 2010.

[32] L. Laiarinandrasana, T. F. Morgeneyer, H. Proudhon, and C. Regrain, "Damage of semicrystalline polyamide 6 assessed by 3D X-ray tomography: From microstructural evolution to constitutive modeling," *J. Polym. Sci. Part B Polym. Phys.*, vol. 48, no. 13, pp. 1516–1525, 2010.

[33] T. F. Morgeneyer, H. Proudhon, P. Cloetens, W. Ludwig, Q. Roirand, L. Laiarinandrasana, and E. Maire, "Nanovoid morphology and distribution in deformed HDPE studied by magnified synchrotron radiation holotomography," *Polymer (Guildf).*, vol. 55, no. 25, pp. 6439–6443, 2014.

[34] M. Rabello and J. White, "The role of physical structure and morphology in the photodegradation behaviour of polypropylene," *Polym. Degrad. Stab.*, vol. 56, no. 1, pp. 55–73, 1997.

[35] P. Gijsman, G. Meijers, and G. Vitarelli, "Comparison of the UV-degradation chemistry of polypropylene, polyethylene, polyamide 6 and polybutylene terephthalate," *Polym. Degrad. Stab.*, vol. 65, no. 3, pp. 433–441, 1999.

[36] T. Corrales, F. Catalina, C. Peinado, N. S. Allen, and E. Fontan, "Photooxidative and thermal degradation of polyethylenes: Interrelationship by chemiluminescence, thermal gravimetric analysis and FTIR data," *J. Photochem. Photobiol. A Chem.*, vol. 147, no. 3, pp. 213–224, 2002.

[37] B. Fayolle, X. Colin, L. Audouin, and J. Verdu, "Mechanism of degradation induced embrittlement in polyethylene," *Polym. Degrad. Stab.*, vol. 92, no. 2, pp. 231–238, 2007.

[38] M. Qayyum and J. White, "The effect of weathering on residual stresses and mechanical properties in injection-moulded semi-crystalline polymers," *Journal of materials science*, vol. 21, no. 7, pp. 2391–2402, 1986.

[39] M. M. Qayyum and J. R. White, "Plastic fracture in weathered polymers," vol. 28, no. 3, pp. 469 – 476, 1987.

[40] M. C. Celina, "Review of polymer oxidation and its relationship with materials performance and lifetime prediction," *Polym. Degrad. Stab.*, vol. 98, no. 12, pp. 2419–2429, 2013.

[41] J. F. Rabek, "Photochemical aspects of degradation of polymers," in *Polym. Photodegradation*, pp. 24–66, Dordrecht: Springer Netherlands, 1995.

[42] J. F. Rabek, "Physical Factors Which Influence Photodegradation," in *Photodegradation Polym.*, pp. 98–108, Berlin, Heidelberg: Springer Berlin Heidelberg, 1996.

[43] J. Verdu, *Oxidative Ageing of Polymers*. ISTE, 2013.

[44] L. Audouin, V. Langlois, J. Verdu, and J. C. M. de Bruijn, "Role of oxygen diffusion in polymer ageing: kinetic and mechanical aspects," *J. Mater. Sci.*, vol. 29, no. 3, pp. 569–583, 1994.

[45] K. T. Gillen, J. Wise, and R. L. Clough, "General solution for the basic autoxidation scheme," *Polymer Degradation and Stability*, vol. 47, pp. 149–161, jan 1995.

[46] M. Sebaa, C. Servens, and J. Pouyet, "Natural and Artificial Weathering of Low-Density Polyethylene (Ldpe) - Calorimetric Analysis," *J. Appl. Polym. Sci.*, vol. 47, no. 11, pp. 1897–1903, 1993.

[47] M. Liu, A. Horrocks, and M. E. Hall, "Correlation of physicochemical changes in UV-exposed low density polyethylene films containing various UV stabilisers," *Polym. Degrad. Stab.*, vol. 49, no. 1, pp. 151–161, 1995.

[48] F. Carrasco, P. Pagès, S. Pascual, and X. Colom, "Artificial aging of high-density polyethylene by ultraviolet irradiation," *Eur. Polym. J.*, vol. 37, no. 7, pp. 1457–1464, 2001.

[49] J. V. Gulmine, P. R. Janissek, H. M. Heise, and L. Akcelrud, "Degradation profile of polyethylene after artificial accelerated weathering," *Polym. Degrad. Stab.*, vol. 79, no. 3, pp. 385–397, 2003.

[50] A. C. Tavares, J. V. Gulmine, C. M. Lepienski, and L. Akcelrud, "The effect of accelerated aging on the surface mechanical properties of polyethylene," *Polym. Degrad. Stab.*, vol. 81, no. 2, pp. 367–373, 2003.

[51] L. Küpper, J. V. Gulmine, P. R. Janissek, and H. M. Heise, "Attenuated total reflection infrared spectroscopy for micro-domain analysis of polyethylene samples after accelerated ageing within weathering chambers," *Vib. Spectrosc.*, vol. 34, no. 1, pp. 63–72, 2004.

[52] D. Briassoulis, A. Aristopoulou, M. Bonora, and I. Verlodt, "Degradation characterisation of agricultural low-density polyethylene films," *Biosyst. Eng.*, vol. 88, no. 2, pp. 131–143, 2004.

[53] S. F. Chabira, M. Sebaa, R. Huchon, and B. De Jeso, "The changing anisotropy character of weathered low-density polyethylene films recognized by quasi-static and ultrasonic mechanical testing," *Polym. Degrad. Stab.*, vol. 91, no. 8, pp. 1887–1895, 2006.

[54] S. Luzuriaga, J. Kovářová, and I. Fortelný, "Degradation of pre-aged polymers exposed to simulated recycling: Properties and thermal stability," *Polym. Degrad. Stab.*, vol. 91, no. 6, pp. 1226–1232, 2006.

[55] M. Salvalaggio, R. Bagatin, M. Fornaroli, S. Fanutti, S. Palmery, and E. Battistel, "Multi-component analysis of low-density polyethylene oxidative degradation," *Polym. Degrad. Stab.*, vol. 91, no. 11, pp. 2775–2785, 2006.

[56] E. Miyagawa, K. Tokumitsu, A. Tanaka, and K. hei Nitta, "Mechanical property and molecular weight distribution changes with photo- and chemical-degradation on LDPE films," *Polym. Degrad. Stab.*, vol. 92, no. 10, pp. 1948–1956, 2007.

[57] Y.-C. Hsu, M. P. Weir, R. W. Truss, C. J. Garvey, T. M. Nicholson, and P. J. Halley, "A fundamental study on photo-oxidative degradation of linear low density polyethylene films at embrittlement," *Polymer (Guildf).*, vol. 53, no. 12, pp. 2385–2393, 2012.

[58] A. Benítez, J. J. Sánchez, M. L. Arnal, A. J. Müller, O. Rodríguez, and G. Morales, "Abiotic degradation of LDPE and LLDPE formulated with a pro-oxidant additive," *Polym. Degrad. Stab.*, vol. 98, no. 2, pp. 490–501, 2013.

[59] V. H. Rolón-Garrido, M. Kruse, and M. H. Wagner, "Size exclusion chromatography of photo-oxidated LDPE by triple detection and its relation to rheological behavior," *Polym. Degrad. Stab.*, vol. 111, pp. 46–54, 2015.

[60] I. Craig, J. White, and P. C. Kin, "Crystallization and chemi-crystallization of recycled photo-degraded polypropylene," *Polymer (Guildf).*, vol. 46, no. 2, pp. 505–512, 2005.

[61] "Single Component Materials," in *Therm. Anal. Polym. Mater.*, pp. 591–704, Berlin/Heidelberg: Springer-Verlag.

[62] D. Briassoulis, "The effects of tensile stress and the agrochemical Vapam on the ageing of low density polyethylene (LDPE) agricultural films. Part I. Mechanical behaviour," *Polym. Degrad. Stab.*, vol. 88, no. 3, pp. 489–503, 2005.

[63] D. Briassoulis and A. Aristopoulou, "Adaptation and harmonisation of standard testing methods for mechanical properties of low-density polyethylene (LDPE) films," *Polym. Test.*, vol. 20, no. 6, pp. 615–634, 2001.

[64] R. A. Duckett, S. Rabinowitz, and I. M. Ward, "The strain-rate, temperature and pressure dependence of yield of isotropic poly(methylmethacrylate) and poly(ethylene terephthalate)," *J. Mater. Sci.*, vol. 5, no. 10, pp. 909–915, 1970.

[65] R. E. Robertson, "Theory for the Plasticity of Glassy Polymers," *J. Chem. Phys.*, vol. 44, no. 10, p. 3950, 1966.

[66] M. Brereton, R. Duckett, S. Joseph, and P. Spence, "An interpretation of the yield behaviour of polymers in terms of correlated motion," *J. Mech. Phys. Solids*, vol. 25, no. 2, pp. 127–136, 1977.

[67] Z. H. Stachurski, "Yield strength and anelastic limit of amorphous ductile polymers," *J. Mater. Sci.*, vol. 21, no. 9, pp. 3237–3242, 1986.

[68] A. S. Argon, "A theory for the low-temperature plastic deformation of glassy polymers," *Philos. Mag.*, vol. 28, no. 4, pp. 839–865, 1973.

[69] E. M. Arruda, M. C. Boyce, and R. Jayachandran, "Effects of strain rate, temperature and thermomechanical coupling on the finite strain deformation of glassy polymers," *Mech. Mater.*, vol. 19, no. 2-3, pp. 193–212, 1995.

[70] P. D. Wu and E. Van Der Giessen, "On improved network models for rubber elasticity and their applications to orientation hardening in glassy polymers," *J. Mech. Phys. Solids*, vol. 41, no. 3, pp. 427–456, 1993.

[71] K. A. A. Chowdhury, R. Talreja, and A. A. Benzerga, "Effects of Manufacturing-Induced Voids on Local Failure in Polymer-Based Composites," *J. Eng. Mater. Technol.*, vol. 130, no. 2, p. 021010, 2008.

[72] S. Kweon and A. A. Benzerga, "Finite element implementation of a macromolecular viscoplastic polymer model," *Int. J. Numer. Methods Eng.*, vol. 94, no. 10, pp. 895–919, 2013.

[73] X. Poulain, A. A. Benzerga, and R. K. Goldberg, "Finite-strain elasto-viscoplastic behavior of an epoxy resin: Experiments and modeling in the glassy regime," *Int. J. Plast.*, vol. 62, pp. 138–161, 2014.

[74] G. Ayoub, F. Zaïri, M. Naït-Abdelaziz, and J. M. Gloaguen, "Modelling large deformation behaviour under loading-unloading of semicrystalline polymers: Application to a high density polyethylene," *Int. J. Plast.*, vol. 26, no. 3, pp. 329–347, 2010.

[75] S. Belbachir, F. Zaïri, G. Ayoub, U. Maschke, M. Naït-Abdelaziz, J. M. Gloaguen, M. Benguediab, and J. M. Lefebvre, "Modelling of photodegradation effect on elastic-viscoplastic behaviour of amorphous polylactic acid films," *J. Mech. Phys. Solids*, vol. 58, no. 2, pp. 241–255, 2010.

[76] M. C. Boyce, S. Socrate, and P. G. Llana, "Constitutive model for the finite deformation stress-strain behavior of poly(ethylene terephthalate) above the glass transition," *Polym. (Guildf).*, vol. 41, no. 6, pp. 2183–2201, 2000.

[77] S. Ahzi, A. Makradi, R. V. Gregory, and D. D. Edie, "Modeling of deformation behavior and strain-induced crystallization in poly(ethylene terephthalate) above the glass transition temperature," *Mech. Mater.*, vol. 35, no. 12, pp. 1139–1148, 2003.

[78] I. M. Ward and J. Sweeney, *An Introduction to the Mechanical Properties of Solid Polymers*. J. Wiley & Sons, 2005.

[79] Y. Wang, X. Han, J. Pan, and C. Sinka, "An entropy spring model for the Young's modulus change of biodegradable polymers during biodegradation," *J. Mech. Behav. Biomed. Mater.*, vol. 3, no. 1, pp. 14–21, 2010.

[80] Y. Wang, J. Pan, X. Han, C. Sinka, and L. Ding, "A phenomenological model for the degradation of biodegradable polymers," *Biomaterials*, vol. 29, no. 23, pp. 3393–3401, 2008.

[81] X. Han and J. Pan, "A model for simultaneous crystallisation and biodegradation of biodegradable polymers," *Biomaterials*, vol. 30, no. 3, pp. 423–430, 2009.

[82] R. N. Shirazi, W. Ronan, Y. Rochev, and P. McHugh, "Modelling the degradation and elastic properties of poly(lactic-co-glycolic acid) films and regular open-cell tissue engineering scaffolds," *J. Mech. Behav. Biomed. Mater.*, vol. 54, pp. 48–59, 2016.

[83] L. Ding, R. L. Davidchack, and J. Pan, "A molecular dynamics study of Young's modulus change of semi-crystalline polymers during degradation by chain scissions," *J. Mech. Behav. Biomed. Mater.*, vol. 5, no. 1, pp. 224–230, 2012.

[84] B. Zhao, O. Awartani, B. O'Connor, and M. A. Zikry, "Microstructural behavior and failure mechanisms of organic semicrystalline thin film blends," *J. Polym. Sci. Part B Polym. Phys.*, vol. 54, no. 9, pp. 896–907, 2016.

[85] B. Zhao and M. A. Zikry, "Oxidation-induced failure in semi-crystalline organic thin films," *Int. J. Solids Struct.*, vol. 109, pp. 72–83, 2017.

[86] J. S. Soares, J. E. Moore, and K. R. Rajagopal, "Constitutive Framework for Biodegradable Polymers with Applications to Biodegradable Stents," *ASAIO J.*, vol. 54, no. 3, pp. 295–301, 2008.

[87] J. S. Soares, K. R. Rajagopal, and J. E. Moore, "Deformation-induced hydrolysis of a degradable polymeric cylindrical annulus," *Biomech. Model. Mechanobiol.*, vol. 9, no. 2, pp. 177–186, 2010.

[88] A. C. Vieira, A. T. Marques, R. M. Guedes, and V. Tita, "Material model proposal for biodegradable materials," in *Procedia Eng.*, vol. 10, pp. 1597–1602, 2011.

[89] A. C. Vieira, R. M. Guedes, and V. Tita, "Constitutive modeling of biodegradable polymers: Hydrolytic degradation and time-dependent behavior," *Int. J. Solids Struct.*, vol. 51, no. 5, pp. 1164–1174, 2014.

[90] Q. Breche, G. Chagnon, G. Machado, B. Nottelet, X. Garric, E. Girard, and D. Favier, "A non-linear viscoelastic model to describe the mechanical behavior's evolution of biodegradable polymers during hydrolytic degradation," *Polym. Degrad. Stab.*, vol. 131, pp. 145–156, 2016.

[91] Q. Breche, G. Chagnon, G. Machado, E. Girard, B. Nottelet, X. Garric, and D. Favier, "Mechanical behaviour's evolution of a PLA-b-PEG-b-PLA triblock copolymer during hydrolytic degradation," *J. Mech. Behav. Biomed. Mater.*, vol. 60, pp. 288–300, 2016.

[92] J. S. Bergström and M. C. Boyce, "Constitutive modeling of the large strain time-dependent behavior of elastomers," *J. Mech. Phys. Solids*, vol. 46, no. 5, pp. 931–954, 1998.

[93] "ASTM G-154 Standard Practice for Operating Fluorescent Ultraviolet (UV) Lamp Apparatus for Exposure of Nonmetallic Materials," *ASTM Int.*, vol. 44, no. 0, pp. 5–10, 2011.

[94] L. El Chaar and L. A. Lamont, "Global solar radiation: Multiple on-site assessments in Abu Dhabi, UAE," *Renew. Energy*, vol. 35, no. 7, pp. 1596–1601, 2010.

[95] M. Sadeq, E. Masad, H. Al-Khalid, O. Sirin, I. Menapace, and M. Nogueira d'Eurydice, "New Protocol Utilising the Accelerated Weathering Tester to Age Fine Asphalt Mixtures with Warm Mix Asphalt Additives," in *7th Int. EATA (Eur. Asph. Technol. Assoc. Conf.*, p. 13, 2017.

[96] A. Rodriguez, B. Mansoor, G. Ayoub, X. Colin, and A. Benzerga, "Effect of uv-aging on the mechanical and fracture behavior of low density polyethylene," *Polymer Degradation and Stability*, vol. 180, p. 109185, 2020.

[97] J. R. White, "Polymer ageing: physics, chemistry or engineering? Time to reflect," *Comptes Rendus Chimie*, vol. 9, pp. 1396–1408, nov 2006.

[98] G. Fedor and P. Brennan, "Comparison Between Natural Weathering and Fluorescent UV Exposures: UVA-340 Lamp Test Results," in *Durability Testing of Nonmetallic Materials*, pp. 91–91–15, ASTM International, mar 2009.

[99] A. Quintana and M. C. Celina, "Overview of DLO modeling and approaches to predict heterogeneous oxidative polymer degradation," mar 2018.

[100] T. Salivon, X. Colin, and R. Comte, "Degradation of XLPE and PVC cable insulators," in *2015 IEEE Conf. Electr. Insul. Dielectr. Phenom.*, pp. 656–659, IEEE, 2015.

[101] M. Da Cruz, L. Van Schoors, K. Benzarti, and X. Colin, "Thermo-oxidative degradation of additive free polyethylene. Part I. Analysis of chemical modifications at molecular and macromolecular scales," *J. Appl. Polym. Sci.*, vol. 133, no. 18, p. 43287, 2016.

[102] X. Colin, C. Monchy-Leroy, and J. Verdu, "Effect of gamma irradiation on tensile properties of low molecular weight polyethylene samples," *Radiat. Phys. Chem.*, vol. 80, no. 8, pp. 895–901, 2011.

[103] H. Lobo and J. V. Bonilla, *Handbook of plastics analysis*. Marcel Dekker, 2003.

[104] J. F. Rabek, "Photodegradation and photo-oxidative degradation of homochain polymers BT - Polymer Photodegradation: Mechanisms and experimental methods," in *Polym. Photodegradation*, pp. 67–254, Dordrecht: Springer Netherlands, 1995.

[105] J. E. Mark *et al.*, *Physical properties of polymers handbook*, vol. 1076. Springer, 2007.

[106] S. Fatahi, A. Ajji, and P. G. Lafleur, "Correlation between Structural Parameters and Property of PE Blown Films," *J. Plast. Film Sheeting*, vol. 21, pp. 281–305, oct 2005.

[107] H. Zhu, Y. Wang, X. Zhang, Y. Su, X. Dong, Q. Chen, Y. Zhao, C. Geng, S. Zhu, C. C. Han, and D. Wang, "Influence of molecular architecture and melt rheological characteristic on the optical properties of LDPE blown films," *Polymer (Guildf).*, vol. 48, pp. 5098–5106, aug 2007.

[108] X. Zhang, S. Elkoun, A. Ajji, and M. Huneault, "Oriented structure and anisotropy properties of polymer blown films: HDPE, LLDPE and LDPE," *Polymer (Guildf).*, vol. 45, no. 1, pp. 217–229, 2004.

[109] L.-B. W. Lee, R. A. Register, and D. M. Dean, "Tear anisotropy in films blown from polyethylenes of different macromolecular architectures," *J. Polym. Sci. Part B Polym. Phys.*, vol. 43, no. 4, pp. 413–420, 2005.

[110] R. H. Somani, L. Yang, L. Zhu, and B. S. Hsiao, "Flow-induced shish-kebab precursor structures in entangled polymer melts," *Polymer (Guildf).*, vol. 46, no. 20, pp. 8587–8623, 2005.

[111] H. Ashizawa, J. E. Spruiell, and J. L. White, "An investigation of optical clarity and crystalline orientation in polyethylene tubular film," *Polym. Eng. Sci.*, vol. 24, pp. 1035–1042, sep 1984.

[112] P. Dilara and D. Briassoulis, "Degradation and Stabilization of Low-density Polyethylene Films used as Greenhouse Covering Materials," *J. Agric. Eng. Res.*, vol. 76, no. 4, pp. 309–321, 2000.

[113] F. Severini, R. Gallo, and S. Ipsale, "Some aspects of the environmental photodegradation of LDPE," *Polym. Degrad. Stab.*, vol. 22, no. 1, pp. 53–61, 1988.

[114] S. Girois, L. Audouin, J. Verdu, P. Delprat, and G. Marot, "Molecular weight changes during the photooxidation of isotactic polypropylene," *Polym. Degrad. Stab.*, vol. 51, no. 2, pp. 125–132, 1996.

[115] K. N. Cundiff, Y. Madi, and A. A. Benzerga, "Photo-oxidation of semicrystalline polymers: Damage nucleation versus growth," *Polymer*, vol. 188, p. 122090, 2020.

[116] J. Hutchinson and Z. Suo, "Mixed mode cracking in layered materials," vol. 29 of *Advances in Applied Mechanics*, pp. 63 – 191, Elsevier, 1991.

[117] H. Kausch, *Polymer Fracture*. Polymers - Properties and Applications, Springer Berlin Heidelberg, 2012.

[118] Z. Bartczak and E. Lezak, "Evolution of lamellar orientation and crystalline texture of various polyethylenes and ethylene-based copolymers in plane-strain compression," *Polymer*, vol. 46, no. 16, pp. 6050–6063, 2005.

[119] Q. Guo, *Polymer morphology: principles, characterization, and processing*. John Wiley & Sons, 2016.

[120] A. Groisman and E. Kaplan, "An Experimental Study of Cracking Induced by Desiccation," *EPL (Europhysics Letters)*, vol. 25, no. 6, p. 415, 1994.

[121] K. A. Shorlin, J. R. De Bruyn, M. Graham, and S. W. Morris, "Development and geometry of isotropic and directional shrinkage-crack patterns," *Physical Review E - Statistical Physics, Plasmas, Fluids, and Related Interdisciplinary Topics*, vol. 61, pp. 6950–6957, jun 2000.

[122] X. Ma, J. Lowensohn, and J. C. Burton, "Universal scaling of polygonal desiccation crack patterns," 2019.

[123] S. S. Pesetskii, B. Jurkowski, Y. M. Krivoguz, and A. I. Kuzavkov, "Oxidation of LDPE and LDPE grafted with itaconic acid, in contact with water," *Polymer*, vol. 41, pp. 1037–1043, feb 2000.

[124] P. K. Roy, P. Surekha, C. Rajagopal, and V. Choudhary, "Effect of cobalt carboxylates on the photo-oxidative degradation of low-density polyethylene. Part-I," *Polymer Degradation and Stability*, vol. 91, pp. 1980–1988, sep 2006.

[125] N. M. Stark and L. M. Matuana, "Surface chemistry changes of weathered HDPE/wood-flour composites studied by XPS and FTIR spectroscopy," *Polym. Degrad. Stab.*, vol. 86, no. 1, pp. 1–9, 2004.

[126] B. Wunderlich, *Thermal analysis of polymeric materials*. Springer Science & Business Media, 2005.

[127] N. Hassini, K. Guenachi, A. Hamou, J. M. Saiter, S. Marais, and E. Beucher, "Polyethylene greenhouse cover aged under simulated sub-Saharan climatic conditions," *Polymer Degradation and Stability*, vol. 75, pp. 247–254, jan 2002.

[128] W. Javed, Y. Wubulikasimu, B. Figgis, and B. Guo, "Characterization of dust accumulated on photovoltaic panels in Doha, Qatar," *Solar Energy*, vol. 142, pp. 123–135, jan 2017.

[129] D. Feldman, "Polymer Weathering: Photo-Oxidation," *J. Polym. Environ.*, vol. 10, no. 4, pp. 163–173, 2002.

[130] X. Poulain, L. W. Kohlman, W. Binienda, G. D. Roberts, R. K. Goldberg, and A. A. Benzerga, "Determination of the intrinsic behavior of polymers using digital image correlation combined with video-monitored testing," *Int. J. Solids Struct.*, vol. 50, no. 11-12, pp. 1869–1878, 2013.

[131] W. Oliver and G. Pharr, "An improved technique for determining hardness and elastic modulus using load and displacement sensing indentation experiments," *J. Mater. Res.*, vol. 7, no. 06, pp. 1564–1583, 1992.

[132] J. R. White and A. V. Shyichuk, "Macromolecular scission and crosslinking rate changes during polyolefin photo-oxidation," *Polym. Degrad. Stab.*, vol. 92, no. 7, pp. 1161–1168, 2007.

[133] M. D. Islam, I. Kubo, M. Ohadi, and A. A. Alili, "Measurement of solar energy radiation in Abu Dhabi, UAE," *Appl. Energy*, vol. 86, no. 4, pp. 511–515, 2009.

[134] D. R. Roshan, M. Koc, A. Abdallah, L. Martin-Pomares, R. Isaifan, and C. Fountoukis, "UV Index Forecasting under the Influence of Desert Dust: Evaluation against Surface and Satellite-Retrieved Data," *Atmosphere*, vol. 11, p. 96, jan 2020.

[135] M. R. Maghami, H. Hizam, C. Gomes, M. A. Radzi, M. I. Rezadad, and S. Hajighorbani, "Power loss due to soiling on solar panel: A review," *Renewable and Sustainable Energy Reviews*, vol. 59, pp. 1307 – 1316, 2016.

[136] B. Kondori and A. A. Benzerga, "Effect of Stress Triaxiality on the Flow and Fracture of Mg Alloy AZ31," *Metall. Mater. Trans. A*, vol. 45, no. 8, pp. 3292–3307, 2014.

[137] A. Peterlin, "Drawing and extrusion of semi-crystalline polymers," *Colloid and polymer science*, vol. 265, no. 5, pp. 357–382, 1987.

[138] A. Galeski, "Strength and toughness of crystalline polymer systems," *Prog. Polym. Sci.*, vol. 28, no. 12, pp. 1643–1699, 2003.

[139] N. Selles, P. Cloetens, H. Proudhon, T. F. Morgeneyer, O. Klinkova, N. Saintier, and L. Laiarinandrasana, "Voiding Mechanisms in Deformed Polyamide 6 Observed at the Nanometric Scale," *Macromolecules*, vol. 50, no. 11, pp. 4372–4383, 2017.

[140] J. R. White and J. W. Teh, "Fatigue of viscoelastic polymers: 2. Fractography," *Polymer (Guildf).*, 1979.

[141] Bernard A. G. Schrauwen, Roel P. M. Janssen, Leon E. Govaert, and H. E. H. Meijer, "Intrinsic Deformation Behavior of Semicrystalline Polymers," *Macromolecules*, vol. 37, pp. 6069–6078, aug 2004.

[142] K. Chowdhury, A. A. Benzerga, and R. Talreja, "A computational framework for analyzing the dynamic response of glassy polymers," *Computer methods in applied mechanics and engineering*, vol. 197, no. 49-50, pp. 4485–4502, 2008.

[143] L. Farge, S. André, and J. Boisse, "Use of digital image correlation to study the effect of temperature on the development of plastic instabilities in a semi-crystalline polymer," *Polymer*, vol. 153, pp. 295–304, 2018.

[144] E. Parsons, M. C. Boyce, and D. M. Parks, "An experimental investigation of the large-strain tensile behavior of neat and rubber-toughened polycarbonate," *Polymer*, vol. 45, pp. 2665–2684, apr 2004.

[145] J. Richeton, S. Ahzi, K. S. Vecchio, F. C. Jiang, and R. R. Adharapurapu, "Influence of temperature and strain rate on the mechanical behavior of three amorphous polymers: Characterization and modeling of the compressive yield stress," *International Journal of Solids and Structures*, vol. 43, pp. 2318–2335, apr 2006.

[146] C. G'Sell, J. Hiver, A. Dahoun, and A. Souahi, "Video-controlled tensile testing of polymers and metals beyond the necking point," *Journal of materials science*, vol. 27, no. 18, pp. 5031–5039, 1992.

[147] K. N. Cundiff, *Experimental Characterization and Modeling of Aging Induced Damage in Semicrystalline Thermoplastics*. PhD thesis, Texas A&M University, College Station, TX, August 2020.

[148] S. Bazhenov, "Non-adiabatic heating of polymer films under drawing," *International Journal of Mechanical and Materials Engineering*, vol. 9, pp. 1–9, dec 2014.

[149] E. M. Arruda and M. C. Boyce, "Evolution of plastic anisotropy in amorphous polymers during finite straining," *Int. J. Plast.*, vol. 9, no. 6, pp. 697–720, 1993.

[150] P. D. Wu and E. van der Giessen, "Computational Aspects of Localized Deformations in Amorphous Glassy Polymers," *Eur. J. Mech. A/Solids*, vol. 15, no. 5, pp. 799–823, 1996.

[151] O. C. Zienkiewicz, R. L. Taylor, R. L. Taylor, and R. L. Taylor, *The finite element method: solid mechanics*, vol. 2. Butterworth-heinemann, 2000.

[152] D. Briassoulis and E. Schettini, "Measuring strains of ldpe films: the strain gauge problems," *Polymer testing*, vol. 21, no. 5, pp. 507–512, 2002.

[153] A. P. And and A. Galeski*, "Plastic Deformation of Crystalline Polymers: The Role of Cavitation and Crystal Plasticity," 2005.

[154] H. D. Hoekstra, J. L. Spoormaker, J. Breen, L. Audouin, and J. Verdu, "UV-exposure of stabilized and non-stabilized HDPE films: physico-chemical characterization," *Polymer Degradation and Stability*, vol. 49, pp. 251–262, jan 1995.

[155] L. Laiarinandrasana, T. F. Morgeneyer, H. Proudhon, F. N'guyen, and E. Maire, "Effect of multiaxial stress state on morphology and spatial distribution of voids in deformed semicrystalline polymer assessed by x-ray tomography," *Macromolecules*, vol. 45, no. 11, pp. 4658–4668, 2012.

APPENDIX A

SUPPLEMENTARY INFORMATION: DAMAGE CHARACTERIZATION

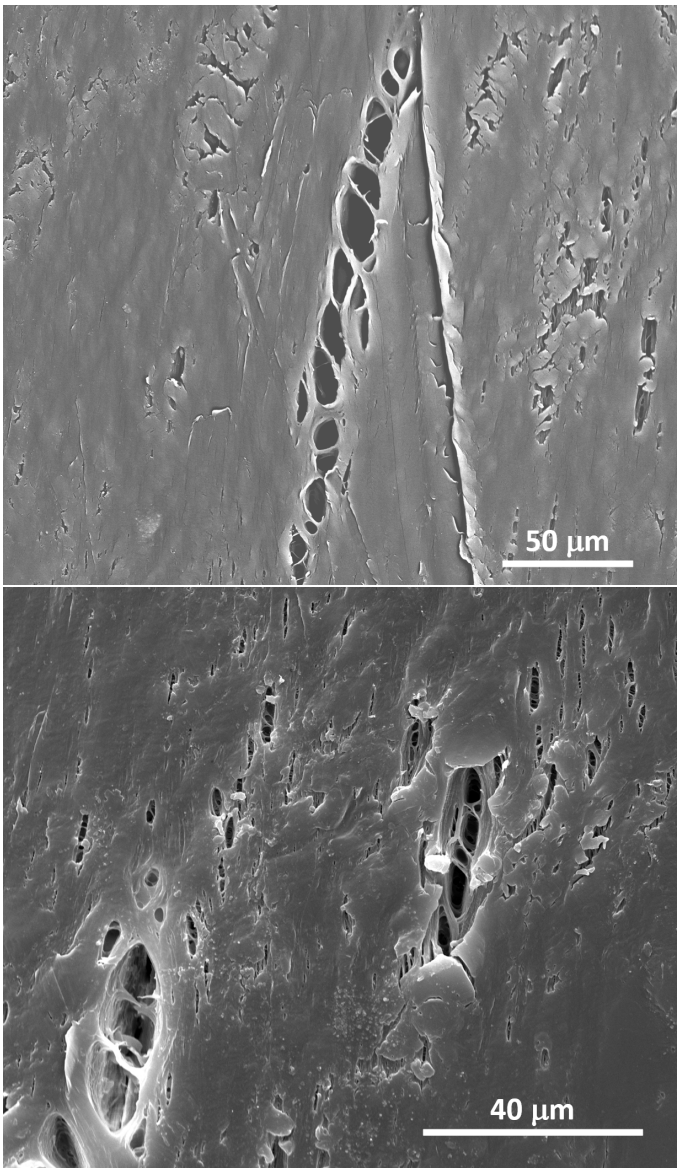

Figure A.1: Fractography of 96 h UV-aged LDPE film showing voids of various sizes and shapes.

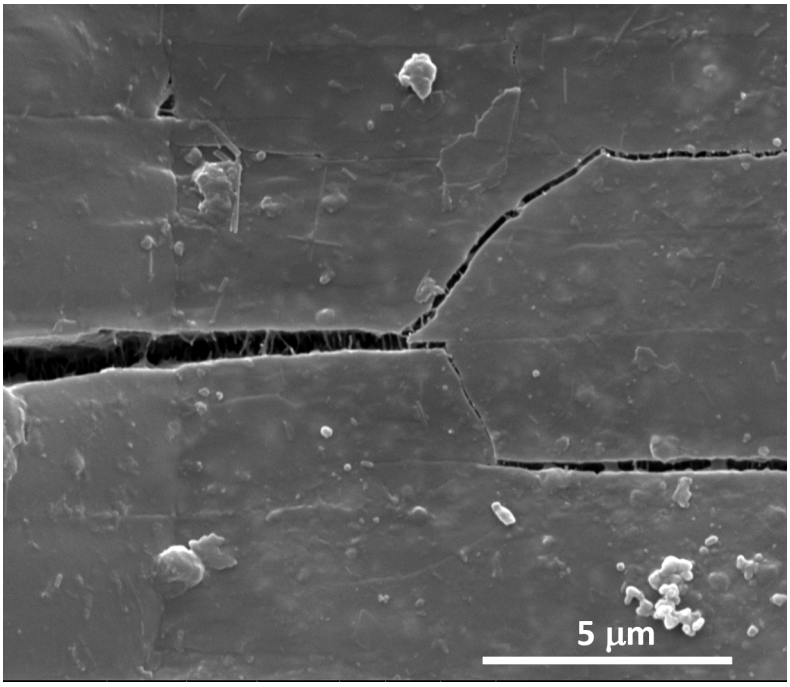

Figure A.2: Detail of cracks in the 2 months naturally aged film.

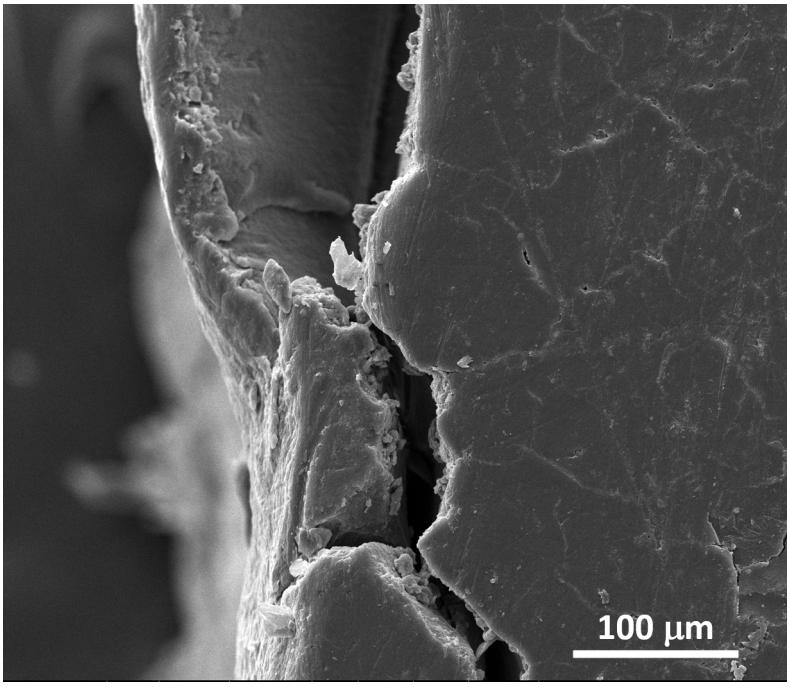

Figure A.3: Detail of delamination in the 8 months naturally aged plate.

APPENDIX B

SUPPLEMENTARY INFORMATION: MACROMOLECULAR MODEL IMPLEMENTATION

B.1 Derivatives for Implicit Time Integration

The following derivatives were used in the implicit time integration:

$$\frac{\partial E}{\partial s} = -\frac{A}{T}E \tag{B.1}$$

$$\frac{\partial E}{\partial M_m} = \frac{3\alpha A}{T}E = -3\alpha\frac{\partial E}{\partial s} \tag{B.2}$$

$$\frac{\partial F}{\partial s} = \frac{A}{T}(1-m)\left(\frac{X_{\text{eq}}}{s-3\alpha M_m}\right)^m F'_x \tag{B.3}$$

$$\frac{\partial F}{\partial M_m} = -3\alpha\frac{A}{T}(1-m)\left(\frac{X_{\text{eq}}}{s-3\alpha M_m}\right)^m F'_x = -3\alpha\frac{\partial F}{\partial s} \tag{B.4}$$

$$\frac{\partial F}{\partial X_{\text{eq}}} = \left(m\frac{A}{T}\left(\frac{X_{\text{eq}}}{s-3\alpha M_m}\right)^{m-1}\right)F'_x \tag{B.5}$$

$$\frac{\partial H_1}{\partial p} = -\frac{h_1}{f\overline{p}}C_x \tag{B.6}$$

$$\frac{\partial H_2}{\partial p} = \frac{h_2}{f\overline{p}}C_x \tag{B.7}$$

$$\text{with} \qquad C_x = \left[\cosh\left((p-\overline{p})/(f\overline{p})\right)\right]^{-2} \tag{B.8}$$

Time discretization leads to the following sets of equations which needs to be solved with respect to the increments ($\mathbf{V}_S = \Delta\boldsymbol{E}$, $\Delta\boldsymbol{b}$, Δp and Δs) of the state variables over a time step Δt:

$$\boldsymbol{R}_E = \Delta\boldsymbol{E} - \Delta F.\boldsymbol{F}^{-1}.E + \Delta p\boldsymbol{E}.\boldsymbol{n}^{\mu} \tag{B.9}$$

$$\boldsymbol{R}_b = \Delta\boldsymbol{b} - \Delta pR : \boldsymbol{n}^{\mu} \tag{B.10}$$

$$R_p = \Delta p - E(s, M_m)F(s, M_m, X_{\text{eq}})\Delta t \tag{B.11}$$

$$R_s = \Delta s - \left(H_1\left(1-\frac{s}{s_1}\right) + H_2\left(1-\frac{s}{s_2}\right)\right)\Delta p \tag{B.12}$$

Solving this system requires the calculation of the associated Jacobian matrix.

The following properties will be used:

$$\frac{\partial \boldsymbol{A}.\boldsymbol{B}}{\partial \boldsymbol{A}} = \mathbf{1}\overline{\otimes}\boldsymbol{B}^T \tag{B.13}$$

$$\frac{\partial \boldsymbol{A}.\boldsymbol{B}}{\partial \boldsymbol{B}} = \boldsymbol{A}\overline{\otimes}\mathbf{1} \tag{B.14}$$

$$\frac{\partial \boldsymbol{A}.\boldsymbol{B}.\boldsymbol{C}}{\partial \boldsymbol{B}} = \boldsymbol{A}\overline{\otimes}\boldsymbol{C}^T \tag{B.15}$$

$$\frac{\partial \boldsymbol{A}^{-1}}{\partial \boldsymbol{A}} = -\boldsymbol{A}^{-1}\overline{\otimes}\boldsymbol{A}^{-T} \tag{B.16}$$

The following derivatives will be used:

$$\boldsymbol{C}_E = \boldsymbol{E}^T.\boldsymbol{E}\,; \qquad \frac{\partial \boldsymbol{C}_E}{\partial \boldsymbol{E}} = \mathbf{1}\overline{\otimes}\boldsymbol{E}^T : T + \boldsymbol{E}^T\overline{\otimes}\mathbf{1} = \mathbf{1}\boldsymbol{E}^T + \boldsymbol{E}^T\overline{\otimes}\mathbf{1} \tag{B.17}$$

The Mandel stress tensor is given by

$$\begin{aligned} \boldsymbol{M} &= J_e\boldsymbol{E}^T.\boldsymbol{E}.\left(C : \frac{1}{2}(\boldsymbol{C}_E - \mathbf{1})\right) = J_e\boldsymbol{C}_E.\left(C : \frac{1}{2}(\boldsymbol{C}_E - \mathbf{1})\right) \\ &= \frac{1}{2}J_e\boldsymbol{C}_E.\left(C : (\boldsymbol{C}_E - \mathbf{1})\right) \end{aligned} \tag{B.18}$$

The derivative of $\boldsymbol{M}$ with respect to $\boldsymbol{C}_E$ can then be computed:

$$\frac{\partial \boldsymbol{M}}{\partial \boldsymbol{C}_E} = \frac{J_e}{2}\left(1\overline{\otimes}(C : (\boldsymbol{C}_E - \mathbf{1}))^T + (\boldsymbol{C}_E\overline{\otimes}\mathbf{1}) : C\right) \tag{B.19}$$

$$= \frac{J_e}{2}\left(1\overline{\otimes}(C : (\boldsymbol{C}_E - \mathbf{1})) + (\boldsymbol{C}_E\overline{\otimes}\mathbf{1}) : C\right) \tag{B.20}$$

Finally

$$\frac{\partial \boldsymbol{M}}{\partial \boldsymbol{E}} = \frac{\partial \boldsymbol{M}}{\partial \boldsymbol{C}_E} : \frac{\partial \boldsymbol{C}_E}{\partial \boldsymbol{E}}$$

With

$$\boldsymbol{n}^\mu = \frac{3}{2}\frac{\boldsymbol{X}}{X_{\text{eq}}} : P^\mu \quad \text{and} \quad \boldsymbol{X} = J : (P^\mu : \boldsymbol{M} - \boldsymbol{b})$$

$$\frac{\partial \boldsymbol{n}^{\mu}}{\partial \boldsymbol{X}} = \frac{3}{2X_{\text{eq}}}\left(I - \frac{3}{2X_{\text{eq}}^2}\boldsymbol{X}\otimes\boldsymbol{X}\right) : P^{\mu} \equiv N^{\mu} \tag{B.21}$$

$$\frac{\partial \boldsymbol{n}^{\mu}}{\partial \boldsymbol{E}} = \frac{\partial \boldsymbol{n}^{\mu}}{\partial \boldsymbol{X}} : \frac{\partial \boldsymbol{X}}{\partial \boldsymbol{M}} : \frac{\partial \boldsymbol{M}}{\partial \boldsymbol{E}} = N^{\mu} : J : P^{\mu} : \frac{\partial \boldsymbol{M}}{\partial \boldsymbol{E}} \tag{B.22}$$

Derivatives of $\boldsymbol{R}_E$

$$\boldsymbol{R}_E = \Delta\boldsymbol{E} - \Delta F.\boldsymbol{F}^{-1}.E - \Delta p\boldsymbol{E}.\boldsymbol{n}^{\mu}$$

$$\frac{\partial \boldsymbol{R}_E}{\partial \Delta \boldsymbol{E}} = I - \left(\Delta F.\boldsymbol{F}^{-1}\right)\overline{\otimes}\mathbf{1} - \Delta p\mathbf{1}\overline{\otimes}\boldsymbol{n}^{\mu T} - \Delta p\left(\boldsymbol{E}\overline{\otimes}\mathbf{1}\right) : \frac{\partial \boldsymbol{n}^{\mu}}{\partial \boldsymbol{E}} \tag{B.23}$$

$$\frac{\partial \boldsymbol{R}_E}{\partial \Delta \boldsymbol{b}} = -\Delta p\left(\boldsymbol{E}\overline{\otimes}\mathbf{1}\right) : \frac{\partial \boldsymbol{n}^{\mu}}{\partial \boldsymbol{X}} : \frac{\partial \boldsymbol{X}}{\partial \boldsymbol{b}} = \Delta p\left(\boldsymbol{E}\overline{\otimes}\mathbf{1}\right) : N^{\mu} : J \tag{B.24}$$

$$\frac{\partial \boldsymbol{R}_E}{\partial \Delta p} = -\boldsymbol{E}.\boldsymbol{n}^{\mu} \tag{B.25}$$

$$\frac{\partial \boldsymbol{R}_E}{\partial \Delta s} = \mathbf{0} \tag{B.26}$$

Derivatives of $\boldsymbol{R}_b$

$$\boldsymbol{R}_b = \Delta\boldsymbol{b} - \Delta pR : \boldsymbol{n}^{\mu}$$

$$\frac{\partial \boldsymbol{R}_b}{\partial \Delta \boldsymbol{E}} = -\Delta pR : \frac{\partial \boldsymbol{n}^{\mu}}{\partial \boldsymbol{E}} \tag{B.27}$$

$$\frac{\partial \boldsymbol{R}_b}{\partial \Delta \boldsymbol{b}} = I - \Delta pR : \frac{\partial \boldsymbol{n}^{\mu}}{\partial \boldsymbol{X}} : \frac{\partial \boldsymbol{X}}{\partial \boldsymbol{b}} = I + \Delta pR : N^{\mu} : J \tag{B.28}$$

$$\frac{\partial \boldsymbol{R}_b}{\partial \Delta p} = -R : \boldsymbol{n}^{\mu} \tag{B.29}$$

$$\frac{\partial \boldsymbol{R}_b}{\partial \Delta s} = \mathbf{0} \tag{B.30}$$

Derivatives of R_p

$$R_p = \Delta p - E(s, M_m)F(s, M_m, X_{\text{eq}})\Delta t$$

$$\frac{\partial R_p}{\partial \Delta \boldsymbol{E}} = -\Delta t \left(\frac{\partial E}{\partial M_m} F + E \frac{\partial F}{\partial M_m} \right) \frac{\partial M_m}{\partial \boldsymbol{M}} : \frac{\partial \boldsymbol{M}}{\partial \boldsymbol{E}} \tag{B.31}$$

$$-\Delta t \left(E \frac{\partial F}{\partial X_{\text{eq}}} \right) \frac{\partial X_{\text{eq}}}{\partial \boldsymbol{M}} : \frac{\partial \boldsymbol{M}}{\partial \boldsymbol{E}} \tag{B.32}$$

$$= -\frac{1}{3} \Delta t \left(\frac{\partial E}{\partial M_m} F + E \frac{\partial F}{\partial M_m} \right) \mathbf{1} : \frac{\partial \boldsymbol{M}}{\partial \boldsymbol{E}} \tag{B.33}$$

$$-\Delta t \left(E \frac{\partial F}{\partial X_{\text{eq}}} \right) \boldsymbol{n}^{\mu} : \frac{\partial \boldsymbol{M}}{\partial \boldsymbol{E}} \tag{B.34}$$

$$\frac{\partial R_p}{\partial \Delta \boldsymbol{b}} = -\Delta t E \frac{\partial F}{\partial X_{\text{eq}}} \frac{\partial X_{\text{eq}}}{\partial \boldsymbol{X}} : \frac{\partial \boldsymbol{X}}{\partial \boldsymbol{b}} = \Delta t E \frac{\partial F}{\partial X_{\text{eq}}} \boldsymbol{n} : J \tag{B.35}$$

$$\frac{\partial R_p}{\partial \Delta p} = 1 \tag{B.36}$$

$$\frac{\partial R_p}{\partial \Delta s} = -\Delta t \left(\frac{\partial E}{\partial s} F + E \frac{\partial F}{\partial s} \right) \tag{B.37}$$

Derivatives of R_s

$$R_s = \Delta s - \left(H_1 \left(1 - \frac{s}{s_1} \right) + H_2 \left(1 - \frac{s}{s_2} \right) \right) \Delta p$$

$$\frac{\partial R_s}{\partial \Delta \boldsymbol{E}} = \mathbf{0} \tag{B.38}$$

$$\frac{\partial R_s}{\partial \Delta \boldsymbol{b}} = \mathbf{0} \tag{B.39}$$

$$\frac{\partial R_s}{\partial \Delta p} = -\left(H_1 \left(1 - \frac{s}{s_1} \right) + H_2 \left(1 - \frac{s}{s_2} \right) \right) \tag{B.40}$$

$$-\left(\frac{\partial H_1}{\partial p} \left(1 - \frac{s}{s_1} \right) + \frac{\partial H_2}{\partial p} \left(1 - \frac{s}{s_2} \right) \right) \Delta p \tag{B.41}$$

$$\frac{\partial R_s}{\partial \Delta s} = 1 + \left(\frac{H_1}{s_1} + \frac{H_2}{s_2} \right) \Delta p \tag{B.42}$$

B.2 Consistent tangent matrix

The calculation of the matrix requires that calculations of the derivatives of the state variable with respect to the input variables ($\mathbf{V}_I = \Delta \boldsymbol{F}$).

$$\boldsymbol{R}_E = \Delta \boldsymbol{E} - \Delta F . \boldsymbol{F}^{-1} . E - \Delta p \boldsymbol{E} . \boldsymbol{n}^{\mu}$$

$$\frac{\partial \boldsymbol{R}_E}{\partial \Delta \boldsymbol{F}} = -\mathbf{1}\overline{\otimes}(\boldsymbol{F}^{-1}.\boldsymbol{E})^T - (\Delta \boldsymbol{F}\overline{\otimes}\boldsymbol{E}^T) : (-\boldsymbol{F}^{-1}\overline{\otimes}\boldsymbol{F}^{-T}) \quad \text{(B.43)}$$

$$= -\mathbf{1}\overline{\otimes}(\boldsymbol{E}^T.\boldsymbol{F}^{-T}) + (\Delta \boldsymbol{F}\overline{\otimes}\boldsymbol{E}^T) : (\boldsymbol{F}^{-1}\overline{\otimes}\boldsymbol{F}^{-T}) \quad \text{(B.44)}$$

When the input variables are changed, the state variables change so that $\mathbf{R} = (\boldsymbol{R}_E, \boldsymbol{R}_b, R_p, R_s)$ remains zero, so that

$$\delta\mathbf{R} = \mathbf{0} = \frac{\partial \mathbf{R}}{\partial \mathbf{V}_S}.\delta\mathbf{V}_S + \frac{\partial \mathbf{R}}{\partial \mathbf{V}_I}.\delta\mathbf{V}_I$$

so that

$$\delta\mathbf{V}_S = -\left(\left(\frac{\partial \mathbf{R}}{\partial \mathbf{V}_S}\right)^{-1}.\frac{\partial \mathbf{R}}{\partial \mathbf{V}_I}\right).\delta\mathbf{V}_I$$

From this equation it is possible to extract the sub-matrix such that:

$$\delta\boldsymbol{E} = K_E : \delta\boldsymbol{F}$$

Calculation of $\partial\boldsymbol{\sigma}/\partial\boldsymbol{F}$

One has:

$$\boldsymbol{\sigma} = \frac{1}{J_e}\boldsymbol{E}^{-T}.\boldsymbol{M}.\boldsymbol{E}^T$$

$\partial\boldsymbol{\sigma}/\partial\boldsymbol{E}$ can be expressed using the sum of three terms.

$$\kappa_1 = (\mathbf{1}\overline{\otimes}(\boldsymbol{E}.\boldsymbol{M}^T)) : (-\boldsymbol{E}^{-T}\overline{\otimes}\boldsymbol{E}^{-1}) : T \quad \text{(B.45)}$$

$$\kappa_2 = (\boldsymbol{E}^{-T}\overline{\otimes}\boldsymbol{E}) : \frac{\partial \boldsymbol{M}}{\partial \boldsymbol{E}} \quad \text{(B.46)}$$

$$\kappa_3 = ((\boldsymbol{E}^{-T}.\boldsymbol{M})\overline{\otimes}\mathbf{1}) : T \quad \text{(B.47)}$$

$$\frac{\partial \boldsymbol{\sigma}}{\partial \boldsymbol{E}} = \frac{1}{J_e}(\kappa_1 + \kappa_2 + \kappa_3) \quad \text{(B.48)}$$

$$\frac{\partial \boldsymbol{\sigma}}{\partial \boldsymbol{F}} = \frac{\partial \boldsymbol{\sigma}}{\partial \boldsymbol{E}} : K_E \quad \text{(B.49)}$$